Title

Performance & Techno-Economic Analysis of Hydrogen Powered Propulsion for Flight

Permalink

https://escholarship.org/uc/item/93q3t0sx

Author

Alsamri, khaled

Publication Date

2024

Peer reviewed|Thesis/dissertation

UNIVERSITY OF CALIFORNIA,
IRVINE

Performance & Techno-Economic Analysis of Hydrogen Powered Propulsion for Flight

DISSERTATION

submitted in partial satisfaction of the requirements
for the degree of

DOCTOR OF PHILOSOPHY

in Mechanical and Aerospace Engineering

by

Khaled Alsamri

Dissertation Committee:
Professor Jack Brouwer, Chair
Assistant Professor Jacqueline Huynh
Professor Vince McDonell

2024

DEDICATION

To the challenges that shaped me, and the dreams that guided me.
To the grace and guidance of God, who has been my strength throughout this journey.
To the unwavering support of my loved ones and the mentors who grew passion within me.

TABLE OF CONTENTS

LIST OF FIGURES

LIST OF TABLES

ACKNOWLEDGMENTS

VITA

Khaled Alsamri

EDUCATION

Doctor of Philosophy in Mechanical and Aerospace Engineering   **2021 - Nov 2024**
University of California, Irvine   *Irvine, CA*
Master of Engineering in Mechanical and Aerospace Engineering   **2020 - 2021**

University of California, Irvine   *Irvine, CA*
Bachelor of Science in Mechanical Engineering   **2016 - 2020**

Florida Institute of Technology   *Melbourne, FL*

REFEREED JOURNAL PUBLICATIONS

- **Khaled Alsamri**, Jessica De la Cruz, Melody Emmanouilidi, Jacqueline Huynh, and Jack Brouwer. "Methodology for Assessing Retrofitted Hydrogen Combustion and Fuel Cell Aircraft Environmental Impacts," *Journal of Propulsion and Power*, 2024, 40(5): 661-676.

- **Khaled Alsamri**, Sajjad Rezaei, Vanessa Chung, Jacqueline Huynh, and Jack Brouwer. "Dynamic Modeling of Hydrogen SOFC/GT Powered Aircraft with Integration Analysis," AIAA 2024-1532. *AIAA SCITECH 2024 Forum*, January 2024.

- Oi Ching Vanessa Chung, **Khaled Alsamri**, Jacqueline L. Huynh, and Jack Brouwer. "Design Methodology of Hydrogen Solid Oxide Fuel Cells Propulsion System in Blended Wing Body Aircraft," AIAA 2024-3664. *AIAA AVIATION FORUM AND ASCEND 2024*, July 2024.

- Rezaei, Sajjad, **Khaled Alsamri**, Elio Simeoni, Jacqueline Huynh, and Jack Brouwer. "Techno-Economic Assessment of Green Hydrogen Infrastructure Implementation: A Case Study for Los Angeles International Airport (LAX), USA." *246th ECS Meeting*. ECS, 2024.

ABSTRACT OF THE DISSERTATION

Performance & Techno-Economic Analysis of Hydrogen Powered Propulsion for Flight

By

Khaled Alsamri

Doctor of Philosophy in Mechanical and Aerospace Engineering

University of California, Irvine, 2024

Professor Jack Brouwer, Chair

Aviation contributes approximately 2.4% of global CO_2 emissions, and with the anticipated increase in flight demand, these emissions are expected to grow significantly, posing a major challenge for the industry's sustainability. Hydrogen propulsion has emerged as a promising solution to mitigate the environmental impact of aviation by providing a pathway toward zero-emission flight.

The exploration of this potential is conducted via a multifaceted approach, encompassing the modeling, performance analysis and retrofit of existing aircraft, the development of next-generation configurations, and the dynamic, electrochemical modeling of conceptualized hydrogen fuel cell powertrain. Additionally, it includes the techno-economic analysis for the transformation of airport infrastructure to support hydrogen-powered aviation, advancing the integration of hydrogen technologies across the aviation ecosystem. This approach ensures a holistic understanding of hydrogen's potential and challenges in revolutionizing the aviation sector.

The research begins with a detailed retrofitting methodology applied to a Cessna Citation XLS+, incorporating hybrid systems that combine hydrogen combustion with Solid Oxide Fuel Cell/Gas Turbine (SOFC/GT) technology. Technical modifications, such as designing cryogenic liquid hydrogen tanks with optimized insulation, sizing, and center of gravity adjustments, achieve a 5% reduction in takeoff weight for hydrogen combustion and a 0.4% reduction for the SOFC hybrid configuration, albeit with reduced passenger capacity to accommodate the tanks. These modifications reveal critical trade-offs in aircraft design, highlighting the balance between weight

reduction and capacity.

Building on this foundation, dynamic modeling of a Cessna S550 Citation S/II equipped with an SOFC/GT system evaluates the system's ability to manage real-time flight dynamics, demonstrating efficiency peaks of up to 71.4% while underscoring the essential role of battery integration to support rapid power needs during takeoff, descent, and landing. This study provides a valuable contribution to understanding the integration and operational efficiency challenges of hydrogen fuel cell systems in aviation.

The research then explores innovative Blended Wing Body (BWB) designs, specifically the BWB-365 and BWB-162 models, revealing fuel efficiency improvements of 22.7% and 28.7%, respectively, over traditional designs. It also identifies the challenges of integrating SOFC/GT powertrains with hydrogen storage into sized Tube-&-Wing aircraft, which may require fuselage modifications to maintain payload capacity, offering insights into the design considerations for future hydrogen-powered aircraft.

Further retrofit analysis is conducted on the ATR42-600, a regional turboprop, retrofitted with hydrogen power systems. Comparisons between PEMFC, SOFC/GT, hydrogen combustion, and battery-electric configurations reveal significant trade-offs, particularly highlighting the limitations of battery-electric technology for regional aircraft.

The narrative culminates in a techno-economic assessment of green hydrogen supply infrastructure at Los Angeles International Airport, projecting that advancements in renewable energy capacity and optimized hydrogen logistics could lower the Levelized Cost of Hydrogen (LCOH) to $3.65/kg by 2050 with a year-round hourly analysis and potentially decreasing further based on seasonal storage methods. This comprehensive analysis provides a pathway to realizing sustainable aviation, balancing technical feasibility, economic viability, and environmental impact.

0.1. Nomenclature

$C_{p,Air}$	=	Specific Heat Capacity of Air
d	=	Height of the Spherical Head
d_1	=	Width of Spherical Head
d_o	=	Radius of Inner Tank
$EI(X)$	=	Emission Index of Species X
e_w	=	Weld Efficiency
FOS	=	Factor of Safety
g	=	Acceleration due to Gravity on Earth
G	=	Mixing Line Slope
h	=	Cruising Altitude
H	=	Hydrogen
h_f	=	Heat Energy Available per Unit Weight of Fuel
K	=	Geometrical Constant
K_{ins}	=	Thermal Conductivity of Insulation
L	=	Length of the Cylindrical Part of Tank
λ_{tank}	=	Total Length of Tank
L_{cyl}	=	Length of Cylinder
LHV_{fuel}	=	Lower Heat Value of Fuel
LH_2	=	Liquid Hydrogen Fuel
$\frac{L}{D}$	=	Lift-to-Drag Ratio
$M_{boiloff}$	=	Mass Boiloff
$m_{filled\ capsule}$	=	Mass of Filled Capsule
M_H	=	Mass of Hydrogen
m_t	=	Mass of Tank
$\dot{m}_{air}$	=	Mass Flow Rate of Air

1

$\dot{m}$	=	Mass Flow Rate
$\dot{m}_{fuel}$	=	Mass Flow Rate of Fuel
$\dot{m}_{H_2}$	=	Mass Flow Rate of Hydrogen
$\dot{m}_{H_2O}$	=	Mass Flow Rate of Water
$\dot{m}_{steam}$	=	Mass Flow Rate of Steam
MAC	=	Mean Aerodynamic Chord
NUD	=	Nusselt Number
P	=	Pressure
P_a	=	Ambient Pressure at Altitude
P_{des}	=	Pressure for Hydrogen Storage
Pr	=	Prandtl Number
q	=	Heat Loss
Q	=	Heat Transfer Rate
r	=	Radius
r_1	=	Radius of Inner Vessel
r_2	=	Radius of Outer Shell
r_{ins}	=	Radius of Insulation
R	=	Range
Re_d	=	Reynolds Number
T	=	Temperature
T_o	=	Outside Temperature
T_i	=	Inside Temperature
T_1	=	Outside Temperature
T_2	=	Inside Temperature
t_w	=	Wall Thickness
t_{wh}	=	Wall Hemisphere Thickness
TWW	=	Tank-to-Wheel

V_i	=	Excess Volume
V_t	=	Tank Volume
V_{out}	=	Volume Out
V_{system}	=	Volume of tank system
WTT	=	Well-to-Tank
WTW	=	Well-to-Wheel
W_{to}	=	Maximum Takeoff Weight
W_{fuel}	=	Fuel Weight
ϵ_{H_2O}	=	Molar Mass of Water over Mass of Dry Air
$\eta_{overall}$	=	Overall Engine Efficiency
λ_t	=	Tank Sizing Constraints
λ_{cabin}	=	Tank Sizing Cabin Constraints
σ_a	=	Tensile Strength of Material for Cryogenic Tank
ρ	=	Density
τ_{allow}	=	Allowable Shear Stress
(h)	=	Property at Altitude
(st)	=	Property at Standard Temperature
(H_2)	=	Property for Hydrogen
$(*)$	=	Per Segment
$C_{p,Air}$	=	Specific Heat Capacity of Air
d	=	Height of the Spherical Head
d_1	=	Width of Spherical Head
d_o	=	Radius of Inner Tank
$EI(X)$	=	Emission Index of Species X
e_{weld}	=	Weld Efficiency
FOS	=	Factor of Safety
g	=	Acceleration due to Gravity on Earth

G	=	Mixing Line Slope
h	=	Cruising Altitude
H	=	Hydrogen
h_f	=	Heat Energy Available per Unit Weight of Fuel
K	=	Geometrical Constant
K_{ins}	=	Thermal Conductivity of Insulation
L	=	Length of the Cylindrical Part of Tank
λ_{tank}	=	Total Length of Tank
L_{cyl}	=	Length of Cylinder
LHV_{fuel}	=	Lower Heat Value of Fuel
LH_2	=	Liquid Hydrogen Fuel
L/D	=	Lift-to-Drag Ratio
$M_{boiloff}$	=	Mass Boiloff
$m_{filledcapsule}$	=	Mass of Filled Capsule
M_H	=	Mass of Hydrogen
m_t	=	Mass of Tank
$\dot{m}_{air}$	=	Mass Flow Rate of Air
$\dot{m}$	=	Mass Flow Rate
$\dot{m}_{fuel}$	=	Mass Flow Rate of Fuel
$\dot{m}_{H_2}$	=	Mass Flow Rate of Hydrogen
$\dot{m}_{H_2O}$	=	Mass Flow Rate of Water
$\dot{m}_{steam}$	=	Mass Flow Rate of Steam
MAC	=	Mean Aerodynamic Chord
Nu_D	=	Nusselt Number
P	=	Pressure
P_a	=	Ambient Pressure at Altitude
P_{des}	=	Pressure for Hydrogen Storage

Pr	=	Prandtl Number
q	=	Heat Loss
Q	=	Heat Transfer Rate
r	=	Radius
r_1	=	Radius of Inner Vessel
r_2	=	Radius of Outer Shell
r_{ins}	=	Radius of Insulation
k	=	Thermal conductivity of the material
R	=	Range
Re_D	=	Reynolds Number
T	=	Temperature
T_o	=	Outside Temperature
T_i	=	Inside Temperature
T_{atm}	=	Atmosphere temperature surrounding the cylinder
h	=	Convective heat transfer coefficient
ε	=	Emissivity of the surface
σ	=	Stefan-Boltzmann constant
t_w	=	Wall Thickness
t_{wh}	=	Wall Hemisphere Thickness
TWW	=	Tank-to-Wheel
V_i	=	Excess Volume
V_t	=	Tank Volume
V_{out}	=	Volume Out
V_{system}	=	Volume of tank system
WTT	=	Well-to-Tank
WTW	=	Well-to-Wheel
W_{to}	=	Maximum Takeoff Weight

W_{fuel}	=	Fuel Weight
ϵ_{H_2O}	=	Molar Mass of Water over Mass of Dry Air
$\eta_{overall}$	=	Overall Engine Efficiency
λ_t	=	Tank Sizing Constraints
λ_{cabin}	=	Tank Sizing Cabin Constraints
σ_a	=	Tensile Strength of Material for Cryogenic Tank
ρ	=	Density
τ_{allow}	=	Allowable Shear Stress
$()_h$	=	Property at Altitude
$()_{st}$	=	Property at Standard Temperature
$()_{H_2}$	=	Property for Hydrogen
$()_t$	=	Property for tank
$()_f$	=	Property for fuel
$()_t$	=	Property for tank
$()_{eq}$	=	equivalent
$()^*$	=	Per Segment
A	=	area
a_{takeoff}	=	takeoff acceleration (m/s^2)
AOA	=	angle of attack
AR	=	aspect ratio
C_p	=	specific heat at constant pressure (J/kg·K)
CAD	=	computer aided design
D_{NAC}	=	nacelle diameter (m)
D_{total}	=	total drag (N)
F_{THRUST}	=	thrust force (N)
GT	=	gas turbine
h	=	heat transfer coefficient (W/m^2·K)

L	=	characteristic length (m)
L/D	=	lift to drag ratio, or aerodynamic efficiency
LH_2	=	liquid hydrogen
LHV	=	lower heating value (J/kg)
Ma	=	Mach number
mac	=	mean aerodynamic chord (m)
MTOW	=	maximum takeoff weight
$\dot{m}_{air,compressor}$	=	air entering the compressor (kg/s)
$\dot{m}_{air,fuelheater}$	=	air entering the fuel heater (kg/s)
$\dot{m}_{air,SOFC}$	=	air entering the SOFC (kg/s)
$\dot{m}_{combustor}$	=	combined flow entering the combustor (from SOFC and fuel) (kg/s)
$\dot{m}_{exhaust}$	=	exhaust flow from turbines (kg/s)
$\dot{m}_{fuel,combustor}$	=	fuel flow directly to the combustor (kg/s)
$\dot{m}_{fuel,pump}$	=	fuel flow towards the fuel pump (kg/s)
$\dot{m}_{loss}$	=	heat loss from the fuel heater (W)
$\dot{m}_{steam}$	=	steam flow towards the SOFC (kg/s)
$\dot{m}_{turbines}$	=	flow from combustor to turbines (kg/s)
n_{GH_2}	=	moles of gaseous hydrogen (mol)
Nu	=	Nusselt number
OEW	=	operating empty weight
P	=	pressure (Pa)
PAX	=	passenger
Pr	=	Prandtl number
$P_{saturation, water}$	=	saturation pressure of water (Pa)
$P_{saturation, ice}$	=	saturation pressure of ice (Pa)
$Q_{conduction}$	=	heat transfer due to conduction (W)
$Q_{convection}$	=	heat transfer due to convection (W)

$Q_{\text{radiation}}$	=	heat transfer due to radiation (W)
Q_{total}	=	total heat transfer (W)
R	=	thermal resistance (Ω)
R_{gas}	=	gas constant (J/mol·K)
Re	=	Reynolds number
SOFC	=	solid oxide fuel cell
T_{NAC}	=	nacelle constant
T_{air}	=	air temperature (K)
T_{surface}	=	surface temperature (K)
T&W	=	tube-and-wing
TOFL	=	takeoff field length (m)
t/c	=	thickness to chord ratio
U_{gas}	=	internal energy of gas (J)
V_{takeoff}	=	takeoff velocity (m/s)
W_{empty}	=	aircraft empty weight (kg)
W_{fuel}	=	fuel weight (kg)
W_{NAC}	=	nacelle weight (kg)
$W_{\text{op. items}}$	=	operating items weight (kg)
W_{payload}	=	payload weight (kg)
$W_{\text{propulsion}}$	=	propulsion weight (kg)
$W_{\text{structure}}$	=	airframe structure weight (kg)
W_{systems}	=	systems and equipment weight (kg)
X_{NAC}	=	nacelle length (m)
ZFW	=	zero fuel weight (kg)
γ	=	climb/descent angle (rad)
$\epsilon_{\text{H}_2\text{O}}$	=	emissivity of water
η	=	efficiency

μ	=	dynamic viscosity (Pa·s)
ρ	=	density (kg/m^3)
V	=	Cell voltage (V)
v_{rev}	=	Standard electrode potential (V)
R	=	Universal gas constant (J/mol·K)
T	=	Temperature (K)
n	=	Number of electrons transferred
F	=	Faraday's constant (C/mol)
ρ	=	Density (kg/m^3)
P_{O_2}	=	Partial pressure of O_2 (atm)
P_{H_2}	=	Partial pressure of H_2 (atm)
$P_{\text{H}_2\text{O}}$	=	Partial pressure of H_2O (atm)
P_{stack}	=	Stack power (kW)
η	=	Overpotential (mV)
j	=	Current (A)
j_0	=	Exchange current density (A/m^2)
C_P	=	Constant pressure specific heat (kJ/kg·K)
C_V	=	Constant volume specific heat (kJ/kg·K)
D_h	=	Hydraulic diameter (m)
G	=	Gibbs free energy (kJ)
h	=	Specific enthalpy (kJ/mol)
h_c	=	Convective heat transfer coefficient (W/m^{2}K)
$\dot{m}$	=	Mass flow rate (kg/s)
$\dot{n}$	=	Molar flow rate (kmol/s)
η	=	Efficiency / overpotential
N_{Flow}	=	Normalized mass flow
N_{RPM}	=	Normalized shaft speed

Nu	=	Nusselt number
PR	=	Pressure ratio
k	=	Thermal conductivity (W/m·K)
U_{fuel}	=	Fuel utilization
Q	=	Heat transferred (kJ)
W	=	Work (kJ)
R	=	Range (m)
g	=	Gravitational constant (m/s^2)
w_{fuel}	=	Weight of fuel (kg)
η	=	Propulsion system efficiency
h_f	=	Fuel specific energy
L/D	=	Aerodynamic efficiency
ρ	=	Density of air (kg/m^3)
v	=	Velocity (m/s)
D	=	Drag (N)
S_{ref}	=	Wing reference area (m^2)
C_{D_0}	=	Profile drag coefficient
C_{D_c}	=	Compressibility drag coefficient
$C_{D_{\text{gear}}}$	=	Landing gear drag coefficient
C_{D_I}	=	Induced drag coefficient
γ	=	Climb angle (°)
RPM	=	Rotations per minute
EFF	=	Efficiency
$T_{\text{cath in}}$	=	Cathode inlet temperature (K)
$T_{\text{anode in}}$	=	Anode inlet temperature
T_{cell}	=	Cell temperature (K)
I_{charge}	=	Charging current (A)

$I_{\text{discharge}}$	=	Discharging current (A)
V_{nom}	=	Nominal voltage (V)
C_{bat}	=	Battery capacity (Ah)
R_{int}	=	Internal resistance (Ω)
D_{charge}	=	Depth of discharge (DoD, %)
SOC	=	State of charge (%)
SOH	=	State of health (%)
E_{battery}	=	Energy capacity (kWh)
P_{battery}	=	Power output (kW)
η_{charge}	=	Charging efficiency (%)
$\eta_{\text{discharge}}$	=	Discharging efficiency (%)
C_{rate}	=	Charge/discharge rate (C-rate)
t_{charge}	=	Charging time (h)
$t_{\text{discharge}}$	=	Discharging time (h)
X_P	=	Performance coefficient (unitless)
λ_{sc}	=	Cooling coefficient (unitless)
T_h	=	Hot side temperature (K)
T_c	=	Cold side temperature (K)
η_c	=	Cooling efficiency (%)
P_c	=	Cryocooler power (kW)
P_s	=	System power (kW)

Subscripts

rev	=	Reversible
act	=	Activation
conc	=	Concentration
a	=	Anode
c	=	Cathode

isen	=	Isentropic
Total Annual Cost	=	Total annual cost (currency)
$CAPEX_i$	=	Capital expenditure for component i (currency)
CRF_i	=	Capital recovery factor for component i (dimensionless)
$OPEX_i$	=	Operating expenditure for component i (currency)
m_{H_2}	=	Annual hydrogen production (kg/year)
Solar_Power_GW (i)	=	Solar power generated at index i (GW)
Solar_Radiation_W_m^2(i)	=	Solar radiation at index i (W/m^2)
solar_area	=	Solar panel area (m^2)
solar_efficiency	=	Solar panel efficiency (dimensionless)
Wind_Power_GW (i)	=	Wind power generated at index i (GW)
air_density	=	Air density (kg/m^3)
sweep_area	=	Turbine sweep area (m^2)
Wind_speed_m_s (i)	=	Wind speed at index i (m/s)
rotor_efficiency	=	Rotor efficiency (dimensionless)
Number_of_Turbines	=	Number of turbines (dimensionless)

1. Introduction and Background

1.1. Introduction

The aerospace industry & specifically the aircraft industry has been using the same fossil fuel powered engines for decades. Whether its jet engines in a Boeing 777 or an Internal combustion powered propeller in a Cessna 172. However, this comes at a great cost, "the EPA reports that the aviation industry contributes 12% of the United States transportation emissions & 3% of total greenhouse emissions" [6]. Aviation also contributed 2.4% of global CO2 emissions in 2018 [6]. The combustion of kerosene is responsible for the emission of other pollutants such as carbon monoxide (CO), hydrocarbons (HC), nitrogen oxides (NOx), sulfur oxides (Sox), & particulate matter. NOx, SOx, CO, HC, and particulate matter are correlated with air quality problems while CO2 and (to a lesser extent) nitrogen dioxide (N2O), and particles are correlated with climate change [7]. As airline traffic is forecasted to increase by approximately 4% annually from 2022 to 2040, the environmental impact and pollution levels in the vicinity of airports have escalated as pressing concerns [8]. However, from the year 2009 to 2020 fuel efficiency of airplanes increased by only 1.5%. Hence, companies are looking for other ways to become more environmentally friendly.

For these reasons, aerospace companies such as Airbus are set to release a commercial aircraft that produces zero emissions by 2035. ZeroAvia has also piloted the first commercial LH2 powered flight in 2020, with a Fuel-cell-electric-motor system [9]. These aircraft applications are (or will be) powered by a variety of engines such as turbo-propeller, turbo-fan engines, battery & fuel cell powered electric motor propellers [10]. In flight all these aircraft produce zero greenhouse gas emissions. While the combustion of renewable fuels produces criteria pollutant emissions in flight, neither fuel cell nor battery powered systems produces any criteria pollutant emissions. Upstream

emissions of either greenhouse gas or criteria pollutant emissions for all these routes depends upon the physics, chemistry, and dynamics of the production of renewable fuels, renewable hydrogen, and renewable electricity.

As promising as these hydrogen dependent power systems are, it is important to acknowledge a few of the obstacles. First, even though liquid hydrogen (at -253 °C ,1atm) has triple the gravimetric energy density of JET-A fuel (at 15°C ,1atm) it also has almost 1/4th the volumetric energy density [11]. This means "hydro-planes" will need much larger fuel storage space dedicated to the aircraft. Other synthetic fuels also tend to have much lower gravimetric and volumetric energy densities compared to petroleum distillate fuels. Other difficulties include startup time of fuel cells, the effect of altitude on fuel cells, the emission of NOx from hydrogen combustion, storing and cooling liquid hydrogen, etc.

Hydrogen-powered Solid Oxide Fuel Cell (SOFC) hybrid systems and SOFC/gas turbine (GT) integrations show considerable promise in reducing emissions and enhancing efficiency, with stationary applications achieving efficiencies of up to 75%, significantly higher than the 40–42% efficiency of current aircraft gas turbines [12]. Hydrogen adoption as a fuel source could decrease CO_2 emissions by 2% to 12% by 2050, as it primarily emits water vapor, NO_x, and minimal greenhouse gases [13]. However, this transition necessitates substantial aircraft design modifications, including larger fuel tanks and trade-offs concerning balance and range. Key challenges include hydrogen storage and cooling, NO_x emissions reduction, and aircraft adaptation to alternative fuels. Addressing these issues requires integration analysis for conventional aircraft, exploration of innovative designs such as Blended Wing Body (BWB), dynamic modeling of hydrogen power systems, and extensive research to validate the feasibility of hydrogen-based technologies under varied flight conditions. This dissertation aims to facilitate the shift to sustainable aviation by proposing solutions for implementing hydrogen in aircraft propulsion.

1.2. Background

1.2.1. Investigation into hydrogen use in aviation:

Hydrogen in application

Research into the combustion of hydrogen and synthetic e-fuels in aviation gas turbines has been ongoing. However, the incorporation of hydrogen fuel cells into aviation is more recent, as their efficiencies have only lately become practical for aviation applications. E-fuels leverage the historical advancements of gas turbines, needing only incremental modifications for integration. Yet, the application of both fuel types is still in developmental stages, requiring further research for their safe flight incorporation. This study will scrutinize and model the key parameters that affect the reliability of aircraft utilizing these fuels. In aviation, mass is a limiting factor; hence, the unsuccessful adoption of lithium-ion batteries for larger aircraft contrasts with their prevalence in electric vehicles. Hydrogen's gravimetric energy density, at 2.6 times that of conventional Jet-A fuel used in aviation, suggests that a hydrogen-fueled aircraft could theoretically be lighter than its kerosene counterpart [7] The practical total weight, however, is influenced by the storage technology implemented, which yields less optimistic figures. Meanwhile, as green hydrogen production becomes more cost-effective with advancing technology, and oil prices are projected to rise due to growing energy demands, green hydrogen emerges as a viable contender to reduce fossil fuel dependence and mitigate environmental impact. Yet, the integration challenges are formidable. With liquid hydrogen at -253°C and 1 atm having a volumetric energy density four times lower than Jet-A fuel at 15°C and 1 atm, the resulting design may require larger aircraft or reduced cargo capacity [7]. The additional weight from more complex fuel systems and heavy storage tanks in fuel-cell applications dilutes the advantage of hydrogen's lower mass. The necessary reconfiguration for existing aircraft production demands significant investments and policy backing.

1.2.2. Bottom of Form Zero emission Commercial Aviation

As of late 2023, the aerospace industry is advancing toward zero-emission flight with key players developing varied sustainable technologies. Airbus's ZEROe project aims to launch hydrogen-fueled aircraft with modified turbines by 2035, representing a significant evolution in engine technology. Boeing is exploring electric propulsion and sustainable fuels to mitigate aviation's environmental impact, with timelines for commercial release still under development [10, 14]. Meanwhile, ZeroAvia focuses on hydrogen-electric engines for regional planes, anticipating market entry by the mid-2020s after successful prototype testing. Pipistrel has already introduced the Velis Electro, the first electric plane certified for training, evidencing the viability of electric powertrains in aviation. Meanwhile, Universal Hydrogen is progressing with hydrogen retrofit kits for turboprops, targeting a 2025 commercial release. This movement toward eco-friendly aviation reflects a growing commitment to reducing carbon emissions through innovative engineering solutions.

It's important to note there's a diverse class of commercial aircraft technologies, each facing a different set of difficulties with integrating low emission powertrains. Smaller, short-range airplanes include piston aircraft, turboprops, electric-propellers and jets. Higher volume, longer range aircraft include Narrow & wide body airliners, and military aircraft. Mid-range aircraft usually are classified as passenger jet or Private jets. That being said, the trajectory of aerospace enterprises indicates a focus on developing large, sustainable aircraft by industry giants like Airbus and Boeing, primarily driven by sustainable fuel sources and hydrogen combustion technologies. In contrast, aerospace startups such as ZeroAvia and Universal Hydrogen are concentrating on the niche of 19-seat aircraft, leveraging Proton Exchange Membrane Fuel Cells (PEMFC), which are currently more prevalent in commercial fuel cell applications.

1.2.3. Hydrogen vs. Kerosene Combustion

Many studies credit LH2 as a possible replacement to Kerosene based jet fuels. The primary reasons for replacing conventional fossil fuel include GHG and criteria pollutant emissions reductions and primary energy resource sustainability. There is also a finite amount of fossil fuels that is non-renewable and will eventually run out. Nevertheless, 95% of hydrogen in the world is formed by reforming natural gas (Gray hydrogen) via steam methane reforming (SMR) method. Using Gray hydrogen means hydrogen-powered airplanes will still be responsible for certain GHG emissions & criteria pollutants.

Renewable & green hydrogen can be produced via electrolysis (splitting water molecules into H_2 & $\frac{1}{2} O_2$) powered by renewable energy. Renewable hydrogen can also be made via biogenic routes (biomass gasification). However, biomass gasification can still be responsible of GHG emissions that can be reduced by crops that offset CO_2. Waste streams must be managed & some of the organic waste can be converted to other fuels (including hydrogen) for this process to be as environment friendly as possible. The inconvenience is green hydrogen costs $3-7.50/kg (IEA, 2018) while gray hydrogen from SMR costs $2/kg in the USA.

According to a detailed analysis done by [7] it was claimed that for a redesigned Airbus A319-100. "Replacing kerosene with LH_2 combustion reduces CO_2 emissions by 140 kg CO_2/MWh for hydrogen produced using low carbon sources". Hydrogen combustion still emits NO_x, but in lower levels than kerosene. Hydrogen properties requires the redesign of many components of an aircraft engine. These changes include a "shorter combuster, changes to fuel system components, pump, supply pipes, control valves, and adding heat exchanger to heat the cryogenic liquid before combustion" [7]. These changes for a hydrogen GT are estimated to reduce engine size by 25% compared to the conventional kerosene-fuelled GT's we have today. Hydrogen would also need to be stored in Liquid phase which requires cryogenic temperatures much lower than Kerosene. Pressurized & well insulated tanks are required for hydrogen, meaning kerosene tanks can't be repurposed.

Hydrogen has a faster flame speed vs. Kerosene, meaning a shorter combustor that requires less cooling & hence a lighter, smaller engine is possible [7]. Other alterations should be done for a LH2 engine to the "fuel system components, pump, supply pipes, control valves, and adding heat exchanger to heat the cryogenic liquid before combustion" [7]. These changes to a hydrogen GT are estimated to reduce engine size by 25% compared to the conventional kerosene-fuelled GT's [15]. Hydrogen would also need to be stored in Liquid phase which requires cryogenic temperatures much lower than Kerosene. Pressurized & well insulated tanks are required for hydrogen, meaning kerosene tanks can't be repurposed. A performance comparison done by (Corchero & Montanes, 2005) between kerosene & hydrogen on a Tu-324/414 aircraft powered by two Rolls-Royce BR710-48 turbo-fan engines, shows a decrease in specific energy consumption of 1.73% at sea level static and 1.06% at cruise phase (36,000 ft & Mach number = 0.8) for hydrogen. The surprising increased performance for hydrogen is credited to decreasing mass flow, decreased mass & changes in fuel composition during combustion [16]. Hydrogen also has a 37K lower Turbine inlet temperature which means longer engine life and lower maintenance costs.

According to most data hydrogen combustion aircraft favors long range, high payload & volume because storing hydrogen will require 4 times more space and hence it makes more sense if integrated into larger aircraft. Research into the safety of hydrogen shows it can be safely contained, and gaseous hydrogen at 1atm can be safer than kerosene if it leaks as it evaporates & rises away rather than forming a burning carpet like kerosene [11]. An assessment in [17] shows in which safety parameters hydrogen loses & outperforms kerosene; no clear winner declared. In general, safely storing, handling & transporting hydrogen is no longer a problem [18]. More research needs to be done for hydrogen's infrastructure & lowering green hydrogen's cost as well as its hydrogen combustion safety & stability in GT jet engines. This dissertation will also help determine if hydrogen combustion is the better option moving forward or hydrogen fuel cells that have increased efficiency and lowered cost in the past years.

1.2.4. Alternative Hydrocarbons

Hydrocarbons, which include Biofuels and synthetic fuels are the carbon neutral options that are most widely deployed in the present time, due primarily to nearly "drop-in" performance in current commercial aircraft. That is, very few modifications to the fuel storage, transport, and GT engine conversion components are required to use these fuels. Biofuels (Methanol, ethanol, etc.) or BTL (bio to liquid) are fuels derived from biomass such as feedstock usually using the Fischer-Tropsch process (produces liquid hydrocarbons using a mixture of CO & H_2) [11]. Biomass fuels can reduce CO_2 emissions in flight by up to 94% [19]. Synthetic fuels or PTL (power to liquid fuels) are hydrocarbon fuels that can be carbon neutral if green H_2 & CO from sustainable sources are used. Some of the conversion methods used are methanization, electrolysis, Haber-bosch, etc [20]. Though, synthetic fuels have lower production efficiency & would consume more renewable energy to make than green hydrogen [19]. Literature shows that BTL is better in the short-term & PTL in the long term. However, biofuel systems require a costly investment for the transitioning infrastructure. Also, biofuels might have some potential if mixed with kerosene but otherwise its unsustainable due the amount of land that would be required. For reference, a mixture of 15% soybeans biofuel (SEM) with Jet-A requires a farming land the size of Florida for the USA fleet alone [15]. That's why, a better plan is to prioritize synthetic fuels from inception [20]. Synthetic fuels from coal, gas, or feedstock that go through the Fischer-Tropsch process have higher $\frac{Hydrogen}{Carbon}$ ratio that result in lower emissions [15]. These fuels are beneficial when used as drop-in fuels into existing gas turbine technology as they mimic kerosene combustion & require little to no adjustment.

For the meantime many countries are looking into mixing these hydrocarbons with Kerosene to lower GHG emissions. E-kerosene or synthetic kerosene is a sustainable aviation fuel (SAF) that can be mixed with kerosene to reduce GHG emissions by as much as 80%. However, cost, low production and the fact that renewable energy may be used only to various degrees in the upstream production processes, and that criteria pollutants may also be emitted in upstream processes are hurdles facing the application. Countries such as Germany have already put plans to integrate

e-kerosene into their aviation industry.

Furthermore, more options exist like liquified hydrocarbons, liquified propane, butane, petroleum gases, dimethoxymethane (DMM) & synthetic Dimethyl ether (DME). However, these gases have storage issues similar to cryogens. Additionally, the alcohols methanol & ethanol are an option for aviation fuel, but they have very bad heats of combustion that make them unfeasible. For example, ethanol has 60% & 64% lower volumetric & gravimetric energy densities. Fuel consumption would increase by 15% for a 926km flight & 26% for a 5,556km flight [15]. Making it especially unfeasible for long range.

Moreover, all hydrocarbons have a great disadvantage against hydrogen because of the direct CO_2 emissions that must either be captured out of the air, or somehow recycled into the production stream (e.g., via plant photosynthesis) to close the carbon balance. There are methods that hydrocarbons can be made with low emissions such as using green hydrogen. However, full combustion of hydrocarbons still releases water & CO_2. Additionally, incomplete combustion, is the bigger problem as it releases many more polluting gases. A few of those toxic pollutants are CO, NO, SO_2 and other organics like benzene & acetone that harm human health. Even with the most modern, advanced and low-polluting of combustion technologies, these pollutant emissions cannot be completely eliminated.

1.2.5. Fuel Cells in Aviation

Fuel cells integration into flight is the least developed in green aviation. Now with increasing cell efficiency, decreasing cost of cells & green H2, fuel cells (FC) show great potential in aviation. Most importantly, green hydrogen powered FC produces zero GHG emissions or pollutants, unlike hydrogen & hydrocarbon's combustion. Two main types of fuel cells are Proton exchange membrane FC's (PEM) & solid oxide FC's (SOFC). Both FC's can run at efficiencies up to 60%. However, Literature shows that both fuel cells lose efficiency with altitude. That is the greatest disadvantage

to fuel cells in aviation.

Proton Exchange Membrane Fuel Cell

Low temperature PEM (LT-PEM) has an operating temperature of 80-120°C and 90-260°C (~160°C optimal) for high temperature PEM (HT-PEM). PEM can't operate at higher temperatures due to structural limitations of the membrane. Electrical efficiencies are around 40-60% & 50-60% for LT & HT-PEM respectively. Literature shows there's a positive correlation between operating temperature of a FC & efficiency, giving HT-PEM the upper hand. That is since heat production is positively correlated to rate of reaction in the FC. HT-PEM also has a higher tolerance to CO content in hydrogen feed, making refueling less complex. It also has good heat releasing systems and less/no humidification required. LT-PEMFC on other hand has features like high gas permeability resistance & is more developed and cost effective [21]. Moreover, since PEM-FC also operates at lower temperatures than SOFC, they have faster start-up times as low as seconds. However, PEM fuel cells are restricted to pure LH_2 unlike SOFC.

Performance of PEM-FC is related to many factors, including "load current, temperature, relative humidity, membrane thickness, membrane-active area, electrode active area, corrosion, purity, pressure, and concentration of hydrogen fuel" [21]. Fuel cell efficiencies drop when voltage drops due to "Activation, ohmic and concentration losses" [21]. In aviation, temperature, pressure & humidity are conditions to be controlled to maintain normal performance levels. Data shows increasing temperature increases efficiency, power, voltage, leakage current & decreases mass crossover & durability [21]. Voltage proportionality with temperature is governed by the Nernst equation. However, temperatures higher than optimal temperature could mean a drop in efficiency and durability. Power production increases by 16% for a temperature change from 50-80°C in a PEM-FC [21]. PEM-FC Temperature drops by about 1.7°C for every 1000ft and remains constant past 36,000ft elevation at the "Tropopause" [21].

Pressure is more critical to FC powered aircraft in flight at high altitudes, PEM included [22]. Literature, including ones published by NFCRL at UCI, have showed there's almost an immediate decrease in output voltage with an increase in altitude and drop below atmospheric pressure [22]. Stack voltage drops by about 43% at 35,600ft. Most performance loss is due to activation losses. However, parameters like airflow can have positive impact at above sea level altitudes. There's also a surprising, insignificant, and positive effect on performance with decreasing pressure at high external resistance (90 Ω) - (low FC load).

Humidity is another factor to be controlled during flight that affects performance. Without reactant gas humidification, the FC membrane will be dehydrated resulting in high ohmic losses & could potentially damage the membrane. PEMFC operating at high temperature results increased performance but also requires a high relative humidity (RH>80%) to maintain performance [23]. Experimental results show that "reducing RH decreases efficiency by increasing membrane resistance, decreasing proton activity in catalyst layers, reducing the electrode kinetics, and increasing the gas mass transfer resistance. For example, "maximum power density dropped from 0.57 to 0.14 W/cm^2 when the RH was changed from 100 to 25%, for a PEMFC with Nafion 112 membrane operating at 120C, 1atm.
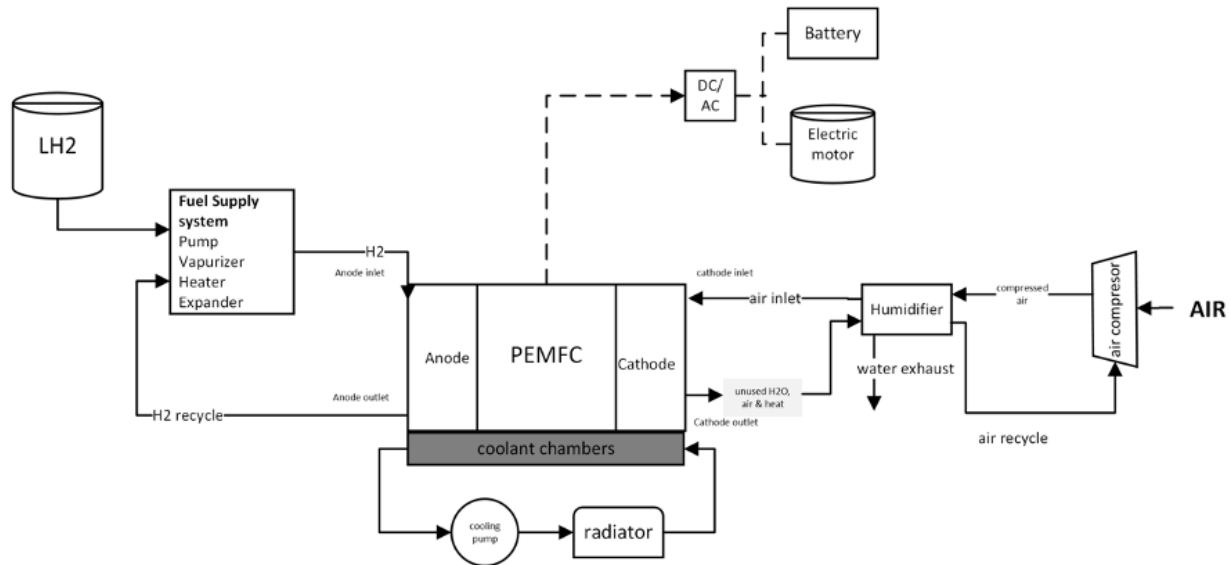
Fig. 1.1 Schematic of a PEMFC-based hydrogen powertrain system with integrated LH2 storage, fuel processing, and air management.

So far LT-PEMFC has been doing well in the automotive industry due to its low operating temperatures and high power density compared to other fuel cell types. It's interesting to see if the same model can be applied in low altitude aviation. Figure 1.1 showcases of conceptualization of PEMFC powertrain system.

Solid Oxide Fuel Cell

SOFC has an operating temperature of about 500-1000°C & electrical efficiency can reach 60%. Since its operating at a much higher temperature than PEM, this is also reflected on cost due to the thermally challenged materials required [24]. The two main types of SOFC are planar & tubular. "Planar SOFC is most common due to its lower cost, higher power density & ease of gas flow management" [24]. "Tubular SOFC has good resistance to thermal stress; but has high cost and low power densities that limit it to small scale power applications" [24].

SOFC's performance also degrades with altitude like PEMFC. Experiments done at APEP (UCI) show that voltage output drops by 16% when pressure is dropped from 25kPa to 7kPa [19]. The

high operating temperature of SOFC also means long start-up times and other thermal stress issues. Thermal expansion properties of the cell require uniform heating of the FC, otherwise thermal stress can develop. This limits the heating rate & thus start-up time of the cell. SOFC average startup time is 5-20 minutes but can reach to an hour depending on stack size and stacking geometry [24]. Planar geometry has slow startup time, but geometries like micro-tubular SOFC can cut the time from an hour to minutes. Yet, start-up time is less critical in flight than it is in automobiles or grid stabilization.

Hydrogen Fuel Cell/Gas Turbine Hybrid System

The high operating temperature of SOFC or molten carbonate FC allows the application of a hybrid system that converts FC waste heat to electric power that can be used to pressurize a fuel cell [25]. Electrochemical energy that isn't converted into electric power in a fuel cell due to losses results in waste heat. This waste heat can be used to power bottoming cycle engines, a GT included. An FC can be placed upstream of the turbine (topping cycle) or downstream (bottoming cycle) [25]. The FC/GT hybrid can use an SOFC waste heat, convert it to electrical power via a GT/generator, which can power a compressor to keep the SOFC at higher operating pressure. An example hybrid system modeled by [26] for aerospace applications consists of an "SOFC, steam reformer, compressor, turbine, several heat exchangers and pumps". A slightly different configuration by [27] adds an oxidizer for gases leaving the SOFC, entering the GT. Air is first taken into a compressor & split into 2 streams, first stream moves through SOFC Heat-exchanger (HX) & into the cathode. The 2nd stream goes into a reformer HX, then into the reformer. Fuel also goes into the reformer, the resulting reformant (usually H2 & CO, depending on fuel), go into the anode. The combined anode & cathode exhaust enters a combustor (to burn remainder anode-gases). Combustor exhaust enters an air HX & then water HX, before entering the turbine & expanding. The turbine then powers a high efficiency generator. The power from the generator can be used to power a compressor that increases pressure in the SOFC [26] [27].

As seen above, high temperatures of SOFC can be a blessing for aviation applications, especially on bigger airplanes that have volume & mass for this system. Unfortunately, even HT-PEM (90-260C) doesn't have high enough temperatures to power a FC/GT hybrid. This makes SOFC a more effective application in high range, payload & altitude applications. The cell voltage of SOFC is governed by the equation below [28].

$$E_{SOFC} = \frac{E_{max} - i_{max} \cdot \eta_f \cdot r_1}{\frac{r_1}{r_2} \cdot (1 - \eta_f) + 1} \tag{1.1}$$

1.2.6. Battery-Electric Aircraft

Battery-electric propulsion converts electrochemical potential in charged batteries to power a high efficiency electric motor. This makes them very efficient propulsion systems with efficiencies up to ~90%. Batter-electric also allows achieving zero GHG emissions & criteria pollutants if renewable energy is used to charge the batteries. Moreover, electric aircrafts have been vastly researched in efforts to replicate the electric automobile's success story. Many companies have already developed & tested electric airplanes. Some of those efforts have been successful but limited to small, short-range airplanes. That is mainly due to the low gravimetric & volumetric energy density of batteries. Their application in larger aircraft will require large batteries with a very high mass that makes long-range flight unfeasible. For example, a jumbo jet like the Boeing 777 would require around 4.5 million kg's of batteries (212 Wh/kg energy density) for a 10-hour flight; that is equivalent to 13 times the take-off weight of the conventional B777 (for the batteries alone). This means that the state of art (SOA) battery technology isn't there yet for long-range aircraft applications. That is unfortunate because 98% of aviation CO2 emissions is released by airplanes with take-off weight above 25 tons [29]. That would include single-aisle, twin-aisle long-range airplanes & mid-range airplanes like regional jets & business jets. Additionally, the global power grid CO2 emissions per kW, is significantly higher than what conventional airliners emit today,

and is expected to do that for at least 25 more years [29]. Hence the application of battery-electric technology onto smaller aircraft "today" would have minimal impact on aviation GHG emissions, especially on a global scale & in countries with conventional power plants.

In an analysis done by [29] on electric propulsion commercial airliners, it was concluded by the model that the energy & power density of the batteries would need to increase by multiple factors to fly the same range. For example, "an electric propulsion system with a gravimetric power density of 12 kW/kg and batteries with 1500 kWh/kg, a range of 300 km is conceivable on an aircraft the size of a B737 or A320". Moreover, the analysis also explores hybrid-electric & turbo-electric systems, where a conventional gas turbine connected to a generator that powers electric motors that drive an aircraft propulsor.

Hybrid-electric allows the gas turbine to power a propeller and power a generator-electric-motor setup at the same time. Hybrid-electric also introduces the idea of energy storage using batteries that can be charged from the grid, reducing fuel consumption. The use of turbo-electric configurations allows regeneration features, noise reduction, energy substitution and load balancing [29]. However, Turboelectric configurations researched so far show little impact on GHG emissions and increases cost. Lithium-ion batteries (100-265 Wh/kg and 250-680 Wh/L) are currently the cell of choice in aviation applications since they have the highest gravimetric power and energy density of any common battery today. It is projected that Li-ion batteries will reach 750 Wh/kg by 2035. Small two- or four-seater electric airplanes today operate at energy densities of 250-270 Wh/kg. For comparison, the Tesla model 3 has an energy density of 260 Wh/kg. For small aircraft applications, a modeling analysis done by [30] compares a conventional I.C. Cessna 172 (small aircraft, short-range) with a battery-electric design powered by a YASA P400 electric motor. The battery-electric aircraft (200 Wh/kg battery) achieved a peak range of 187 km (at a speed of 45 km/hr), while the kerosene (12,000 Wh/kg) powered aircraft achieved a range of 2329 km (at a speed of 60 km/hr). The range of battery-electric increases with increasing battery energy density, achieving up to 1000 km for an 800 Wh/kg battery. This shows that battery-electric aircraft must operate at lower speeds, have

higher mass (330% higher), and use energy densities higher than the state of the art (800 Wh/kg) to achieve about half the range (1000 km) of a small conventional aircraft.

1.2.7. Transitioning to Hydrogen Propulsion

Adopting a hydrogen propulsion system in aviation necessitates significant redesigns of traditional aircraft structures. Retrofitting current models with new hydrogen technologies is feasible, albeit with certain drawbacks. Initially, retrofitting may be the most practical strategy, but future aircraft designs, like the blended wing body, offer greater flexibility for integrating new components such as cryogenic hydrogen storage, fuel cells, and heat exchangers, alongside existing systems like auxiliary power units, compressors, and propellers. On the other hand, substituting fossil fuels with synthetic hydrocarbons can be done with minimal adjustments to the current aircraft infrastructure, affecting only fuel expenses, energy density, and operational range. Conversely, battery-electric aircraft require extensive modifications akin to hydrogen fuel cell systems due to their reliance on electric propulsion, necessitating greater power output for takeoff due to the low energy density of lithium-ion batteries.

Hydrogen Tanks

Knowing the gravimetric & volumetric energy densities of both kerosene & hydrogen; we see that one of the critical components of a hydrogen aircraft is redesign of the tanks. Due to the high pressure & cryogenic temperatures, LH2 tanks are assessed to be 12cm thick with a mass of 10kg/m^2; This includes insulation & structure for an aircraft design to fly at 20,000-25,000 altitudes [11]. However, there's more to deigning an aircraft tank than these constant values. First, there's an integral & non integral tank structure [31]. Integral integrates the airframe of the aircraft & supports any loads that may come with it, which is preferred. The non-integral is separate from the airframe and supports only internal pressure & dynamic loads. In medium range passenger aircraft, a non-integral design is recommended where small tanks could be placed above passenger cabins &

one big tank at the rear end. These could result in 9-16% [32] increased fuel consumption fuel if this top-tank design is used because these types of tanks are heavier. In contrast, integral tanks (suitable for large aircraft), can increase efficiency by 12%. Therefore, many researchers conclude hydrogen combustion is optimal in long-range large aircraft. There are other factors to designing a tank such as storage density, shape, internal & external changing pressures, material & position/placement on an aircraft (mass distribution). Another interesting, though not efficient way of storying hydrogen on aircraft is via metal hydrides, where it can be released by increasing temperature or decreasing pressure.

In comparison with kerosene tanks, Liquid hydrogen systems have 2.35 times better storage density. On a modeling analysis done by [31]; when fueled the hydrogen & kerosene tank systems weigh 2988kg & 9187 kg for the same range [31]. This gives hydrogen storage systems a competitive advantage. However, volume occupied for the same mass is nearly 3 times for hydrogen tank systems. Overall, it seems harder to universalize hydrogen tanks like we've done for kerosene due to the more parameters effecting it; this typically consequences in oversizing the system due to insulation & safety concerns. This disadvantage could be minimized & motivates more research into the full propulsion system rather than just one component & with original design tactics. Additionally, fuel cells higher efficiency (up to 60% compared to GT 40%) is a factor that should be considered due to lower fuel consumption & hence less storage required.

Components effected

Changing the design of one component in an aircraft has repercussion & requires even further changes in design. For starters, hydrogen tanks being heavier, larger tanks require a heavier, larger fuselage. The fuselage is on average 6% heavier in such an integration of hydrogen into existing aircraft. In the case of the redesign of a hydrogen ATR-72 freighter aircraft, the fuselage was extended by 3.8m to house 2 big tanks [11]. Also, for passenger aircraft, kerosene tanks are traditionally placed in the wings. With LH2, that's hard to do unless many small tanks are used, or a blended wing aircraft is

28

used. Hence, wings in a hydrogen aircraft can be made smaller and even a bit heavier to augment structural integrity. These changes can negatively affect aerodynamic efficiency. They also lead to an increase of mass that nearly diminishes the lower mass advantage hydrogen storage systems have over kerosene. Furthermore, hydrogen isn't necessarily a drop in fuel like hydrocarbons can be. Hence, changes to a conventional engine need to be made to manage the different properties of hydrogen combustion. Hydrogen engines can be smaller, especially for long-range aircraft. Overall, these changes along many others, estimate production & maintenance costs to be 25% higher [32] than current aircraft design when hydrogen technologies such as combustion or fuel cell are used.

1.2.8. Operational Cost and Range Comparisons

The current theory about hydrogen applications in aviation can be categorized into long-range, large aircraft (for LH2 combustion) & short/medium-range small aircraft (for LH2 FC) [32]. Battery electric is only feasible in the small-short-range aircraft segment. Whilst Synthetic Hydrocarbons can have similar properties to kerosene & hence would work well to replace any segment. It seems more reasonable for synthetic fuel systems to focus on long-range, passenger aircraft since that's where hydrogen struggles today due to design & safety restraints.

A design study done a Boeing 737 also validates that hydrogen combustion is better in long range. The study showed that energy efficiency decreases by 28% for a 926km trip & by only 2% on a 5,556km trip [15]. The same study showed that a modified LH2 combustion aircraft would be 5% lighter, with 5% smaller wings. Hydrogen combustion range & cost is also compared to kerosene in a freighter aircraft [11]. The Range that hydrogen combustion propeller system provided was 1600km compared to 4100km for a kerosene propellor system at maximum payload (8094kg) [11]. The data showed propeller systems provide slightly longer range over jet systems. The DOC (directing operating cost-$/ton-km) is fortunately only 2-3% higher for hydrogen. However, green hydrogen is not used here. The cost of fuels in the reference mission is $1.7/kg for hydrogen & $0.57/kg for kerosene. Green hydrogen from electrolysis via renewable energy can be anywhere from $3-15/kg.

Hence, cost of the same mission would increase considerably.

On the other hand, battery electric is shown to show highest potential in small aircraft, short range segment. That's due its low gravimetric & volumetric energy densities. Similarly, H2 Fuel cells aren't normally correlated with long range or large aircraft. That is since long-range usually means high altitude & low pressure (lower efficiency). A generally true statement is that fuel cells have higher potential in lower power aircraft. FC's also show lower efficiency in high throttle scenarios, in contrast with GT's efficiency that shows proportionality with maximum power rating. Thus, this could be another reason FCS performs better in short range, small aircraft. Nonetheless, FC's can have some sort of a positive relationship with range. Since if the same FCS mass is maintained, higher range means mass of FC becomes less dominant. Fuel cells also become very heavy when powering large aircraft. Current FCS technology have an estimated weight of 1.6kW/kg for the FC & 5.8kW/kg for the electric motors [33]. For reference, a study mission done on a conventional airbus A320 has 9187kg fuel storage system (6980kg is kerosene), 2331kg/engine for the two CFM-56-5A3 jet engines [33]. Hence the total mass would be 13,849kg for a flight that requires 27.6MW of power. In comparison, a FCS with current technology would result in double the mass (25,028kg) for the same flight & power requirement. A lot of it also has to do with the tanks & fuel cell mass. The electric motors (4758kg) aren't much heavier than the jet engines (4662 kg), and electric motor power-to-weight ratio is only expected to get better as the industry invests in them. Fortunately, Fuel-cells mass are also expected to decrease by 22% in the future [33].

The Future of flight: Hydrogen vs. Kerosene Cost Implications

A study done by [19] In 2020 compares a A320/A320neo (short-range) & A330-300 (medium range aircraft that run on kerosene & hydrogen. Both scenarios are in 2035 & use literature predications to estimate the increased performance characteristics. The propulsion efficiency of all 4 aircraft is around 40-42%. All aircraft are also designed to fly the same range 1500 & 4000 nm (nautical miles) for short & medium range respectively. Number of passengers is also the same (180 & 290)

and the cruise Mach number is 0.78 & 0.83 for short & medium range respectively. Green hydrogen cost in 2035 is used. The result is that for short-range-H2 propulsion, energy demand is 12% higher & the direct operating costs (DOC) is 6% higher. For medium-range-H2 aircraft sees an increase in energy demand by 18% & 10% increase in DOC. The increased energy demand for H2 aircraft is majorly due to the longer fuselage, less aerodynamic design that is caused by changes in tank design & other components due to the snowball effect. The Air-freighter mission [11] study showed only an increase of 2-3% in DOC from its kerosene competitor & with modern day technology. However, that mission study was long-range (where H2 combustion performs better), used gray hydrogen (cheaper), and had much lower range and cargo space than kerosene. The results from [19] are more realistic if the exact same flight is to be replaced by hydrogen aircraft.

Moreover, [19] compares cost of green hydrogen "delivered" with kerosene in 2035. Kerosene is predicted to be $1.7/kg. hydrogen costs range from $1-4.3 in the optimistic scenario, $2.8-7.3/kg in base scenario, and $4.6-11.8/kg in pessimistic scenario. Also, [19] shows the cost breakdown for hydrogen delivery infrastructure to airports. Where "60% is hydrogen production, 31% for liquification, 4% for LH2 storage, 3% transportation & 2% for airport refueling. In the best-case scenario of delivered LH2 cost in 2035, total DOC could slightly decrease for both aircraft. However, DOCtotal may also increase by 10-70% or 15-102% for short & medium range aircraft respectively. This concludes that the hydrogen aviation economy highly depends on cheap hydrogen production & delivery infrastructure to be feasible.

1.2.9. Retrofitting Aircraft with Hydrogen Technologies: Numerical Insights from Literature

Recent studies on retrofitting existing aircraft with hydrogen technologies provide a quantitative basis for assessing the feasibility and impact of such modifications. For example, Abu Kasim et al. [34] designed a retrofit for the Cessna 208 Caravan using a Proton-Exchange Membrane Fuel Cell Power System (PEM-FCPS) powered by liquid hydrogen. This system, which incorporates four 140 kW Ballard PEMFC stacks and two Garrett G25-550 turbochargers, achieved a 43% efficiency and a

hydrogen consumption rate of 28 kg/h over a 1.5-hour flight (350 km). The retrofit demonstrated reliability with a failure rate below 1.6 per million hours, comparable to commercial jet engines, highlighting its viability for short-range, small aircraft.

Further, findings from Hypoint and Massaro et al. [35] suggest that by 2025, a regional aircraft retrofitted to carry 75 passengers over 800 nautical miles could be viable with a PEMFC powertrain at 3 kW/kg. However, this would result in a 2.21% increase in energy requirements and a 26% increase in maximum takeoff weight (MTOW) compared to conventional aircraft, showcasing the trade-offs associated with hydrogen retrofits. Despite these increases, PEMFCs have demonstrated efficiencies exceeding 50%, with potential for further optimization.

The study by Rupiper et al. [36] explored retrofitting aircraft with flame-assisted Solid Oxide Fuel Cells (SOFCs) integrated into a gas turbine system. This configuration reduced the need for external heating and achieved a 24.5% increase in overall system efficiency compared to conventional gas turbines. Additionally, the SOFC retrofit yielded up to a 62% reduction in NO_x emissions and a 7.1% improvement in block fuel burn [37].

1.2.10. Hydrogen blended wing body aircraft

In the context of sustainable aviation, blended wing body (BWB) aircraft have demonstrated significant potential, especially when paired with hydrogen propulsion. For instance, studies like that of Adler and Martins highlight the capacity of hydrogen-powered aircraft to achieve greater climate impact reductions at lower costs compared to biofuels. Although hydrogen requires a higher storage volume, the BWB configuration is considered particularly efficient for accommodating large fuel tanks. When comparing optimized kerosene and hydrogen versions of BWB and traditional tube-and-wing (T&W) aircraft, the study finds that a hydrogen-powered BWB incurs a 3.8% energy penalty relative to its kerosene counterpart, whereas the T&W hydrogen design faces a 5.1% energy penalty compared to its kerosene equivalent. Karpuk et al. [39]focus on the environmental impact.

They demonstrate that hydrogen-powered BWB aircraft can reduce CO2 emissions significantly compared to kerosene-powered models: by 15% and 81% for blue and green hydrogen, respectively, and by 44% and 88% when compared to a conventional B777-300ER aircraft. These findings are in contrary to most literature and makes this area of research inconclusive. Further research by Valencia et al. examines a hydrogen-powered hybrid gas turbine and solid oxide fuel cell (SOFC/GT) within a Turboelectric Distributed Propulsion system based on the NASA N3-X blended wing body planform [40, 41]. This study reveals that using liquid hydrogen in this configuration could potentially reduce Thrust Specific Fuel Consumption (TSFC) by 70%. However, it also identifies significant challenges, including hydrogen storage issues and a 40% increase in propulsion system weight due to the incorporation of fuel cells [40]. In summary, the integration of hydrogen powertrains in BWB aircraft, as demonstrated by these studies, offers a promising avenue for the aviation industry to reduce its environmental impact and improve energy efficiency. My dissertation contributes to this field by focusing on the practical aspects of conceptualization, design, application, and impact assessment of these innovative hydrogen power systems.

1.2.11. Dynamic modeling for SOFC/GT for flight

Dynamic models for SOFC/GT have been developed and tested through a modeling framework reported by Rossi et al. [42], and via a pressurized ground simulation by Roberts and Brouwer [43], which could portray the system behavior at different pressures/altitudes of flight conditions. Mueller et al. [44] demonstrated a control design strategy for a bottoming SOFC/GT system. Pourabedin & Ommi employed a dynamic modeling approach to study the behavior of an auxiliary power unit (APU) system for a regional jet aircraft comprising a planar SOFC system with a jet fuel external reformer [45]. The duration required for these dynamic operating conditions can range from several seconds to minutes, influenced by the fuel cell type and operating scenarios. To ensure hybrid SOFC-GT system viability within these parameters, a control strategy tailored to its dynamic stability is imperative. Chakravarthula studied an SOFC (with microtubular structure)/GT system

performance for aviation applications [46]. This work demonstrated that, through a simple enthalpy comparison, an SOFC/GT system can achieve approximately 24% higher efficiency compared to a conventional turbo-generator system. Previous research indicates that SOFC systems, sometimes including some battery energy storage have evolved to feature highly dynamic operation, with transient response time now aligning closer to traditional power systems, enhancing the SOFC-GT system performance and potential for use in aircraft. For instance, Zhang et al. [47] reported a rapid turndown response of 48.4% in just 10 s for a 373.6 kW system. On the other hand, Ahrend [48] observed a significant turndown of 66.2% over approximately 40,000 s for a 3,310 kW system that was not designed for rapid response. Similarly, ramp-up times vary, with Ferrari et al. [49] noting a 20.1% increase in load within 900 s for a 278-kW system. On the larger scale, a study by McLarty [50] showed a 10% load increase for a 100 MW system over 120 s. These previous studies suggest a need for advancement and design of control strategies and advancement in the dynamic response capabilities of larger power systems to match the agility seen in kW-scale counterparts.

1.2.12. Hydrogen airport infrastructure

Accordingly, it is estimated that hydrogen-powered aircraft could make up almost 13% to 32% of the world aviation energy demand by 2050 [51]. Substantial global capital investments ranging from $700 B to $1.7 T are projected for a shift to hydrogen-powered flights by 2050 [52], with the majority allocated to renewable electricity generation, hydrogen electrolysis, and liquefaction. In a comprehensive techno-economic assessment, Hoelzen et al. [53] evaluated three LH_2 delivery routes for five different locations (Saudi Arabia, Morocco, Scotland, Denmark, and Germany) using non-linear energy system optimization. They demonstrated that, in a base case scenario for on-site production at a medium-large airport in 2050, final LH_2 prices at the dispenser could reach $2.04/kg LH_2, making hydrogen flying economically viable in places with strong renewable energy source conditions. Amy and Kunycky [54] investigated the economic aspects of providing sustainable hydrogen to aircraft fleets at Los Angeles International Airport (LAX) via on-site electrolysis

production. This work showed more than a two-fold increase in fuel costs (on an energy basis) for hydrogen ($4.5/gge) compared to jet fuel ($2/gge), with electricity and the capital expenditures (CAPEX) of electrolysis and liquefaction being the most dominating factors for the hydrogen case.

2. Goal and Objectives

2.1. Goal

Investigate and quantify the feasibility, operational performance, and environmental benefits of hydrogen as a power source for aviation, focusing on both retrofitting existing aircraft and sizing conventional or futuristic concepts. This research will explore hydrogen combustion and fuel cell technologies, along with storage solutions, the response dynamics of these systems, and necessary changes in airport infrastructure. The study aims to address gaps not currently covered by existing industry solutions and academic literature, while evaluating the associated monetary and environmental costs.

2.2. Objectives/Tasks

Here are the objectives to meet the research goal:

1) Conduct a comprehensive literature review on green aviation and the integration of hydrogen-powered propulsion technologies.

2) Develop conceptual powertrain models for various hydrogen propulsion systems, including H_2 combustion, SOFC/GT/Battery, and PEMFC/Battery.

3) Build a dynamic model of an SOFC/GT system to evaluate its robustness and response during various flight conditions.

4) Apply and evaluate hydrogen power systems and their associated components in aviation, focusing on retrofitting existing aircraft and sizing for both conventional and Blended Wing Body (BWB) designs.

5) Assess the environmental and economic impacts of hydrogen power systems and the required airport infrastructure modifications.

The objectives aim to evaluate the feasibility of hydrogen aircraft from multiple perspectives. This begins with understanding the current literature on hydrogen aircraft and associated infrastructures. Following this, the objective is on conceptualizing and understanding hydrogen powertrain models, including H_2 combustion, SOFC/GT, and PEMFC systems, tailored for various aircraft categories. By developing these models, the next objective is to create and apply retrofitting methodologies for existing aircraft, as well as sizing conventional and Blended Wing Body (BWB) designs while integrating the hydrogen energy system. Dynamic modeling will be employed to evaluate the response of SOFC/GT/Battery systems during flight, addressing gaps in the literature. The final objective is to assess the overall environmental and economic impacts of hydrogen adoption, including the necessary hydrogen infrastructure, to determine scalability and sustainability in aviation.

2.3. Approach

Task 1: Conduct a comprehensive literature review on green aviation and the integration of hydrogen-powered propulsion technologies.

An extensive literature review will be conducted on the following topics:

- Retrofitting existing aircraft for hydrogen propulsion, including retrofit methodologies.
- Hydrogen storage modeling, focusing on safety, efficiency, and regulatory standards.
- Hydrogen fuel cell and gas turbine hybrid systems (SOFC/GT).
- Battery-electric, LT-PEM, and HT-PEM fuel cells for short- and mid-range flights.
- Adoption of alternative fuels, such as synthetic and biofuels, alongside hydrogen in aviation.
- Dynamic modeling and control strategies for SOFC/GT systems.
- Sizing of both conventional and Blended Wing Body (BWB) aircraft for hydrogen integration.

- Hydrogen airport infrastructure and delivered costs.

Task 2: Develop conceptual powertrain models for various hydrogen propulsion systems, including H_2 combustion, SOFC/GT/Battery, and PEMFC/Battery.

- Design of hydrogen powertrain systems for various aircraft classes: light/short-range, midsize/mid-range, and heavy/long-range.
- Development of hydrogen storage solutions tailored to aviation safety, efficiency, and regulatory standards.
- Creation of retrofitting methodologies for converting existing aircraft powertrains to hydrogen fuel systems.
- Performance analysis and techno-economic evaluation of hydrogen powertrain systems across the specified aircraft classes.
- Application of existing literature and models to guide the conceptual design and technology adaptation for hydrogen aircraft powertrain systems.

Task 3: Build a dynamic model of an SOFC/GT system to evaluate its robustness and response during various flight conditions.

- Develop dynamic models to assess the robustness and response of SOFC/GT systems to operational variability for flight dynamics under aviation safety regulations.
- Model the battery response to complement and support the load deficiencies of SOFC/GT systems, optimizing overall performance and reliability during flight.

Task 4: Apply and evaluate hydrogen power systems and their associated components in aviation, focusing on retrofitting existing aircraft and sizing for both conventional and Blended Wing Body (BWB) designs.

- Perform conceptual evaluations of hydrogen power systems across a range of aircraft models, including retrofitted and sized conventional aircraft, to assess adaptability, performance, and

integration challenges.

• Size and analyze the application and effectiveness of hydrogen power systems specifically in Blended Wing Body (BWB) aircraft configurations, considering aerodynamic, structural, and propulsion system interactions in comparison to kerosene-powered systems.

Task 5: Assess the environmental and economic impacts of hydrogen power systems and the required airport infrastructure modifications.

• Evaluate greenhouse gas emissions, water vapor, and pollutants from hydrogen power systems.

• Conduct a techno-economic analysis to assess the benefits and challenges of transitioning to hydrogen aircraft.

• Assess the economic feasibility of hydrogen adoption, including associated costs and savings of retrofits.

• Analyze the costs of developing and maintaining hydrogen infrastructure at airports.

• Investigate the necessary infrastructure changes and viability for large-scale airport adoption.

3. Assessment of the Benefits and Limitations of Hydrogen Retrofit Aircraft

Parts of this chapter, in parts or in whole, are co-authored by and published in:

Khaled Alsamri, Jessica De la Cruz, Melody Emmanouilidi, Jacqueline Huynh, and Jack Brouwer. "Methodology for Assessing Retrofitted Hydrogen Combustion and Fuel Cell Aircraft Environmental Impacts," *Journal of Propulsion and Power*, 2024, 40(5): 661-676.

This chapter explores the potential of hydrogen-based propulsion systems, including hydrogen fuel cells and combustion engines, to reduce emissions and improve efficiency in aviation. Hydrogen is highlighted as a promising alternative due to its high gravimetric energy density and zero-carbon emissions, despite challenges related to production costs, storage complexities, and infrastructure needs. The focus is on retrofitting existing aircraft, such as the Cessna Citation 560XLS+, with liquid hydrogen (LH$_2$) tanks and solid oxide fuel cell (SOFC) powertrains. This approach is analyzed using a lifecycle emissions assessment and mission-level cost analysis to compare the retrofitted aircraft with conventional kerosene-powered models. Drawing on literature that suggests hydrogen-powered business jets could achieve significant energy consumption reductions of up to 34% [55, 56] and notable cuts in greenhouse gas emissions, this chapter aims to provide a simplified methodology to assess the feasibility of hydrogen integration and retrofitting in aviation.

3.1. Methodology to Assess Emissions and Performance Trade-Offs for a Retrofitted Solid Oxide Fuel Cell and Hydrogen Powered Aircraft

The methodology to model the alternative fuel emissions for a proposed aircraft vehicle is presented in Fig. 7.1. The inputs to the modeling framework include the aircraft characteristics, such as empty and takeoff weights, overall efficiency and lift-to-drag ratio. In addition, the alternative fuel type is

defined by the heat energy available per unit weight of fuel and mission characteristics such as range and cruising altitude. These parameters define the aircraft cruising performance in the flight profile module. Within the flight profile module, the weight of the fuel necessary to complete the mission is determined and inputted into the H_2 tank configuration module and the emissions module. The tank configuration module models the shape, insulation, and volume of an H_2 cylindrical tank that meets the power requirements defined by the weight of the fuel. The tank volume and mass are then outputted into the center of gravity Module. This module determines the center of gravity (CG) change within the flight envelope of the aircraft by simultaneously placing the tanks in the interior layout. A tank sizing constraint is fed back into the tank configuration module if such CG requirements are not feasible for the same number of passengers. The tank configuration module updates the tank design and the weight of the fuel is remodeled to account for the weight of passenger removal. If such changes occur, either a refueling stop is required or a second flight of the same mission will keep the number of passengers constant for the same range. Such consequence is accounted for in the lifecycle emissions and cost modeling covered in detail in the following section.

Furthermore, the weight of the fuel, the mission atmospheric conditions, and the power plant for each alternative fuel type are inputted into the emissions module. Within this module, the emissions per segment are analyzed by their emission indexes, greenhouse gas emissions, and contrails. Such segment emissions are then inputted into the environmental impact module. This module implements the mentioned lifecycle assessment and cost analysis to output the trade-offs between alternative fuel power plants per mission. The details of this framework are further discussed in the following sections.
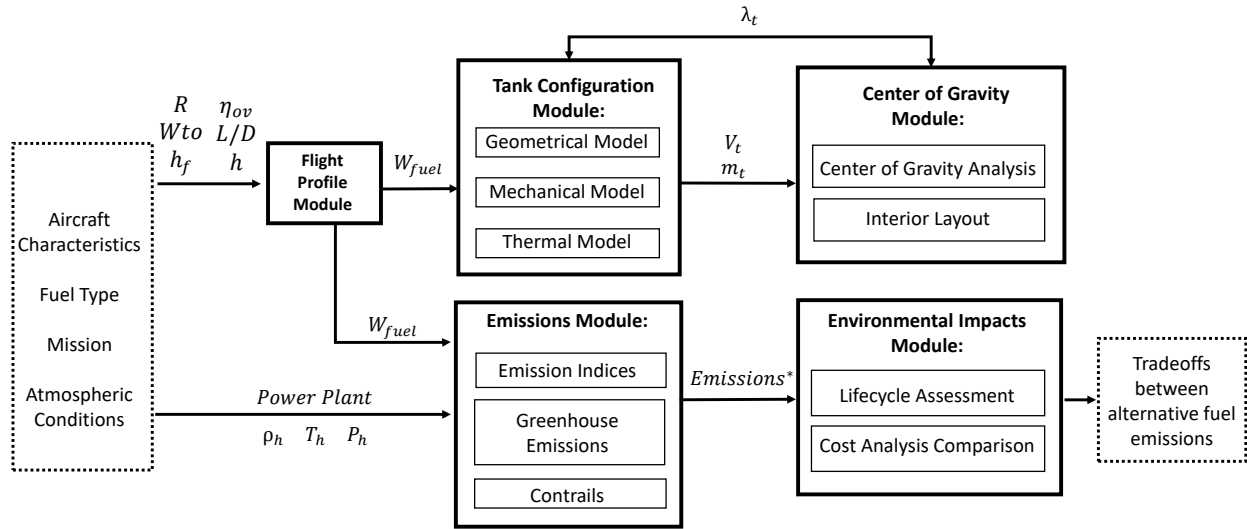
Fig. 3.1 **Modeling framework of the methodology to assess emissions and performance trade-Offs for a retrofitted SOFC hybrid and H$_2$ Powered Aircraft**

3.1.1. Flight Profile Module

The methodology presented in the previous section consists of a baseline range mission profile to compare the alternative fuel sources with a baseline kerosene gas turbine combustion flight procedure. A constant range approach analysis is implemented in order to design an alternative fuel tank and power train that satisfies insulation, center of gravity and power constraints. The Breguet range equation determines the weight of the fuel required to fly the given mission for the baseline and alternative fuel sources [57].

Hydrogen combustion would require some changes to the design of the engines due to the different properties of hydrogen such as higher adiabatic temperature and faster flame speeds. Such changes include a smaller combustion chamber, the addition or modifications of a pump, supply pipes, control valves, heat exchanger and turbine system, as depicted in Fig. 3.2, which outlines a hydrogen fueled multistage gas turbine layout. The aforementioned hydrogen combustion system replaces the conventional turbofan for the H$_2$-combustion powered aircraft studied in this paper, portrayed in Fig. 3.3. In addition, a heat exchanger must also be added to heat the cryogenic hydrogen liquid fuel

42

before combustion [58]. Stefan et al.'s review highlights key challenges for hydrogen combustion in aviation, particularly the need for materials that withstand high temperatures and hydrogen-induced corrosion, as found in hydrogen-fired gas turbines. Stefan et al. emphasizes the importance of developing advanced coatings and alloys, especially considering the larger temperature gradients and increased steam content in hydrogen combustion, which pose risks to component durability and efficiency. The study also notes the necessity for further research into hydrogen embrittlement, particularly for parts made via additive manufacturing [59]. These material challenges form a crucial part of the overall technological hurdles in integrating hydrogen combustion systems into aviation.

Cryogenic hydrogen tanks become very heavy depending on the design parameters, stored pressure, temperature, and acceptable boil-off rates. Fortunately for aircraft applications, less insulation is required for short periods of flight at a relatively high boil-off rate. Design choices of a number of tanks and storage locations affect the final mass and volume of the hydrogen storage system. The high gravimetric energy density of hydrogen of a 120 MJ/kg is favorable since mass reduction is critical during flight. Hydrogen needs to be stored at its critical temperature and pressure of 33.15 Kelvin and 1300 kPa. However, the main challenge in aviation lies in the mass and volume that such cryogenic tanks occupy. Hydrogen density varies between a low of 0.08375 kg/m^3 in gaseous form and a high of 81-89 kg/m^3 in cryo-compressed liquid form [60]. Such densities are low when compared to the densities of kerosene variation from a low of 775 kg/m^3 to a high of 840 kg/m^3.
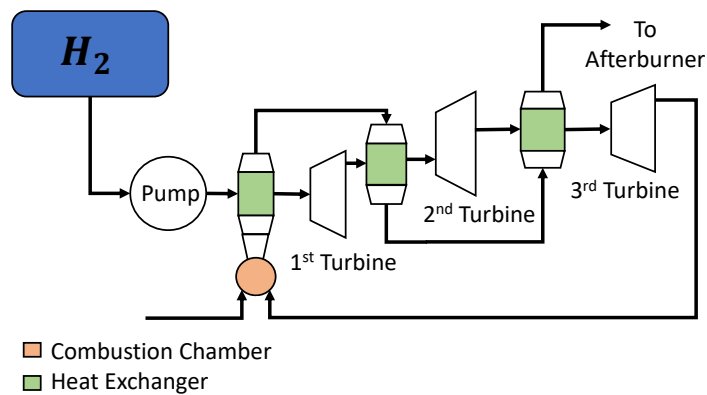
Fig. 3.2   Hydrogen fueled multistage gas Turbine configuration

43
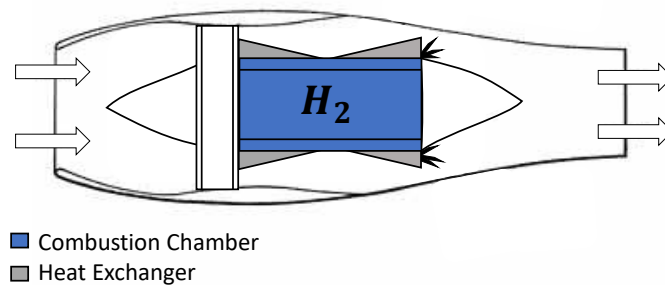
Fig. 3.3   Hydrogen combustion gas turbine

Another alternative, SOFC hybrid power plant configuration, is evaluated for a constant range mission. Such SOFC hybrid includes a battery and liquid H_2 tanks to provide electrical power with zero emissions. Proton exchange membrane fuel cells (PEMFC) and SOFC advantages include independent power and energy scaling at efficiencies up to 60%. Unfortunately, fuel cells lose efficiency with altitude due to lower atmospheric pressure. Hence for aircraft applications, a hybrid SOFC gas-turbine system can convert fuel cell waste heat to electric power and pressurize a fuel cell. The overall power system efficiency has been shown to provide slightly higher efficiencies in the range of 10% to 20% approximately for a conventional aircraft. Wilson et al. [61] presents a thermodynamic model aimed at evaluating the feasibility and performance of a high-performance SOFC/GT hybrid power system tailored for electric aviation. Their findings highlight the potential of such systems to achieve fuel-to-electricity conversion efficiencies significantly higher than those of conventional gas turbine engines, thereby underscoring the importance of these hybrid systems in the pursuit of net zero emissions for the aviation sector. Challenges remain, particularly in balancing plant design and integrating dynamic simulation capabilities to fully realize the potential of these technologies. The validation of their model against NASA's SOFC model and its application in constructing a 1 MW SOFC/GT hybrid power system for aircraft propulsion demonstrate the feasibility of achieving efficiencies greater than 75% under standard cruise conditions, pointing towards the necessity of further research and development to address the identified challenges and enhance system reliability and lifespan [61].

In the retrofit model assumptions for the SOFC hybrid system, which includes components such as a gas turbine, heat exchangers, a compressor, a generator, a battery, and an LH_2 tank. Power assumptions for the fuel cell, battery, and motor-specific densities are based on state-of-the-art (SOA) technology expected to be commercially available. Specifically, the SOFC exhibits gravimetric and volumetric power densities of 2.5 kW/kg and 7.5 kW/L, respectively [62]. These figures suggest that the SOFC hybrid, as designed, offers up to five and seven times higher gravimetric and volumetric power densities than those found in commercially available designs to date. Advanced research indicates even higher specific densities for fuel cells and motors, with findings pointing to 4.0 kW/kg for fuel cells and 10 kW/kg for motors [32]. The SOFCs exit temperature is noted to be 944°C, showcasing the potential of recycling heat within the system [61]. The battery technology utilized within this hybrid system features a volumetric energy density of 0.67 kWh/L and a gravimetric energy density of 0.35 kWh/kg [63]. Moreover, the gas turbine, integral to the SOFC hybrid configuration, is characterized by a volumetric density of 8000 kg/m^3 and a gravimetric power density of 4.4 kW/kg, illustrating the compact and efficient design achievable in modern gas turbines [64]. The cycle efficiency of the SOFC/GT system is conservatively assumed 70%, still indicating an improvement over conventional systems [63]. Lastly, the inclusion of a cryo-cooler with a mass specific power of 3 kg/kW further demonstrates the comprehensive approach taken to address thermal management challenges within the system [65]. The gas turbine's power output is chosen as 538 kW to be aligned with the SOFCs capacity to ensure optimal integration and performance efficiency within the hybrid system [64]. This assumption set shown in Table 5.1 forms the basis for the SOFC hybrid power train.

Table 3.1   Power train for SOFC hybrid

Parameters	Values
SOFC Volumetric Density (kW/kg)	2.5 [62]
SOFC Gravimetric Density (kW/L)	7.5 [62]
SOFC Exit Temperature ($^{\circ}C$)	944 [61]
Motor Density (kW/kg)	7.06 [32]
Battery Volumetric Density (kWh/L)	0.67 [63]
Battery Gravimetric Density (kWh/kg)	0.35 [63]
SOFC/GT Cycle Efficiency (%)	70 [63]
GT Volumetric Density (kg/m^3)	8000 [64]
GT Gravimetric Density (kW/kg)	4.4 [64]
Cryo-cooler Mass Specific Power (kg/kW)	3 [65]
Gas Turbine Power (kW)	538 [64]
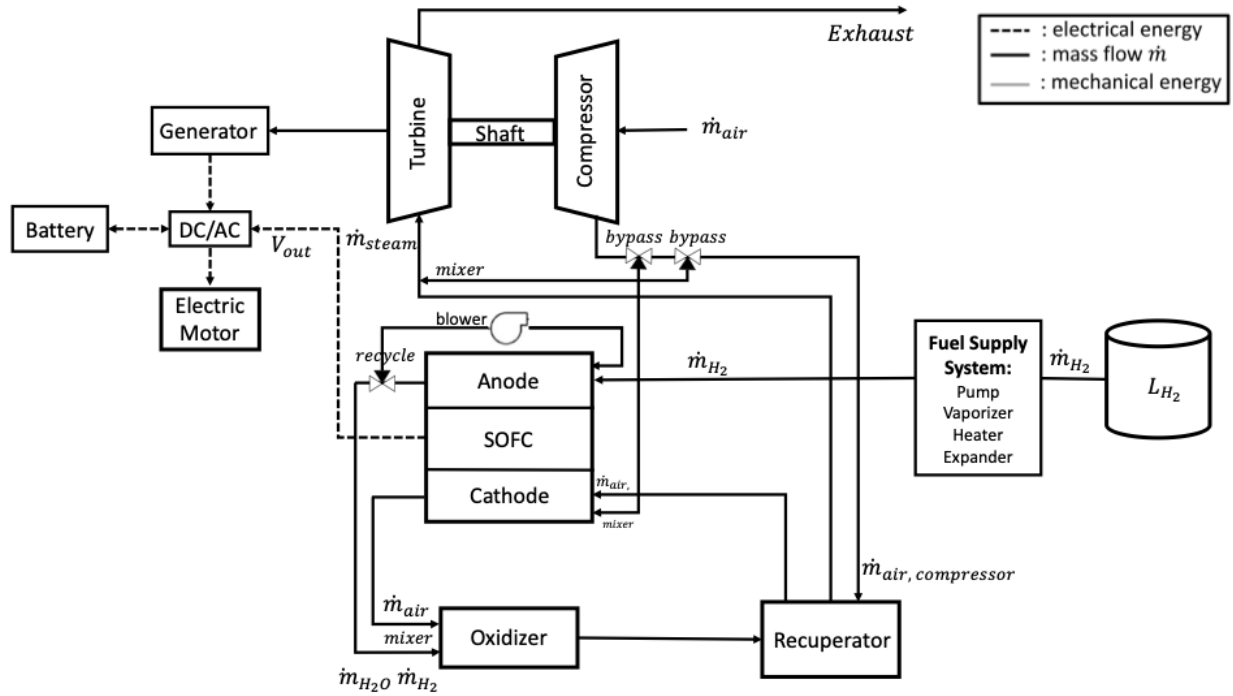
Fig. 3.4　Power train SOFC hybrid for Medium-Range and Long-Range aircraft designed for fuel cell hybrid

The SOFC hybrid power train system consists of multiple components such as an electric motor, the SOFC, a generator a pump, a cryogenic tank, and other components seen in Fig. 3.4. The cryogenic tank stores liquid hydrogen fuel which vaporizes once vented from the tank. The hydrogen is then heated in a heat exchanger (HX) that acts as a fuel heater. The HX recycles heat that exits the turbine, and a fuel pump pressurizes the H_2 that is inserted the anode. Oxidation reactions occur within the anode and compressed air from the compressor is then heated in the combined HX. Such air then inlets into the cathode where the reduction reactions occur. Compressed air flow helps maintain and increase the fuel cell performance at flight altitude. The turbine is utilized to power the compressor and generator while the generator produces electricity that can be stored in the battery or used for propulsion in the electric motor.

The aforementioned H_2-combustion and SOFC hybrid system are utilized to power the constant range from the baseline kerosene flight procedure. The Breguet range equation heat energy available

per unit weight accounts for such changes within this module and results in the fuel weight outputted into the tank module. A sample implementation of this methodology for both H_2-combustion and SOFC hybrid system is performed on a business jet in Section 3.2.

3.1.2. Tank Configuration Module

Given the design fuel weight from the previous module, tanks are modeled for a retrofitted aircraft in the tank configuration module. The design of such tanks follows the approach in Fig. 3.5. The tank module evaluates geometrical, material and thermal models that serve as feasible variables within the design space [66]. Such tank modelling is governed by equations 3.1 to 3.9.
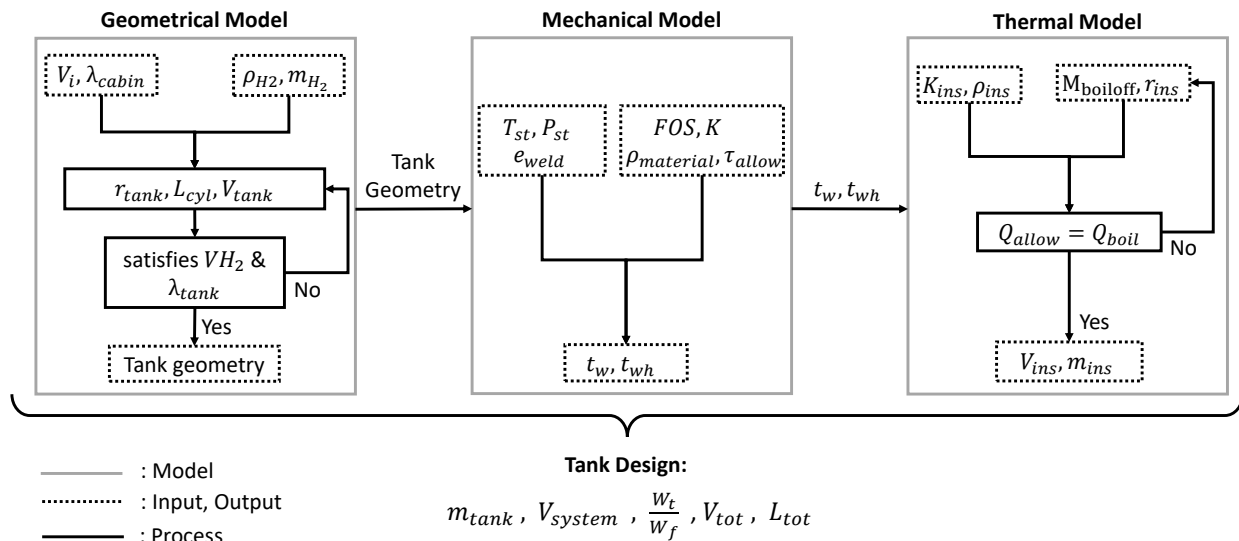
Fig. 3.5   Tank configuration module flowchart

Geometrical Model

The geometrical model rigorously defines the tank geometry and the necessary volume of storage to satisfy power constraints. The tank is architecturally shaped as a cylinder with hemispherical ends—a design celebrated for its superior pressure distribution, making it a prevalent choice for pressurized vessels [32]. To buffer pressure variations due to hydrogen boil-off, an excess volume V_i,

set at 7.2%, is accounted for in the calculations. The storage volume, V_t, is meticulously calculated to ensure that the tank can accommodate the required mass of hydrogen, M_{H_2}, while compensating for boil-off through an additional volume, V_i, and considering the density of liquid hydrogen, ρ_{LH_2} as shown in Equation 3.1. The choice of a cylindrical tank with hemispherical ends optimizes the pressure distribution within the tank, minimizing stress concentrations and enhancing structural integrity, as the volume of this specific geometrical configuration is represented in Equation 3.2. Further, the mass of the filled capsule is determined by Equation 3.3 to assess the impact of the stored hydrogen on the overall aircraft structure, a crucial factor affecting aircraft performance and fuel efficiency. The tank's design also incorporates meticulous calculations for the wall thickness. Equation 3.4 determines the wall thickness of the cylindrical section, considering the design pressure P_{des}, the material's tensile strength σ_a, and the efficiency of the welding process e_{weld}. This ensures that the tank wall can withstand internal pressures without compromising safety or integrity. Moreover, the hemispherical ends of the tank, which are subject to unique stress distributions, require a specialized approach for determining their thickness, as captured by Equation 3.5. This formula takes into account the design pressure, the stress factor K, the material properties, and the welding quality, reinforcing the tank's structural integrity comprehensively. In essence, these equations are meticulously chosen to ensure a holistic and accurate representation of the tank's geometrical, physical, and mechanical properties. They collectively safeguard the tank's structural integrity, aligning with mechanical, safety, and performance specifications, ultimately delivering a reliable and effective hydrogen storage solution.

$$V_t = \frac{M_{H_2}(1 + V_i)}{\rho_{LH_2}} \tag{3.1}$$

$$V_t = \frac{4\pi r^3}{3} + r^2 \pi L \tag{3.2}$$

$$m_{filledcapsule} = \rho \pi r_1^2 (L_1 - \frac{2}{3} r_1) \tag{3.3}$$

$$t_w = \frac{P_{des} d_o}{2 \tau_{allow} e_{weld} + (0.8 P_{des})} \tag{3.4}$$

$$t_{wh} = \frac{P_{des} d_o K}{2 \tau_{allow} e_{weld} + 2 P_{des} (K - 0.1)} \tag{3.5}$$

$$K = \frac{1}{6} (2 + \frac{d}{d_1}) \tag{3.6}$$

Mechanical Model

In the mechanical model, the derived geometry and selected materials precisely determine the tank wall thickness. Aluminum (4.4% Cu) 2014-T6 is chosen for its optimal strength-to-weight ratio and fatigue resistance, crucial for aerospace applications. This material, coupled with evacuated aluminum foil and fluffy glass mats for insulation as recommended by Rivard, et al. [67], creates a robust yet lightweight barrier, effectively reducing thermal conductivity. The Factor of Safety (FOS) is judiciously set at 1.3, aligning with standard engineering practices to balance durability and material efficiency. This ensures the tanks are resilient yet not overdesigned, maintaining a weight that is typically 15% to 30% of the LH_2 weight, potentially less than 15% with reduced hydrogen vaporization rates as noted by Baroutaji et al. [32]. Such optimization is crucial for aircraft

performance and fuel efficiency. The model integrates the inner vessel within a vacuum, defined by precise geometrical thickness, to minimize heat transfer and enhance the thermal stability of LH_2. These dimensions, along with the selected materials, are integrated into the thermal module to determine the optimal insulation thickness, ensuring the system meets stringent thermal requirements while optimizing for weight and structural integrity, reflecting sophisticated aerospace engineering.

Thermal Model

The thermal model is developed to determine the optimal wall insulation thickness by considering the material properties, an acceptable boil-off rate, and the corresponding acceptable rate of heat transfer. The design criteria are based on equations 3.7 to 3.10, which are instrumental in modeling the heat transfer dynamics within the insulation layer. The insulation thickness is specifically tailored to maintain a boil-off rate of 0.1% per hour, as suggested by Baroutaji et al. [32]. This particular rate is chosen because it strikes a balance between insulation performance and the minimization of insulation material, which in turn reduces both cost and mass of the system. The design allows for 20% of the stored hydrogen to be vented per hour, optimizing the system for a 288.15 Kelvin outer surface temperature to maximize the range and flight time of the aircraft. The inner vessel, situated within a vacuum, is designed with precise geometrical thickness and insulation parameters to meet the tank sizing constraint λ_{tank}, as illustrated in Fig. 3.6. This constraint is crucial as it feeds into the center of gravity (CG) module, influencing the overall aircraft design. The equations forming the core of the thermal model are instrumental in elucidating and forecasting the system's behavior under a spectrum of conditions. The Nusselt number (Nu) in equation 3.7, as derived from Colozza and Kohout [68], serves as a fundamental component in hydrogen tank thermal modeling, signifying the ratio of convective to conductive heat transfer across the boundary layer. Tailored for cylindrical tank geometries, this specific correlation incorporates the flow characteristics of hydrogen, captured by the Reynolds number (Re_D), and the fluid's intrinsic properties, as indicated by the Prandtl number (Pr). This correlation is instrumental in determining the convective heat

transfer coefficient, a key factor in accurately modeling the temperature distribution and managing heat flow in and out of the hydrogen storage tank. Equation 3.8, which delineates the rate of heat transfer (Q), is foundational for deducing the energy requisite for the phase transition of hydrogen, taking into account the mass flow rate ($\dot{m}$) and the latent heat of vaporization (h_{fg}). The set of equations introduces a more comprehensive approach to heat transfer analysis, taking into account conduction (Q_{cond}), convection (Q_{conv}), and radiation (Q_{rad}) heat transfers, represented in the total heat transfer equation (Q_{total}). These equations collectively form a robust framework for designing an efficient and effective thermal management system for hydrogen storage in aircraft applications. These equations are critical for ensuring the thermal management system is designed with precision, taking into account the necessary physical phenomena to maintain the hydrogen in its desired state, ensuring safety, efficiency, and effectiveness of the aircraft's power system.

$$Nu_D = \left[0.60 + 0.287 \frac{Re_D^{\frac{1}{6}}}{\left[1 + \left(\frac{0.559}{Pr} \right)^{\frac{9}{16}} \right]^{\frac{8}{27}}} \right]^2 \tag{3.7}$$

$$Q = \dot{m} \times h_{fg} \tag{3.8}$$

$$Q_{\text{total}} = Q_{\text{cond}} + Q_{\text{conv}} + Q_{\text{rad}} \tag{3.9}$$

$$Q_{\text{total}} = \frac{2\pi L k (T_o - T_i)}{\ln(r_2 r_1)} + \frac{4\pi r_1 r_2 k (T_o - T_i)}{r_2 - r_1} + h(2\pi r_2 L + 4\pi r_2^2)(T_o - T_{\text{atm}}) + \varepsilon\sigma(2\pi r_2 L + 4\pi r_2^2)(T_o^4 - T_{\text{atm}}^4)$$

$$(3.10)$$
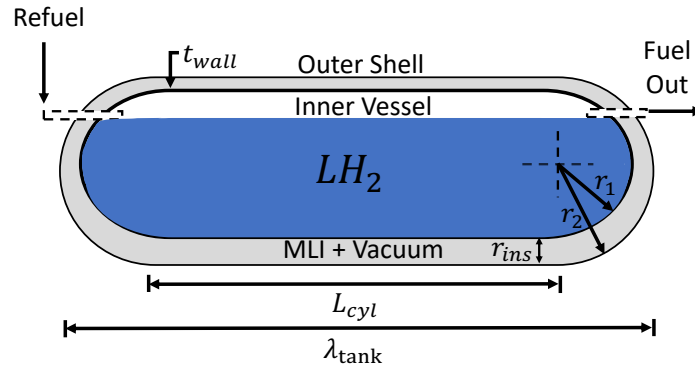
Fig. 3.6   H$_2$ Cryogenic Tank geometry definition

3.1.3. Center of Gravity Module

Center of Gravity

A weight and balance analysis evaluates the feasibility of the tank design outputted from the tank configuration module. The change in CG location from the operational limits of the retrofitted conventional kerosene powered aircraft is modeled from an already existing FAA-approved operational envelope found in [69]. The net change in CG is modeled to determine if the new retrofitted CG is within the minimum and maximum limits of the aforementioned envelope. Assuming the CG lies at 25 percent Mean Aerodynamic Chord (MAC) in the existing weight and balance diagram, the change in CG is determined with the shifted weight and potential moment arm [70]. Such moment arm is simultaneously obtained in the interior layout of the aircraft within this module. The weight per passenger is estimated to be 93 kg for domestic flights [71]. The weight of a fully stocked refreshment center is assumed to be 147 kg, with two full carts, while the weight of the lavatory is

estimated to be 60 kg. The change in weight from each alternative retrofitted fuel configuration is obtained by summing all changes in moments from either removing a seat or adding a tank, among others.

Interior Layout

Simultaneously within the center of gravity module, a potential change in the moment arm is obtained from an interior layout map of the existing aircraft. A sample case interior layout for a business jet is used in Section 3.2, to obtain the dimensions of the interior, the baggage compartment, and the overall aircraft specifications for a Cessna Citation 560XLS+ . Such dimensions are used to evaluate and constrain the size of the tanks by placing them in a position that results in a feasible CG within the aforementioned envelope limits and FAA aisle width and seat pitch regulations. After a feasible tank sizing constraint is reached in the tank configuration module, the final weight of the fuel is inputted into the emissions module. Such weight of the fuel will account for passenger weight removal in case passenger seats need to be removed to make room for tanks.

3.1.4. Emissions Module

The emissions analysis provides a comparative study of traditional kerosene and advanced H_2-combustion and SOFC Hybrid propulsion systems. The study models complete kerosene combustion to yield CO_2 and H_2O, while incomplete combustion produces CO, NO_x, SO_x, and HC. In contrast, complete H_2-combustion is expected to emit only H_2O, with NO_x as the primary byproduct during incomplete combustion, without the emissions of CO, HC, or SO_x. The analysis assumes minimal unburnt H_2 emissions due to the employment of advanced H_2 management and combustion technologies, including lean fully premixed (LFP) combustors, which are designed to ensure thorough mixing and complete combustion of hydrogen fuel. This assumption is supported by the work of Palies [72], who indicates that LFP combustors are effective in reducing unburnt fuel, aligning with the goal of zero-unburnt fuel in hydrogen-powered aviation. This premise is supported

by computational simulations that demonstrate the efficacy of LFP combustors in reducing unburnt fuel, aligning with the zero-unburnt fuel efficiency posited for LFP configurations in hydrogen combustion scenarios [72]. While the ideal scenario presents negligible H_2 emissions, practical implementations will require strategies for capturing or neutralizing any unburnt H_2 to fully leverage the environmental benefits and maintain safety standards [73]. The SOFC Hybrid system, which also utilizes H_2 as a fuel, is mainly associated with the emissions of H_2O and NO_x. The detailed emission profiles of these advanced propulsion systems will be further discussed in the following sections, offering insights into their potential environmental impacts.

The emissions analysis provides a comparative study of traditional kerosene and advanced hydrogen (H_2)-combustion, as well as SOFC Hybrid propulsion systems. This study models the complete combustion of kerosene to yield CO_2 and H_2O, while incomplete combustion produces CO, NO_x, SO_x, and HC. In contrast, complete H_2-combustion is expected to emit only H_2O, with NO_x being the primary byproduct during incomplete combustion, without the emissions of CO, HC, or SO_x. The analysis assumes minimal unburnt H_2 emissions due to the employment of advanced H_2 management and combustion technologies, including lean fully premixed (LFP) combustors. These combustors are designed to ensure thorough mixing and complete combustion of hydrogen fuel. This assumption is supported by the work of Palies [72], indicating that LFP combustors are effective in reducing unburnt fuel, thereby aligning with the goal of achieving zero-unburnt fuel in hydrogen-powered aviation. Furthermore, computational simulations have demonstrated the efficacy of LFP combustors in reducing unburnt fuel, aligning with the zero-unburnt fuel efficiency posited for LFP configurations in hydrogen combustion scenarios [72]. While the ideal scenario presents negligible H_2 emissions, practical implementations will necessitate strategies for capturing or neutralizing any unburnt H_2 to fully leverage the environmental benefits and maintain safety standards [73]. The SOFC Hybrid system, which also utilizes H_2 as fuel, is primarily associated with the emissions of H_2O and NO_x. The detailed emission profiles of these advanced propulsion systems will be further discussed in subsequent sections, offering insights into their potential environmental impacts.

Emission Indices

The International Civil Aviation Organization (ICAO) Engine Emissions Databank (EED) is employed to acquire the Emission Indices (EI) for non-cruise phases of flight for kerosene-powered aircraft. The EI for incomplete combustion of HC and CO during cruise are averaged at 0.4 g/kg and 0.6 g/kg, respectively, as reported by Wayson et al. [74]. Emissions of SO_x are omitted in this analysis due to the absence of corresponding data in the ICAO databank. The investigation concentrates on the principal emissions shared across the three technologies under review. Typically, the EI for NO_x ranges from 12 to 16 g/kg [74], influenced by the engine design's flame temperature. For simplicity, a median value of 14 g/kg is adopted for cruise conditions. This assumption is considered safe and pragmatic for comparative purposes, especially when specific combustion conditions (lean vs. rich) or the application of emission mitigation technologies are not explicitly detailed. It is acknowledged that NO_x emissions from hydrogen combustion can vary significantly depending on the technology used for emission mitigation. For instance, Therkelsen et al. [75] have shown that hydrogen combustion can lead to higher NO_x emissions due to the higher flame temperatures associated with hydrogen, despite efforts to achieve near-uniform fuel/air mixing. This underscores the inherent challenges in managing NO_x emissions from hydrogen-fueled engines, where even advanced mixing technologies cannot fully mitigate the thermal NO_x formation inherent to hydrogen's combustion properties. Conversely, advancements in emission reduction technologies have shown significant potential in lowering NO_x emissions from hydrogen-fueled aircraft, with reductions up to 90% compared to kerosene combustion, achieved through the implementation of technologies such as water injection [76, 77]. This illustrates the effectiveness of such technologies in overcoming the thermal NO_x challenges associated with hydrogen combustion. Furthermore, the Rich-Quick-Lean (RQL) combustion strategy proposed by Ingenito et al. [78] provides an effective framework for reducing NO_x emissions in high-speed hydrogen-fueled vehicles to ICAO acceptable values. By optimizing the equivalence ratio in the rich combustion stage and taking advantage of the wider flammability limits of the hydrogen flames in the lean combustion stage dramatic reduction in NO_x emissions were demonstrated, further supporting the argument for technological variability

in hydrogen combustion outcomes [78]. Given the vast variability in hydrogen combustion NO_x emissions influenced by technology and operational conditions, adopting a median EI_{NO_x} value of 14 g/kg for comparative purposes across all technologies analyzed, including the SOFC hybrid system. In this context, NO_x emissions are primarily generated not by the fuel cell itself but by a hydrogen combustor/micro gas turbine system operating at potentially higher temperatures. This standardized assumption facilitates a consistent comparison while acknowledging the diverse technological landscape and the potential for significant emission reductions with the right combination of fuel, technology, and operational strategies. Furthermore, in the case of kerosene combustion, the fuel composition significantly influences H_2O and CO_2 emissions, with a higher H/C ratio yielding more water and less CO_2. The EI for CO_2 is calculated by considering the carbon content in the fuel, the molar mass of CO_2, and the molar mass of carbon, resulting in 3.15 kg/kg. Similarly, the EI for H_2O, derived through the same methodology, is found to be 1.25 kg/kg. This approach ensures a consistent and comparative framework for assessing the environmental impact of both hydrogen and kerosene-fueled aircraft across different flight conditions.

Emissions

The CO_2 and H_2O emissions of kerosene are compared to the retrofitted H_2-combustion and SOFC Hybrid system powered aircraft. Such an emissions model assumes a constant percent thrust per segment and a constant aircraft Thrust-specific fuel consumption (TSFC). Each segment emission is modeled by dividing the flight profile into the segments seen in Table 3.2. The flight profile is designed to optimise aircraft ground operations to reduce emissions and local air quality impact [79][80]. The thrust per engine is taken at 100% for takeoff, 85% for climb, 30% for approach, and 7% for descent and idle, which matches the suggestions of the ICAO standard landing and takeoff cycle regulations [81]. The time to climb and descent is assumed to be 30 minutes. Although Taxi/Idle time varies by airport, an average value of 23 minutes is assumed for this analysis. This choice is justified by aiming to represent a typical ground operation time that balances between

shorter duration at less congested airports and longer periods at major hubs. Thereby providing a realistic and rather conservative average for a broad spectrum of flight operations. For the cruise portion of the flight, equation 3.11 models the mass fuel burned to obtain the complete emissions of CO_2, H_2O, CO, HC, and NO_x. A sample of implementing this methodology for modeling emissions is demonstrated in detail on Section 3.2.1.

$$E_x = m \times EI(X) \tag{3.11}$$

Table 3.2 Assumed flight profile segments

Segment	Duration (min)	Thrust (%)
Takeoff	0.7	100
Climb	30	85
Descent	30	7
Approach	4	30
Taxi/Idle	23	7

Contrails

The likelihood of contrail formation using kerosene, H_2-combustion fuel, and a SOFC hybrid-powered aircraft is modeled using mass and energy balances to determine the mixing line slope G. An aircraft exhaust plume mixes isobarically with exhaust air and can lead to the possibility of contrail formation [82]. Contrails may form by the mixing of hot and humid air with cold ambient air below a critical temperature threshold, as defined by the "Schmidt-Appleman" criterion [82], which is modeled by equation 3.12.

$$G = \frac{P_a EI(H_2O)C_{p,Air}}{\epsilon_{H_2O} LHV_{fuel}(1 - \eta_{overall})} \qquad (3.12)$$

Such contrails are evaluated since they can increase the overall warming effect due to trapped heat in the atmosphere and affect cooling from reflected sunlight [83]. The overall efficiency of the aircraft is assumed constant for all three configurations. The H_2-combustion and SOFC hybrid are expected to have a shallower slope than kerosene due to a higher LHV_{fuel} value of 120 MJ/kg. Such value is higher when compared to the conventional lower 43 MJ/kg kerosene LHV_{fuel}, as seen in Section 3.2.1. However, an increase in the mixing slope G arises from the higher EI of H_2O when using liquid hydrogen fuel. The persistence of contrails is not explored due to the location dependence of atmospheric conditions at every point of the duration of a single flight.

3.1.5. Environmental Impacts Module

Lifecycle Assessment

A complete lifecycle analysis (LCA) of CO_2 evaluates the environmental effects of a conventional kerosene powered aircraft, a retrofit H_2-combustion aircraft, and a retrofit SOFC hybrid powered aircraft. The lifecycle emissions are modeled for the various stages of fuel extraction, transport, processing, and storage sectors known as Well-to-Tank (WTT), and a combustion sector known as Tank-to-Wing (TTW), as seen in Fig. 3.7. Such LCA evaluates the consequences of eliminating the dependency of aviation upon dwindling crude oil resources, as well as, the overall contribution of aviation to the anthropogenic greenhouse effect [84]. The carbon intensity of kerosene fuel can vary depending on the region, the refinery and the crude oil well. Various studies have estimated that the carbon intensity of jet fuel ranges from 85 to 95 g of CO_2/ MJ [85]. The combustion of fuel contributes to a portion of 73 g of CO_2 eq/MJ, while the rest is generated by transportation, processing, and the refinement process [85]. The Well-to-Wing (WTW) CO_2 emissions for kerosene

fuel are modeled at 84.5 g $CO_{2\ eq}$/MJ with an 87% in combustion emissions [85]. Finally, the complete lifecycle of kerosene WTW is found by adding WWT to TTW CO_2 emissions of kerosene and LH_2 fuel sources from the extraction of crude oil or fuel to its combustion during flight.

The WTW for both H_2-combustion and the SOFC hybrid is estimated using green and gray hydrogen. Green hydrogen refers to the hydrogen produced via renewable energy, while gray hydrogen refers to the hydrogen produced using steam methane reformation without any greenhouse gas (GHG) emissions capture. More than 95% of hydrogen produced today is produced using fossil fuels like natural gas and coal [86]. Meanwhile, green hydrogen requires a renewable energy-powered grid which is not yet available in many parts of the world. However, most countries have plans to reach 100% renewable grids within the next 30-50 years [86]. The LCA estimation utilizes the Greenhouse Gases, Regulated Emissions, and Energy Use in Technologies (GREET) model to estimate the transportation lifecycle emissions via a mathematical framework that accounts for various pollutants such as CO_2 [87]. In addition, green hydrogen solar electrolysis is assumed to emit 41.29 g of $CO_{2\ eq}$/MJ for the full lifecycle, as referenced by Al-Breiki and Bicer [87]. Similarly, the gray hydrogen solar electrolysis full lifecycle is assumed to emit 75.6 g $CO_{2\ eq}$/MJ, as sourced by [88]. The mentioned LCA model does not include the production or life expectancy of lithium-ion batteries and the SOFC. The model is thus focused on the fuel WTW lifecycle. Although, the environmental effects of producing those components are mainly from mining, not enough current data and research are available on the lifecycle analysis of the SOFC hybrid system. TTW CO_2 emissions for all alternative fuel sources are modeled from the weight of the fuel inputted from the flight profile module as discussed in Section 3.1.4.
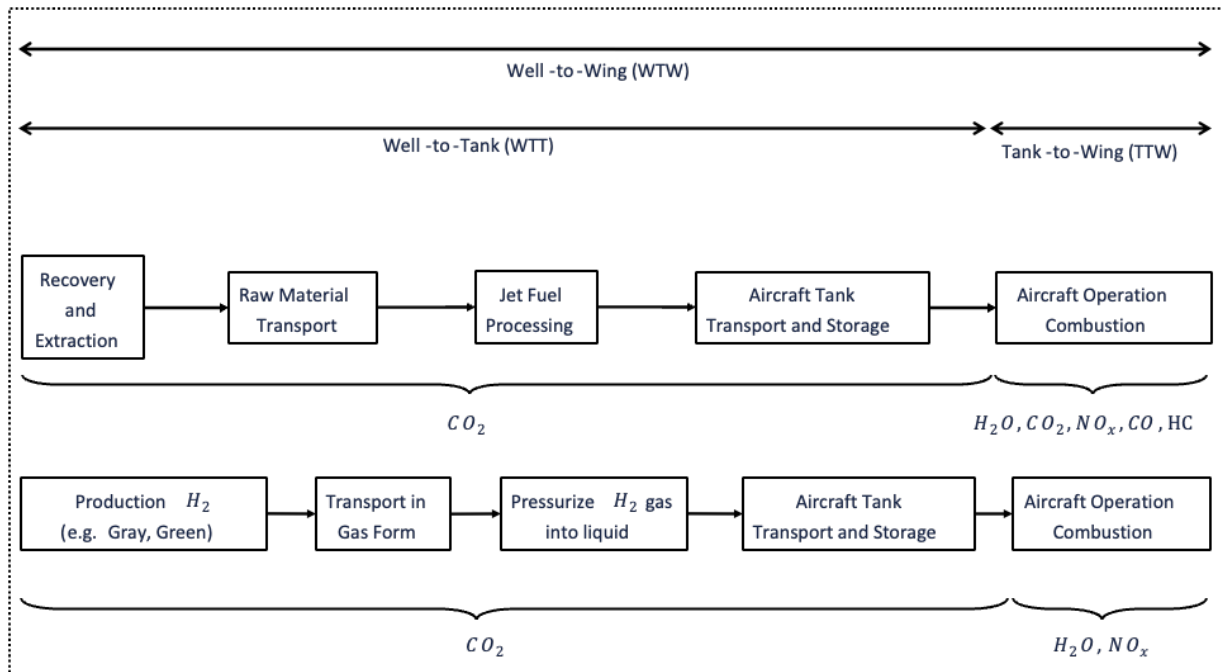
Fig. 3.7   Lifecycle Assessment (LCA) boundary of Jet-A Fuel (Top) and LH$_2$ fuel (Bottom)

Cost Analysis

The change in fuel cost of implementing alternative fuel sources for one constant range flight profile
is determined to further analyze the trade-offs of implementing a retrofit. The fuel burned per
segment from the emissions module is utilized to model the fuel price per flight for this mission,
in addition to the change in capital cost of the alternative fuel source. The cost for kerosene is
determined from the full-service average kerosene Jet-A fuel price per gallon for the U.S. western
pacific region for the current year. The price at the pump is assumed to already contain the production
and transportation costs of kerosene. The cost of utilizing LH$_2$ for the proposed flight is modeled
per segment in order to compare the change in fuel cost from a conventional kerosene powered flight.
The H$_2$-combustion change in fuel costs are estimated for both green and gray hydrogen. The cost
of production for green hydrogen (electrolysis) was set to 5.5 USD/kg while the production for gray
carbon capture hydrogen was taken at 1.55 USD/kg, as suggested by Ajanovic et al. [89]. The cost
liquefaction of both was set to 2.75 USD/kg as suggested by Ghorbani et al. [90], while the cost for

transportation was set to 5 USD/kg, as referenced by Hoelzen, et al. [91].

In assessing the capital costs of retrofitting aircraft with hydrogen fuel systems, the focus is primarily on the integration of cryogenic tanks, estimated at \$74.96 per kg of maximum LH_2 fuel capacity, following Yang et al. [92]. The initial cost analysis excludes heat exchanger costs based on the rationale that hydrogen combustion's expected thermal efficiency gains could diminish the necessity for comprehensive heat exchanger upgrades. Given their modular nature, heat exchangers are considered a lower priority in early evaluations, especially when compared to the substantial investments in cryogenic storage and fuel cell technologies. This approach prioritizes components critical to the retrofit's feasibility, with a detailed review of heat exchanger needs and other components like fuel lines, pumps, and valves deferred until further design specification in future analysis. The SOFC hybrid cost is modeled per segment for the purpose of comparison with LH_2 prices are determined as stated above. In addition, the stack cost at a high production volume of SOFC can be assumed to be 238 USD per kilowatt of energy, as suggested by Xing et al. [93]. A 500 kW microturbine is assumed to be in a mid-range market price of 900 dollars per kW following the California Distributed Energy Resources (DER) guide on microturbines and resourced by Chua et al.[94]. The lithium-ion battery cost is estimated to be 135 USD per kilowatt hour for the current year as resourced by Varbanov et al.[95].

3.2. Methodology Demonstration for Alternative Fuel Retrofit on a Business Jet

The developed methodology in the previous section evaluates the potential to lower emissions for a single flight by utilizing a retrofit analysis. When compared to an existing aircraft, business jets show a greater 34% net energy consumption reduction in emission values when utilizing H_2 fuel, as suggested by Nojoumi et al. [56]. Therefore, a business jet is chosen for this study since they have the greatest energy consumption reduction and a greater potential to lower all emissions including water vapor emissions. As global demand for private jet activity has risen by 7% in 2021, the

implementation of the aforementioned methodology on the Cessna Citation 560 XLS+ business jet presents a potential opportunity for carbon mitigation [96]. A summary of key mission and performance specifications for the mentioned aircraft are found in Table 3.3:

Table 3.3   Cessna Citation 560 XLS+ performance specifications

Parameter	Value
Cruise Range	3,889.2 km
Maximum Number of Passengers	9
Maximum Speed Limit	0.75 Mach
Maximum Operating Altitude	13,716 m
Thrust Specific Fuel Consumption	0.045 kg/Nhr

The methodology presented in Section 3.1 is utilized to model the performance and emissions of the standard kerosene powered Cessna Citation 560XLS+ in order to compare the trade-offs resulting from a retrofitted H_2-combustion fuel and SOFC hybrid powered aircraft. In the flight profile module, these two alternative fuel power sources are examined for the same mission profile as the kerosene baseline procedure. The weight of the fuel required for this mission is determined for all three power plants as a function of heat energy available per unit weight of fuel, range, and other Breguet range equation parameters as seen in Section 3.1.1. Such weights are utilized to design the tanks as stated in Section 3.1.2 and evaluated for feasibility in the center of gravity module, as shown in Section 3.1.3. A few passengers might be omitted if tank sizing volume constraints are required to power the same mission or a refueling stop might be added. A new fuel weight that accounts for such changes is then outputted into the emissions module. The flight emissions are then used to assess the lifecycle assessment and costs of implementing each retrofit. An overall analysis of the trade-offs in performance and emissions by a retrofit methodology is outputted.

3.2.1. Analysis of Results

The conventional kerosene, the H_2-combustion, and the SOFC hybrid powered retrofit aircraft are all able to power the cruise mission specifications from Table 3.3. The fuel weights obtained from the flight profile module in Section 3.1.1 are seen in Table 3.4:

Table 3.4   Fuel weights for cruise

Cruise Weights	Jet-A (kg)	H_2-combustion (kg)	SOFC (kg)
W_{start}	$9,223.35$	$8,685.22$	$9,187.86$
W_{end}	$8,146.54$	$8,282.74$	$8,912.17$
W_{fuel}	$1,077.81$	401.68	271.31

The power requirements and constraints of the H_2-combustion fuel and SOFC hybrid powered aircraft follow the energy assumptions described in Section 3.1.1, and are seen in Table 3.5. The power rating of the electric propulsion system is defined based on the maximum takeoff velocity of the aircraft and the thrust of the conventional aircraft. The Battery size is defined as providing maximum thrust for 15 minutes. Such parameters and the fuel weight are used as design constraints in the tank configuration module.

Table 3.5   Power and SOFC energy requirements

Parameters	Values
Thrust Per Engine (N)	$18,322$
Maximum T/O Velocity (km/hr)	230
Engine Max Power (kW)	2,344.96
Energy Required by H_2-combustion (MJ)	$32,546.51$
Energy(kWh)	$9,040.70$
Fuel Cell Power (75%)(kW)	1,758.72
Battery Power (25%)(kW)	586.24
Battery Size (kWh)	146.56
Cryocooler Maximum Power (kW)	23.45

The hydrogen cryogenic tanks are designed with insulation and altitude pressure as added design constraints. The resulting tank materials, properties, and characteristics are seen in Table 3.6. The design of insulation maximizes flight temperature as specified in the Thermal module in 3.1.2. The tanks specified above are then evaluated for feasibility in the center of gravity module. The three interior layout arrangements that satisfied the maximum and minimum CG envelope limits are seen in Fig. 3.8. The FAA minimum 30 cm aisle width regulation (for airplanes less than 10 passengers [70], is exceeded for passenger comfort and evacuation regulations in all three configurations. The conventional arrangement of the Cessna 560 XLS+ is seen in Fig. 3.8a with a forward refreshment center and an aft lavatory. The LH_2 tank design and layout results in six small tanks each of 157 cm distributed in the forward section of the cabin, and four aft tanks, two of small size, one of mid-size and one of large-size all with 271 cm in length as seen in Fig. 3.8b and Fig. 3.9. Such tank designs are subject to sizing and feasibility constraints and are seen in Table 3.6. However,

passenger tables between seats 3 and 5 and 4 and 6 must be removed in order to fit the 6 small forward tanks. Nonetheless, the FAA minimum required first-class seat pitch of 96.5 cm is exceeded for all seats after such removal [70]. The H_2-combustion and SOFC layout required the removal of seats 1,2 and 9, as well as, the removal of the aft closet in order to fit the aft mid-size LH_2 tank 25.4 cm into section a-a of the cabin aft section, as seen in Figs. 3.8b and 3.8c. However, the SOFC required the shift of the forward lavatory and refreshment center since the aft section of the cabin is used to house the SOFC power train seen in pink in Fig. 3.8c.

Table 3.6   Cryogenic LH_2 tanks

Parameters	Front Tanks		Aft Tanks	
Size	*Small*(6)	*Large*(1)	*Medium*(1)	*Small*(2)
r_{tot} (cm)	25.60	60.20	23.08	20.07
L_{tot} (cm)	157	271	271	271
V_{tot} (m³)	0.288	0.392	0.393	0.300
t_w (cm)	0.089	0.211	0.081	0.070
Insulation Thickness (cm)	0.0079	0.008	0.008	0.008
W_t/W_f (%)	23.8	23.5	24.1	24.1

(a) Jet-A

(b) H$_2$-combustion

Lavatory
Kitchen
LH_2 Tanks
SOFC Power Train
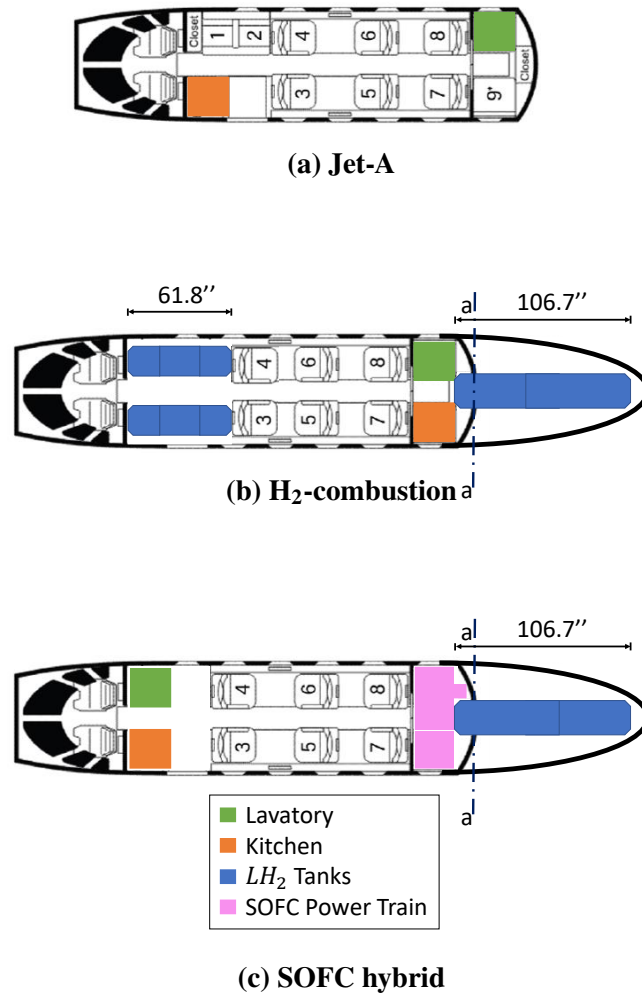
(c) SOFC hybrid

Fig. 3.8   Interior layouts for retrofit analysis

The final design for both the retrofitted H$_2$-combustion and the SOFC hybrid both resulted in six passengers. For the H$_2$-combustion these changes result in a 5% decrease in overall aircraft weight when compared to the conventional aircraft. For the SOFC such changes result in a 0.4% decrease in mass when compared to the conventional aircraft. This change of mass is observed due to the more energy-dense hydrogen, the choice of SOA materials, and the loss of three passengers, their seats, and luggage. The highest weights in the H$_2$-combustion aircraft are the empty weight and the weight of the passenger and bags, while the main weights in the SOFC are the empty weight and
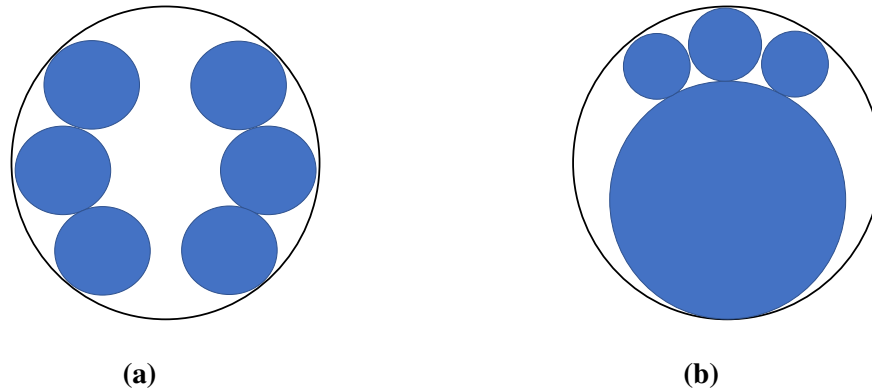
Fig. 3.9   Cross section of fuselage: (a) forward six small tanks (b) aft four tanks: one large size, one medium, and two small tanks

the fuel cell mass, as seen in Fig. 3.10. An H_2-combustion and SOFC hybrid powered aircraft can be designed where the same number of seats and cabin area is maintained. However, this would require a refueling stop and result in higher energy requirements and higher emissions for both the H_2-combustion and the SOFC hybrid aircraft.
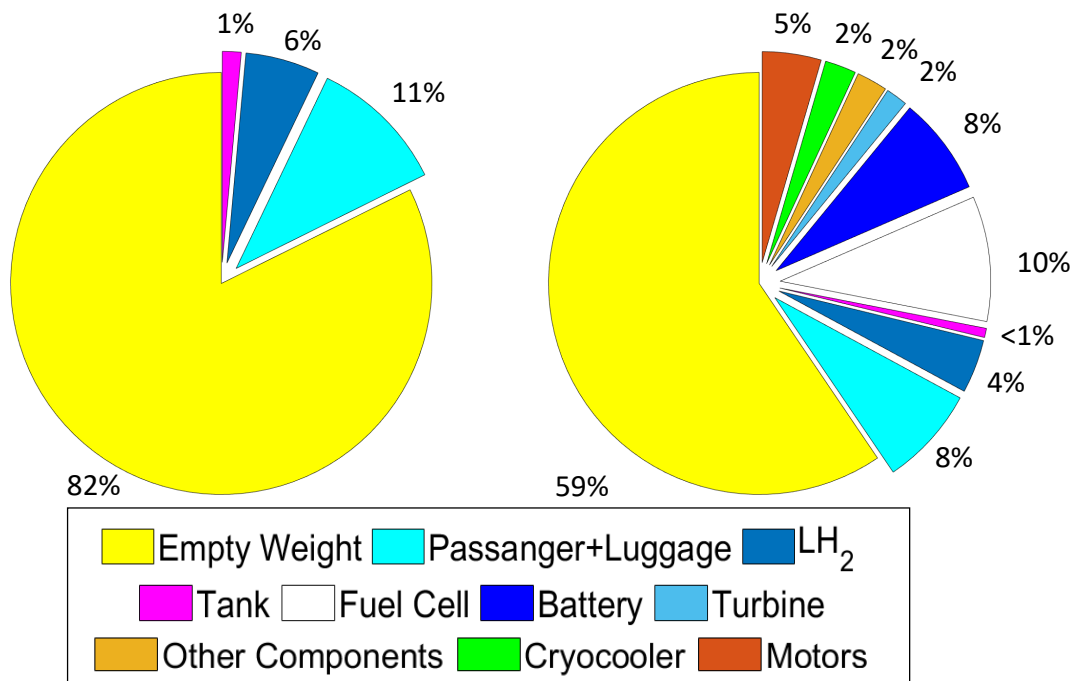
Fig. 3.10   Resulting fractional weights from implementing a retrofit on a H_2-combustion (Left) and a SOFC hybrid (Right) powered Cessna Citation 560XLS+

As expected, H_2-combustion and the SOFC hybrid produce zero CO_2 emissions, as seen in Fig. 3.11 Such figure also shows that kerosene fuel CO_2 and H_2O emissions are the highest during the cruise segments, with the second highest during the climb. Such a result is expected since emissions from these segments are dependent on how much time is spent while fuel is being burned. In comparison, higher emissions of CO and HC occur during idle and descent than CO_2 and H_2O emissions, due to incomplete combustion. H_2-combustion and the SOFC hybrid both results in higher water vapor emissions and could therefore have a likelihood of contrail formation. When compared to a conventional aircraft, the G-factor increases due to high vapor emissions and the possibility of the low static temperature of the exhaust. In addition, fuel cells can produce condensation phenomena at the earth's surface if the weather is cold and close to frost. However, these are short-living phenomena, which will disappear after a few seconds (outside of fog) and thus the term "contrail" should not be used for such a transient phenomenon.
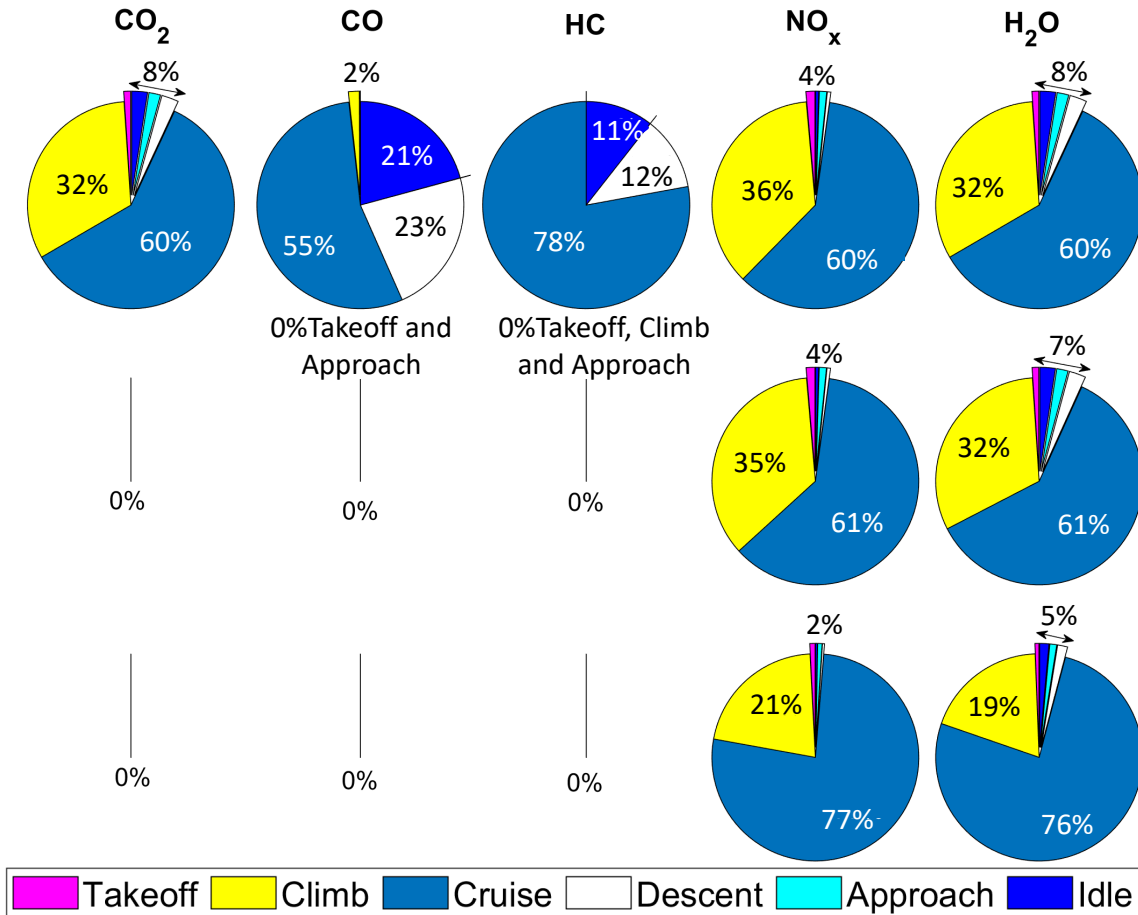
Fig. 3.11   CO$_2$, CO, HC, NO$_x$ and H$_2$O emissions per segment of conventional kerosene (Top), H$_2$-combustion (Middle), and retrofit SOFC-powered aircraft (Bottom)

As seen in Table 3.7, The NO$_x$ emissions per passenger-km are 2.81×10^{-4} kg, 3.94×10^{-4} kg, and 2.12×10^{-4} kg for the conventional, H$_2$-combustion, and SOFC hybrid aircraft, respectively. The water vapor (H$_2$O) emissions per passenger-km are 0.062 kg, 0.255 kg and 0.137 kg for the conventional kerosene powered aircraft, H$_2$-combustion, and SOFC hybrid powered aircraft, respectively. The contrailing of the water vapor emissions depends on the environment, combustion temperature, altitude and mixing line "G" shown in equation 3.12. Thus, hydrogen combustion has the highest water vapor emissions per passenger-km, about 4 times more than conventional kerosene. To effectively mitigate contrail formation, a multifaceted approach is needed, considering

the varying impacts of different powertrain technologies. Firstly, optimizing flight paths using real-time meteorological data can significantly reduce contrail formation, potentially by up to 20%, by avoiding areas prone to contrailing . Moreover, evading or reducing night time flight or flying at lower altitudes are possible solutions but must be critically assessed. Eliminating night flights would require a substantial increase in daytime airport and aircraft capacity, potentially inflating infrastructure costs significantly. Additionally, fuel consumption can increase by 10-15% when flying at lower altitudes compared to optimal cruise altitudes due to denser air at lower altitudes.. Hence, addressing contrail formation requires balancing operational feasibility with environmental goals[56, 97].

Table 3.7 NO_x and H_2O total emissions per passenger-km

Emissions	Jet-A (kg/passenger-km)	H_2 (kg/passenger-km)	SOFC Hybrid (kg/passenger-km)
NO_x	2.81×10^{-4}	3.94×10^{-4}	2.12×10^{-4}
H_2O	0.062	0.255	0.137

The full lifecycle of CO_2 results are categorized in two cases, as seen in Table 3.8. Case (i) stands for one flight with nine passengers for the conventional kerosene powered aircraft, one flight with six passengers for the retrofit H_2-combustion-powered aircraft, and one flight with six passengers for the retrofit SOFC hybrid powered aircraft. Whereas, case (ii) models taking an additional flight for the full lifecycle of the retrofit H_2-combustion and the retrofit SOFC hybrid aircraft. Such a model is obtained by keeping the same original amount of passengers (9) for the same range and adding an additional flight for both alternative fuel configurations. The results seen in Table 3.8 also show the full lifecycle as a function of the hydrogen sourcing production technique to compare emissions from both sourcing gray and green. As seen in Table 3.8, 86.8% of CO_2 emissions for the kerosene powered aircraft happen during the combustion process in the TTW path of the fuel seen in Fig. 3.7 in Section 3.1.5. However, if tank sizing constraints did not require a second flight for the H_2 and the SOFC powered aircraft, the results would have been closer to the values obtained for

all case (i) instances.

In case (ii), where an additional flight is required for the H_2 and SOFC powered aircraft to carry the same number of passengers as the Jet-A powered aircraft, the CO_2 emissions per passenger-km change significantly. The gray retrofit H_2-combustion powered aircraft shows an 83.42% increase in Well-to-Wing (WTW) CO_2 emissions compared to the kerosene powered aircraft. Surprisingly, the green retrofit H_2-combustion powered aircraft does not show any change in WTW CO_2 emissions, remaining at a 0% difference. For the SOFC configurations, the gray retrofit SOFC hybrid shows a slight decrease of 1.60% in WTW CO_2 emissions, while the green retrofit SOFC hybrid demonstrates a more substantial decrease of 46% in WTW CO_2 emissions compared to the kerosene powered aircraft. Such results arise from the carbon emissions during extraction, sourcing, transportation, and storage, as seen in the WTT path in Fig. 3.7 in Section 3.1.5. These results highlight the nuanced environmental impact of transitioning to alternative fuel sources in aviation, especially when considering operational constraints like fuel tank sizing. While the adoption of green energy sources like the green H_2 and SOFC can lead to significant reductions in CO_2 emissions, operational factors such as the need for additional flights can offset these environmental benefits, as evidenced by the increased emissions for the gray retrofit H_2-combustion powered aircraft in case (ii).

However, case (i) shows a significant reduction in Well-to-Wing (WTW) CO_2 emissions for three out of four configurations of the retrofit H_2-combustion aircraft (green), and the retrofit SOFC-powered aircraft (gray and green) when compared to the conventional kerosene powered aircraft WTW CO_2 emissions. These percentages are: -25.13% for the green retrofit H_2-combustion-powered aircraft, -26.20% and -59.63% for the gray and green retrofit SOFC hybrid powered aircraft, respectively. Lastly, the carbon emissions from the gray retrofit H_2-combustion-powered aircraft show an 37.43% increase compared to the conventional kerosene powered aircraft WTW CO_2 emissions. This contrast in CO_2 emission reductions and increases across different fuel types emphasizes the complex interplay of factors in aviation's transition to greener alternatives. The significant decrease in CO_2 emissions for green H_2 and SOFC technologies highlights their potential in reducing the

aviation sector's carbon footprint. However, the increase in emissions for the gray H_2-combustion aircraft underscores the challenges in selecting appropriate hydrogen sourcing methods. It reflects the necessity of considering the entire fuel production and consumption cycle when evaluating environmental impacts. The results from case (i) suggest that while alternative fuels can offer substantial environmental benefits, their adoption must be coupled with sustainable production methods to realize their full potential in reducing aviation's environmental impact.

Table 3.8   CO$_2$ emissions for full lifecycle analysis of all configurations (kg/passenger-km)

Path	Case	Jet-A	Gray H_2	Green H_2	Gray SOFC	Green SOFC
Well-to-Tank CO$_2$	(i)	0.0247	0.257	0.140	0.138	0.0755
	(ii)		0.343	0.187	0.184	0.101
Tank-to-Wing CO$_2$	(i)	0.162	0	0	0	0
	(ii)		0	0	0	0
Well-to-Wing CO$_2$	(i)	0.187	0.257	0.140	0.138	0.0755
	(ii)		0.343	0.187	0.184	0.101

To enhance the clarity in emission comparisons among different configurations, we assessed the Global Warming Potential (GWP) in terms of kg $CO_{2\ eq}$ emissions per passenger-km. This assessment considers GWP values over a 100 years derived from relevant literature [98–100]. The GWP factors employed in our analysis include: CO_2 at a factor of 1, HC at 21, CO at 1.7, NO_x at 40, and H_2O at 0.059. Utilizing these factors, the Tank-to Wing kg $CO_{2\ eq}$ emissions were calculated to be 0.177 kg $CO_{2\ eq}$/passenger-km for Jet-A aircraft, 0.0308 kg $CO_{2\ eq}$/passenger-km for single-flight H_2 combustion, and 0.0165 kg $CO_{2\ eq}$/passenger-km for single-flight SOFC Hybrid system. It is crucial to recognize that these values may vary depending on numerous factors, including the geographic location of the flight. These assumptions are specific to North American airspace, where the reference flight is conducted. The Tank-to-Wing (TTW) emissions associated with hydrogen fuel

consumption exhibit significantly lower Global Warming Potential (GWP) across both configurations when compared to the combustion of Kerosene. Incorporating Well-to-Tank (WTT) CO_2 emissions, as detailed in Table 3.8, reveals that Jet-A fuel possesses a GWP of 0.217 kg CO_2 $_{eq}$/passenger-km, whereas green hydrogen demonstrates a GWP of 0.171 kg CO_2 $_{eq}$/passenger-km. Additionally, green SOFC technology presents a GWP of 0.092 kg CO_2 $_{eq}$/ passenger-km.

The integration of Solid Oxide Fuel Cells (SOFC) in aviation, while promising for emissions reduction, is constrained by several technical and operational limitations. Firstly, the lifespan of SOFCs in aviation contexts is a critical issue. SOFCs exhibit degradation rates of 1 - 3% per 1000 operating hours depending on operation, whereby less than 0.5%/1000 h are required for economic efficiency [101, 102]. Stationary power systems are commercially available today with stacks that exhibit very long lifetimes in the range of 40,000-70,000 hours [103] but for more highly dynamic and more rigorous transport application SOFC lifetime is expected to be 4,000-5,000 hours after intense degradation [104, 105], contrasting with the average lifespan of conventional aircraft engines like the Pratt & Whitney Canada PW545C, which can exceed 6,000 hours before an engine overhaul is required [71]. Hence, more frequent replacement of the SOFC is expected to increase life-cycle emissions costs. The production of a 1 kW planar SOFC CHP system is estimated to result in the emission of approximately 700–950 kg of CO_2. These impacts are further amplified when accounting for the production of replacement stacks [106].This discrepancy in lifespan could require more frequent replacements for SOFCs, thereby imposing higher lifecycle emissions and maintenance costs.

Additionally, SOFCs' sensitivity to fuel impurities, especially when powered by gray hydrogen containing contaminants like sulfur or carbon monoxide, can degrade cell performance and reduce efficiency. These impurities can poison the Ni-based anode, leading to a decrease in the electrochemically active surface area and a deterioration of the cell performance. A 1% contamination by volume can decrease cell lifespan by up to 10% [107, 108]. Moreover, fast temperature changes during flight pose durability challenges. The thermal management of SOFC systems, which must

74

maintain a constant operating temperature for maximum performance, may face difficulties as a result of this temperature variation [109]. Additionally, the impact of aircraft vibrations on SOFC integrity is notable. Vibrations can lead to microcracks in the cell structure, affecting performance. Under conditions of intense vibration, the ceramic materials used in SOFCs can exhibit brittleness, making them prone to mechanical breakdowns, especially at high temperatures. Electrochemically, microcracks in SOFCs impair performance by disrupting the electrolyte layer's ability to conduct oxygen ions, thus decreasing ionic conductivity and electrochemical efficiency. These cracks also allow fuel and oxidant gases to mix, reducing fuel efficiency and potentially causing cell failure. Furthermore, microcracks in the electrode layers reduce the active surface area, further diminishing the cell's electrochemical performance [110]. Thermal management also presents a substantial challenge. SOFCs operate at high temperatures, necessitating advanced cooling systems that increase weight and complexity. Controlling the heat output of SOFCs in an aircraft's confined space is crucial. Present thermal management solutions can restrict SOFC power output to the kW scale, which falls short of the requirements for medium-sized aircraft. These limitations underscore the necessity for considerable advancements in SOFC technology and infrastructure to make them a feasible option for aircraft applications [111].

Table 3.9   Total fuel cost per segment per passenger-km

Segments	Case	Jet-A ($)	Gray H_2 ($)	Green H_2 ($)	SOFC H_2 Gray ($)	SOFC H_2 Green ($)
Takeoff ($x10^{-3}$)	(i)	1.26	2.75	3.84	0.892	1.25
Climb ($x10^{-3}$)	(i)	38.3	83.3	116	27.1	37.8
Cruise	(i)	70.6	160	224	108	151
Descent ($x10^{-3}$)	(i)	3.15	6.86	9.58	2.23	3.12
Approach ($x10^{-3}$)	(i)	2.16	4.71	6.58	1.53	2.14
Taxi/Idle ($x10^{-3}$)	(i)	2.90	6.31	8.83	2.05	2.87
Entire flight ($x10^{-3}$)	(i)	118	264	369	142	198
Entire flight ($x10^{-3}$)	(ii)		352	492	189	264
Total fuel cost for mission	(i)	4,143.18	6,161.55	8,612.92	3,310.33	4,627.34
	(ii)		12,323.10	17,225.84	6,620.66	9,254.68

Two cases were evaluated following the same approach as the lifecycle emissions for cases (i) and (ii). From an economic perspective, significant changes in fuel costs per passenger-km result from replacing kerosene with alternative fuel sources. In case (i), as seen in Table 3.9, the fuel cost per passenger-km for gray H_2-combustion is 123.73% higher than kerosene, while green H_2 shows an even greater increase of 212.71% due to the higher cost of green H_2 production. The SOFC gray H_2 configuration offers a 20.34% increase in fuel cost per passenger-km compared to kerosene, while the SOFC green H_2 configuration sees an increase of 67.80%.

In case (ii), where two flights are required to carry the same number of passengers, the fuel costs per passenger-km change more significantly. The SOFC gray H_2 shows a 198.31% increase in fuel cost per passenger-km, while green H_2 shows a staggering 316.95% increase when compared to kerosene for case (i). The SOFC hybrid configurations also exhibit increases in fuel costs per passenger-km, with the gray SOFC hybrid showing a 60.17% increase and the green SOFC hybrid showing a 123.73% increase compared to kerosene for case (i).

The change in capital cost for purchasing the SOFC hybrid includes a total of 919,497.27 USD for the cryogenic tanks plus the SOFC power train, while the change in capital costs for the H_2-combustion aircraft is 49,661.50 USD from the cryogenic tanks. Additionally, when examining the "Total fuel cost for mission" as presented in Table 3.9, a significant economic implication emerges for both cases. In case (i), the total fuel cost for alternative fuels ranges from \$3,310.33 to \$8,612.92, with the green H_2 being the most expensive, highlighting the premium associated with greener options. Conversely, in case (ii), the total fuel cost escalates substantially for the H_2 and SOFC configurations due to the requirement of an additional flight, with costs ranging from \$6,620.66 to \$17,225.84, thereby emphasizing the economic impact of operational constraints in the adoption of alternative fuels. These cost changes highlight the economic challenges associated with transitioning to alternative fuels in aviation. While some configurations show significant increases in fuel costs, particularly in scenarios requiring additional flights, they reflect the current state of technology and the premium associated with greener fuel options. This underscores the importance of considering

both environmental and economic factors in the adoption of alternative fuels in the aviation industry.

3.3. Conclusion

The proposed methodology models the performance, emissions, lifecycle and costs of a retrofitted H_2-combustion and a retrofitted SOFC hybrid powered aircraft. Such methodology consists of a constant range and airframe analysis to design liquid hydrogen fuel tanks that satisfy insulation, sizing, center of gravity, and power constraints. The interior layout analysis results in a 5% and 0.4% decrease in takeoff weight for the H_2-combustion and SOFC hybrid aircraft respectively. However, the resulting mass change is achieved at the cost of removing a few passengers and their luggage to account for cryogenic tank sizing and weight constraints for the same range. Therefore, neither H_2-combustion nor the SOFC hybrid aircraft are able to carry the same number of passengers for the same range as the kerosene powered aircraft. Although kerosene powered aircraft can transport a greater amount of passengers per trip, carbon emissions are higher since conventional kerosene combustion has the highest WTW CO_2 kg emissions of 6,546 kg per flight. However, for kg CO_2 per passenger-km, gray H_2-combustion aircraft surprisingly results in the highest WTW CO_2 emissions. Nevertheless, great advantage for potential carbon mitigation arises from utilizing hydrogen alternative fuels since kerosene combustion also produces other GHG emissions besides NO_x, CO_2, and H_2O that all systems share. The NO_x emissions per passenger-km are highest in H_2 combustion aircraft and lower in the Kerosene and SOFC hybrid aircraft consecutively.

In terms of WTW CO_2 emissions per passenger-kilometer, the study reveals varied impacts depending on the fuel type and operational scenario. Case (i) shows that green hydrogen and SOFC technologies significantly reduce CO_2 emissions in aviation, with reductions of 25.13% and 59.63% respectively, compared to conventional kerosene. However, the gray H_2-combustion aircraft increases emissions by 37.43%. However, other greenhouse emissions must be evaluated when comparing the SOFC hybrid to the H_2-combustion. H_2O TTW emissions are highest for the H_2-combustion aircraft and therefore have a likelihood for contrail formation. Addressing contrail formation is crucial

given its radiative forcing impact, comparable in magnitude to CO_2 emissions from kerosene combustion [112]. However, alternatives like avoiding night-time flights or flying at lower altitudes must be evaluated against practical and economic constraints. For instance, restricting night flights significantly increases demand on daytime airport and aircraft capacity, potentially escalating infrastructure costs. Moreover, lower altitude flights could lead to increased fuel consumption and emissions, offsetting the benefits of reduced contrail formation. This necessitates a balanced approach, where strategies are tailored to optimize both environmental impact and operational feasibility. Further exploration into efficient flight routing, advanced aircraft designs, and alternative fuels could provide more viable solutions for managing contrail effects without disproportionate cost implications. The economic analysis also reveals significant increases in fuel costs per passenger-km for both H_2-combustion and SOFC configurations, compared to kerosene. The most notable is green H_2 shows a 212.71% increase for the green H_2-combustion variant, which is likely due to the higher production costs associated with green hydrogen. Meanwhile, the SOFC gray H_2 configuration offers the cheapest change in the price with a 20.34% increase in fuel cost per passenger-km due to the lower cost of gray hydrogen and higher efficiency of the system. However, a more expensive one-time capital cost of \$919,497.27 comes from purchasing the SOFC power train. Such is a potential trade-off that aids carbon mitigation in the near future for the cost of omitting a few passengers for the same range.

Moreover, in our exploration of retrofitting business jets with alternative propulsion systems, we have carefully considered a range of crucial factors such as the aircraft's weight, operational range, cabin size, and engine types such as turbofan, turbojet, and turboprop. The focus of our study, primarily on the Cessna Citation XLS+, has yielded a methodology robust and versatile enough to be applied across various aircraft categories and engine types. However, it is imperative to also account for the specific maintenance requirements and operational efficiencies of different aircraft models in any comprehensive retrofitting strategy. Our research, while detailed for the Cessna Citation XLS+, provides a foundation for subsequent studies. The findings indicate that, generally, medium-sized business jets with similar cabin sizes and power requirements in the same

range (around 13 cubic meters and 2.3MW, respectively) are likely to be suitable candidates for similar retrofitting processes. Business jets of similar size and lower power requirements should particularly expect positive retrofitting results. Importantly, the analysis we conducted also suggests the need to validate the generalizability of our success with the Cessna Citation XLS+ to other similar medium-sized, 9-seater business jets. This validation is crucial, as it will confirm the broader applicability and potential effectiveness of our retrofitting methodologies across a wider array of aircraft within the aviation industry.

The results presented in the retrofit, cost and emissions analysis illustrate the complex balance between environmental benefits and economic considerations in the aviation sector's transition to alternative fuels. While alternative fuels like hydrogen and SOFC technologies offer potential reductions in CO_2 emissions, their economic viability and the operational adjustments required (such as passenger capacity reductions for the same flight range) must be carefully considered. The methodology presented is adaptable to various aircraft categories and engine types, but its broader application requires an assessment of these multifaceted variables.

4. Dynamic Modeling and Integration Analysis of Hydrogen SOFC/GT-Powered Aircraft

Parts of this chapter, in parts or in whole, are co-authored by and published in: Khaled Alsamri, Sajjad Rezaei, Vanessa Chung, Jacqueline Huynh, and Jack Brouwer. "Dynamic Modeling of Hydrogen SOFC/GT Powered Aircraft with Integration Analysis," AIAA 2024-1532. *AIAA SCITECH 2024 Forum*, January 2024.

Despite these appealing attributes, SOFC/GT systems adoption in aviation has been hindered partially due to a lack of comprehensive research including dynamic modeling to verify its operational viability under the wide range of dynamic and harsh flight conditions. This chapter strives to fill this significant gap in the literature. The dynamic behavior of a hydrogen-powered SOFC/GT system in an aviation context remains relatively unexplored, forming the basis of our investigation. We present a novel approach to dynamic modeling of a representative retrofitted SOFC/GT powered Cessna S550 Citation S/II, meticulously accounting for the intricate complexities of flight conditions. This study is critical as the robustness of the SOFC/GT system under dynamic conditions is the key to ensuring the system safety, reliability, and commercial viability.

4.1. Dynamic Simulation Methodology

The methodology for modeling SOFC/GT powered aircraft primarily utilizes Efficient Allocation of Grid Energy Resources including Storage (EAGERS) and SpaTially Resolved Integrated Dynamic modeling of Electro-chemical Systems (STRIDES), dynamic modeling tools within MATLAB. EAGERS, developed by University of California Irvine and Washington State University, is an open-source platform recognized for its extensive capabilities in analyzing and optimizing various energy systems [113]. Its scalable, modular design is ideal for designing, simulating, and controlling

district energy systems. STRIDES complements EAGERS by facilitating non-linear simulation of energy system components, such as heat exchangers, batteries, inverters, and fuel cells, which can be integrated into larger systems and networks. This tool's strength lies in its ability to perform high-fidelity and spatially-resolved simulations using both detailed physical models and simplified reduced-order models, with local controllers for each component, enhancing its applicability to aircraft powertrain simulations.

The primary focus of the model is the dynamic response of the system to varying power demands, alongside a comprehensive analysis of its electrochemical characteristics. The model will be configured using the EAGERS platform to represent the SOFC/GT system and its components accurately, followed by the definition of the governing equations and system constraints. The research emphasizes investigating the complex interaction between the dynamic behavior of the power system and the underlying electrochemical processes within the SOFC. This synergistic modeling approach aims to identify potential areas for system optimization and improvement.

For an effective dynamic model of an SOFC/GT system, it is essential to incorporate specific thermochemical conditions, SOFC properties, GT transfer functions, and geometrical component specifications. These conditions, encompassing input, output, and internal system flows, can be figured out using built-in fuel-cell stack design modules under both nominal and partial loads. Key SOFC characteristics such as the polarization curve, cell count, operating temperature, and fuel type are also input, alongside the GT compressor and turbine maps that characterize performance at varied loads, pressure ratios, and speeds. The model also requires precise controls for regulating fuel and air supply, temperature, and potentially load adjustments on the GT to avoid surge or stall events, ensuring a realistic and safe operation.

The simplified framework, as depicted in Fig. 7.1, presents an integrative framework for the dynamic modeling of an SOFC as part of an aircraft power system. The model emphasizes the initialization process with the design point SOFC operating conditions, including temperature, flow rates, fuel utilization, and an initialization of each component in isolation. This modular approach facilitates

81

targeted optimizations and adjustments, ensuring each component reaches a steady operational state before integration into the larger system.
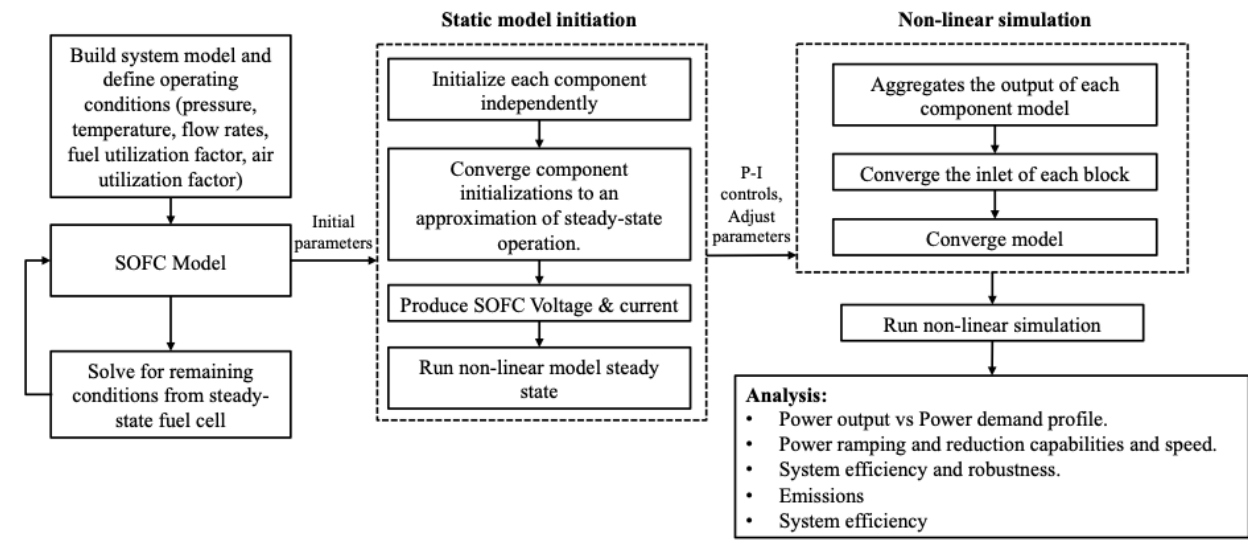
Fig. 4.1   Flowchart of SOFC/GT system modeling and analysis process.

Once the system is constructed and initial parameters are established, the SOFC model solves the system of dynamic governing equations for a long period of time in order to garner an initial steady-state set of operating conditions for the fuel cell system. The physical period of time typically required for solving the non-linear model to achieve this steady state is a 24-hour period. After achieving a steady state, Proportional-Integral (PI) controls are fine-tuned, allowing the model to dynamically respond to a demand profile over time. The outputs of each component are aggregated, and the inlets of each component block are combined before the model converges and reacts to the power demand profile, converging at each time-step. This convergence enables a comprehensive analysis of the system's behavior over time. The analysis focuses on power output relative to power demand profiles, which reflects the system's capacity to meet the aircraft's operational requirements. Moreover, the model rigorously examines the capabilities for power ramping and reduction, which are crucial for aircraft systems that need to rapidly adapt to fluctuating power requirements.

The model shown in Fig. 4.2, depicting the powertrain SOFC/GT hybrid setup for Medium-Range and Long-Range aircraft, will be primarily employed. The design will be realized and scrutinized via the

modeling and simulation in STRIDES. The cell/stack model, governed by Eq. (1-22), encompasses an electrochemical model and energy balance of the positive electrode-electrolyte-negative electrode (PEN) structure, as well as the energy balance of fuel and air streams and interconnect plates. A comprehensive dynamic mass balance equation for the entire system is established. The core of the system design is the heat and power production by the quasi-3D SOFC model, wherein the fuel cell is integrated into the hybrid cycle as a topping cycle to the GT. An oxidizer raises the exit temperature for use in a recuperator, which increases SOFC compressed air inlet temperatures. The resulting heated flow drives a turbine that mechanically operates the compressor, maintaining a pressurized system at 3 atm. Surplus mechanical energy from the turbine is harnessed to generate electricity through a generator. In this design, the waste heat and oxidized anode tail-gas from the SOFC provide all of the energy required for air compression and additional electricity (from the GT and generator).
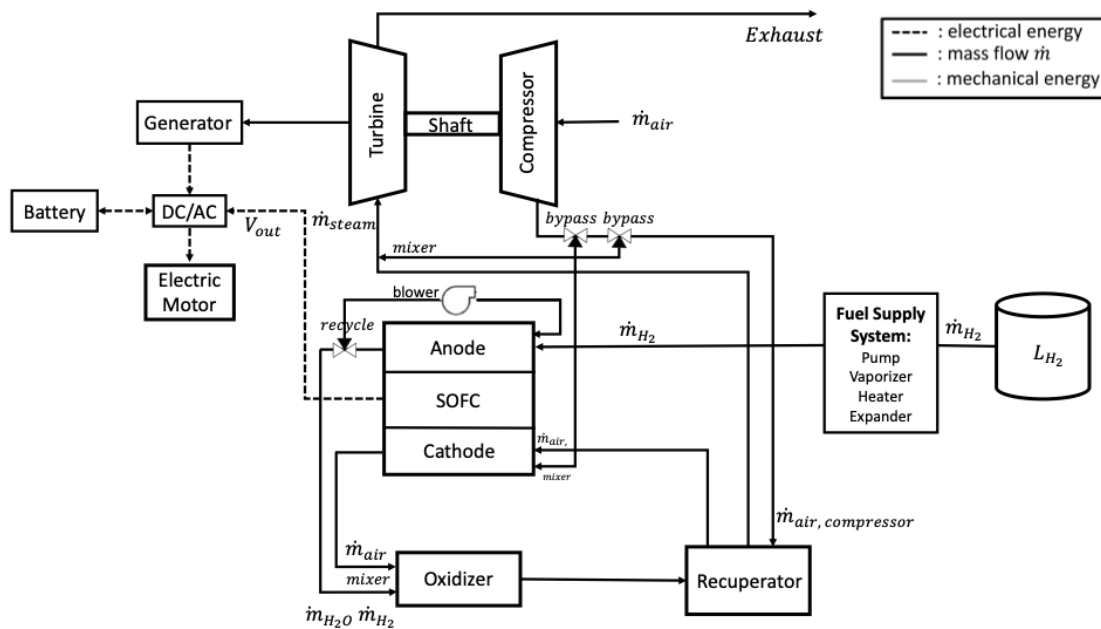
Fig. 4.2   Schematic of a Solid Oxide Fuel Cell/Gas Turbine (SOFC/GT) hybrid power System, illustrating the flow of electrical energy, mass, and mechanical energy. Key components include the fuel heater, recuperator, fuel pump, and various flow paths for hydrogen and air.

The system of Fig. 4.2 was designed and selected for its pressurized operation at altitude and

potential high efficiency throughout a flight. Integrating the FC directly, instead of using indirect heating, removes the need for extra heat exchangers and their corresponding mass and volume. Pressurizing the fuel cell boosts its performance and increases power density (also reducing mass and volume). The system's design, featuring bypass options and cathode recirculation, facilitates the control of air flow rate and cathode inlet temperature, even at a constant turbine speed. Additionally, air compression not only pre-heats the air but also increases the heat available for the turbine, thereby generating more electricity via a generator.

Pressurizing an SOFC/GT system offers efficiency benefits but raises concerns. Increased pressure can risk cell fracture, especially during rapid pressure changes, and may lead to stall or surge issues in the cathode due to high air volume between the compressor and turbine. To ensure safety, the design must choose robust cell materials, actively control the system to ensure gradual pressure changes, and employ advanced control systems for pressure and thermal management.

4.1.1. Governing Equations

The main power source of the proposed system is a Solid Oxide Fuel Cell (SOFC) operating with hydrogen as fuel, characterized by power densities of 2.5 kW/kg and 7.5 kW/kg. The SOFC stack is modeled using a quasi-3-D approach, where the unit cell is divided into five control volumes: two bipolar plates, two flow channels, and the Positive Electrode-Electrolyte-Negative Electrode (PEN) assembly. These control volumes are arranged in a 5x5 node grid, with each node computing electrochemistry, mass, momentum, and energy conservation, along with heat and mass exchange within each node and between adjacent nodes.

In SOFCs, electrochemical reactions occur simultaneously on both the anode and cathode sides. Hydrogen is oxidized at the anode, while oxygen is reduced at the cathode. To complete the electrical circuit, electrons released during the anodic reaction travel to the cathode through an external circuit, while oxygen ions (O^{2-}) produced at the cathode are transported through the ceramic oxygen

84

ion-conducting electrolyte to the anode. The reactions are given by [114]:

$$\text{Anodic reaction: } H_2 + O^{2-} \rightarrow H_2O + 2e^- \tag{4.1}$$

$$\text{Cathodic reaction: } O_2 + 4e^- \rightarrow 2O^{2-} \tag{4.2}$$

$$\text{Overall Reaction: } H_2 + \frac{1}{2}O_2 \rightarrow H_2O \tag{4.3}$$
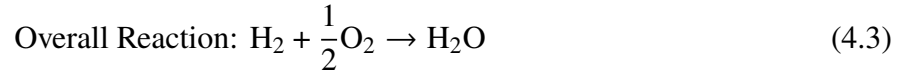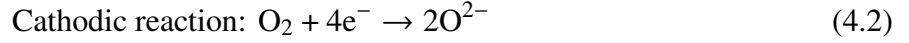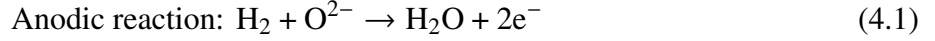
The Nernst equation for calculating the reversible voltage of the SOFC system as follows [115] :

$$V_{\text{rev}} = -\frac{\Delta G_0}{nF} + \frac{RT}{nF} \ln \left(\frac{P_{H_2} \cdot P_{O_2}^{0.5}}{P_{H_2O}} \right) \tag{4.4}$$

where ΔG_0 is the Gibbs free energy at operating conditions, n is the number of electrons transferred, F is Faraday's constant (96485 C/mol e$^-$), R is the universal gas constant, T is the cell operating temperature, and P_i is the partial pressure of the reacting gas i.

SOFC operation results in cell voltage losses due to activation, ohmic, and concentration polarizations. The operating cell voltage is given by:

$$V_{\text{cell}} = V_{\text{rev}} - \eta_{\text{activation}} - \eta_{\text{ohmic}} - \eta_{\text{concentration}} \tag{4.5}$$

where the voltage drops can be determined following the procedures outlined by McLarty et al. [116]: Activation losses:

$$\eta_{\text{act}} = \frac{RT}{\alpha nF} \ln \left(j_0 + \frac{RT}{\alpha nF} \ln \left(\frac{j}{\frac{2RT}{nF}} \right) \sinh^{-1} \left(\frac{j}{2j_0} \right) \right) \tag{4.6}$$

Ohmic losses:

$$\eta_{\text{ohm}} = j \times \frac{t_i T}{\sigma_{0,i} e^{-\Delta G_{\text{act}}/RT}} \tag{4.7}$$

Concentration losses:

$$\eta_{\text{con,a}} = -\frac{RT}{nF} \ln\left(\frac{P_{\text{H}_2}}{P_{\text{H}_2\text{O}}}\right) = -\frac{RT}{2F} \ln\left[\frac{1 - \frac{RT}{2F}\frac{jt_a}{D_{\text{a,eff}}P_{\text{H}_2,\text{in}}}}{1 + \frac{RT}{2F}\frac{jt_a}{D_{\text{a,eff}}P_{\text{H}_2\text{O},\text{in}}}}\right] \tag{4.8}$$

$$\eta_{\text{con,c}} = -\frac{RT}{nF} \ln\left(\frac{P_{\text{O}_2}}{P_{\text{O}_2,\text{in}}}\right) = -\frac{RT}{4F} \ln\left[\frac{P_c/\delta_{\text{O}_2} - (P_c/\delta_{\text{O}_2} - P_{\text{O}_2,\text{in}}) \times e^{\frac{RT\delta_{\text{O}_2} t_c}{4FD_{\text{c,eff}}P_c}}}{P_{\text{O}_2,\text{in}}}\right] \tag{4.9}$$

$$\delta_{\text{O}_2} = \frac{D_{\text{O}_2,\text{k(eff)}}}{D_{\text{O}_2,\text{k(eff)}} + D_{\text{O}_2-\text{N}_2,\text{k(eff)}}} \tag{4.10}$$

Here, α, j_0, j, t, σ_0, ΔG_{act}, and D represent the charge transfer coefficient (0.5), exchange current density, current density, material thickness, electrical conductivity, activation energy, and diffusivity, respectively.

The SOFC stack power is calculated by:

$$P_{\text{stack}} = \frac{V_{\text{cell}} \times n \times j \times A}{1000} \tag{4.11}$$

The current density of the SOFC stack is [117]:

$$j = 4 \times F \times \dot{n}_{\text{O}_2} \tag{4.12}$$

where $\dot{n}_{\text{O}_2}$ is the molar consumption rate of oxygen in the SOFC cathode.

The energy balance for the interconnect plates is:

$$m_{\text{plate}} C_{\text{plate}} \frac{dT}{dt} = Q_{\text{conv}} + Q_{\text{cond}} + Q_{\text{rad}} \tag{4.13}$$

where m_{plate} and C_{plate} are the plate mass and heat capacity. Q represents the heat transferred.

The energy balance for the PEN assembly is:

$$\rho V C_{\text{PEN}} \frac{dT}{dt} = Q_{\text{conv}} + Q_{\text{cond}} + Q_{\text{rad}} + Q_{\text{gen}} \tag{4.14}$$

where ρ, V, and C_{PEN} are the density, volume, and heat capacity of the PEN, respectively.

Local convective heat transfer is calculated assuming fully developed laminar flow and uniform temperature:

$$h_c = \frac{\text{Nu}_D \cdot k}{D_h} \tag{4.15}$$

where h_c is the convection heat transfer coefficient, Nu_D is the Nusselt number, D_h is the hydraulic diameter, and k is the thermal conductivity.

The energy conservation equations for the flows are calculated by the dynamic balance of enthalpy flows in and out of each control volume plus all heat exchanged with adjacent control volumes as follows:

$$\dot{n}_{\text{air}} C_P \frac{dT}{dt} = \dot{n}_{\text{in}} h_{\text{in}} - \dot{n}_{\text{out}} h_{\text{out}} + Q_{\text{conv}} + Q_{\text{cond}} + Q_{\text{rad}} - Q_{\text{ion}} \tag{4.16}$$

$$\dot{n}_{\text{fuel}} C_P \frac{dT}{dt} = \dot{n}_{\text{in}} h_{\text{in}} - \dot{n}_{\text{out}} h_{\text{out}} + Q_{\text{conv}} + Q_{\text{cond}} + Q_{\text{rad}} + Q_{\text{cond}} + Q_{\text{ion}} - P_{\text{gen}} - Q_{\text{gen}} \tag{4.17}$$

In the above equations, $\dot{n}$, C_p, and h are the molar flow rate, specific heat capacity, and specific

enthalpy of the flows in the channels. Q_{ion} denotes the heat transferred by oxygen ions, and P_{gen} represents the power generated. All the mass balance equations used in this model are solved using the general dynamic mass balance equation shown in Equation 4.18. The mass balance equations for the flow channels are as follows:

$$\dot{n}\frac{dX_i}{dt} = \dot{n}_{\text{in}}X_{i,\text{in}} - \dot{n}_{\text{out}}X_{i,\text{out}} + R_{\text{consumed}} \tag{4.18}$$

$$\dot{n}_{\text{fuel}} = \frac{I}{2U_{\text{fuel}}F} \tag{4.19}$$

where X is the molar ratio of reactants, and R is the reaction rate. Equation is used to calculate the anode inlet flow rate, where U_{fuel} is the fuel utilization.

Fuel utilization can be determined as follows [26]:

$$U_{\text{fuel}} = \frac{\Delta n_{\text{H}_2}}{\dot{n}_{\text{H}_2,\text{in}}} \tag{4.20}$$

The overall efficiency of the SOFC stack is calculated as follows [26]:

$$\eta_{\text{overall}} = \frac{U \times P_{\text{stack}}}{\Delta \dot{H}} \tag{4.21}$$

where $\Delta \dot{H}$ is the difference in inlet and outlet stream enthalpy flows. The electrochemical efficiency of the cell is determined by the following equation:

$$\eta_{\text{electrochem}} = \frac{V_{\text{cell}}}{V_{\text{rev}}} \tag{4.22}$$

In the proposed powertrain system, an oxidizer is employed after the SOFC to oxidize the remainder

of hydrogen in the anode tail-gas. This configuration can increase the outlet temperature of the SOFC system to reach higher temperatures that are more suitable for good turbine performance [118]. The energy balance of the oxidizer is as follows:

$$\dot{n}_{\text{out}} C_p \frac{dT}{dt} = \sum (\dot{n}_{\text{in}} h_{\text{in}} - \dot{n}_{\text{out}} h_{\text{out}}) \tag{4.23}$$

For the compressor and turbine, a dynamic model is employed which includes industry-standard performance maps and dynamic conservation equations. Shaft speed, flow rate, and pressure ratio are normalized as previously reported by Lee and McLarty et al. [118, 119]:

$$N_{\text{RPM}} = \frac{\text{RPM}}{\text{RPM}_{\text{des}}} \sqrt{\frac{T_{\text{in}}}{T_{\text{des}}}} \tag{4.24}$$

$$N_{\text{Flow}} = \frac{\text{Flow}}{\text{Flow}_{\text{des}}} \frac{\sqrt{\frac{T_{\text{in}}}{T_{\text{des}}}}}{\frac{P_{\text{in}}}{P_{\text{des}}}} \tag{4.25}$$

$$N_{\text{PR}} = \frac{P_{\text{out}}}{P_{\text{in}} \text{PR}_{\text{des}}} \tag{4.26}$$

$$\text{PR}_{\text{new}} = 1 + (\text{PR}_{\text{des}} - 1) \frac{\text{PR}_{\text{orig}} - 1}{\text{PR}_{\text{des,orig}} - 1} \tag{4.27}$$

In the above equations, N_i is the normalized value for property i, PR is the pressure ratio, T_{in} and T_{des} are inlet and design temperatures, and PR_{orig} is the original pressure ratio.

The compressor model inputs involve inlet temperature, pressure, and concentrations, shaft speed, and exhaust pressure. Empirical correlations are used to estimate the flow rate into the compressor. Then, compression efficiency is obtained from look-up tables based on the normalized speed, flow rate, and pressure of the compressor map. The compressor work is calculated using the method reported by Lee [118]:

$$\dot{W}_C = \frac{\dot{n}_{\text{out}}(h_{\text{isen}} - h_{\text{in}})}{\eta_C} \tag{4.28}$$

$$\dot{n}_C C_V \frac{dT_{\text{fluid}}}{dt} = \dot{W}_C + \dot{E}_{\text{in}} - \dot{E}_{\text{out}} + \dot{Q}_{\text{conv}} \tag{4.29}$$

$$\dot{m} C_P \frac{dT_{\text{solid}}}{dt} = \dot{Q}_{\text{conv}} + \dot{Q}_{\text{rad}} \tag{4.30}$$

where $\dot{W}_C$ is the compressor work, $\dot{n}$ is the molar flow rate, $\dot{m}$ is the mass flow rate, η_C is the compressor efficiency, h_{isen} is the isentropic enthalpy, h_{in} is the inlet enthalpy, $\dot{E}_{\text{in}}$ and $\dot{E}_{\text{out}}$ are the energy flows of the inlet and outlet, and C_P and C_V are the heat capacities.

The turbine model operates with inlet temperature, concentrations, inlet flow rate, and exhaust pressure. A control volume method is used to determine the pressure just before the initial turbine stage, involving a dynamic mass balance of the incoming and exhaust flow rates, allowing for mass accumulation between the compressor and turbine. The scaled performance map calculates the exhaust flow rate using Equation (31). The turbine work is calculated from expansion efficiency and pressure ratio as shown in Equation (32). The energy balance equations are completed through the inclusion of turbine work and heat transfer between the solid turbine components and the working fluid. These equations are then used to determine the temperatures of the solid metal and fluid exhaust, as shown previously in [50, 118] via Equations (33) and (34).

$$V \frac{dP}{dt} = (\dot{n}_{\text{in}} - \dot{n}_{\text{out}}) R T_{\text{in}} \tag{4.31}$$

$$\dot{W}_T = \dot{E}_{\text{in}} - \dot{n}_{\text{out}} \left(h_{\text{in}} - \eta_T (h_{\text{isen}} - h_{\text{in}}) \right) \tag{4.32}$$

$$\dot{n}_C C_V \frac{dT_{\text{fluid}}}{dt} = \dot{W}_T + \dot{E}_{\text{in}} - \dot{E}_{\text{out}} + \dot{Q}_{\text{conv}} \tag{4.33}$$

$$\dot{m} C_P \frac{dT_{\text{solid}}}{dt} = \dot{Q}_{\text{conv}} + \dot{Q}_{\text{rad}} \tag{4.34}$$

where V is volume, P is pressure, R is the universal gas constant, and $\dot{W}_T$ is the turbine work.

4.1.2. Initialization and Control Modeling Framework

As depicted in Fig. 1, building a model in STRIDES involves initializing and aligning the components assembled in the plant variable, then steering them towards a steady-state operating condition. This process ensures all variables are appropriately scaled and normalized, mitigating numerical problems and rounding errors in subsequent computations. Crucially, the states of each component are consolidated into a single vector to be later used in an ordinary differential equation solver. An essential part of this process involves a two-step component initialization, adjusting the model to approximate steady-state operation. The EAGERS user manual contains detailed instructions for the model's construction and operation [113].

The STRIDES model for an SOFC/GT system involves detailed initialization and control parameters. The initialization function sets fixed component parameters that are independent of inlet values or operational conditions. It also includes an estimate of all states and appropriate scaling factors. The correct choice of these initial values and scales is crucial to ensure system stability. They are stored in a structure that preserves their order throughout the operation of the system. The initialization function also defines the inlet and outlet port names and assigns initial conditions to each. For ports connected to other components, the initial value will be overridden, but for unconnected ports, it remains constant. The initial conditions can also be updated if necessary [113].

Controllers in the STRIDES model have the same structure and requirements as component functions. They are initialized last, which gives them access to parameters from any of the components. This ordering is important in the context of system linearization, where the controller is left in place to enable the development of optimal MPC (Model Predictive Control) controllers that match the input/output ports of the original controller. In summary, the careful selection of initial values and precise controls is paramount in the STRIDES model. These choices affect the system's stability and its ability to respond to changes in operational conditions. A more detailed discussion regarding the control strategy and selection of initial values is to be explored further in the text.
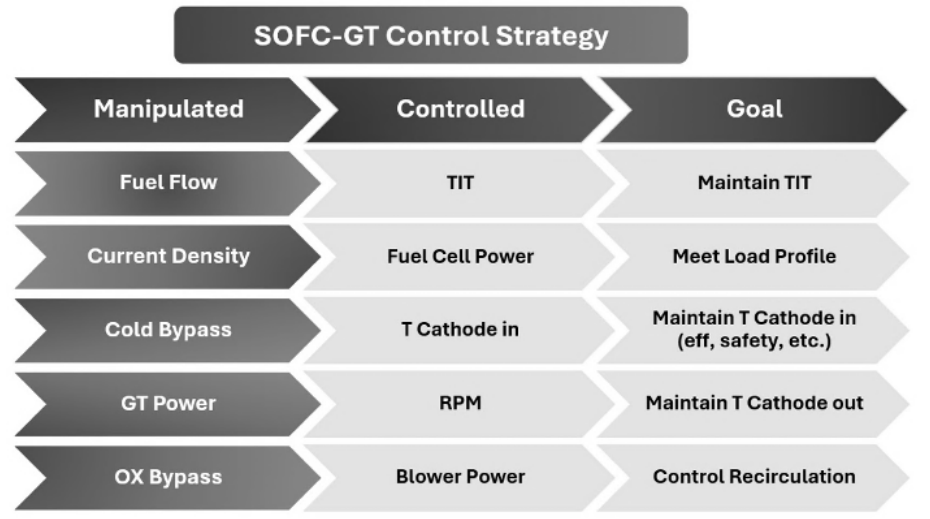
Fig. 4.3 Simplified control strategy for SOFC/GT simulation.

In advancing SOFC/GT systems for aeronautical applications, key control strategies, outlined in Fig. 3 and Table 1, are crucial. The control strategy adopted here is adapted from multiple sources [25, 118]. The Power Ratio (PR) sets essential operational parameters, informing linear functions for specific temperature targets: cathode outlet temperature, cathode inlet temperature, and Turbine Inlet Temperature (TIT). RPM control combines feedback from $T_{\text{cath\_out}}$ and fuel cell power targets with feedforward mechanisms for faster response while managing thermal transients. The GT power set point, vital for RPM stability, operates independently from the GT actual output to allow generator power on the GT shaft to float so that the SOFC temperature control (via inlet air flow and temperature control) is prioritized. Cathode inlet temperature is regulated through an air bypass valve to maintain ideal thermal conditions. Recuperator Bypass is used to maintain set TIT at 1155 K under varying loads; the system adjusts flow accordingly as changes in load necessitate recalibration of inlet/outlet temperatures and TIT targets for thermal stability. Maintain TIT sustains stability and high efficiency of the turbine and stays within limits of the turbine map. Regular recalibration of feedforward RPM settings, involving adjustments in gain and coefficients, refines control accuracy. Finally, oxidizer bypass is used to control recirculation of the anode exit using a blower. The implemented strategies collectively control the SOFC/GT system for safe dynamic operation and evaluation for aircraft powertrains.

Table 4.1   Control Strategy Description

Component	Description
Power Ratio Calculation	Calculate Power Ratio for set points.
Temperature Set Points	Set cathode outlet, cathode inlet, and Turbine Inlet Temperature targets using Power Ratio-dependent linear functions.
RPM Control	Control Revolutions Per Minute using cathode outlet temperature feedback and fuel cell power target feedforward.
Gas Turbine Power Set Point	Determine Gas Turbine power for RPM control, independent of actual output.
Cathode Inlet Temperature Control	Regulate cathode inlet temperature through a bypass valve.
Fuel Cell Power Matching	Align fuel cell power with load demand by adjusting current density.
Temperature Target Adjustment	Modify inlet and outlet temperatures and reduce Turbine Inlet Temperature targets in response to load changes.
Recalibration of Feedforward RPM	Update feedforward Revolutions Per Minute settings by tuning gain and coefficient values.

4.2. Demonstration of Dynamic Model on Example Cessna Flight Trajectory

4.2.1. Integration Analysis

The integration analysis is demonstrated on a representative Cessna S550 Citation S/II. Private jets are attractive for this analysis because they offer a compact yet practical platform for testing and validating advanced powertrain systems with high emissions reduction potential. Our previous work [120] assessed the feasibility of such a system in a Cessna Citation XLS+, which has a cabin volume of 422 ft³, excluding baggage storage. Both aircraft are designed to carry 8 passengers. The XLS+ is marginally larger, with about 15% more height and 13% more width than its predecessor. In comparison, as depicted in Table 2, the Cessna Citation S/II offers slightly less spacious cabin dimensions, with a typical length of about 16 ft (4.88 m), a width of approximately 4.10 ft (1.49 m), and a cabin height of around 4.9 ft (1.46 m) [121].

However, the primary focus of this paper is not to detail the integration analysis but rather to

Table 4.2   Cessna S550 Citation S/II Interior Dimensions

Interior Dimensions	Measurement
Cabin Length	16 ft (4.88 m)
Cabin Width	4.10 ft (1.49 m)
Cabin Height	4.9 ft (1.46 m)
Cabin Volume (excluding baggage)	422 ft^3

demonstrate the feasibility of integrating an SOFC/GT system and evaluating its dynamic response, following the initial design analysis based on the retrofit methodology developed in our previous work [120]. The Citation S/II is preferred due to its longer range (energy required) and lower thrust and power requirements, making the lightweight hydrogen energy and smaller heavy SOFC/GT powertrain attractive. The design follows the same approach for tank integration and the SOFC/GT powertrain at the rear of the aircraft.

As shown in Table 3, the Cessna S/II can carry a maximum fuel payload of 2,267 kg, which is equivalent to 815.6 kg of hydrogen for the same flight distance using combustion. The estimated efficiencies for SOFC systems in the literature range from 65% to 75% [44], significantly higher than the approximate 34% efficiency of the conventional Pratt & Whitney JT15D-4 turbofan engines. For a maximum range flight of 2000 miles, approximately 570 kg of hydrogen is required, based on SOFC/GT efficiency estimates from literature assuming 70%. This initial assessment suggests an integration advantage for SOFC-powered aircraft. Considering the lower thrust and power requirements of approximately 1.3 MW for the S/II, the 0.9 MW SOFC analyzed would weigh 360 kg, the 66 kW gas turbine would weigh 15.4 kg, and the electric motors, based on a density of 7 kW/kg for advanced electric motors, would weigh 182 kg.

The cryocooler, essential for maintaining the superconducting state of the SOFC system, is estimated to weigh approximately 39.8 kg, based on a cryocooler power fraction X_P of 0.0006 and a specific mass of 3 kg/kW of input power, as shown in the equations below. Assuming typical values based on the paper: the hot temperature T_h is 300 K, the cold temperature T_c is 50 K, the cryogenic

inefficiency λ_{sc} is 0.0017 for advanced HTS systems, and the second-law efficiency η_c is 0.3, which is 20% of Carnot efficiency [122].

$$X_P = \frac{\lambda_{sc} \cdot T_h}{\eta_c \cdot (T_h - T_c)} = \frac{0.15}{50} = 0.01 \tag{4.35}$$

$$P_c = X_P \times P_s = 0.01 \times 1300 \text{ kW} = 13.26 \text{ kW} \tag{4.36}$$

$$\text{Cryocooler mass} = 3 \text{ kg/kW} \times 13.26 \text{ kW} = 39.78 \text{ kg} \tag{4.37}$$

This setup would replace the two JT15D-4 engines, each with a dry weight of 253 kg.

Fuel payload for 2000mi		
Jet A	**Hydrogen combustion**	**Hydrogen SOFC/GT**
2,267 kg	815.6 kg	570 kg

The SOFC/GT system is assessed for its capability to meet the entire load profile of 1.29 MW alone, without the assistance of a battery for rapid response. In this case, the SOFC/GT system must provide the full power requirement. However, an alternative scenario involves using a battery that can produce 25% of the power rating for 15 minutes. In this scenario, the SOFC/GT system would only need to provide 75% of the power demand, which equates to 967.5 kW. This second scenario is implemented in the mass analysis provided below. The aircraft remains well below the maximum takeoff weight (MTOW) requirements.

The weight reduction highlighted in Table 4 is primarily attributed to the lighter hydrogen fuel and the reduced payload resulting from fewer passengers and seats. The reduced fuel and payload enable a more efficient configuration, enhancing the aircraft's overall performance and compensating for the additional weight of the SOFC/GT system and its associated components, such as the cryocooler and electric motors.

The SOFC unit occupies a volume of approximately 5.65 ft³, while the gas turbine occupies about 0.09 ft³. Given that the standard Cessna S/II has a cabin volume of 422 ft³ (excluding

Table 4.3   Mass Analysis of Retrofitted Aircraft

Component	Mass (kg)
MTOW	6849
SOFC System	360
Gas Turbine	15.4
Electric Motors	182
Cryocoolers	39.8
JT15D-4 Turbofan Engine	253 each
Battery	268
Fuel	570
Tanks	78
Total Takeoff Mass	6195 < MTOW

baggage storage), the SOFC system would occupy about 1.34% (5.65 ft^3) of the cabin volume in a block-shaped setup. The GT occupies 0.09025 ft^3. The battery, sized to 322 kW power output and 80.63 kWh, would occupy a volume of 4.25 ft^3, considering an energy density of 0.67 kWh/L. This volume analysis indicates that the powertrain system can be accommodated in the rear of the aircraft while remaining within the required center of gravity envelope.

4.2.2. Implementation Analysis

To assess the viability of integrating an SOFC engine into a conventional aircraft, a demonstration of the dynamic model on an example existing subsonic business jet configuration was utilized. In this model, all the technical specifications of the Cessna S550 Citation S/II were retained, with the sole modification being the replacement of the jet engines and a retrofit with SOFC engines as done in our previous work [120].

To demonstrate the dynamic modeling, a representative thrust profile of an observed trajectory of this aircraft from surveillance data was modeled. The observed trajectory selected was a flight from Dulles International Airport (IAD) near Washington DC to Cyril E. King Airport (STT) in the Virgin Island of St. Thomas by an existing Cessna S550 Citation S/II, as depicted in Fig. 4.4.

The required percentage of maximum thrust per time of the retrofit SOFC engine for the chosen flight trajectory was determined using a low fidelity performance model of the aircraft under the conditions shown in Table 4.4. This necessitated the determination of the drag and lift profile, weight distribution profile, distance traveled, and altitude of the flight trajectory.

Table 4.4   Flight Conditions for Example Flight Trajectory of Cessna S550 Citation S/II from Washington Dulles International Airport (IAD) to St. Thomas' Cyril E. King Airport (STT)

Parameters	Values
Maximum Takeoff Weight (lbs)	15,100
Range (nmi)	1551
Takeoff Field Length (ft)	10,501
Cruise Mach Number	0.67
Cruise Altitude (ft)	42,950
Pressure at Cruise Altitude (atm)	0.16
Temperature at Cruise Altitude (°R)	389.97
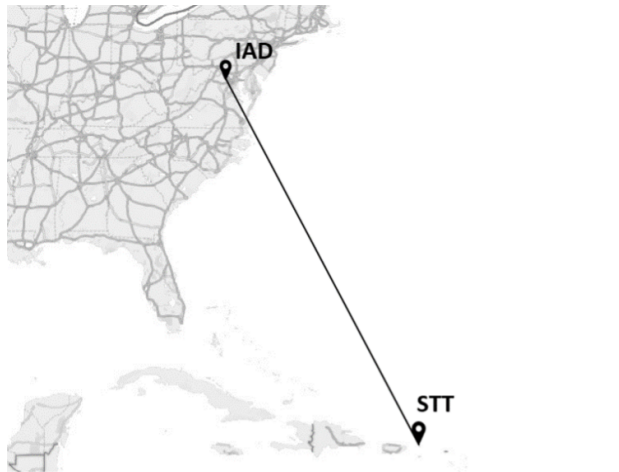
Fig. 4.4   Example flight trajectory of Cessna S550 Citation S/II from Washington Dulles International Airport (IAD) to St. Thomas' Cyril E. King Airport (STT).

This preliminary analysis was conducted using data acquired from "FlightRadar24" to obtain the coordinates and velocity profile necessary for subsequent calculations. It is important to emphasize that only ground speed data was available for this analysis. Consequently, ground speed was used in the performance model to simplify the calculations. Although ground speed does not account for wind effects and may differ from true airspeed, it provides a consistent basis for this demonstration,

which primarily focuses on dynamic modeling. Given that this trajectory serves as a demonstration, the use of ground speed is deemed sufficient for illustrating the dynamic modeling process.

The thrust profile was determined by considering various factors such as the aircraft's weight during each flight segment, the climb or descent angle during ascent or approach phases, and the aerodynamic efficiency. Assuming the aircraft as a point mass, the thrust was calculated for each timestamp of the flight trajectory using the following equation:

$$\text{Thrust} = w \left(\sin(\gamma) + \frac{1}{L/D} \right) \tag{35}$$

By using the great circle distance equation, along with the longitude and latitude coordinates of the flight trajectory, the altitude, distance traveled by the aircraft, and flight path angle (γ) can be obtained. To acquire the thrust needed per each flight segment, the weight of the aircraft was determined using the Breguet Range Equation over incremental segments of the flight:

$$w_{\text{fuel}} = \frac{w_{\text{initial}}}{e^u} \quad ; \quad u = \frac{R \cdot g}{\left(\frac{L}{D} \eta_h \right)} \tag{36}$$

where R and g represent the range of the flight and gravitational force, respectively. In addition, the weight variation using the SOFC engine is found to be small. This is due to the power efficiency and small fuel consumption and light weight of liquid hydrogen. Kerosene has a specific energy of 43 MJ/kg while liquid hydrogen has roughly a specific energy of 120 MJ/kg. This, in turn, lowers the fuel weight carried by the aircraft by 25%. However, this will raise a new challenge for the fuel tanks, as is later discussed in the conclusion section.

To obtain the thrust profile, drag must also be calculated using temperature, Mach number, pressure, and density at a specific altitude. This is important as both the parasite drag and induced drag take into account density and the Reynolds number. Drag, depicted in Fig. A.1, can then be calculated

using the equation below:

$$D = \frac{1}{2}\rho v^2 S_{\text{ref}} \left(C_{D_c} + C_{D_o} + C_{D_{\text{gear}}} + C_{D_I} \right) \tag{37}$$

where the compressibility drag coefficient is only accounted for during the cruise phase. Additionally, the landing gear is deployed only during takeoff, approach, and landing operations of the flight trajectory.

Fig. 4.4 recreates the flight trajectory, flying from IAD to STT, by utilizing the longitude and latitude coordinates retrieved from the flight tracking website FlightRadar24 [5]. The result acquired from Eq. (35) is illustrated in Fig. 4.6, showing the changes in maximum thrust needed for the takeoff, climb, cruise, approach, and landing phases. From the graph, it is observable that the thrust needed for the cruise phase is approximately 22%. This aligns closely with what typically is required for a Boeing 737-800 [123]. The landing phase of the trajectory exhibits significantly higher thrust requirements due to factors such as reverse thrust, deployed landing gear, and flaps. This methodology was examined for multiple flight trajectories to study the sturdiness and resilience of the dynamic model. The results of additional flight paths, demonstrated on the same Cessna S550 Citation S/II flying from Cyril E. King Airport (STT) to Treasure Coast International Airport (FPR), can be found in the appendix Fig. A-C.

For dynamic modeling, the power demand illustrated in this profile will be pivotal. However, recognizing the potential variability in real-world scenarios, we will also investigate more challenging mission profiles with additional complications such as adverse weather and high turbulence. The profile will be adapted accordingly to reflect these variables. Moreover, the system's ability to deliver the necessary power even in the event of a propulsion unit failure is important for safety during critical flight stages such as take-off or climb. Guided by the FAA's airworthiness standard (§23.21220) [124], a minimum power requirement is derived to ensure a climb gradient of 2% under a One Engine Inoperative (OEI) scenario at Second Segment Climb (SSC).
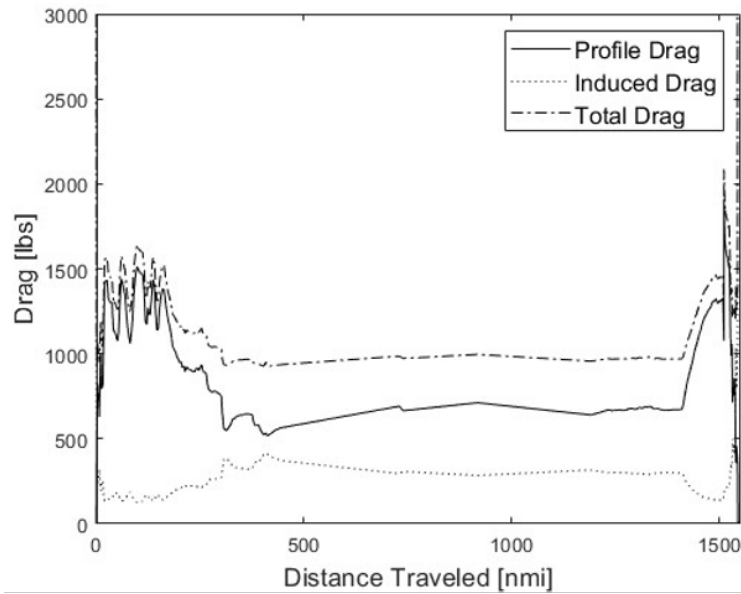
Fig. 4.5   Aircraft drag profile of the example Cessna S550 Citation S/II flight trajectory.
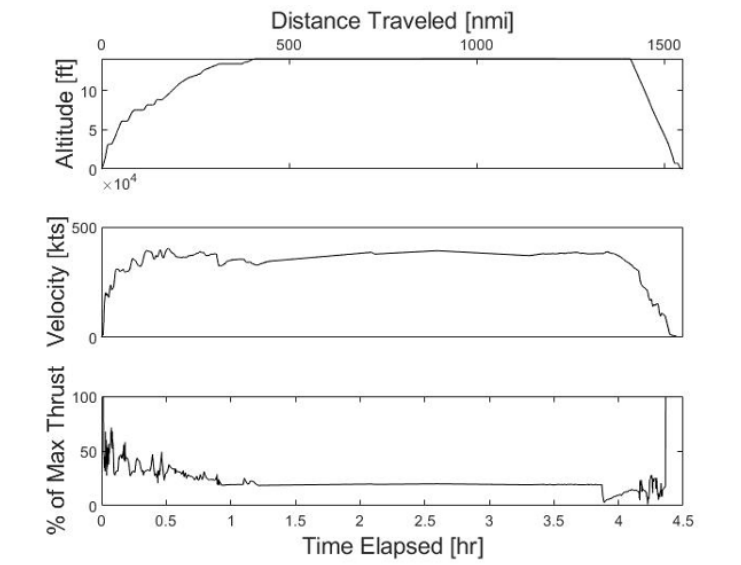
Fig. 4.6   Aircraft altitude, velocity, and modeled percentage of maximum thrust versus distance traveled and time of the example Cessna S550 Citation S/II flight trajectory.

100

4.2.3. Steady-State Modeling

As mentioned previously, the unit cell is discretized into five control volumes: two bipolar plates, two flow channels, and a PEN assembly. Table 4.5 shows the properties of the unit cell. The key assumptions of this stack/cell model include treating gases as ideal due to operating conditions, unidirectional electrical current flow, instantaneous electrochemical reactions, and uniform gas distribution across the flow channels. Each gas node functions as a continuously stirred tank reactor, and a lumped temperature approach is adopted for the cell's solid structure. The model assumes adiabatic boundaries at cell inlets and outlets, high electrical conductivity with equipotential surfaces for electrodes and interconnects, a constant Nusselt number, and laminar flow regimes in both cathode and anode streams. Lastly, it disregards external heat losses. These assumptions are reasonable for a model focusing on internal dynamics, though they might limit real-world applicability under varying conditions [125].

Table 4.5   Thermal and physical properties of SOFC components

Properties	Value
Electrolyte conductivity	6.19 W/m·K
Membrane thickness	5e-6 m
Cathode thickness	295e-6 m
Anode thickness	50e-6 m
SOFC diameter	0.02025 m
SOFC length	0.040 m
Number of cells per kW	27

The system begins with an assumption of an ambient pressure of 1 atm, but is pressurized to 3 atm. During flight, this assumption becomes less accurate as the cabin is typically pressurized to only 0.7-0.8 atm at cruise altitude, potentially decreasing efficiency if the pressure were assumed to start at 0.7 atm—a factor not considered in our simulations. The stack is designed to operate with an inlet temperature of 998 K, and a turbine inlet temperature to be kept above 1155 K. The topping cycle benefits from operating on hydrogen, where the reaction in the PEN is exothermic, without any endothermic reforming that reduces temperature. This, however, raises additional concerns

regarding thermal management and degradation of the cell and control complexities. The average temperature of the PEN is 1190 K, with a PEN temperature gradient found to be 73 K.

4.2.4. Dynamic Modeling

Fig. 4.7 presents the transient simulation results for both the compressor and turbine operating points throughout the flight path. For the turbine, the operational data points are suitably located within a high-efficiency region, maintaining a safe distance from the surge/stall region, which signifies good performance without approaching the area where surge/stall events might occur. Likewise, the compressor's operational points throughout the flight path are strategically positioned in a zone of high efficiency, well clear of the surge lines, thus preventing the risk of operational instability or reverse flow phenomena. The compressor and turbine maps were resized and scaled from turbines and compressors adapted from the STRIDES library.
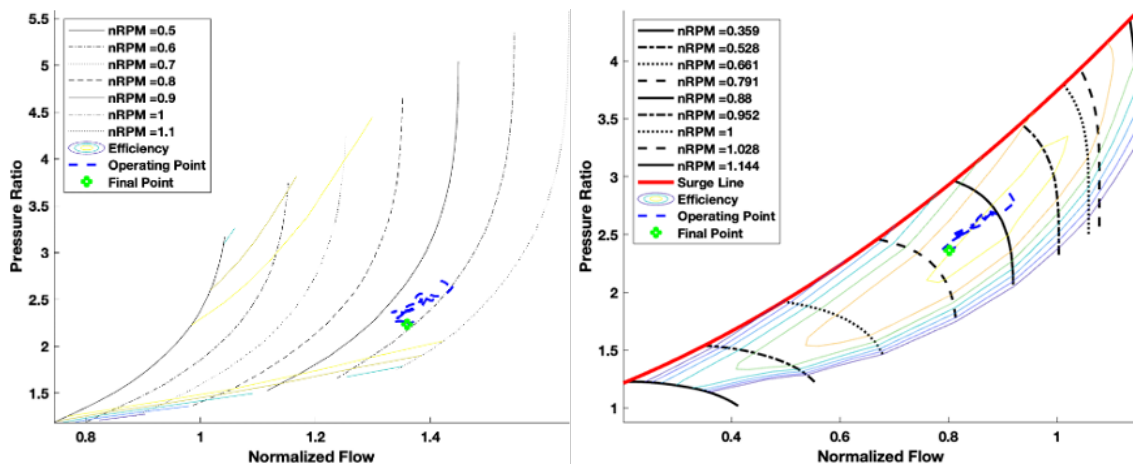
Fig. 4.7   Operation points throughout our simulation of A) turbine, B) compressor

Fig. 4.8 depicts the operational efficiency of the compressor and turbine throughout the flight simulation. As anticipated, the compressor exhibits relatively consistent efficiency characteristics, as reflected in the simulation results in response to varying power demands. In contrast, turbine efficiency demonstrates a slightly greater degree of sensitivity, exhibiting a gradual and minor decline before stabilizing at a small level of decrease. System efficiency is shown as "Controller Eff"

in Fig. 8 and achieves an efficiency of 71.4%.
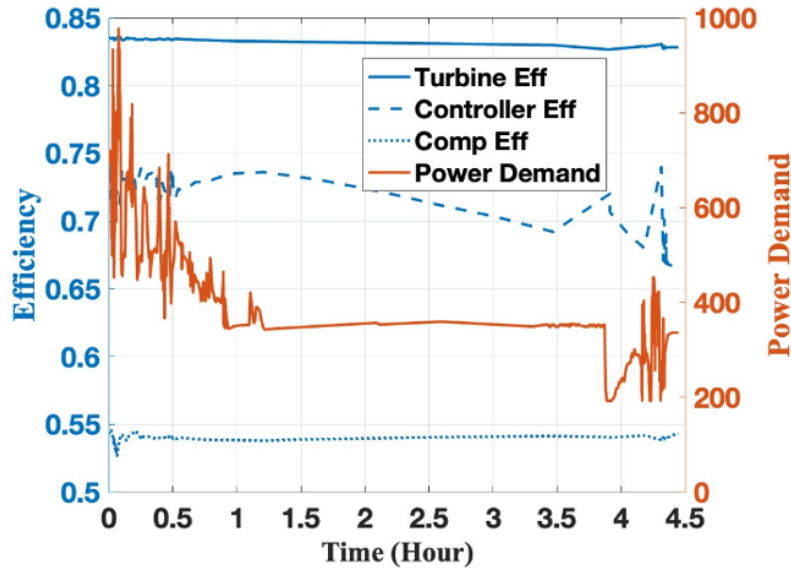
Fig. 4.8   Efficiency curves & power demand

Upon successful completion of the static modeling and the generation of test profiles, the control strategy for the SOFC/GT system was iteratively refined to achieve faster response to the varying power demands of different mission profiles. It was observed that each profile elicited a distinct reaction from the control strategies and parameters implemented. This included the profile detailed in the implementation analysis section. Broadly, the system demonstrated proficiency in managing the majority of dynamic response scenarios, barring extreme conditions of rapid power escalation (ramp-up) and reduction (ramp-down). The FC did most of the heavy lifting of power output (both magnitude and dynamic response) whilst the GT contributed about 95 kW of electric power (via generator) in the beginning of the flight and gradually decreased over time due to the increasing requirement of airflow from the compressor to the SOFC.

For the profile depicted in Fig. 4.9, the SOFC/GT system exhibited a robust and rapid response to the power demands. Total power demand shows a peak at the beginning, indicating the high power requirements of takeoff, which then stabilizes and gradually declines over the period of cruise. Power output from the FC demonstrates a sharp increase initially and then stabilizes at a lower value compared to the peak of total power demand, suggesting that the fuel cell can respond to the initial

103

demand but power output does not match the total demand dynamics associated with the noticeably short ramp-up and ramp-down times in the periods of take-off (first 0.5 hours) and landing (hours 4.25 to 4.50). Notably, the system maintained an output close to the cruising level even during rapid power variations in the descent phase. Overall, the system displayed good rapid response capabilities and an aptitude for adapting to the dynamic requirements of the flight. However, during the last hour of flight, the system overpowers the demand by approximately 14
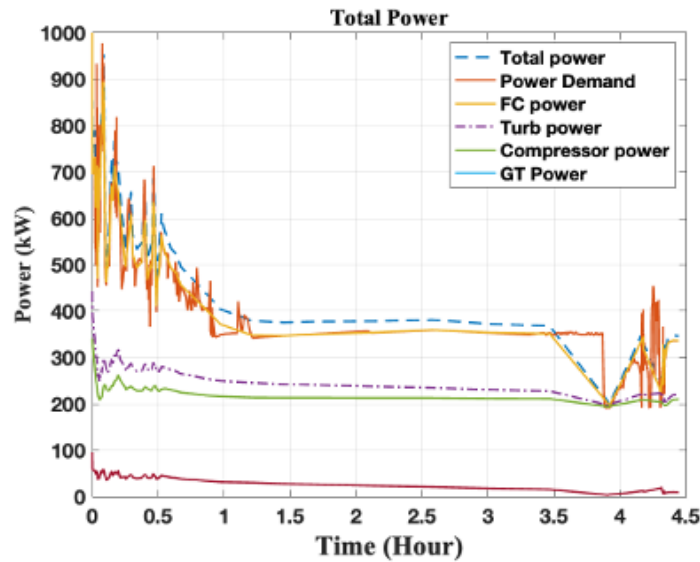
Fig. 4.9   Power demand vs Power of components

From a technical standpoint, SOFC/GT systems are often praised for their efficiency and reduced environmental footprint. However, their ability to rapidly respond to load variations, particularly at higher operational magnitudes, remains an area of focus. While it might seem that smaller-scale systems exhibit faster load response times, as suggested by Kandepu et al. [126], who demonstrated a 40% load change within a 5-second window in a 278-kW system, this is not necessarily due to their size. Contrary to this assumption, larger systems, such as the one studied by Brouwer [127], which managed a 17.46% turndown in 43.200 seconds for a 1150 kW system, were not designed with rapid response as the primary goal. The literature, including studies by Mueller et al. [44], indicates that rapid response can be achieved regardless of system size, depending on the control strategies and objectives implemented. Therefore, the variability in response times across different SOFC/GT systems is more accurately attributed to differing control goals and implementations

rather than inherent size limitations.

A second flight profile was assessed from East Hampton Airport (HTO) in Connecticut to Palm Beach International Airport (PBI) in Florida (details available in the Appendix). This profile experienced a very sudden increase to maximum throttle in the last minutes, likely due to wind, weather, and/or turbulence during landing conditions. The implementation of the control strategy appeared to react differently based on multiple factors. Most notably, if the system is unable to cope with rapid fluctuations in demand throughout the profile, it sets the total power demand slightly higher to remain on the positive side of the fluctuation. Again, if a battery is integrated to power 25% of the aircraft, this kind of increase in energy could be stored in the battery. Furthermore, the battery itself has relatively rapid response due to fast charge/discharge capabilities, which have been proven in practice and in the literature to be capable of managing electric vehicles and aircraft [128–130].

The SOFC/GT system demonstrated remarkable efficiency, achieving an overall efficiency of 71.4% over the entire flight path considered, a testament to its promising potential for aviation applications. However, this efficiency declines during the latter stages of the flight, particularly under conditions of high dynamic operation at part-load conditions. This observed decrease in efficiency can be attributed to several factors, including reduced utilization (for safe operation during highly dynamic operation) and variations in reactant concentrations under these dynamic operating conditions. In terms of specific operational parameters, the dynamic model of the SOFC/GT system for aviation applications encompassed 36,300 cells, indicating a substantial size for robust power generation, with an average power output of 34 W/cell. Depicted in Fig. 4.10, the average cell voltage was maintained at 0.86 volts, and the current density at 0.255 A/cm^2, is on the lower end of the spectrum (0.2 to 1.5 A/cm^2) of operation most likely due to operating under low partial load conditions. The average cell voltage was maintained between 0.85 and 0.93 volts, and the current density varied from 0.22 to 0.46 A/cm^2, which is on the lower end of the spectrum (0.2 to 1.5 A/cm^2) of that which SOFC technology is capable of. The highest current densities of around 0.46 A/cm^2 are achieved at the beginning of the flight when higher power is required for take-off.
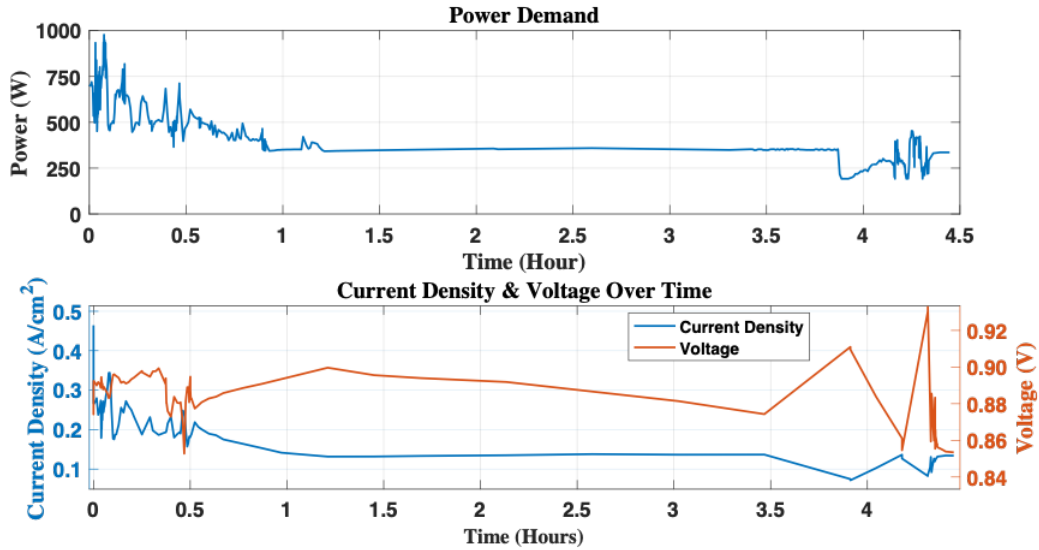
Fig. 4.10   Power Demand (a) and Current density & voltage (b) vs time

During the turbulent descent phase of the aircraft, as observed in the mission profile analysis, the synergy between the battery and the SOFC/GT system was proved to be required. The current work does not simulate the battery contributions to the powertrain's response to the load profile. The results show that the SOFC/GT cannot respond to the most rapid power demand dynamics, demonstrating that including a battery is essential to SOFC/GT systems intended for aircraft, since they cannot efficiently and safely respond to the fastest demand dynamics. This integration would be essential in maintaining continuous, stable power supply and reducing stress on the fuel cells, thereby ensuring the aircraft's safe and efficient operation during the critical take-off and landing phases.

In scenarios where the SOFC/GT system undergoes a rapid 20% power ramp-up, the battery can immediately supply up to 40% of the required power, ensuring a swift response. This capability is crucial for maintaining the SOFC's operating temperature within its optimal range, thereby enhancing fuel efficiency and prolonging cell lifespan. The simulation considers a battery with a capacity of approximately 87 kWh and a maximum power output of 322 kW, which is particularly important during critical flight phases such as takeoff and landing. Fig. 4.11 illustrates the load

106

profile of the simulated battery, highlighting its charge and discharge behavior in response to the power surplus or deficit encountered throughout the mission, as determined by the difference between the total power demand and the SOFC/GT supply.
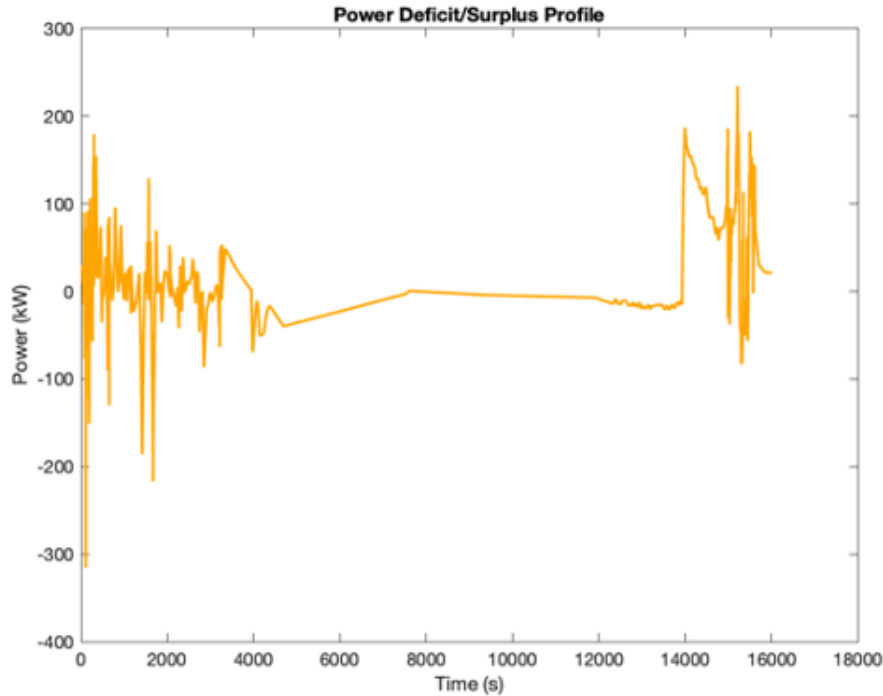
Fig. 4.11   Power deficit/surplus post SOFC/GT power supply over time

The choice of parameters for the model includes a nominal cell voltage of 3.7 V and a cell capacity of 3.0 Ah, with 162 cells connected in series and 179 strings in parallel. This configuration yields a total pack voltage of 600 V and a maximum current of 537 A, providing an overall power output of approximately 322 kW.

The methodology for this battery model is adapted from several key sources, including Sabatier et al. [131], Yao et al. [132], and Clarke and Alonso [130], providing a foundation for modeling lithium-ion battery behavior under varying conditions. The open-circuit voltage (OCV) vs. state of charge (SOC) relationship plots are based on data provided by Wang et al. [133] for a 3.7V nominal voltage ICR 18650 battery, as shown in Figure 4.12, which closely matches the characteristics of

the battery used in our model. Other sources [113, 134, 135] show very similar experimental and simulation data for the OCV plots, reinforcing the validity of the approach.
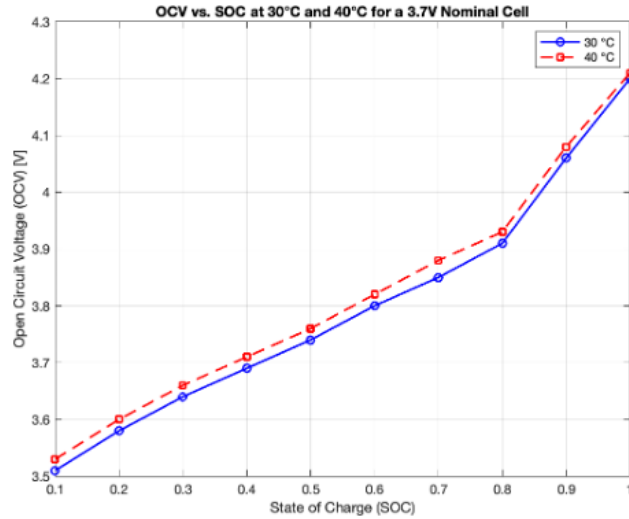
Fig. 4.12   Open-circuit voltage at 30°C and 40°C vs. state of charge for a 3.7V Li-ion cell

The simplified battery model integrates key factors, including degradation, self-discharge, the OCV-SOC relationship, thermal behavior, and temperature dependence. Power load data is converted into current to compute the state of charge (SOC), incorporating a temperature-dependent self-discharge mechanism, represented by:

$$k_{\text{self-discharge}} = k_0 \cdot \exp\left(-\frac{E_a}{R \cdot T_{\text{op}}}\right) \tag{4.38}$$

where k_0 is the base self-discharge rate constant, E_a is the activation energy, R is the gas constant, and T_{op} is the operating temperature.

Battery degradation is modeled using three equations: calendar aging, cycle aging, and resistance growth. The equations quantify capacity loss due to time (t), cycle count (N), and operational parameters like temperature (T) and Depth of Discharge (DoD) [135]:

Calendar aging:

$$Q_{\text{loss,cal}} = A \cdot \exp\left(-\frac{E_a}{RT}\right) \cdot t^n \tag{4.39}$$

Cycle aging:

$$Q_{\text{loss,cyc}} = B \cdot N^b \cdot (1 - \exp(-k \cdot \text{DoD})) \tag{4.40}$$

Resistance growth:

$$R_{\text{growth}} = R_0 \cdot (1 + C \cdot (1 - \exp(-D \cdot N))) \tag{4.41}$$

The thermal model simplifies heat generation into Joule heating and entropy-related heating [130]:

$$q_{\text{heat}} = I_{\text{load}}^2 \cdot R_{\text{pack}} - T_{\text{cell}} \cdot \frac{\Delta S \cdot I_{\text{load}}}{nF} \tag{4.42}$$

where R_{pack} is internal resistance, T_{cell} is cell temperature, ΔS is entropy change, n is the number of electrons, and F is the Faraday constant. Temperature change is modeled using the lumped thermal mass approach and logarithmic mean temperature difference (LMTD).
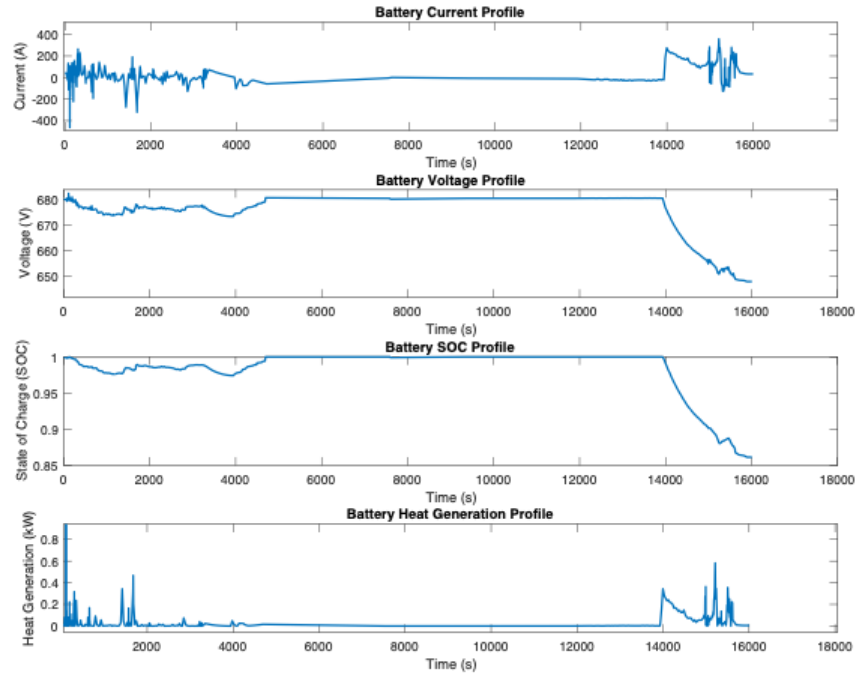
Fig. 4.13   Current, voltage, SOC, and heat generation of battery vs. time

Figure 4.13 shows the current, voltage, SOC, and heat generation of the battery over time. The battery system dynamics exhibit a stable current profile ranging from -200 to 200 A, with controlled charging and discharging throughout the flight. The voltage remains around 680 V, above nominal, due to the battery maintaining a high SOC for most of the flight. The SOC reflects dynamic charging and discharging patterns, with a reduction to 85% during landing to accommodate high dynamic loads. Heat generation remains low for most of the flight but spikes up to approximately 0.4 kW at the beginning and near the end of the discharge cycle, associated with increased internal resistance and high current demands. These results demonstrate expected performance characteristics, consistent with behavior observed in electric vehicle batteries.

4.3. Summary and Conclusion

Our study of retrofitting the Cessna S550 Citation S/II jet with a hydrogen Solid Oxide Fuel Cell/Gas Turbine (SOFC/GT) engine underscores the potential and challenges of this innovative technology in

110

aviation. The low-fidelity analysis of a typical flight profile demonstrated the dynamic capabilities of the SOFC/GT system, achieving an efficiency of 71.4%. This high efficiency and responsive dynamic characteristics observed may make the SOFC/GT technology a viable propulsion alternative. The SOFC/GT exhibited desirable rapid dynamic response to varying power demands compared to similarly sized systems found in the literature. However, the hydrogen-fueled SOFC/GT system still lacks the response time needed to meet the highly dynamic power demands during take-off, descent, and landing.

These results highlight the importance of integrating a battery energy storage system as part of the powertrain, which was not considered in this work. The simulation models in Figures 4.11 and 4.13 demonstrate that a 322 kW battery, capable of supplying 25% of the maximum power output, is appropriately sized to handle rapid changes in the load profile that the SOFC/GT system alone cannot meet. In the example flight, the battery's output only peaked at 200 kW at certain points.

The mass analysis indicates that a retrofitted SOFC/GT/Battery aircraft would remain well within the maximum take-off weight limits, underscoring the practicality of this approach. This feasibility is largely due to the lighter fuel weight and lower payload from a reduced number of passengers and seating.

Moreover, the study revealed critical areas for further development. The observed power fluctuations during the final hour of flight and the decline in efficiency under dynamic conditions suggest the need for further optimization of the system. Fine-tuning and adopting different control strategies, such as PID control parameters, could improve results. Additionally, future comprehensive analyses using advanced aircraft optimization tools are essential. These analyses should focus on the aircraft performance with the new engines and address the challenges posed by using liquid hydrogen as a fuel source.

In summary, while the initial results are promising, highlighting the SOFC/GT system's efficiency and dynamic operating capabilities, the need for a battery capable of approximately 25% of the

power output is emphasized. Significant research and development efforts are required to address these challenges and advance the system for practical aviation use. As the industry moves toward more sustainable and efficient energy sources, advancements in SOFC technology and its integration with energy storage solutions offer a promising avenue for the future of aviation.

5. Sizing, Design, and Comparative Analysis of Conventional and Hydrogen-Powered Blended Wing Body Aircraft

Parts of this chapter, in parts or in whole, are co-authored by and published in: Oi Ching Vanessa Chung, Khaled Alsamri, Jacqueline L. Huynh, and Jack Brouwer. "Design Methodology of Hydrogen Solid Oxide Fuel Cells Propulsion System in Blended Wing Body Aircraft," AIAA 2024-3664. *AIAA AVIATION FORUM AND ASCEND 2024*, July 2024.

This chapter explores retrofitting aircraft with hydrogen technologies, such as Solid Oxide Fuel Cells (SOFC), focusing on their integration into blended wing body (BWB) designs. Studies show that hydrogen-powered BWB aircraft could reduce CO_2 emissions by up to 88% compared to conventional aircraft [136] while maintaining competitive energy efficiency, with only a 3.8% energy penalty compared to kerosene versions [38]. This study evaluates the performance of hydrogen-powered BWB configurations against conventional and hydrogen tube-and-wing (T&W) designs using modeling and simulation tools to analyze fuel consumption, emissions, and overall efficiency. Section 5.1 details the design framework and integration methods; Section 5.2 presents the performance analysis; Section 5.3 offers conclusions and directions for future research.

5.1. Aircraft sizing methodology

The integration of a Solid Oxide Fuel Cell/Gas Turbine propulsion system into a Blended-Wing-Body (BWB) aircraft demands a rigorous and methodical approach. This entails developing a comprehensive mission profile that accurately reflects typical operational conditions. This study explores the aerodynamic, propulsion, and structural facets of the design using weight

estimations from NASA's Flight Optimization System Weights Estimation Method (FLOPS) and SOFC propulsion system design to conceptualize and evaluate the performance of this innovative initiative [137]. Subsequently, initial airframe and propulsion system dimensions are determined, and OpenVSP (Open Vehicle Sketch Pad) is employed to create a mesh, which is then utilized to configure visual representations in SolidWorks [138].

To facilitate a meaningful comparison, the widely adopted conventional Boeing 777-300ER and 737-800 aircraft are used as benchmarks. These models serve as references for evaluating the benefits and challenges associated with the incorporation of the hydrogen SOFC/GT propulsion system. By subjecting all aircraft to a consistent mission profile, which will be elaborated in the results section, the comparative performance metrics are evaluated. Additionally, two capacities of aircraft configurations accommodating 365 passengers and 162 passengers, respectively, are assessed. Each capacity will include a conventional aircraft, hydrogen-powered BWB designs, and hydrogen-powered T&W configurations.

Ensuring safety is paramount in this study, necessitating a thorough examination of the aircraft's center of gravity (CG). The stability and control analysis is crucial for evaluating the overall safety and controllability of the aircraft, particularly when integrating a novel propulsion system. It is essential to note that for a rigorous and fair comparison, an identical SOFC/GT propulsion system, scaled according to the specific power requirements of each aircraft, is utilized.

5.1.1. Aircraft Sizing Framework

The framework for defining aircraft geometries and weight estimation is illustrated in Figure 5.1. The initial weight assumptions and power requirements for each aircraft configuration are modeled and analyzed using weight estimation methods from FLOPS, with outputs subsequently used for post-processing evaluations.

Initial Design Parameters

The design process begins with defining initial mission profile parameters, including range, payload, and flight conditions. These parameters, along with wing geometry and payload specifications, serve as the foundation for the design process. Decisions regarding the number and placement of engines, whether on the wing or fuselage, are also made at this stage. For Blended Wing Body (BWB) aircraft, cabin dimensions were determined using the methodology in [139]. This approach is based on the fuselage layout and efficiency, taking into account the number of abreast seats, seat pitch, and total passenger count to determine the number of bays required to accommodate the payload. The method also specifies the necessary fixed passenger equipment (such as galleys, lavatories, and closets), which establishes the cabin's width and length.

Aerodynamic Analysis

Given the initial sizing parameters, aerodynamic forces such as lift and drag are calculated using parameters like the mean aerodynamic chord, cruise velocity, and wing loading. The maximum Lift-to-Drag (L/D) ratios for the BWB and conventional T&W configurations, which are 27 and 18, respectively, are used to calculate fuel consumption using the Breguet-Range Equation [140]. These coefficients are essential for determining the aircraft's aerodynamic efficiency and performance. The results from the aerodynamic analysis, combined with liftoff acceleration derived from the takeoff field length and liftoff velocity from the mission profile, determine the maximum thrust per engine required for takeoff, which is crucial for propulsion system sizing. The rolling friction coefficient, obtained from relevant literature [141], is also considered in these analyses. A detailed methodology for thrust and power estimations will be discussed in the Propulsion System Sizing section 5.1.2.

Weight Estimation Process

Accurate weight estimation is critical, as the initial maximum takeoff gross weight (MTOW) significantly influences engine power requirements, which in turn affects the minimum thrust needed and the size of the hydrogen tanks and associated SOFC/GT powertrain components, including the solid oxide fuel cell stacks, gas turbine, cryo-cooler, battery, and high-temperature superconducting (HTS) motor. The structural weight estimation involves evaluating components such as the wing, fins, fuselage, landing gear, paint, and nacelles. Each component's weight is calculated based on its dimensions, material properties, and structural requirements. The systems and equipment weight group includes surface control systems, instruments, hydraulic systems, electrical systems, avionics, furnishings, and anti-icing systems. These weights are estimated considering factors such as MTOW, wing area, cabin floor area, and cruise range. For propulsion system weight estimation, required thrust is translated into power output, and the weight of the SOFC/GT powertrain components is calculated. Gravimetric and volumetric densities of the respective components provide a preliminary weight estimation for the entire propulsion system. The operating items weight includes fixed equipment for the flight crew, miscellaneous passenger service weights, and cargo containers, which are essential for operational efficiency and serviceability.

Iterative Design Process

The iterative design process involves increasing the initial MTOW estimation at each step until convergence at the final MTOW is achieved, marking the completion of the vehicle design process. Upon convergence, the process proceeds to the center of gravity (CG) analysis and CAD configuration.

Model Validation

To ensure model accuracy, validation tests were conducted by comparing the computed results against existing data from online sources. The discrepancies between the calculated and reference

maximum takeoff gross weights were found to be minimal, with deviations of 0.28% for the baseline BWB-450, 6.8% for the B777-300ER, and 0.46% for the B737-800. Equations for each major weight group and the derivation of the maximum takeoff gross weight are provided, with a detailed breakdown in the Results section.

$$W_{\text{empty}} = W_{\text{structure}} + W_{\text{propulsion}} + W_{\text{systems}} \tag{5.1}$$

$$\text{OEW} = W_{\text{empty}} + W_{\text{op. items}} \tag{5.2}$$

$$\text{ZFW} = \text{OEW} + W_{\text{payload}} \tag{5.3}$$

$$\text{MTOW} = \text{ZFW} + W_{\text{fuel}} \tag{5.4}$$
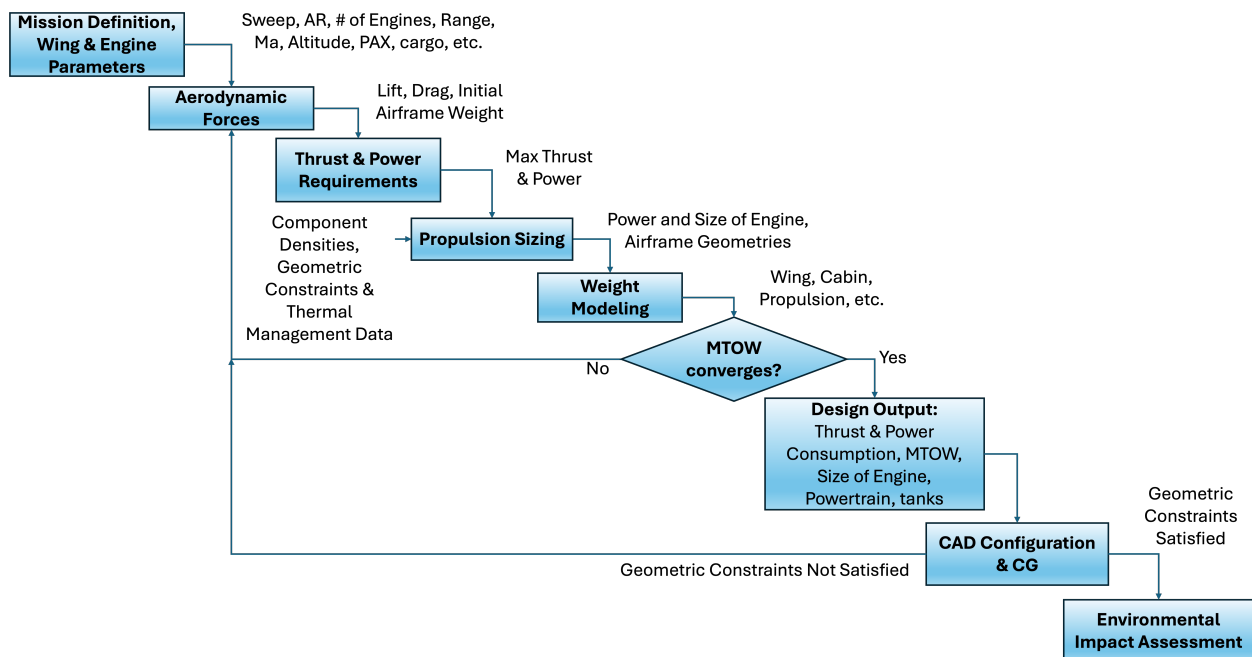
Fig. 5.1   Aircraft sizing framework.

5.1.2. Propulsion System Sizing

The methodology for determining thrust and power during various phases of flight involves a detailed set of equations that take into account specific flight conditions such as altitude and range. The method systematically dissects the various portions of the flight, namely taxi, takeoff, climb, cruise, descent, and landing, following a predefined flight trajectory. Equations 5.5 and 5.6, coupled with the aircraft remaining weight, parasitic drag, lift induced drag, and compressible drag, were used to determine the thrust and climb/descent angle, denoted as γ, at each phase.

The power required for each aircraft configuration is fundamentally tied to the computation of the takeoff thrust. The maximum thrust, referred to as the takeoff thrust, is a function of the takeoff acceleration, as shown in Equation 5.7. This equation also considers the aircraft takeoff gross weight, the number of engines, lift and drag forces, and rolling friction taken from the literature [141].

$$\text{Thrust} = D_{\text{total}} \quad \text{for cruise} \tag{5.5}$$

$$\text{Thrust} = (\text{Weight}) \sin(\gamma) + D_{\text{total}} + ma \quad \text{for all others} \tag{5.6}$$

$$a_{\text{takeoff}} = \frac{V_{\text{takeoff}}^2}{2 \cdot \text{TOFL}} \tag{5.7}$$

where a_{takeoff}, V_{takeoff} , and TOFL represent takeoff acceleration, takeoff velocity, and takeoff field length in Eq. 5.7.

The power generated during takeoff is then computed as a function of the thrust force and takeoff velocity, as described in Equation 5.8. This methodology ensures precise calculations of thrust and power tailored to different flight phases. The equations incorporate various dynamic factors such as lift, acceleration, rolling friction, and engine thrust to provide a complete analysis of the aircraft's performance throughout its operation.

$$\text{Power}_{\text{takeoff}} = \text{Thrust}_{\text{takeoff}} \times V_{\text{takeoff}} \qquad (5.8)$$

SOFC/GT System Design

The SOFC/GT hybrid system predefined in chapter 3 in Figure 4.2 operates by using hydrogen from the cryogenic pressurized storage tank. Following the power system schematic depicted in Figure 4.2, its design must be refined to ensure compactness, efficient thermal distribution, and safety compliance. Historically, such systems have been configured in dense, engine-like structures, while others have adopted designs that allocate more space to individual components, resulting in larger overall volumes. Our design, conceptualized in Figure5.2 aims to optimize volume, mass, thermal efficiency, and electrical efficiency. This integration process includes a comprehensive analysis of the aircraft's CG, ensuring that it remains within safe operational limits and predefined envelopes.
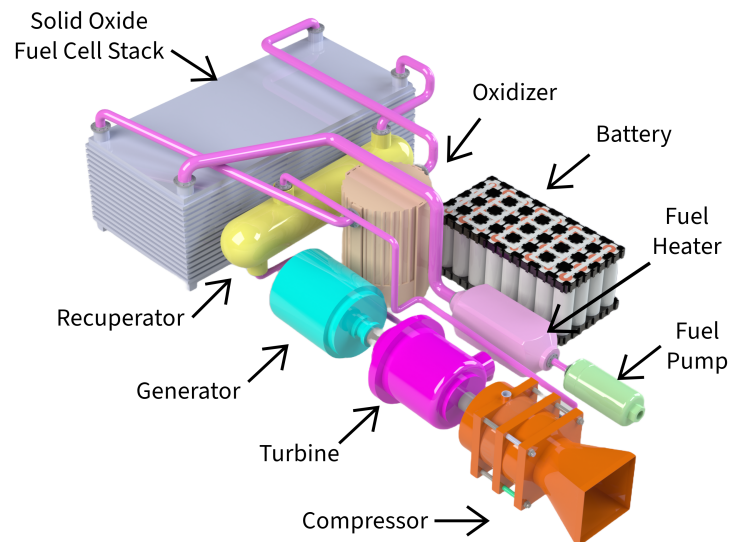
Fig. 5.2   CAD model of the SOFC/GT hybrid power system, showing the arrangement and integration of major components.

The powertrain model design is adapted and modeled from previous work [142], which demonstrated its capability in responding to power profiles with the aid of a battery in MW-scale systems. The

SOFC/GT technology has been extensively verified in both literature and commercial stationary power applications , and while not currently commercially available with fast dynamic response capabilities, extensively evaluated for its ability to respond to dynamic changes while offering durability and a long operational lifetime [142–144]. This paper focuses on the design and integration of the SOFC/GT system within aircraft. The SOFC/GT system presents several challenges that need to be addressed. These include the placement of hydrogen tanks, insulation, leakage prevention, and thermal management of high temperatures. Specific design choices in this aircraft aim to mitigate these issues, ensuring the efficient and safe operation of the powertrain system. Only by addressing these and all other technical considerations, including some not addressed herein, like susceptibility to impact loading, can the SOFC/GT system be effectively integrated into aviation applications, paving the way for more sustainable power solutions in the industry.

SOFC/GT Weight Analysis

For the conventional kerosene-powered B777-300ER and B737-800, the turbofan engine weight estimations from FLOPS were utilized. The lack of commercial components for complex hybrid powertrain systems, particularly in aviation applications where component weight is critical, contrasts with stationary power applications where SOFC/GT systems have been primarily utilized. The assumptions for weight analysis of these advanced concepts present in the literature make it challenging to settle upon specific values.. Hence, this paper focuses on developing a methodology to examine the synergy of the BWB concept with hydrogen and fuel cell technology, highlighting potential benefits and challenges rather than performing a detailed mass analysis, which would require modeling and designing each component—a significant objective for future work. Currently, there is also limited to no comprehensive mass analysis for SOFC/GT systems, especially for aviation applications at mega watt (MW) scales. Table 5.1 lists the main assumptions for gravimetric energy density. The fuel cell, the heaviest component of the powertrain, references experimental work by NASA Glenn Research Center, achieving a 2.5 kW/kg density, at least twice the commercially

120

available power density but still lower than current turbofans with a range of 3.33 to 10 kW/kg [40, 63]. "Rather than heavy metal interconnects, Glenn's innovative bi-electrode supported cell (BSC) uses a thin layer of electrically conductive $LaCaCrO_3$ (LCC) for current collection. To improve strength during thermal cycling and to simplify stack manufacture, its design is structurally symmetrical with a thin yttria-stabilized zirconia (YSZ) electrolyte supported on either side by a porous support structure" [145, 146]. Moreover, Collins and McLarty estimates net system power density of SOFC/GT for aviation to be 0.92 kW/kg. Until recently, SOFC development has not focused on weight reduction, resulting in PEMFC and HT-PEMFC achieving better experimental claims and commercial applications such as the fuel cell system of the Toyota Mirai, which claims a 4 kW/kg commercially.

Furthermore, the SOFC/GT system is sized to provide 75% of the take-off power requirement (maximum power), while the battery provides 25%. In addition to the assumptions in Table 5.1, the remaining components in Table 5.8 are scaled based on the scaling factors from [40, 63, 64]. The net system power density of the SOFC/GT is estimated to be 1.5 kW/kg.

Table 5.1   Component Densities of SOFC/GT Powertrain

Parameters	Values
SOFC Volumetric Density (kW/kg)	2.5 [62]
SOFC Gravimetric Density (kW/L)	7.5 [62]
Battery Volumetric Density (kWh/L)	0.67 [63]
Battery Gravimetric Density (kWh/kg)	0.35 [63]
GT Volumetric Density (kg/m^3)	8000 [64]
GT Gravimetric Density (kW/kg)	4.4 [64]
SOFC/GT Cycle Efficiency (%)	71.4 [142]

HTS Motor and Nacelle Design for Hydrogen Powertrain

The HTS motor design for the hydrogen powertrain uses assumptions from the N3-X motors [41, 147]. Key parameters include a motor density of 29.14 kW/kg and a volumetric density of 100 kW/m³, optimizing the balance between power output, weight, and volume [40]. The nacelle dimensions are scaled from N3-X specifications, with the average diameter assumed as:

$$D_{\text{NAC}} = \frac{50.6 \times (\text{Power})}{5.74} \tag{5.9}$$

where D_{NAC} is the average scaled diameter of the nacelle and Power is the power output of the motor converted to unit of MW.

The nacelle weight is:

$$W_{\text{NAC}} = 0.25 \times T_{\text{NAC}} \times D_{\text{NAC}} \times X_{\text{NAC}} \times F_{\text{Thrust}}^{0.36} \tag{5.10}$$

where W_{NAC} is the weight of the nacelle, T_{NAC} is a constant related to nacelle weight (unitless), D_{NAC} is the average scaled diameter of the nacelle, X_{NAC} is the average scaled length of the nacelle, and F_{THRUST} is the thrust force.

Air Duct Design for Optimal Performance in Cruise and Taxi Phases

Selecting the correct air duct dimensions is crucial for balancing operational requirements during cruise and taxi phases. Choosing an air velocity of 30 m/s for duct design accounts for high-speed airflow during cruise and low-speed requirements during taxi operations. A small blower ensures adequate airflow during ground operations. For an assumed fuel cell power output of $P = 45$ MW and an efficiency of $\eta = 0.714$, the hydrogen fuel consumption rate is modeled. The required airflow

rate, based on a stoichiometric air-to-fuel ratio of 34.3, is determined. Given standard air density and an air velocity of 30 m/s, the duct cross-sectional area is found. Two rectangular ducts are proposed for the largest BWB configuration designed in this paper, each with a height of 30 cm and a width of 81.7 cm. These ducts are positioned on the sides of the aircraft, similar to some conventional designs, to minimize drag. During ground operations, a small blower provides the necessary airflow, ensuring the SOFC system remains operational to avoid very long start-up times and durability concerns. Appropriate insulation can keep a shut-down SOFC warm enough over an entire 24-hour period for a very quick startup [148].

Thermal Management and Insulation for Cryogenic Hydrogen Storage Tanks

The use of liquid hydrogen as a cryogenic fuel source introduces additional considerations. Advanced temperature-controlled fuel tanks are required to handle the cryogenic conditions. The choice of materials for these tanks, as well as for the propulsion components and wing structure, plays a significant role in determining the overall weight and stability of the aircraft. Material selection impacts not only the structural integrity and durability but also the thermal insulation properties essential for maintaining the hydrogen in a liquid state. Furthermore, following the simplified methodology from [149] for liquid hydrogen tank modeling for aircraft purposes, Figure 5.3 portrays design choices. The analysis evaluates the thermal performance of Vacuum Insulation Panels (VIP) and Multi-Layer Insulation (MLI) for a cylindrical hydrogen storage tank by calculating the heat transfer through conduction, radiation, and convection. The tank dimensions and environmental conditions are specified, and the thermal properties of the insulation materials are considered. The analysis computes the heat transfer rates and the boil-off rates of hydrogen over a range of insulation thicknesses. Additionally, it analyzes the heat gain over time for a selected insulation thickness.

The methodology involves several key steps. First, the surface area of the tank (A_{tank}) is computed to include the cylindrical and hemispherical parts. The thermal resistances (R) for VIP and MLI are

determined using their respective thermal conductivities and insulation thicknesses (t) (Equation 5.11). The heat transfer due to conduction ($Q_{\text{conduction}}$) is then calculated using Equation 5.12. Radiation heat transfer ($Q_{\text{radiation}}$) is considered using the Stefan-Boltzmann law (Equation 5.13). Forced convection heat transfer ($Q_{\text{convection}}$) is evaluated using the Nusselt number (Nu) which is derived from the Reynolds (Re) and Prandtl (Pr) numbers (Equations 5.15-5.17). Finally, the total heat transfer (Q_{total}) and the corresponding hydrogen boil-off rates are computed (Equation 5.19). Thermal properties of the materials are considered constant and do not vary with temperature. The ambient temperature is assumed to be constant at 288 K. Forced convection is calculated using standard empirical correlations that are suitable for external flow over a cylinder. Additionally, the analysis is performed under steady-state conditions.

$$R = \frac{t}{k \cdot A} \tag{5.11}$$

$$Q_{\text{conduction}} = \frac{T_{\text{surface}} - T_{\text{air}}}{R} \tag{5.12}$$

$$Q_{\text{radiation}} = \alpha \cdot \sigma \cdot A \cdot (T_{\text{surface}}^4 - T_{\text{air}}^4) \tag{5.13}$$

$$Q_{\text{convection}} = h \cdot A \cdot (T_{\text{surface}} - T_{\text{air}}) \tag{5.14}$$

$$Re = \frac{\rho \cdot v \cdot L}{\mu} \tag{5.15}$$

$$Pr = \frac{c_p \cdot \mu}{k} \tag{5.16}$$

$$Nu = 0.644 \cdot Re^{0.5} \cdot Pr^{0.33} \tag{5.17}$$

$$h = \frac{Nu \cdot k}{L} \tag{5.18}$$

$$\text{Boil-off Rate} = \frac{Q_{\text{total}}}{\text{Latent Heat of Hydrogen}} \tag{5.19}$$
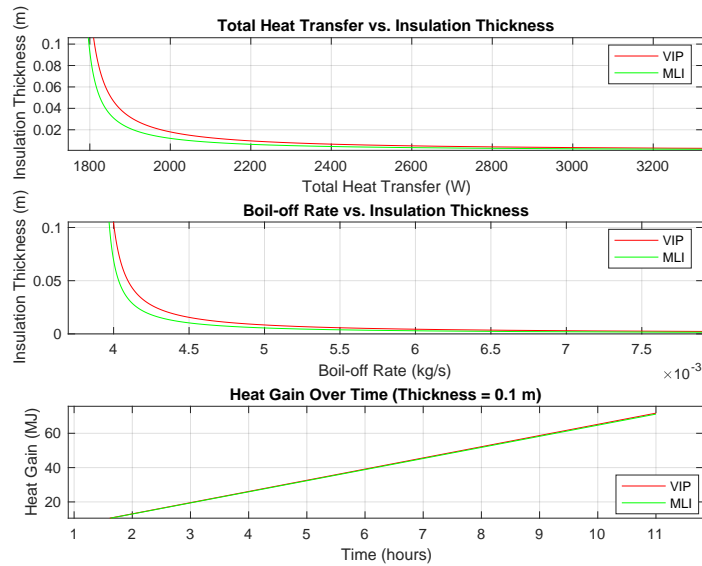
Fig. 5.3   Thermal performance of VIP and MLI insulation: total heat transfer, boil-off rate vs. insulation thickness, and heat gain over time for 0.1 m thickness.

Figure 5.3 illustrates the methodology for designing tank insulation for an example cryogenic liquid hydrogen tank of 2916 kg, 9 m length, and 1.1 m diameter used in hydrogen BWB-365. The top graph shows that increasing insulation thickness from 0.02 m to 0.1 m reduces total heat transfer from approximately 2250 W to 1750 W, with MLI performing better than VIP. The middle graph indicates that boil-off rates decrease from about 5 g/s to 3.8 g/s with increased insulation thickness, with MLI showing lower rates than VIP. The bottom graph demonstrates that over 11 hours, MLI

results in cumulative heat loss of around 70 MJ, compared to slightly higher values for VIP. These results, supported by the thermodynamic model described above, underscore the importance of effective insulation in minimizing heat ingress and boil-off rates in cryogenic tanks and help with making informed tank design choices.

5.1.3. Simulation of Cryogenic Hydrogen Tank Operation

Hydrogen can be stored in liquid form by cooling it to cryogenic temperatures. Its liquefaction temperature is $-252.78°$C (20.37 K) at atmospheric pressure. Liquid hydrogen tanks need to be well-insulated to minimize vaporization losses, as external heat causes liquid hydrogen to turn into gas. Despite high-quality insulation, some vaporization will still occur due to heat inflow. When liquid hydrogen vaporizes, its specific volume increases significantly, expanding about 53 times from 0.0141 m^3/kg to 0.7507 m^3/kg at atmospheric pressure [150]. At all times, hydrogen will coexist as both liquid and gas phase within the tank. The vaporized gas from heat inflow raises the temperature and pressure inside the tank. Fuel consumption from the tank towards the fuel cell system acts as the pressure relief mechanism or otherwise boil off to atmosphere [150]. The process of hydrogen boil-off, fuel consumption, and changes in temperature and pressure within a tank is modeled using the methodology described by [150, 151].

The heat transfer coefficients for the liquid and gas regions of the storage tank are given along with the respective surface areas. The latent heat of vaporization and specific heat of GH$_2$ are also defined. For each time step, the heat transfer rates to the liquid and gas regions are calculated. The boil-off mass flow rate is computed based on the heat transfer rate to the liquid region. The mass changes for LH$_2$ and GH$_2$ are then updated using the mass flow rate of the fuel to the propulsion system and the boil-off rate. The internal energy change in the gas region is computed to update the temperature, and the pressure is updated using the ideal gas law.

The heat transfer rates $q_{\text{heat,liq}}$ and $q_{\text{heat,gas}}$ are calculated using:

126

$$q_{\text{heat,liq}} = h_{\text{wall,liq}} A_{\text{liq}} (T_{\text{amb}} - T_{\text{liq}}) \tag{5.20}$$

$$q_{\text{heat,gas}} = h_{\text{wall,gas}} A_{\text{gas}} (T_{\text{amb}} - T_{\text{gas}}) \tag{5.21}$$

The boil-off mass flow rate $\dot{m}_{\text{boil}}$ is computed as:

$$\dot{m}_{\text{boil}} = \frac{q_{\text{heat,liq}}}{L} \tag{5.22}$$

The mass changes for LH$_2$ Δm_{liq} and GH$_2$ Δm_{gas} are updated For each time step i, using:

$$\Delta m_{\text{liq}} = -\dot{m}_{\text{boil}} \Delta t - \dot{m}_{\text{fuel,LH}_2} \Delta t \tag{5.23}$$

$$\Delta m_{\text{gas}} = \dot{m}_{\text{boil}} \Delta t - \dot{m}_{\text{fuel,GH}_2} \Delta t \tag{5.24}$$

The internal energy change ΔU_{gas} in the gas region is given by:

$$\Delta U_{\text{gas}} = \left(q_{\text{heat,gas}} \cdot \Delta t + q_{\text{boil}} \cdot \Delta t - q_{\text{fuel,gas}} \cdot \Delta t \right) - \left(P \cdot \left(\dot{m}_{\text{boil}} + \dot{m}_{\text{fuel,GH}_2} \right) \cdot \Delta t \right) \tag{5.25}$$

The temperature T_{gas} and pressure P in the tank are updated iteratively, with pressure calculated using the ideal gas law:

$$P = \frac{n_{\text{GH}_2} R T_{\text{gas}}}{V} \tag{5.26}$$

where n_{GH_2} is the moles of GH_2, R is the gas constant, and V is the tank volume. The simulation results, including the mass of LH_2 and GH_2, temperature, and pressure over time, are plotted to analyze the system behavior. An example case study results are presented in Figure 5.11.

This analysis of dynamic tank operation behavior has significant implications for flight operations and safety. The steady and controlled fuel consumption rates prevent rapid depressurization and temperature drops, ensuring that the hydrogen fuel system operates within safe thermal limits. The gradual temperature decrease and predictable pressure decline facilitate more efficient thermal management and reduce the risk of thermal stress on the tank materials, thus enhancing the overall reliability and longevity of the hydrogen storage system. Understanding these thermal and pressure dynamics is crucial for designing effective insulation and cooling systems that can handle the thermal loads during prolonged flight segments.

5.1.4. Center of Gravity and Airframe Configuration

The previously mentioned propulsion system sizing and weight models will generate an initial airframe geometry, alongside determining the volume of the SOFC/GT powertrain and dimensions required for hydrogen fuel tanks. Subsequently, the design process advances to ensure feasible integration of all aircraft components within the airframe to meet the CG requirements. This phase utilizes SolidWorks for physical placement, visualization, and CG analysis of the entire system. Should a component fail to fit within the airframe, it is imperative to revisit the initial aircraft sizing model to implement necessary modifications.

It is imperative to shield the hydrogen fuel tanks adequately while ensuring sufficient volume to support the defined mission, especially considering the tapering of the wing from root chord to tip. Equally critical is the aircraft's ability to satisfy CG requirements for all for loading scenarios, as shown in Equation 5.27: 1) fully loaded with payload and fuel tanks, 2) fully loaded with payload and empty tanks, 3) empty payload with full tanks, and 4) empty payload and tanks. Compliance with

these scenarios is essential as the aircraft routinely encounters each scenario, with non-compliance risking significant performance instability.

$$CG = \frac{\sum (x_{\text{component}} \cdot \text{weight}_{\text{component}})}{\sum \text{weight}_{\text{scenario}}} \qquad (5.27)$$

where $x_{\text{component}}$ denotes the location of each components with respect to the origin defined, $weight_{\text{component}}$ is the weight of a specific component, and $weight_{\text{scenario}}$ is the total weight of each scenario.

5.1.5. Environmental Impact Assessment

To assess the environmental impacts of aviation, this section focuses on evaluating the gaseous emissions produced by aircraft propulsion systems. Key metrics used in this analysis include emissions indices for CO_2 (Carbon Dioxide), H_2O (Water Vapor), CO (Carbon Monoxide), HC (Hydrocarbons), and NO_x (Nitrogen Oxides), quantified in kilograms per passenger nautical mile (kg/pax-nmi). Global Warming Potential (GWP) 100 values are applied to calculate equivalent CO_2 emissions, which account for the climate impact of non-CO_2 gases. Emissions for each flight segment are analyzed, with emission indices determined based on stoichiometric equations and ICAO (International Civil Aviation Organization) databank values. Additionally, the potential formation of contrails is examined, comparing predictions for hydrogen-powered aircraft versus conventional kerosene-powered aircraft using a predictive model based upon water partial pressures. This comprehensive assessment aims to provide a detailed understanding of the environmental footprint of conventional aircraft and alternative-fueled during various flight segments.

To calculate the Emission Indices (EI) for CO_2 and H_2O for different flight segments of the B777-300ER with GE90-115 engines and the B737-800 with CFM56-7B18 engines, we utilized ICAO databank [152] values for HC, CO, and NOx emissions. The stoichiometric equation used to

balance these emissions is given by:

$$C_{12.5}H_{24.4} + aO_2 + bN_2 \rightarrow xCO_2 + yCO + zH_2O + wHC \qquad (5.28)$$

For each flight segment, the mass of carbon in kerosene was distributed among CO, HC, and CO_2. The total mass of carbon in kerosene was calculated using the molar masses, and the carbon in CO and HC was determined based on their respective EIs. The remaining carbon was attributed to CO_2, and its mass was calculated accordingly. Similarly, the mass of hydrogen in kerosene was distributed among HC and H_2O, with the remaining hydrogen attributed to H_2O.

The mass of CO_2 was determined using the formula:

$$\text{mass}_{CO_2} = \text{mass}_{C, \, CO_2} \times \left(\frac{M_{CO_2}}{M_C} \right) \qquad (5.29)$$

where $\text{mass}_{C, \, CO_2}$ is the remaining carbon mass attributed to CO_2, and M_{CO_2} and M_C are the molar masses of CO_2 and carbon, respectively. The EI for CO_2 was then obtained by dividing the mass of CO_2 by the mass of kerosene.

The mass of H_2O was determined using the formula:

$$\text{mass}_{H_2O} = \text{mass}_{H, \, H_2O} \times \left(\frac{M_{H_2O}}{2 \times M_H} \right) \qquad (5.30)$$

where $\text{mass}_{H, \, H_2O}$ is the remaining hydrogen mass attributed to H_2O, and M_{H_2O} and M_H are the molar masses of H_2O and hydrogen, respectively.

For fuel cell aircraft, it is established that the only byproduct is water vapor when fueled by pure hydrogen. However, the SOFC/GT system includes a combustor/oxidizer that raises the fuel cell exit

flow temperature to about 1200K. It is fair to assume some thermal NOx will form at this temperature, as established in the literature [153]. Hasanzadeh et al. demonstrated a similar SOFC/GT system operating with comparable combustion temperatures, showing an NOx emission rate of 1.2 kg NOx/MWh. The study shows peak system temperatures of 1233°C (1496K) at the combustor exit. In comparison, a methane-powered SOFC/GT system has been documented to emit 0.04 kg/MWh (5 ppmv) of NOx, with an exhaust flow rate and temperature of 34 kg/s and 360°C, respectively [154]. Furthermore, results from Sinha et al. indicate 0.3 g NOx/kg of methane for combustion at 1200K, while He et al. report 5 g NOx/kg fuel for combustion at 1200K [155], [156]. Moreover, Fuel Cell Energy's SOFC 250 kW system mentions values of 0.005 kg NOx/MWh for the SOFC stack [157]. Based on the reviewed data and to maintain consistency, our emissions model assumes 0.04 kg NOx/MWh as the most reasonable estimate based on after burner temperatures and exit flow temperatures. This translates to 0.94 g NOx/kg of hydrogen based on hydrogen's energy content and SOFC/GT system efficiency 71.4%. This is significantly smaller than what is observed from data from the conventional aircraft at 14 g/kg kerosene.

Figure 5.4 illustrates a phase diagram of water vapor pressure versus temperature, comparing the saturation pressures of liquid water and ice with the mixing lines for conventional aircraft and hydrogen fuel cell aircraft. The saturation vapor pressures were calculated using the Goff-Gratch Equations [158] (Equations 5.31 and 5.32). The Schmidt-Appleman criterion was then applied to derive the mixing lines for both types of aircraft, taking into account parameters such as ambient pressure, emission indices, specific heat capacity, lower heating values, and efficiencies.

$$
P_{\text{saturation, water}} = \exp\left(54.842763 - \frac{6763.22}{T} - 4.210\log(T) + 0.000367T\right.
$$
$$
\left. + \tanh(0.0415(T - 218.8))\left(53.878 - \frac{1331.22}{T} - 9.44523\log(T) + 0.014025T\right)\right)
$$

(5.31)

$$P_{\text{saturation, ice}} = \exp\left(9.550426 - \frac{5723.265}{T} + 3.53068\log(T) - 0.00728332T\right) \tag{5.32}$$

$$G = \frac{P \cdot EI_{\text{H}_2\text{O}} \cdot C_p}{\epsilon_{\text{H}_2\text{O}} \cdot LHV \cdot (1 - \eta)} \tag{5.33}$$
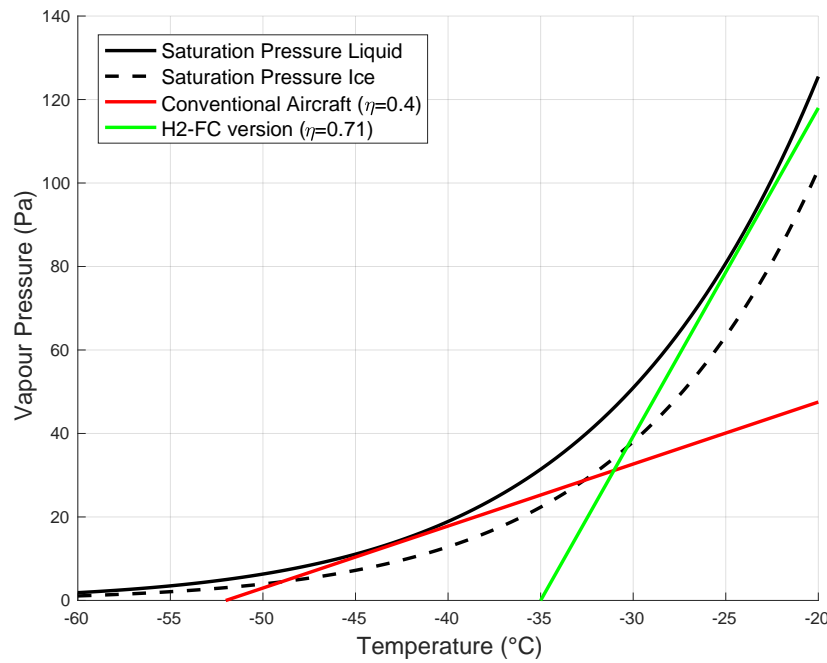
Fig. 5.4   Example Schmidt-Appleman criterion for assessing contrail formation for hydrogen FC and Jet-A at 40,000 ft.

The Schmidt-Appleman criterion provides a framework for determining the atmospheric conditions conducive to contrail formation. According to this criterion, contrails form when the exhaust plume of an aircraft, which is initially hot and moist, mixes with the colder and drier ambient air. The mixing process must result in a supersaturated state with respect to water vapor, allowing for the condensation and subsequent freezing of water droplets, leading to contrail formation. When comparing contrail formation from hydrogen fuel cells and Jet-A fuel, several complex and interrelated factors come into play like temperature, pressure, and humidity. Theoretical models, as

illustrated in Figure 5.4 above, demonstrate that the mixing slopes for hydrogen and Jet-A fuels differ significantly, indicating that contrails would form under distinct sets of atmospheric conditions. Hydrogen fuel cells, characterized by hydrogen's lower molecular weight, higher diffusivity, and higher efficiency, produce a steeper G-mixing line in the exhaust plume compared to hydrocarbon fuels. The values of G for conventional Jet-A fuel ($G_{\text{Jet-A}} = 1.4853$) and hydrogen ($G_{\text{H}_2} = 7.8655$) highlight this difference. Hence, hydrogen-fueled aircraft tend to form contrails at higher ambient temperatures compared to conventional Jet-A fueled aircraft. This is primarily due to the higher water vapor emission index of hydrogen combustion and the increased propulsion efficiency associated with hydrogen fuel cells [83].

The climate impact of contrails depends upon their persistence, which leads to the formation of contrail cirrus clouds. This persistence occurs when the ambient air's partial pressure of water vapor reaches or exceeds the ice saturation curve. The mixing trajectories depicted in FIgure 5.4 show that hydrogen and Jet-A fuels achieve ice saturation at different temperatures after initially reaching water saturation. This differential behavior underscores the unique conditions required for contrail formation with each type of fuel. Hydrogen's propensity to form contrails at higher temperatures is particularly notable, given its higher water vapor emission and efficiency metrics. In summary, while both hydrogen and Jet-A fuels can produce contrails, the specific conditions under which they do so vary due to differences in their emission characteristics and mixing dynamics with ambient air. Understanding these distinctions is crucial for assessing the potential climate impacts of transitioning to hydrogen fuel in aviation.

A summary of emissions indices determined for the different flight segments is presented in Table 5.2 and Table 5.3. These tables provide detailed emissions indices of each flight segment for conventional aircraft. The data includes key metrics and is essential for understanding the environmental impact across different stages of flight. Note that environmental effects of water emissions cannot be fully explained by emissions indices alone. Contrail prediction models are needed for a more accurate assessment of their impact.

Table 5.2   Emission indices for different flight segments for conventional B777-300ER

Segment	HC EI (g/kg)	CO EI (g/kg)	NOx EI (g/kg)	CO_2 EI (g/kg)	H_2O EI (g/kg)
T/O (take off)	0.032	0.125	51.068	3147.5	1257.7
C/O (climb)	0.024	0.137	36.44	3147.5	1257.8
Approach	0.048	2.16	16.166	3144.3	1257.6
Idle	3.636	34.578	5.511	3088.9	1236.5
Cruise	0.012	0.07	40	3147.6	1257.8
Descent	0.018	0.5	20	3146.9	1257.8

Table 5.3   Emission indices for different flight segments for conventional B737-800

Flight Segment	HC EI (g/kg)	CO EI (g/kg)	NOx EI (g/kg)	CO_2 EI (g/kg)	H_2O EI (g/kg)
T/O (take off)	0.1	0.6	20.5	3146.7	1257.3
C/O (climb)	0.1	0.5	17.4	3146.8	1257.3
Approach	0.1	3.2	9.5	3142.6	1257.3
Idle	3.1	25.9	4.3	3103.2	1239.6
Cruise	0.05	0.3	15	3147.2	1257.6
Descent	0.2	1.5	7	3145.1	1256.7

5.2. Results & Discussion

5.2.1. Mission Definition

In this paper, two distinct sample flight trajectories obtained from FlightAware [159] are utilized: one representing a journey from San Francisco International Airport (SFO) to Hong Kong International Airport (HKG) aboard a Boeing 777-300ER, and the other from SFO to Boston Logan International Airport (BOS), as depicted in Figures 5.5 and 5.6, respectively [159]. The objective is to assess the efficacy of the design and to evaluate and compare the correlation between the SOFC/GT powertrain and payload capacity across all studied aircraft configurations.

The flight profile from SFO to HKG was applied to the hydrogen-powered BWB-365 design as well as to both the hydrogen-powered T&W-365 and the kerosene-powered B777-300ER reference aircraft. For clarity, hydrogen T&W-365 refers to a retrofitted B777-300ER, essentially integrating the SOFC/GT powertrain and hydrogen storage systems to produce power within the existing aircraft geometry. This naming convention is similarly applied to the hydrogen T&W-162. The flight trajectory from SFO to BOS was applied to our hydrogen-powered BWB-162, hydrogen-powered T&W-162, and the reference aircraft B737-800. These flight profiles serve as practical scenarios for evaluating the performance and efficiency of the proposed aircraft designs under real-world conditions.
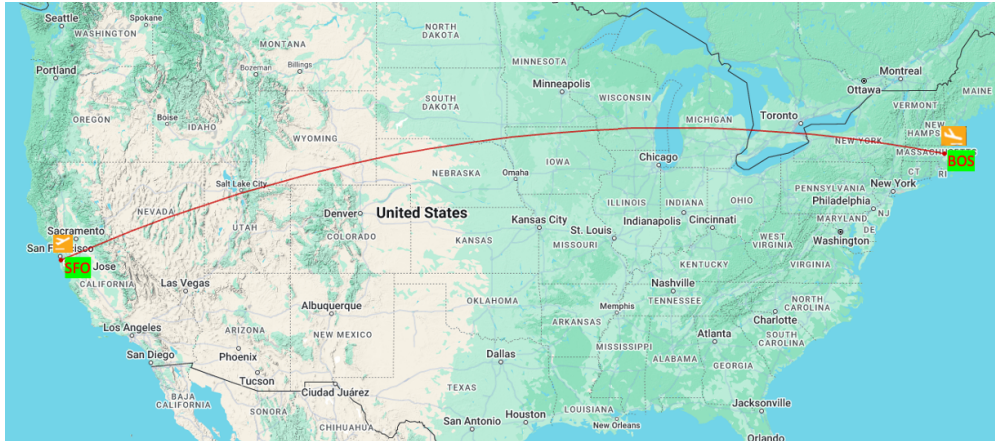
Fig. 5.5 Flight trajectory of example aircraft B737-800 from San Francisco International Airport (SFO) to Boston International Airport (BOS).
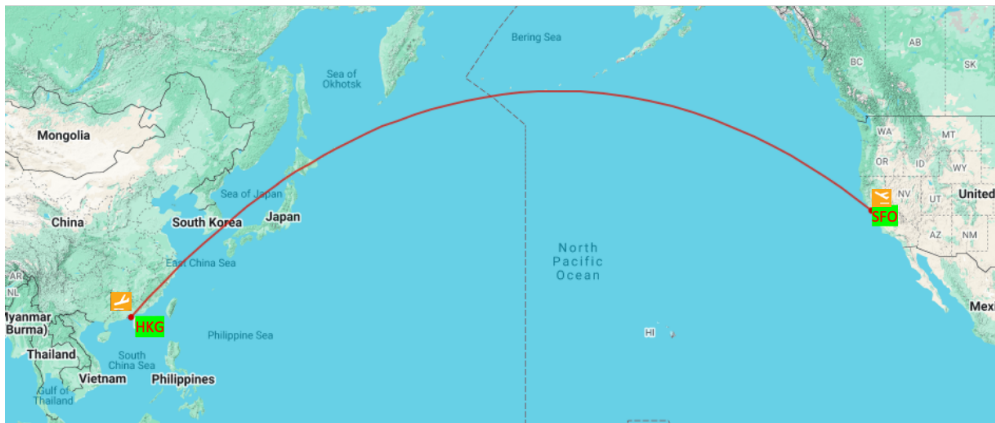
Fig. 5.6 Flight trajectory of example aircraft B777-300ER from San Francisco International Airport (SFO) to Hong Kong International Airport (HKG).

The relative flight conditions and assumptions for these missions are detailed in Table 5.4. This includes considerations such as altitude, speed, payload, and fuel type, ensuring a comprehensive and rigorous comparison of the different aircraft configurations. By using actual flight data, we aim to provide a realistic assessment of the potential benefits and challenges associated with the integration of the SOFC/GT propulsion system in commercial aviation.

Table 5.4   Mission definition assumptions per aircraft

	Hydrogen BWB-365	Kerosene B777-300ER	Hydrogen T&W-365	Hydrogen BWB-162	Kerosene B737-800	Hydrogen T&W-162
PAX	365	365	365	162	162	162
Cargo [kg]	15422	15422	15422	2268	2268	2268
Cruise Ma	0.84	0.84	0.84	0.78	0.78	0.78
Cruise Range [nmi]	6574	6574	6574	2415	2415	2415

5.2.2. Aircraft Layout Comparison

The cabin and wing geometry were sized based on the passenger capacity required for specific flight profiles. This study divides the aircraft into two classes: one configuration accommodates 365 passengers, and the other accommodates 162 passengers. These numbers were derived from existing sources representing typical passenger capacities for reference aircraft [160].

365 passenger layouts

Figure 5.7 provides a visual representation of the designed hydrogen-powered BWB-365. The span of the designed aircraft is 62.2 meters, with a root chord of 37.5 meters. The overall shape and wing geometries, including aspect ratio (AR) and sweep angle, of the aircraft is based on the baseline BWB-450 [139], with the wing geometries scaled according to the payload requirements. Multiple wing designs were evaluated, and it was found that the design featuring a flat upper wing and centerbody was the most advantageous for arranging the cabin layout (3-class configuration) and hydrogen tanks. This specific design also offers significant potential for scalability, allowing the geometry to be adjusted according to different needs.
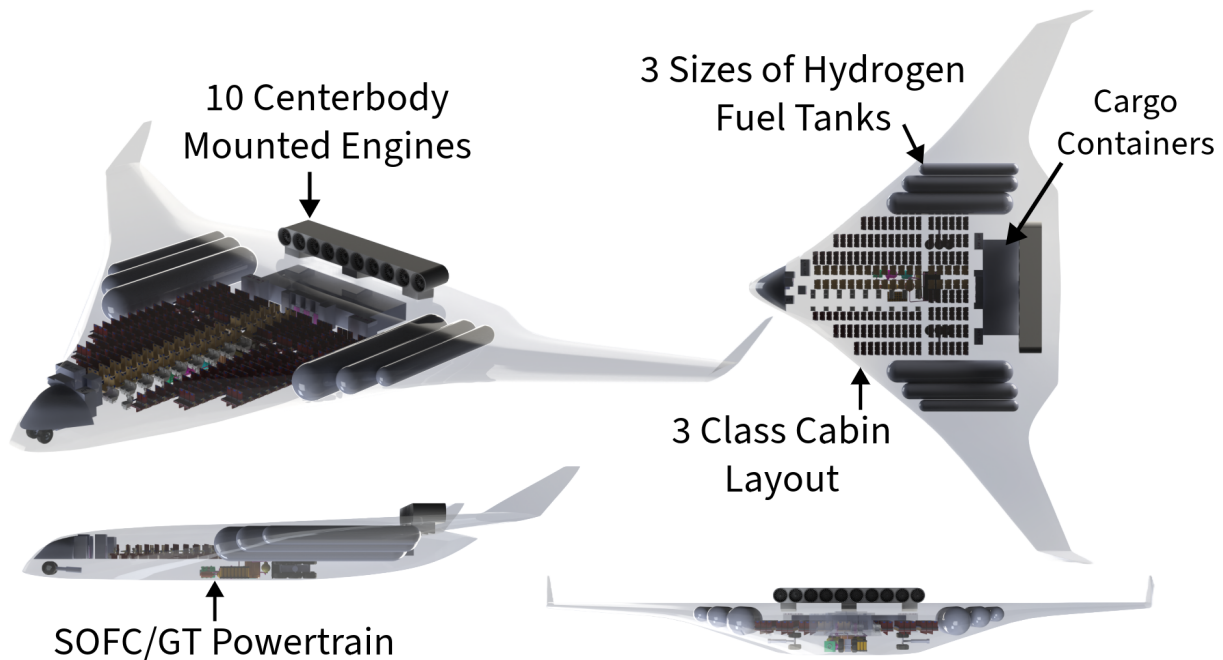
Fig. 5.7 Hydrogen BWB-365.

.

Three differently sized cylindrical hydrogen tanks are positioned on each side of the wings for optimal pressure distribution. Tank sizing considers geometric constraints, thermal management, and material properties. Safety assessments for potential accidents or leaks evaluate flammability limits, density, diffusivity, ignition energy, and fuel-oxidant mixing to determine relative risk.

The SOFC/GT powertrain is placed 22.9 meters from the aircraft tip, balancing the CG, approximately half the root chord length. Cargo containers are positioned 32.5 meters from the tip, while engines are mounted on the center aft body at 35.6 meters. The BWB-365 has ten engines, scaled from the N3-X model [41], providing a total of 59.9 MW.

Component placement meets the four critical CG cases: fully loaded payload and tanks, fully loaded payload with empty tanks, empty payload with full tanks, and empty payload with empty tanks. CG calculation results are provided in Table 5.5. Stability was evaluated by analyzing the wing CG positions from 15% to 35% of the mean aerodynamic chord to ensure the overall CG location was acceptable.

Table 5.5   Center of gravity for four different scenarios of hydrogen BWB-365

Components	Case 1: Full Cargo + PAX, Full Tank			Case 2: Full Cargo + PAX, Empty Tank		
	Weight [kg]	Location [m]	Moment [kg-m]	Weight [kg]	Location [m]	Moment [kg-m]
Nacelle + Pylon	3973.8	35.6	141306.9	3973.8	35.6	141306.9
Fuselage	57079.6	22.9	1304839.0	57079.6	22.9	1304839.0
Wing	27310.9	24.4	666518.8	27310.9	24.4	666518.8
Powertrain	38081.2	22.9	870536.0	38081.2	22.9	870536.0
Main Landing Gear	3558.5	25.4	90385.5	3558.5	25.4	90385.5
Nose Landing Gear	392.6	7.8	3050.5	392.6	7.8	3050.5
Fuel + Tank	21535.0	28.8	620257.3	0.0	28.8	0.0
Fixed Equipment	45490.5	24.4	1110187.3	45490.5	24.4	1110187.3
Passenger	44701.5	22.9	1021876.1	44701.5	22.9	1021876.1
Cargo	18279.8	32.5	594311.5	18279.8	32.5	594311.5
Sum:	260403.3			238868.3		
CG [% of MAC]:	**25.3**			**24.9**		

Components	Case 3: Empty Cargo + PAX, Full Tank			Case 4: Empty Cargo + PAX, Empty Tank		
	Weight [kg]	Location [m]	Moment [kg-m]	Weight [kg]	Location [m]	Moment [kg-m]
Nacelle + Pylon	3973.8	35.6	141306.9	3973.8	35.6	141306.9
Fuselage	57079.6	22.9	1304839.0	57079.6	22.9	1304839.0
Wing	27310.9	24.4	666518.8	27310.9	24.4	666518.8
Powertrain	38081.2	22.9	870536.0	38081.2	22.9	870536.0
Main Landing Gear	3558.5	25.4	90385.5	3558.5	25.4	90385.5
Nose Landing Gear	392.6	7.8	3050.5	392.6	7.8	3050.5
Fuel + Tank	21535.0	28.8	620257.3	0.0	28.8	0.0
Fixed Equipment	45490.5	24.4	1110187.3	45490.5	24.4	1110187.3
Passenger	0.0	22.9	0.0	0.0	22.9	0.0
Cargo	0.0	32.5	0.0	0.0	32.5	0.0
Sum:	197422.1			175887.1		
CG [% of MAC]:	**24.9**			**24.4**		

To integrate a hydrogen fuel tank in a conventional tube-and-wing aircraft without reducing cabin space, two options are typically considered: sacrificing cabin space or extending the fuselage. In this case study, to preserve the payload capacity of the hydrogen-powered tube-and-wing aircraft, the fuselage was extended by 6.67 meters to accommodate the hydrogen fuel tank behind the cabin while maintaining the original wing geometry (aspect ratio and sweep angle) of the B777-300ER.// Figure 5.8 shows the modified layout, with the hydrogen fuel tank positioned behind the cabin and the SOFC/GT powertrain components strategically placed in front of the wing at 25.4 meters from the aircraft tip to maintain the center of gravity (CG) within an operable range.// Ten engines, scaled from existing models, are mounted on the wings, delivering a total power output of 53.1 MW. Cargo containers and the fuel tank are positioned aft of the wing, at 54.7 meters and 72.2 meters from the aircraft tip, respectively, preserving the original cabin layout and passenger capacity of the B777-300ER.// By extending the fuselage and optimizing the placement of the hydrogen fuel tank and powertrain components, the design maintains operational efficiency and capabilities while integrating a hydrogen propulsion system. This approach explores hydrogen-powered aviation's potential without compromising payload capacity or passenger comfort.
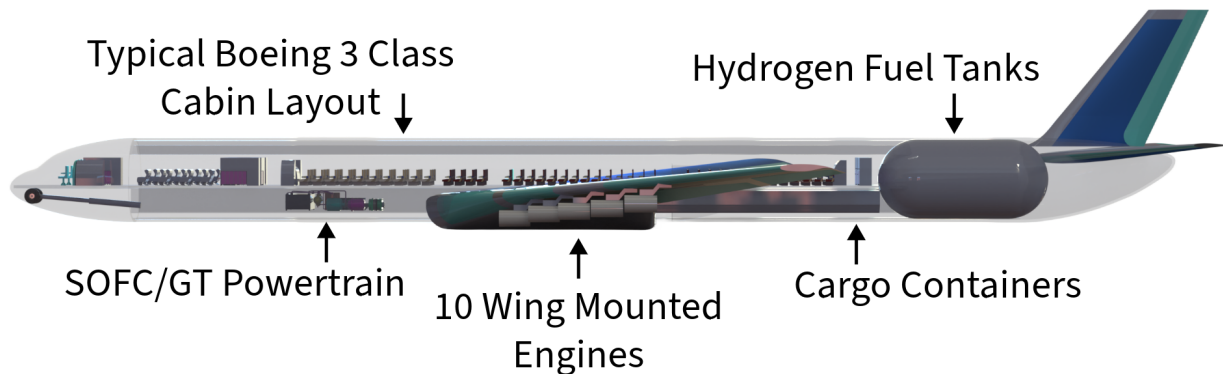
Fig. 5.8   Hydrogen T&W-365 side profile.

162 passenger layouts

This paper also conducts a comparative analysis of the performance of the designed aircraft for shorter flight durations and fewer passengers. The hydrogen BWB-162 and B737-800 were evaluated

for a cruise range of 2415 nautical miles and a passenger capacity of 162. The aircraft's span, based on its passenger capacity, is 34.5 meters, with a root chord of 16.5 meters. The hydrogen fuel tanks shown in Figure 5.9 represent the necessary fuel volume for the flight mission while maintaining a fixed cargo weight. However, Figure 5.9 does not show the maximum dimensions of the fuel tanks. This wing geometry allows for larger tanks, providing flexibility to increase cruise range or payload capacity.

The figure also shows cargo containers positioned between the cabin and hydrogen fuel tanks. For extended or heavier missions requiring larger tanks, the cargo containers can be relocated to the bottom of the cabin to keep the center of gravity within acceptable limits. The proposed hydrogen BWB-162 incorporates a pivot gear design by JetZero for commercial BWB aircraft [161]. This design reduces the airframe size by placing cargo containers on each side of the cabin. JetZero's innovative landing gear design also features a fully passive motion system that enhances braking effectiveness by 30%. As with the hydrogen BWB-365, the placement of the SOFC/GT powertrain was carefully chosen to satisfy CG requirements for all four scenarios.
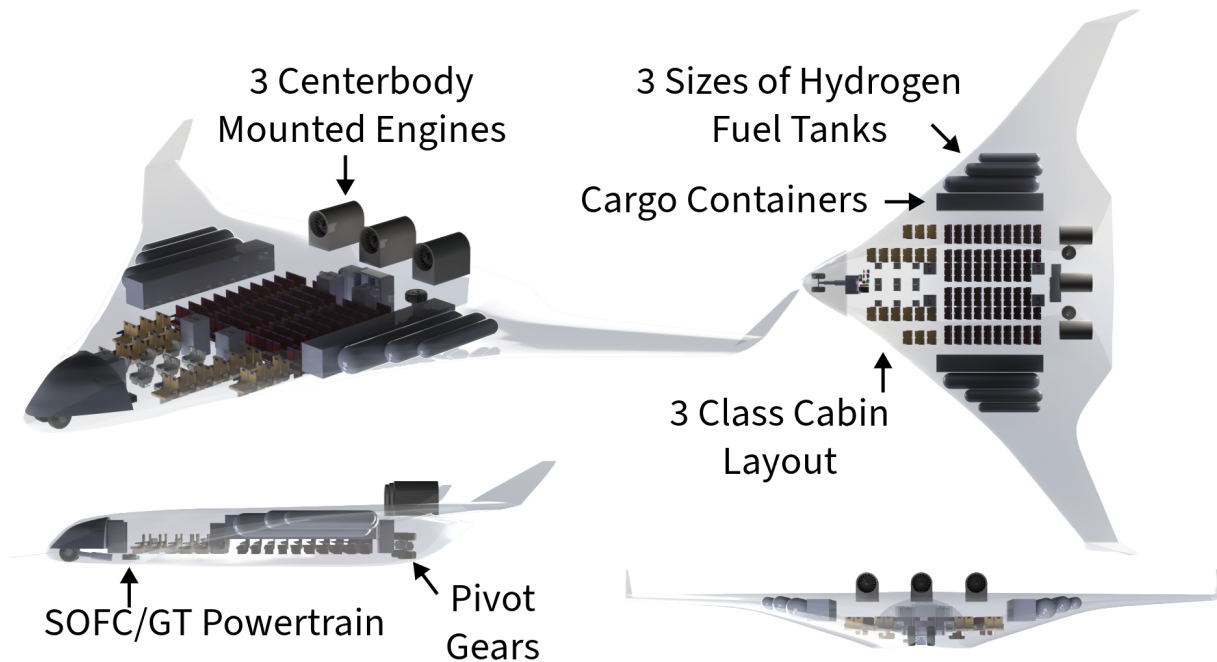
Fig. 5.9   Hydrogen BWB-162.

The hydrogen-powered B737-800 follows a similar design approach to the hydrogen-powered B777-300ER. To maintain the payload capacity, the fuselage was extended by 2 meters to accommodate the hydrogen tanks without sacrificing passenger or cargo space. The aircraft includes four wing-mounted engines with a total power output of 10.2 MW. The cabin layout, including passenger service equipment such as galleys, lavatories, and closets, remains identical to the conventional B737-800 to ensure passenger comfort and operational efficiency. By extending the fuselage and integrating the hydrogen fuel tanks and powertrain components, the design balances the hydrogen propulsion system with the existing structural and operational requirements of the B737-800. This approach explores the viability of hydrogen-powered aviation while preserving the aircraft's key characteristics and performance.
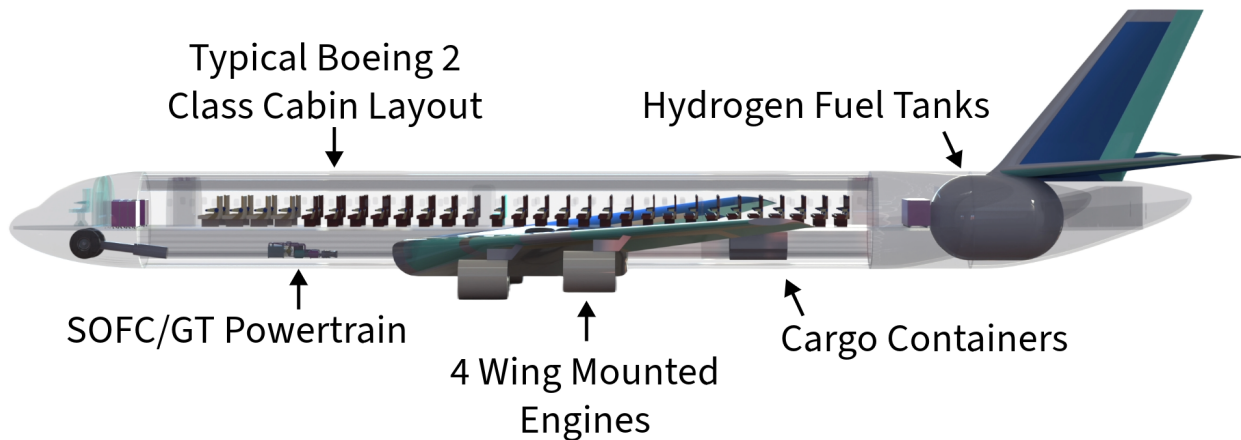
Fig. 5.10   Hydrogen T&W-162 side profile.

5.2.3. Simulation of Cryogenic Hydrogen Tank operation for an Example Mission

In the simulation results presented in Figure 5.11, the hydrogen boil-off, fuel consumption, temperature and pressure change process in a tank over the flight duration of 11 hours is modeled. Initial conditions include the liquid hydrogen (LH_2) mass and gaseous hydrogen (GH_2) mass calculated based on a 2916 kg total hydrogen load and a 7.2% GH_2 fraction.
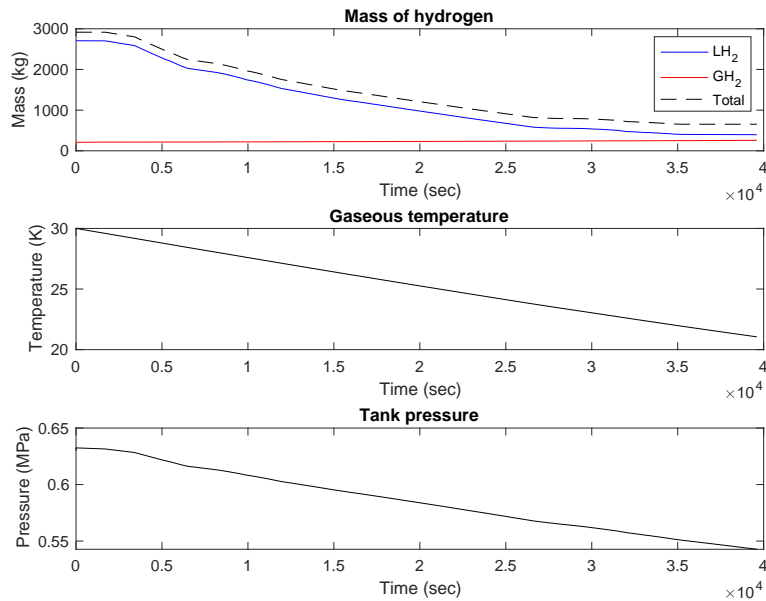
Fig. 5.11   Dynamic tank operation during the cruise phase for 2916 kg H$_2$ tank with changing consumption rate with an average rate of 69.3 g/s for example flight trajectory from SFO to HKG

The dynamic tank operation plots in Figure 5.11 illustrate the mass of hydrogen, gaseous temperature, and tank pressure over time during an example flight of the hydrogen BWB. Due to the lengthy cruise phase (9.5 hours) compared to other flight segments, the fuel consumption rate appears constant. The average fuel flow rates to the propulsion system for each section are as follows: for the taxi phase, the flow rate is 0.00693 kg/s; for the takeoff phase, it is 0.092589 kg/s; for the climb phase, the rate is 0.08316 kg/s; during the cruise phase, the flow rate is 0.0693 kg/s; and for the descent phase, the flow rate is 0.04851 kg/s. The plot shows the mass of hydrogen, with the total mass displaying a consistent decline, reflecting nearly steady consumption on average.

The system experiences a heat flux of approximately 10 W/m². As hydrogen is discharged, the available volume in the tank increases, causing the gaseous hydrogen pressure to expand into this larger volume. This expansion leads to a pressure drop within the tank, which is accompanied by a corresponding decrease in temperature, as described by the ideal gas law. The steady decline

143

in tank pressure from about 0.65 MPa to 0.55 MPa, along with the gradual decrease in gaseous temperature from approximately 30 K to 24 K, reflects the cooling dynamics associated with hydrogen consumption and phase change [162]. Notably, the mass of gaseous hydrogen remains relatively constant throughout the flight because it is primarily the liquid hydrogen that is vaporized and consumed. This counter-intuitive result, considering the fact that heat gain and boil-off are usually a concern for liquid hydrogen storage, can be observed from Figure 5.11, which illustrates the steady-state behavior of gaseous hydrogen mass despite ongoing consumption and phase transition processes with concurrent heat gain from the environment. Understanding the natural boil-off and consumption behavior, along with tank insulation modeling as illustrated in Figure 5.3, aids in making design choices that balance natural boil-off with the boil-off that will be effectively utilized by the aircraft. The tank is designed with a 4 g/s natural boil off based on results from Figure 5.3 with a 10 cm MLI insulation. For reference, the lowest fuel flow rate during taxi for the BWB-365 flight case study is 6.93 g/s meaning no fuel will be vented to environment. Given that the SOFC will remain constantly operational, it is unnecessary to design tanks with additional insulation, which would add unnecessary weight and volume.

5.2.4. Hydrogen vs. Conventional Aircraft Comparison

Figure 5.12 illustrates the comparison between the Operating Empty Weight (OEW), shown in blue bars, and the combined payload and fuel weight, depicted in orange bars, for all six aircraft configurations. It is important to note that the fuel type used in this comparison is consistent with the naming convention of each column Figure 5.12. The payload for each aircraft is identical within their respective classes, as detailed in Table 5.6.

144

Table 5.6   Comparison of performance metrics between hydrogen and kerosene-powered aircraft configurations under different operational scenarios

	Kerosene B777-300ER	Hydrogen BWB-365	Hydrogen T&W-365	Kerosene B737-800	Hydrogen BWB-162	Hydrogen T&W-162
# of Engines	2	10	10	2	3	4
Total Power [MW]	77.96	59.9	53.1	10.74	11.91	10.2
TOGW [kg]	334211	260403	233698	70307	78687	68328
OEW [kg]	136559	182334	150346	36334	54555	43382
Payload Weight [kg]	60124	60124	60124	22108	22108	22108
Fuel Weight [kg]	137522	17946	23229	11859	2024	2838
Weight per PAX [kg]	916	713	640	434	486	422
Payload + Fuel [kg]	197646	78069	83352	33968	24132	24946

For the 365-passenger class, the hydrogen BWB-365 design exhibits a lower MTOW compared to the conventional B777-300ER using Jet-A fuel. However, it remains 10% heavier than the retrofitted hydrogen T&W-365. Conversely, the MTOW of the hydrogen BWB-162 surpasses both the retrofit hydrogen T&W-162 and the conventional B737-800.

A notable trend across both classes is the progressive increase in OEW, ascending from conventional baseline aircraft to hydrogen baseline aircraft, and finally to the hydrogen BWB configurations. To scrutinize the causes of this OEW increase, Table 5.7 presents a detailed MTOW breakdown for the hydrogen T&W-365 and hydrogen BWB-365.

Due to a higher aerodynamic coefficient and the enhanced performance efficiency, the fuel weight for the BWB is expected to be lower than that of a conventional T&W configuration. Within the

aircraft empty weight category, the propulsion weight groups and structural weight groups for the hydrogen BWB-365 are more significant compared to those of the hydrogen T&W-365. The weight of all components within the SOFC/GT powertrain was calculated based on the power required for each aircraft. Specifically, the hydrogen BWB-365 requires 12.7% more power output compared to the hydrogen T&W-365. Consequently, it is natural to observe a higher propulsion weight, because the fuel cell system has much lower power density compared to a gas turbine so that a larger system is needed to generate the necessary power.

In the structural weight group, the wing of the hydrogen BWB-365 is approximately 12,000 kg heavier. This increase is primarily attributed to a larger wing area, increased control surfaces area, and an additional aft body weight portion, which is a function of the cabin planform area—36% higher in the BWB configuration. Despite the longer length of the T&W configuration, the centerbody weight of the hydrogen BWB-365 is higher due to the overall increase in cabin planform area. This increase in surface area for the BWB configuration aligns with findings in the literature [140]. Kimmel and Bradley also observed a similar trend in OEW growth for the BWB design.

Table 5.7   Detail weight breakdown of Hydrogen BWB-365

					Parameters	Hydrogen T&W-365	Hydrogen BWB-365
					Average cruise L/D	15	23.4
Maximum Takeoff Gross Weight	Zero Fuel Weight	Operating Empty Weight	Aircraft Empty Weight	Structural Weight	Wing [kg]	14305.4	26087.2
					Empennage [kg]	4180.2	–
					Centerbody [kg]	–	57079.6
					Fuselage [kg]	35561.2	–
					Landing Gear [kg]	3972.5	3951.1
					Fins [kg]	–	1223.7
					Nacelle [kg]	1260.1	1316.4
					Paint [kg]	3776.8	2081.7
					Total [kg]:	63056.2	91739.8
				Propulsion Weight	SOFC [kg]	15940.2	17981.5
					Battery [kg]	4953.6	5588.0
					Gas Turbine [kg]	2768.5	3123.0
					Cryo-cooler [kg]	1619.0	1828.1
					HTS Motor [kg]	1821.6	2056.9
					Thrust Reverser [kg]	1221.3	1379.1
					Hydrogen Tanks [kg]	4645.8	3589.2
					Other Components [kg]	7757.3	8781.9
					Total [kg]:	40727.3	44327.7
				Systems & Equip. Weight	Surface Control Sys. [kg]	1675.3	2890.9
					Instruments System [kg]	1517.0	2069.9
					Hydraulic System [kg]	1921.9	3168.3
					Electrical System [kg]	4665.8	4102.2
					Avionics System [kg]	4790.6	5815.2
					Furnishings [kg]	23136.3	19329.1
					Anti-icing System [kg]	201.7	237.0
					Total [kg]:	37908.7	37612.6
					$W_{empty} [kg]$:	141692.2	173680.1
			Operating Items Weight		Fixed Equipment [kg]	1959.5	1959.5
					Passengert Service [kg]	3836.6	3836.6
					Cargo Containers [kg]	2857.6	2857.6
					Total [kg]:	8653.8	8653.8
					$W_{op. \; items} [kg]$:	8653.8	8653.8
					OEW [kg]:	**150346.0**	**182333.8**
					Payload [kg]	60123.6	60123.6
					ZFW [kg]:	210469.6	242457.5
					Fuel [kg]:	23228.8	17945.9
					MTOW [kg]:	233698.4	260403.3
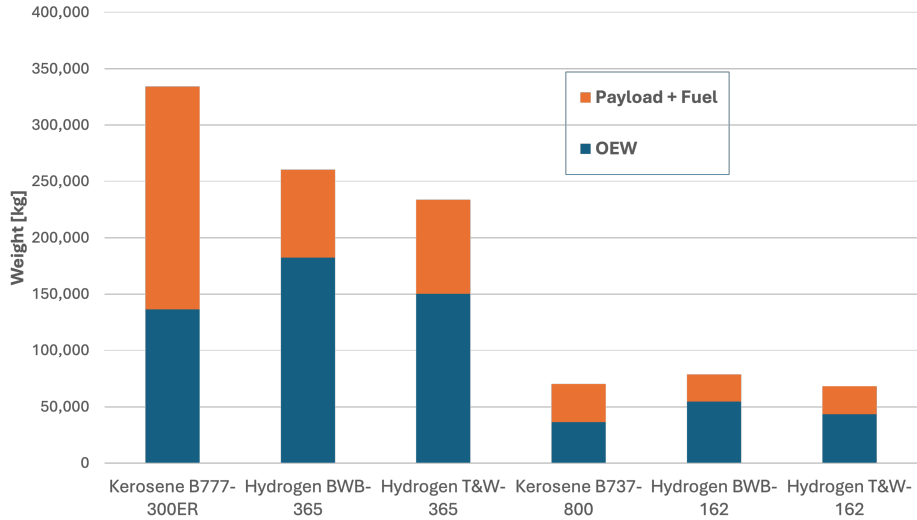
Fig. 5.12   Operating empty weight and combined payload and fuel weight bar chart for all six studied aircraft configurations

Table 5.8 provides a detailed mass breakdown of the components for a 45 MW SOFC/GT system coupled with a 15MW, 3.75 MWh battery used in the BWB-365. Table 5.8 lists each component along with its mass. The SOFC is the heaviest component at 17,970 kg, followed by the recuperator/heat exchanger at 4,199 kg, and the gas turbine at 3,123 kg. Other components like the oxidizer/combustor, recycling blower, and hydrogen delivery system also contribute to the total mass. The total mass is 29,860 kg, and with the battery included, the total mass reaches 35,448 kg. Table 5.8 provides a more granular view of the SOFC/GT system components, while the overall propulsion system breakdown is depicted in Table 5.7.

Table 5.8   SOFC/GT components breakdown Mass and Percent of Total Mass for 45MW SOFC/GT and 3.75MWh battery

Component	Mass (kg)	% of mass
SOFC	17970	60.18%
GT	3123	10.46%
Compressor	226	0.76%
Recuperator/HX	4199	14.06%
Oxidizer/combustor	2524	8.45%
Recycling Blower	337	1.13%
Air Blower	112	0.38%
Electric Generator	474	1.59%
Fuel Pump	163	0.55%
Fuel Heater	163	0.55%
Hydrogen Delivery System (pump + tankflow conditioning + tubing)	569	1.90%
Total Power Train Mass	29860	100.00%
Battery (kWh)	5588	
Total with Battery	35448	

Figure 5.13 illustrates the relationship between OEW and seating capacity for various aircraft models, including hydrogen-powered BWB designs. The hydrogen BWB-365 shows 33% and 21% higher OEW compared to B777-300ER and hydrogen T&W-365. This increase in OEW is partly due to the non-circular pressurized body of the BWB, which requires more structural material to maintain integrity, larger area of the cabin, greater airfoil thickness to achieve higher lift, unique landing gear

configuration, weight of hydrogen storage systems and the SOFC/GT powertrain. Additionally, the BWB is overall a larger aircraft, which inherently requires more material and structural support, further increasing the OEW.

Previous alternative analyses of BWB have produced different conclusions with some claiming lower and other higher TOGW than T&W aircraft. Adler and Martins determined that the hydrogen combustion BWB is 13% lighter MTOW than the hydrogen T&W counterpart and with lower fuel consumption, yet still the wing is 19% heavier [38]. Sgueglia et al. conducted a comparative analysis of the A320 Neo and three BWB baselines. In all cases, the MTOW and the OWE of BWB were greater than those of the reference aircraft, primarily due to the center-body structure. The more complex design necessitates reinforcements to handle pressurization and the bending moment of the outer wing, resulting in a heavier structure compared to a tubular fuselage. Despite fuel consumption is 18% lower in the best case [163]. Another comparison done by Reist and Zingg arrives at the conclusion that BWBs are more aerodynamically efficient than T&W's but are heavier, reducing the expected benefits in drag and fuel burn. Regional and narrow-body BWBs show minimal fuel-burn reduction compared to T&W's [164]. Hence, the literature is inconclusive regarding whether a BWB aircraft is heavier than its T&W counterpart, but consistently concludes, together with the current study, that BWB provides fuel savings due to the higher L/D and better aerodynamic efficiency.
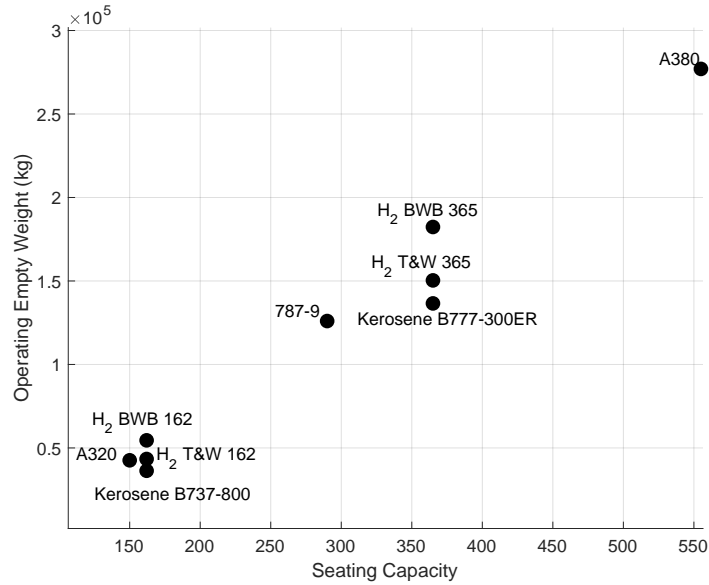
Fig. 5.13 Operating empty weight for BWB's and various hydrogen and conventional aircraft models.

Figure 5.14 compares fuel consumption per passenger-kilometer against seating capacity. Hydrogen aircraft models exhibit significantly lower fuel consumption per passenger-kilometer than conventional aircraft, such as the A320 and B777-300ER. This highlights the efficiency advantage of hydrogen power, leveraging its higher energy density to achieve lower fuel consumption metrics. Furthermore, hydrogen BWB has even further fuel/px-km savings compared to T&W aircraft despite the initial weight penalty and larger size of the BWB design with combined aerodynamic and propulsion efficiency benefits. This is consistent with other BWB designs such as Liebeck demonstrating that a BWB designed for around 800 passengers and a range of 7000 nautical miles achieves a 27% reduction in fuel consumption per passenger-km compared to a conventional aircraft using Jet-A fuel [140].
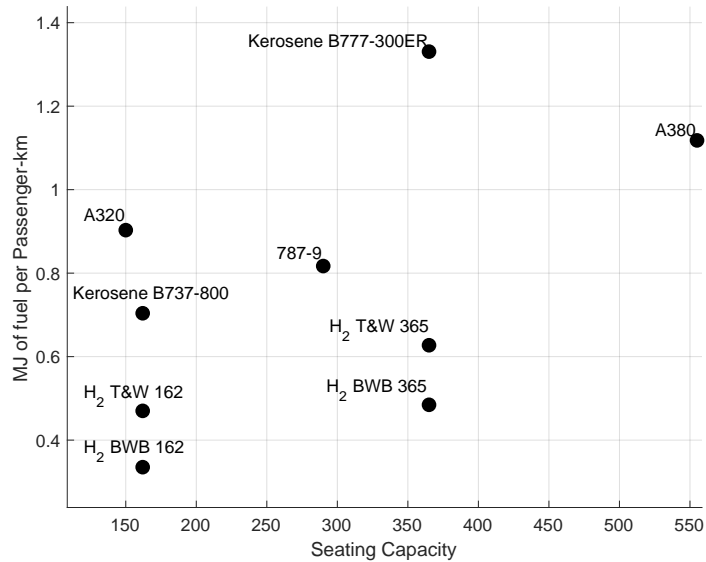
Fig. 5.14 Fuel Consumption per Passenger-Kilometer of BWB's and various hydrogen and conventional aircraft models.

Key results reveal that scaling down from the hydrogen BWB-365 to the hydrogen BWB-162 resulted in unexpectedly positive outcomes. The weight per passenger for the hydrogen BWB-162 was 486 kg, compared to 713 kg for the hydrogen BWB-365, representing a reduction of approximately 31.8%. Additionally, the fuel consumption per passenger-kilometer decreased significantly, with the hydrogen BWB-162 achieving a 30% reduction compared to its larger counterpart. These improvements underscore the potential for hydrogen propulsion systems to enhance operational efficiency across different aircraft sizes.

One possible scientific explanation for these results is the square-cube law, which states that as a shape grows in size, its volume increases faster than its surface area. This leads to disproportionate increases in structural weight and aerodynamic drag for larger aircraft. In the case of the hydrogen BWB-162, the reduced size may result in more efficient aerodynamics, lower structural weight, and more favorable wing loading, thereby improving overall weight and fuel efficiency per passenger. Additionally, the hydrogen BWB-365's higher range necessitates larger and heavier tanks, which could contribute to the less favorable weight and efficiency metrics observed in the larger aircraft.

The reduced structural requirements and optimized design approaches possible with the smaller hydrogen BWB-162 likely further enhance these efficiency gains.

5.2.5. Environmental Impact Assessment

Figure 5.15 presents a comparative analysis of the emissions composition by flight phase for conventional (777-300ER, 737-800) and hydrogen-powered (BWB-450 & T&W-365 and BWB-162 & T&W-162) aircraft models, highlighting significant differences in environmental impact. The pie charts show that for conventional models like the Boeing 777-300ER and Boeing 737-800, the cruise phase is the predominant contributor to emissions, particularly CO_2, H_2O, and NO_x. For instance, during the cruise phase, the Boeing 777-300ER emits 414,160 kg of CO_2 and 165,500 kg of H_2O, with 5,263 kg of NO_x. In contrast, during the taxi phase, the emissions are significantly lower, with the Boeing 777-300ER emitting 282 kg of CO_2, 112.9 kg of H_2O, and 0.503 kg of NO_x. Notably, CO emissions during taxiing are relatively high at 3.158 kg due to incomplete combustion at lower engine power settings typical of ground operations.

The hydrogen-powered models (BWB-450 & T&W-365 and BWB-162 & T&W-162) demonstrate significantly reduced emissions. However, hydrogen-fueled aircraft, with a higher water vapor emission index and greater propulsion efficiency, produce a steeper G-mixing line (G_{H2} = 7.8655) compared to kerosene-fueled aircraft (G_{Jet-A} = 1.4853), as shown in Figure 5.4. Consequently, hydrogen-powered aircraft tend to form contrails at higher ambient temperatures. For the BWB-450, H_2O emissions are highest during the cruise phase at 154,534.90 kg, while NO_x emissions during the same phase are significantly lower at 16.35 kg. In the taxi phase, H_2O emissions are 107.25 kg, and NO_x emissions are nearly negligible at 0.01 kg. Similarly, the BWB-162 shows substantial reductions in emissions, with H_2O emissions during the cruise phase at 16,150.5 kg and NO_x emissions at 1.71 kg, compared to the taxi phase, which has 24.38 kg of H_2O and no measurable NO_x emissions. More details for the breakdown of emissions are found in Tables B1, B2, B3 and B4. These results underscore the significant potential hydrogen-powered aviation to reduce greenhouse

gases and other pollutants, thereby offering a more sustainable alternative to traditional jet fuel.
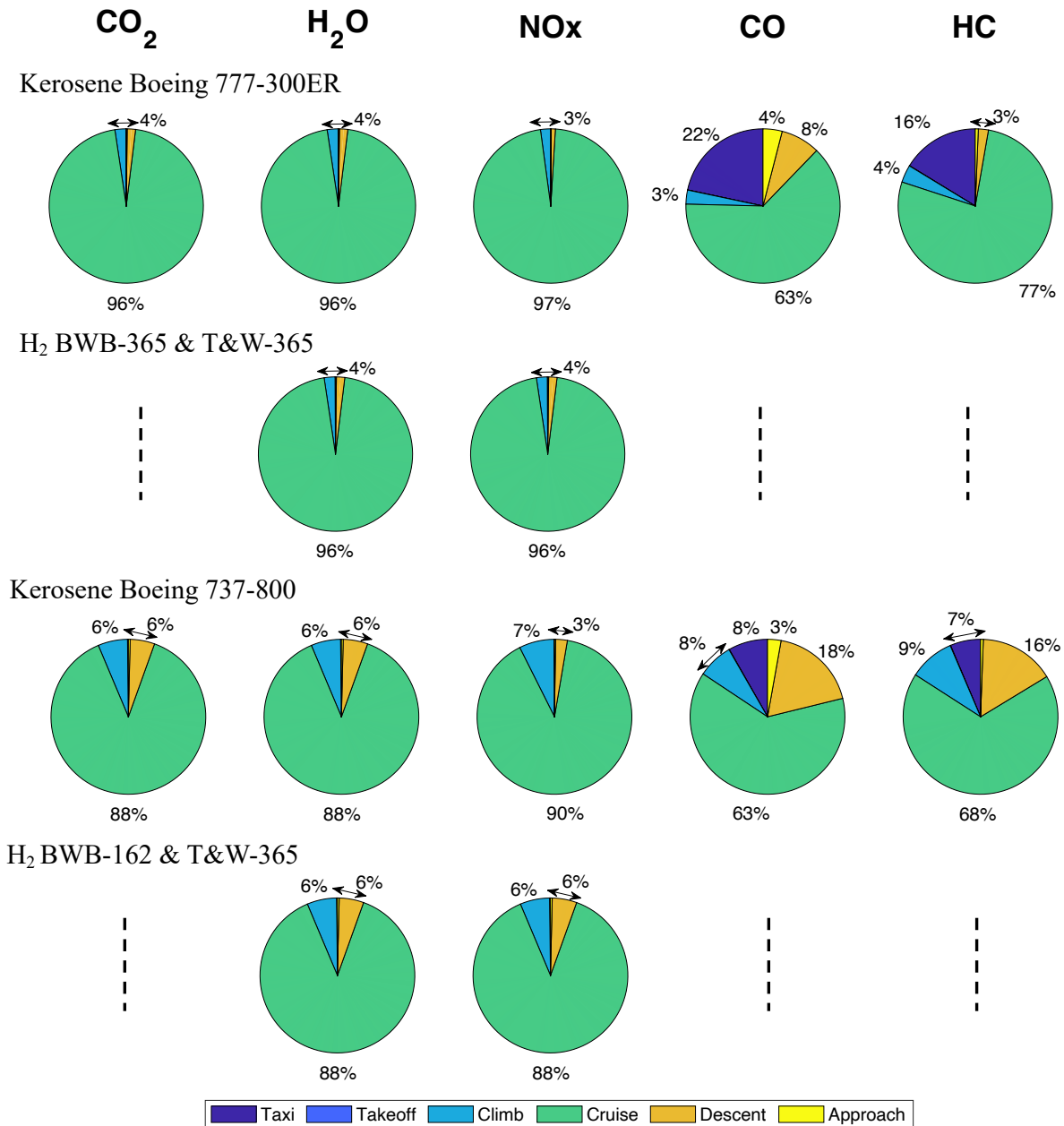
Fig. 5.15 Emission composition for the flight phase for conventional (777-300ER, 737-800) and hydrogen-powered (BWB-365 & T&W-365, BWB-162 & T&W-162) aircraft models.

Figure 5.16 presents a comparison of total emissions (CO_2, H_2O, NO_x, CO, HC) for various aircraft models, including both conventional (777-300ER, 737-800) and hydrogen-powered configurations

154

(BWB-365, BWB-162, T&W-365, T&W-162). This comparative analysis highlights that hydrogen-powered aircraft generally emit significantly lower CO_2 and NO_x compared to kerosene-powered models. Specifically, the hydrogen BWB-162 model exhibits the lowest total emissions, particularly noteworthy for its minimal NO_x emissions. To illustrate further, the total emissions for the kerosene-powered 777-300ER show a significant amount of CO_2 (432780 kg) and NO_x (5431.6 kg). In contrast, the hydrogen BWB-365 exhibits significantly lower emissions, with total H_2O emissions at 161485 kg and NO_x emissions at 17.08 kg. These results underscore the potential of hydrogen-powered aircraft to reduce aviation's environmental footprint. However, the increased H_2O emissions from hydrogen-fueled aircraft, as seen in the significant H_2O emissions in the hydrogen BWB-365 and the hydrogen BWB-162 model, require further exploration due to their potential short-term radiative forcing effects. More details of these emissions impacts can be found in the Appendix.
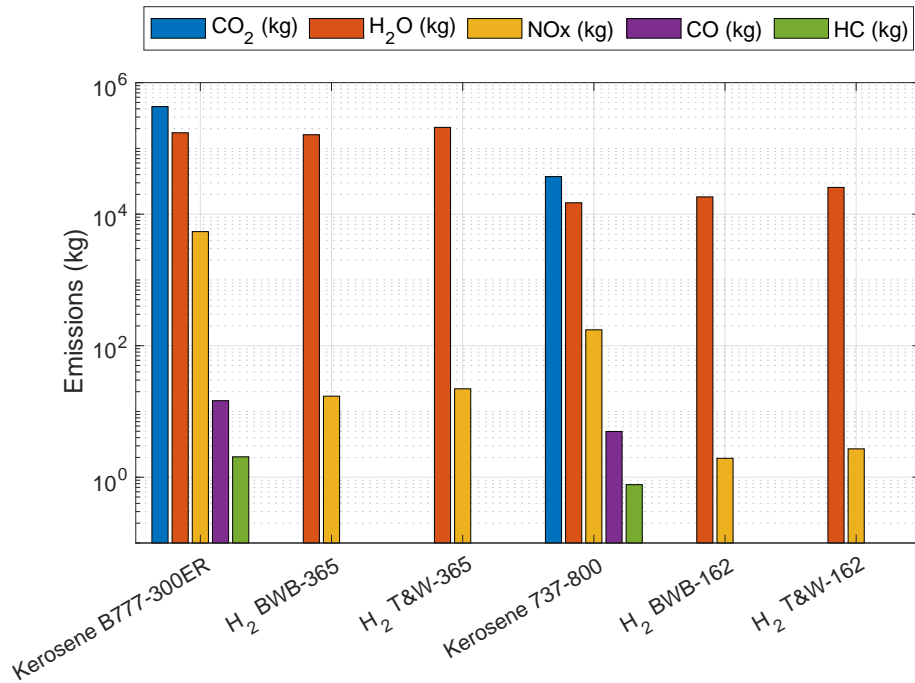
Fig. 5.16 **Comparison of total emissions (CO_2, H_2O, NOx, CO, HC) for various aircraft models, including conventional (777-300ER, 737-800) and hydrogen-powered configurations (BWB-365, BWB-162, T&W-365, T&W-162).**

To assess the climate impacts amongst the configurations considered here, we assessed the Global Warming Potential (GWP) in terms of kg CO_2 equivalent emissions per passenger-km as presented in

Figure 5.17. This assessment considers GWP values over a 100-year horizon derived from relevant literature. The GWP factors used in our analysis include CO_2 at a factor of 1, HC at 21, CO at 1.7, NOx at 40, and H_2O at 0.059 [98, 100, 101]. This comparative assessment reveals the significant differences in emissions between hydrogen and kerosene-fueled aircraft. Notably, hydrogen-powered aircraft configurations exhibit substantially lower CO_2 equivalent emissions, particularly in the hydrogen BWB-162 model, with a value of approximately 1.84×10^{-3} kg/passenger-km. In contrast, kerosene-powered models like the Kerosene 737-800 and Kerosene 777-300ER show much higher emissions, with the latter reaching 1.71×10^{-1} kg/passenger-km. It is important to note that 100-year CO_2 equivalent is not the only useful metric for assessing for the the climate impacts of emissions like water, especially since radiative forcing from water emissions is usually limited to hours.
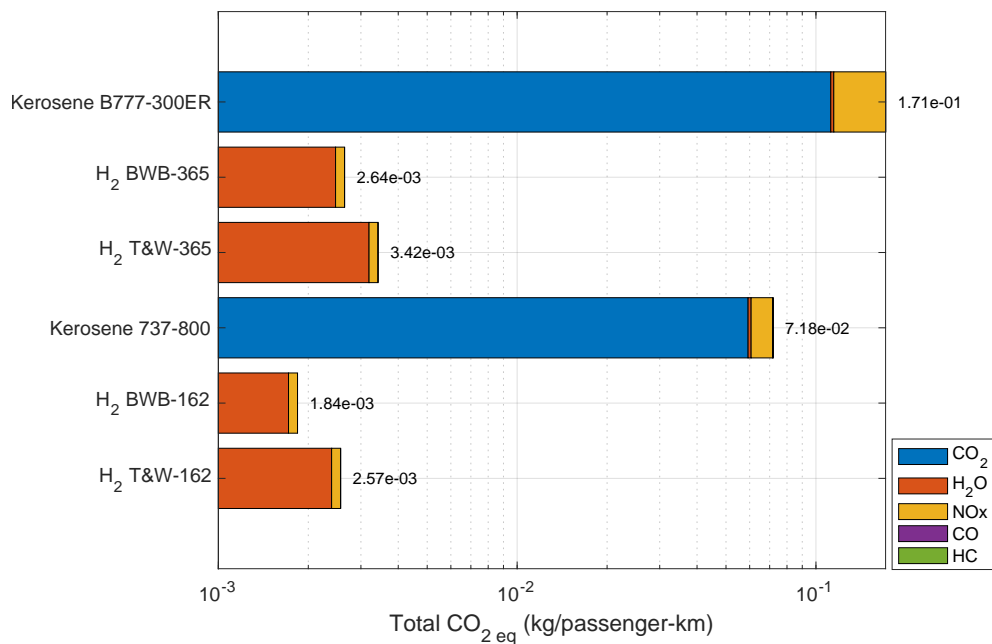
Fig. 5.17 CO_2 Equivalent Emissions per PAX-km by Aircraft, with 100-year GWP for CO_2, H_2O, NOx, CO, HC.

5.3. Conclusion

Six distinct aircraft configurations are designed and comparatively analyzed within their respective classes. A notable trend of increasing OEW was observed for both the hydrogen-powered BWB-365

and BWB-162, primarily due to the increased wing surface area and cabin planform area. Despite a higher OEW, the hydrogen BWB-365 and BWB-162 exhibited superior fuel efficiency, with a 22.7% and 28.7% lower fuel weight compared to hydrogen T&W-365 and hydrogen T&W-162, respectively. This is mainly attributed to their higher aerodynamic coefficients and the greater energy density of hydrogen fuel. Moreover, hydrogen-powered BWB-365 achieved a 61% reduction in MJ of fuel consumption per passenger-kilometer and a 22% reduction in total takeoff weight per passenger compared to the conventional Boeing 777-300ER. Similarly, the hydrogen BWB-162 showed a 52% decrease and 11% increase compared to the conventional Boeing 737-800, respectively.

Integrating a SOFC/GT powertrain into aircraft necessitates careful consideration of the additional space required for hydrogen fuel tanks. Storing fuel within the wings, as is common in conventional tube-and-wing (T&W) designs, is deemed impractical due to the narrow spaces provided. To maintain the same payload and passengers capacity as T&W aircraft without sacrificing cargo space, extending the fuselage is necessary. However, this extension raises concerns regarding the stress and loading experienced by the aircraft during flight.

The centerbody design of the BWB offers significant potential for scaling the aircraft to accommodate varying payloads. The flat and wide centerbody allows for lateral expansion of the cabin. As demonstrated by Liebeck and the current results, which show that this design can accommodate from 162 to 800 passengers. Nonetheless, challenges exist in ensuring the overall structural integrity of the BWB design and effectively integrating a hydrogen-powered SOFC/GT propulsion system.

Regarding the environmental impacts of hydrogen-powered aircraft, a significant advantage is that the only byproduct of using pure hydrogen as a fuel source is water vapor. Although there are some thermal NOx emissions due to the oxidizer and fuel cell exit flow temperature, the overall impact is considerably lower compared to Jet-A powered aircraft. Notably, NOx emissions for the hydrogen BWB-365 are 99.6% lower than those for a kerosene-powered B777-300ER, and 98.9% lower for the hydrogen BWB-162 compared to a conventional B737-800. Moreover, despite hydrogen fuel

157

aircraft have higher emissions index per kg of fuel, the BWB-365 results in 6% lower H_2O emissions than the B777-300ER and the BWB-162 18% higher than the B737-800.

In conclusion, hydrogen BWB designs show promising advantages in fuel efficiency, significant synergy with hydrogen tanks and promising scalability. Results indicate a positive trend when scaling down from a 365-passenger to a 162-passenger layout, with weight per passenger reduced by approximately 31.8%. Further research is required to address the structural complexities and integration challenges associated with these innovative propulsion systems integrations and configurations. One disadvantage of the SOFC/GT powertrain is the longer start-up time required by the solid oxide fuel cell stack compared to conventional turbojet engines, which may be overcome by significant thermal mass and reasonable amounts of insulation, which was not assessed in the current work. Despite the slow start-up time, fuel cell stacks typically have a lower failure rate in terms of electricity production and offer a long operational lifetime. Electrifying the aircraft also allows for distributed propulsion which which provides aerodynamic and environmental advantages. Nevertheless, leveraging the characteristics of BWB designs, hydrogen fuel, and fuel cell technology, while addressing the associated challenges, will enable the aviation industry to progress towards more sustainable and efficient aircraft designs.

6. Comparative Evaluation of Retrofit Options for Hydrogen Adoption Across Different Aircraft Categories

To understand how hydrogen propulsion can be effectively integrated into aircraft, it is crucial to examine its application across different aircraft categories, each presenting unique challenges and opportunities. Regional turboprop aircraft, for instance, typically require less power than larger turbofan-powered aircraft and operate at lower altitudes over shorter distances. These characteristics make them particularly suitable for hydrogen retrofitting, especially using technologies like PEMFC and battery-electric, which have not been explored in previous chapter retrofits due to technical limitations with the constant range approach. This chapter focuses on evaluating the potential for hydrogen adoption in regional turboprops and the conclusive comparison of all aircraft analyzed in previous chapters, considering their distinct operational profiles and the specific retrofit strategies that may enable sustainable aviation across various segments. Conclusive results, such as kilograms of hydrogen per passenger per kilometer, are highlighted, offering insights into the efficiency and viability of hydrogen propulsion across different aircraft categories. From this, it is observed that generally, larger aircraft make retrofitting easier and allow for more flexibility, but not necessarily in terms of mass change or fuel consumption in comparison to conventional aircraft.

6.1. Simplified Retrofit Analysis of ATR42-600 (Regional Airliner)

The ATR 42-600 serves as a compelling case study for analyzing the potential of hydrogen retrofitting in regional aircraft, specifically turboprops. These aircraft generally consume less energy, require less power, and operate at lower altitudes compared to their larger counterparts, making them theoretically

159

more suitable for hydrogen retrofit applications. This section utilizes the same methodology and assumptions outlined in Chapter 3 to evaluate the feasibility of a hydrogen retrofit for the ATR 42-600.

Table 6.1 summarizes the key parameters of the ATR 42-600, including a mechanical power of 2160 shp, maximum cruise speed of 611 km/h, and a range of 703 nautical miles. These parameters establish the baseline characteristics of the aircraft for comparison with hydrogen retrofit configurations [1].

Table 6.1   Conventional ATR 42 Parameters

Parameter	Value
Mechanical power (shp)	2160
TSFC (g/kNs)	25
Max cruise speed (km/h)	611
Limit Mach	0.45
Max range (nmi)	703
Max operating altitude (ft)	25,000
Cabin length (m)	14.72
Cabin height (m)	1.90
Cabin width (m)	2.56
Cargo compartment volume (m^3)	4.4

Table 6.2 shows the fuel consumption for the ATR 42-600 in its conventional configuration. The initial weight is 18,561 kg, with a fuel weight of 5,670 kg for typical maximum range operations. This provides a reference for evaluating the reduction in fuel weight with a hydrogen retrofit.

Table 6.2   Conventional ATR 42 Fuel Consumption

Cruise	Jet Fuel
W_{initial}	18,561 kg
W_f	12,891 kg
W_{fuel}	5,670 kg

A Proton Exchange Membrane Fuel Cell (PEMFC) system is considered for the hydrogen retrofit due to its efficiency and power density. The parameters for this system, shown in Table 6.3, include a power density of 2.1 kW/kg and a cycle efficiency of 60% at ground level, which are suitable for retrofitting within the ATR 42-600.

Table 6.3   PEMFC System Parameters at Ground Level

Parameter	Value	Unit/Description
PEMFC Power Density (kW/kg)	2.1	BSC PEMFC SOA
PEMFC Volumetric Density (kW/L)	3.1	kW/L
PEMFC Exit Temperature	70	°C
Motor Power Density	7.064	kW/kg
Battery Volumetric Density	0.67	kWh/L
Battery Gravimetric Density	0.265	kWh/kg
GT-PEMFC Cycle Efficiency	60%	Ground-level efficiency

The parameters for an alternative battery-electric configuration are provided in Table 6.4. This configuration assumes a total mass of 18,638.73 kg, with a battery capacity of 1.127 MWh and a power rating of 3.22 MW. The assumptions made here are conservative, aligning the lithium-ion battery specifications with those used in previous SOFC/GT/Battery and PEMFC/Battery systems. These assumptions reflect a cautious approach, considering current lithium-ion battery technology rather than more futuristic advancements. Despite recent improvements, lithium-ion batteries have reached a performance plateau, primarily constrained by the limits of current materials and chemistries. This plateau suggests that further significant gains in energy density or power output will likely require breakthroughs in new battery technologies or materials, such as solid-state batteries or lithium-sulfur chemistries [129, 130]. Consequently, these conservative assumptions ensure a realistic evaluation of the battery-electric retrofit potential for the ATR 42-600, acknowledging the

161

current state of battery technology and its limitations.

Table 6.4   Parameters for Battery Retrofit of ATR 42-600

Parameter	Value	Unit
Total Mass	18,600	kg
Battery Power Rating	3.22	MW
Battery Capacity	1.127	MWh
Motor Power Density	7.064	kW/kg
Battery Volume Density	0.67	kWh/L
Battery Gravimetric Density	0.25	kWh/kg
Battery Power Density	1	kW/kg
Motor Energy Density	7	kWh/kg
Battery Power-to-Energy Ratio	2	-
Max Power	3,222	kW
Battery Energy Design	1,092.23	kWh
PMAD Density	20	kW/kg
Cable Weight (Nickel-Plated Aluminum)	0.00324	kg/Amp/m
Range (Cruise)	150	nmi
Number of Passengers	30	-

The PEMFC-powered aircraft experiences a significant reduction in seating capacity due to the absence of a compressor, which reduces efficiency by 0.5% to 1% per 1,000 feet, leading to an overall power loss of 18% at 13,000 feet [22]. This lower efficiency necessitates an increased hydrogen volume, further decreasing seating capacity. Despite more commercial progress, PEMFC

technology has a lower volumetric density than SOFCs at the stack level, and recent advancements suggest a plateau in PEMFC development while SOFC technology continues to evolve, driven mainly by higher operating temperatures [165]. For example, a PEMFC-retrofitted ATR 42-600 is 6.2% lighter (17,453.44 kg vs. 18,600.05 kg original) but suffers a 46% seating reduction (26 seats from 48). In contrast, the SOFC/GT variant, 4.5% lighter (17,769.62 kg vs. 18,600.05 kg), reduces seating by 29% (34 seats from 48). Meanwhile, the hydrogen combustion variant achieves a 12% weight reduction (16,372.53 kg vs. 18,600.05 kg) but decreases seating by 38% (30 seats) due to hydrogen storage occupying 45% of the available volume. These trade-offs highlight the challenges of integrating hydrogen power systems into current aircraft designs, balancing weight, storage, and capacity impacts.

While a fully battery-electric retrofit of the ATR 42-600 is technically possible, as shown in Table 6.4, it results in a significantly reduced range and passenger capacity. Using the battery parameters specified in Table 6.3 and assuming a 95% efficiency for the electrical system, the analysis included key components such as the aircraft's empty weight, passenger and baggage weight, mass of batteries, motors, Power Management and Distribution (PMAD) system, cryocooler, and cables. The results demonstrate that, although the aircraft can remain within the Maximum Takeoff Weight (MTOW), it cannot maintain the same range as the conventional version. With a fully battery-electric configuration, the aircraft achieves only 278 km (approximately 150 nautical miles) of range, which is considerably lower than its kerosene-powered counterpart. Moreover, the passenger count is reduced to 30, as it is not possible for the aircraft to stay below MTOW with the conventional passenger count. This conclusion aligns with the prevailing literature on retrofitting the ATR 42-600, where most studies emphasize hybrid-electric configurations rather than fully battery-electric options. Hybrid-electric powertrains are considered more viable for regional aircraft due to the limited energy density of current battery technologies. The limitations of battery-electric designs in commercial applications have led almost all companies, outside of those focused on Unmanned Aerial Vehicles (UAVs), to shift towards hybrid powertrains to balance energy storage, range, and payload capacity [166]. The literature further suggests that hybrid configurations allow for a more feasible integration

of battery systems by combining them with conventional or alternative power sources, effectively overcoming the weight and range limitations that currently restrict fully battery-electric options for larger regional aircraft like the ATR 42-600. Our analysis shows that a 1.1 MWh battery is the maximum capacity that can be installed without exceeding the MTOW, compared to the 30.58 MWh needed to achieve the same range with the same number of passengers. This retrofit results in approximately 30 minutes of cruise capability (or less) compared to the 3.12 hours of cruise time required for the full-range flight estimates in the remaining retrofit scenarios.

The different configurations for hydrogen tanks in the ATR 42-600 aircraft, as shown in Figure 6.2, significantly impact seating capacity and weight based on a 30-inch economy seating standard. The SOFC/GT retrofit (b) supports 34 seats. This configuration uses a back tank with a length of 5.925 meters, a volume of 15.11 m^3, and a total mass of 289.37 kg, aiming to balance the tank volume while minimizing the reduction in passenger seating.

The PEMFC retrofit (c) features a larger back tank with a length of 7.29 meters, a volume of 19.01 m^3, and a mass of 365.82 kg. This setup results in a weight ratio relative to fuel weight (Wtank/Wfuel) of approximately 23.9%. Due to the increased tank size, the seating capacity is reduced to 26 seats under the 30-inch economy seating standard.// The hydrogen combustion retrofit (d) accommodates 30 seats and incorporates a combination of a front tank with a length of 7.58 meters and a volume of 19.84 m^3, and two back tanks with lengths of 2 meters and 1.6 meters and volumes of 1.32 m^3 and 0.40 m^3 respectively. The total mass is 382.07 kg for the front tank, 24.88 kg for the first back tank, and 7.63 kg for the second back tank, with weight ratios (Wtank/Wfuel) of around 24.0%, 0.23%, and 0.24% respectively. Compared to the standard configuration (a), which provides 48 seats, these retrofits highlight the trade-offs in seating capacity and weight management necessary when integrating hydrogen storage solutions into the aircraft design.
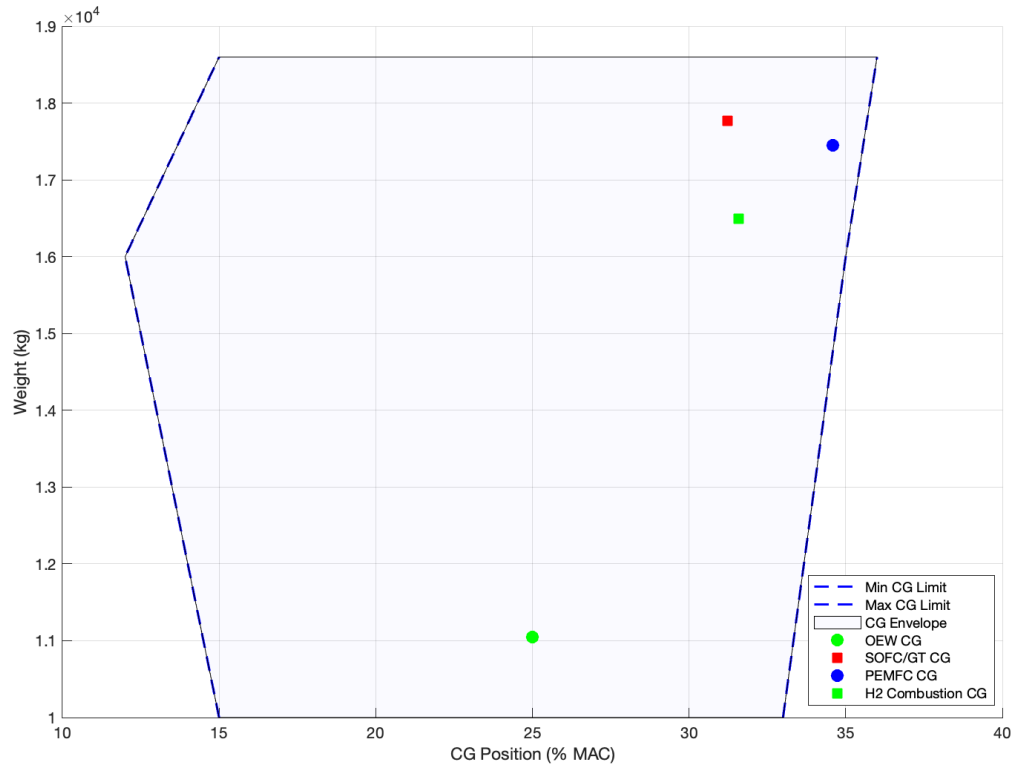
Fig. 6.1   CG Envelope for ATR 42-500/600 Retrofitted with Hydrogen Tanks, Fuel Cell, and Passengers. The plot shows the minimum and maximum CG limits, the original CG, and the new CG positions after retrofit, including PEMFC and H2 Combustion CG points.

The analysis shown in Figure 6.1 evaluates the center of gravity (CG) shift for the ATR 42-600 aircraft retrofitted with hydrogen tanks, fuel cells, and additional passenger accommodations. Using the mean aerodynamic chord (MAC) length of 2.65 meters [167] and a Leading Edge of the Mean Aerodynamic Chord (LEMAC) located at 10.025 meters from the front of the plane (datum). The new CG positions for all configurations are found to be within the acceptable limits defined by the CG envelope for the aircraft, as cited in [168], The SOFC/GT, PEMFC, and H2 combustion CG positions are within the acceptable range, indicating compliance with stability requirements, with each configuration showing a slightly different mass distribution, as seen in Figure 6.2. Overall, the results support the feasibility of these retrofits.

To calculate the CG position in terms of the percentage of the Mean Aerodynamic Chord (MAC), the following equation is used:

$$\text{Percent of MAC} = \left(\frac{\text{CG} - \text{LEMAC}}{\text{MAC}}\right) \times 100 \qquad (6.1)$$

Where:

- CG is the center of gravity position measured from the front of the plane (datum).

- LEMAC is the Leading Edge of the Mean Aerodynamic Chord.

- MAC is the Mean Aerodynamic Chord.
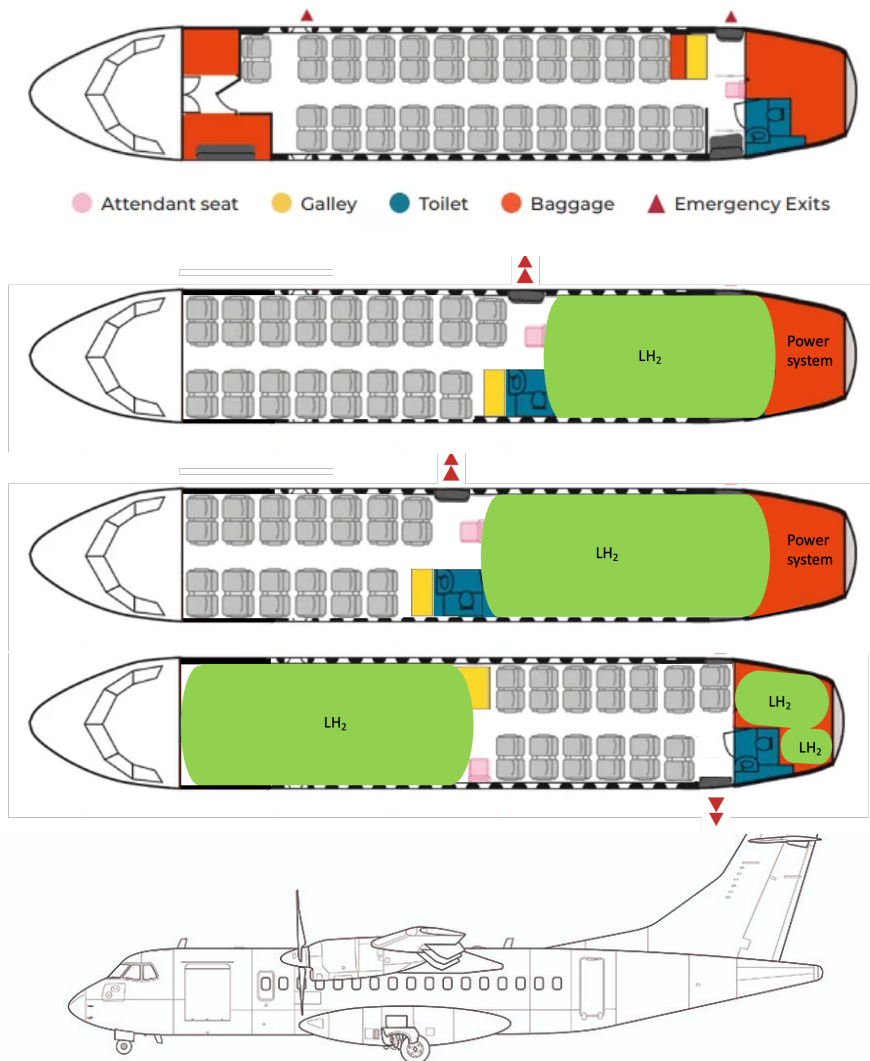
Fig. 6.2   ATR 42-600 layouts: (a) Standard configuration (48 seats), (b) Hydrogen SOFC/GT retrofit (34 seats), (c) Hydrogen PEMFC retrofit (26 seats), (d) Hydrogen combustion retrofit (30 seats), (e) external schematic. [1, 2]
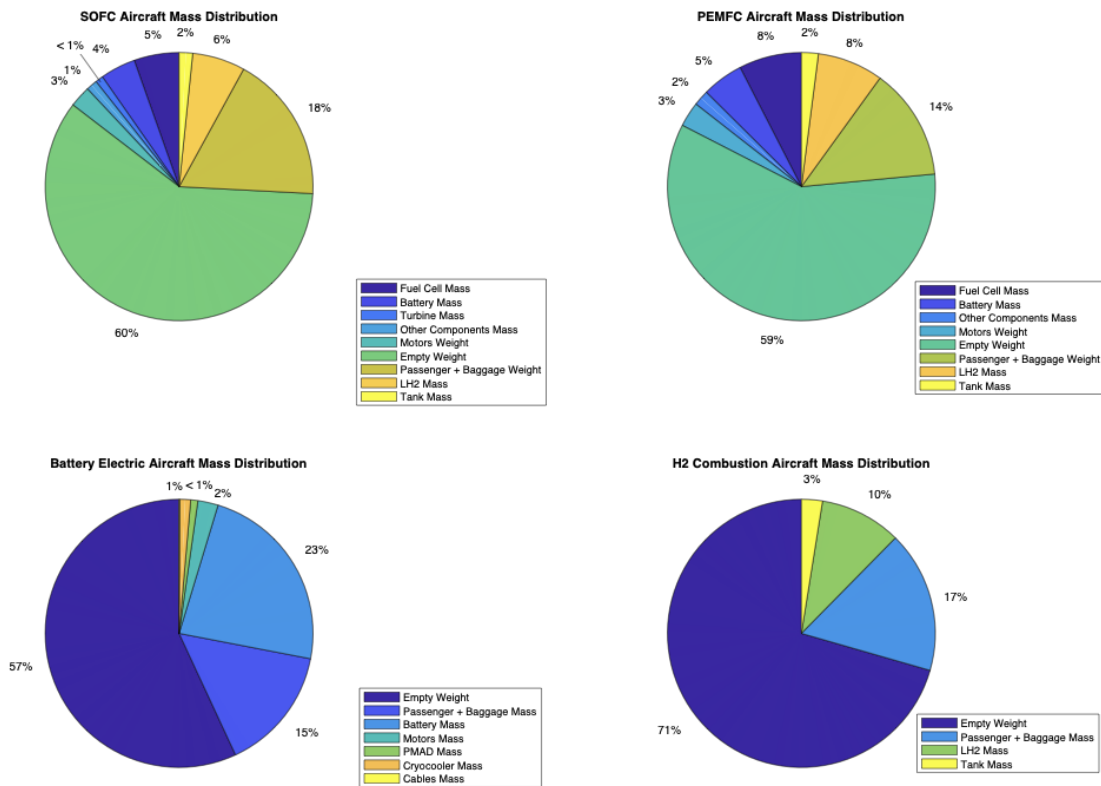
Fig. 6.3 Mass distribution comparisons for different ATR 42-600 configurations: (1) SOFC Hybrid Aircraft, dominated by empty weight, passenger load, and added fuel cell, battery, and turbine mass; (2) PEMFC Hybrid Aircraft, with larger fuel cell, battery mass, and increased LH2 storage; (3) Battery Electric Aircraft, dominated by empty weight and battery mass; (4) Hydrogen Combustion Aircraft, primarily characterized by empty weight, passenger load, and contributions from LH2 and tank mass.

Figure 6.3 illustrates the mass distribution for different ATR 42-600 hydrogen-powered configurations. The SOFC hybrid aircraft shows a significant contribution from passenger and baggage weight (17.8%), with notable percentages attributed to the fuel cell (5.4%), battery (4.3%), and LH2 storage masses (6.4%). The PEMFC hybrid aircraft also reflects a substantial passenger and baggage weight (14%), along with contributions from the fuel cell (7%), battery (5.0%), and LH2 storage masses (7.9%). The Battery Electric Aircraft's mass is primarily influenced by the battery (23.3%), demonstrating the substantial weight of electrical energy storage, followed by the empty weight (56.9%) and passenger and baggage weight (15.0%). In contrast, the Hydrogen Combustion Aircraft

is characterized by a higher empty weight (70.5%), a significant passenger load (17.1%), and LH2 mass (9.8%), with a relatively smaller impact from the tank mass (2.5%). These differences highlight the distinct weight distributions required by each powertrain type.

6.1.1. Comparisons with Conventional Aircraft

Table 6.5   Combined Aircraft Configurations with Fuel Weights

Aircraft	Max Power (MW)	MTOW (kg)	Range (km)	Passengers	Fuel Weight (kg)
Cessna Citation XLS+ (Kerosene)	2.3	9,223.35	3,889.2	9	1077
Cessna Citation XLS+ (H2-Combustion)	2.3	8,685.22	3,889.2	6	401.7
Cessna Citation XLS+ (H2-SOFC)	2.3	9,187.86	3,889.2	6	271
Cessna Citation S550 II (Kerosene)	1.3	6,849	2,872	8	2267
Cessna Citation S550 II (Hydrogen SOFC)	1.3	6,195	2,872	4	570
ATR42-600 (Kerosene)	3.22	18,600.05	1,302	48	4500
ATR42-600 (H2 Combustion)	3.22	16,372.53	1,302	30	1612
ATR42-600 (H2-SOFC)	3.22	17,769.62	1,302	34	1132
ATR42-600 (PEMFC)	3.22	17,453.44	1,302	26	1423
ATR42-600 (Battery Electric)	3.22 (1.1 MWh)	18,600.05	278	30	-
B737-800 (Kerosene)	10.74	70,307	4,474	162	11859
BWB-162 (H2-SOFC)	11.91	78,687	4,474	162	2024
T&W-162 (H2-SOFC)	10.2	68,328	4,474	162	2838
B777-300ER (Kerosene)	77.96	334,211	12,171	365	137522
BWB-365 (H2-SOFC)	59.9	260,403	12,171	365	17946
T&W-365 (H2-SOFC)	53.1	233,698	12,171	365	23229

Table 6.5 showcases the summary of all sized and retrofit results analyzed in the dissertation. As seen, all cases are retrofitted using a constant range approach, with the exception of the battery-electric ATR42-600 due to technical limitations. Moreover, the data highlights that the most significant compromise across all hydrogen-powered configurations is the reduction in passenger capacity. For smaller jets, such as the Cessna Citation series, the shift to hydrogen power—whether through combustion or SOFC—results in a noticeable decrease in passenger count to accommodate the additional mass and volume required for hydrogen storage and power systems. For the ATR42-600,

while each hydrogen configuration maintains the original range, this comes at the expense of a reduced number of passengers, particularly in the PEMFC and battery-electric variants. In contrast, for larger aircraft like the B737-800 and B777-300ER, hydrogen-powered versions—both T&W and BWB configurations—manage to sustain the same range and passenger capacity, demonstrating the feasibility of hydrogen retrofitting in larger aircraft, albeit with significant design modifications.
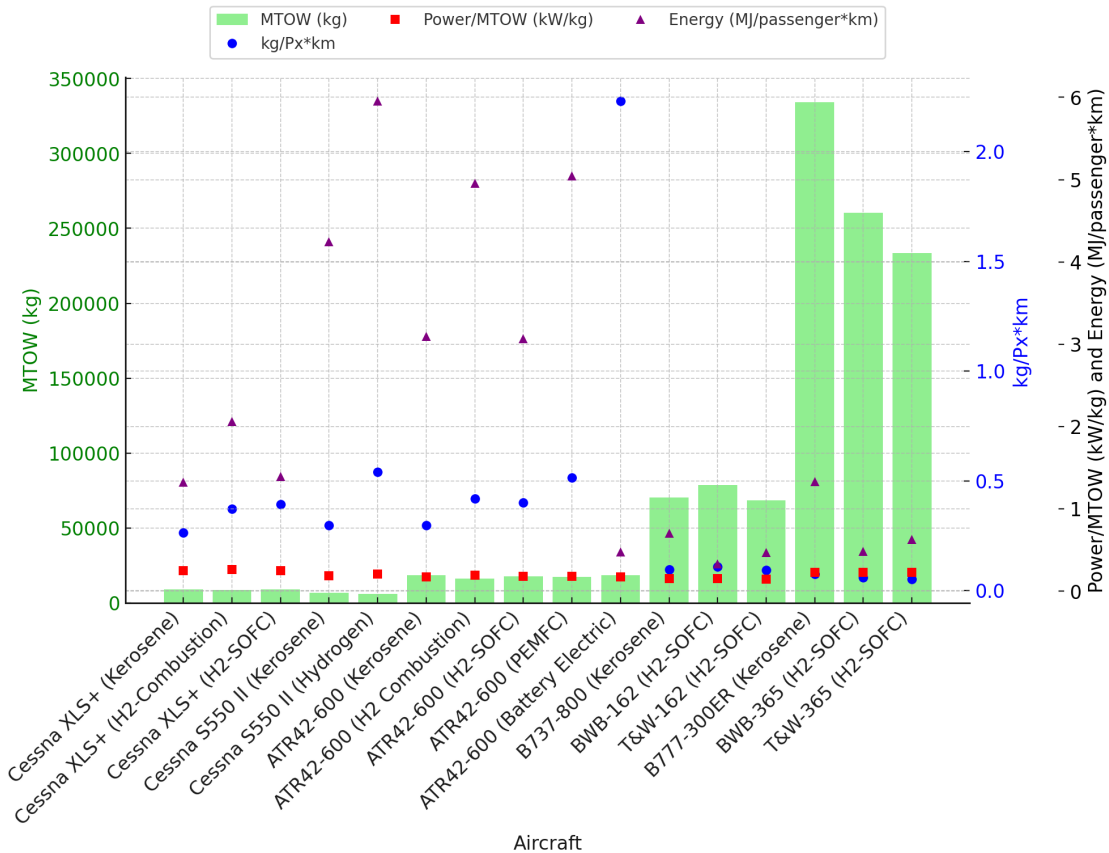
Fig. 6.4 Clustered chart comparing aircraft configurations. Bars represent MTOW, while dots show kg/Px*km, Power/MTOW, and Energy per passenger*km. Highlights weight efficiency, power-to-weight ratio, and energy use across kerosene and hydrogen-powered aircraft.

Figure 6.4 compares various aircraft configurations, highlighting key metrics: Maximum Takeoff Weight (MTOW), MTOW per passenger*km, and Power/MTOW. Hydrogen-powered configurations demonstrate varied impacts on MTOW, such as the ATR42-600 (H2 Combustion) at 16,372.53 kg compared to 18,600.05 kg for its kerosene counterpart, with trade-offs like an increased MTOW

per passenger*km (e.g., 0.42 and 0.40 kg/passenger*km for the ATR42-600 H2-combustion and H2-SOFC, respectively, in comparison to the conventional ATR at 0.30 kg/passenger*km). The Power/MTOW ratio also varies significantly; smaller hydrogen aircraft, like the Cessna Citation XLS+ (H2-SOFC) at 0.25 kW/kg, exhibit relatively high values compared to larger models such as the T&W-365 (H2-SOFC) at 0.23 kW/kg. In contrast, the BWB-365 (H2-SOFC) shows a slightly higher ratio of 0.23 kW/kg, while the BWB-162 (H2-SOFC) demonstrates the lowest value of 0.15 kW/kg, indicating different performance efficiencies and trade-offs across aircraft types and fuel configurations.

7. Techno-Economic Assessment of Hydrogen Adoption in Airport Infrastructure

Parts of this chapter, in parts or in whole, are co-authored by:

Rezaei, Sajjad, Khaled Alsamri, Elio Simeoni, Jacqueline Huynh, and Jack Brouwer. "Techno-Economic Assessment of Green Hydrogen Infrastructure Implementation: A Case Study for Los Angeles International Airport (LAX), USA." *246th ECS Meeting*, ECS, 2024 (unpublished manuscript).

This chapter outlines a comprehensive methodology for evaluating various scenarios related to the transformation of hydrogen-powered airports, using Los Angeles International Airport (LAX) as a case study. In 2023, LAX accommodated approximately 75 million passengers [169]. Analysis of emissions data, including particle number (PN), black carbon, and fine particulate matter ($PM_{2.5}$), indicates that LAX significantly contributes to local pollution levels, surpassing the emissions from the nearby freeways [170]. Consequently, this study aims to facilitate LAX's transition to sustainable operations by conducting a techno-economic assessment of the implementation of both on-site and off-site green hydrogen infrastructure.

7.1. Methodology for Transforming and Evaluating Airport Fuel Supply to Green Hydrogen

7.1.1. Framework

Figure 7.1 illustrates the proposed hydrogen supply chain model for LAX. The framework encompasses three main components: Inputs, H2 Infrastructure Design and Cost Analysis, and Outputs. The Inputs include the assessment of energy resources availability, future demand scenarios for LAX in 2030 and 2050, and relevant financial and environmental data. The H2 Infrastructure Design

and Cost Analysis phase involves mapping the availability and dynamics of clean energy resources, appropriately sizing the storage and transmission and distribution assets, conducting a levelized cost analysis (LCA), and evaluating emissions during hydrogen production, transmission, and storage processes. The final Outputs section provides a green hydrogen ecosystem layout for LAX, including the LCOH and its global warming potential (GWP). This structured approach aims to systematically evaluate the integration of hydrogen as a sustainable energy source for airport operations, ensuring economic viability and environmental sustainability.
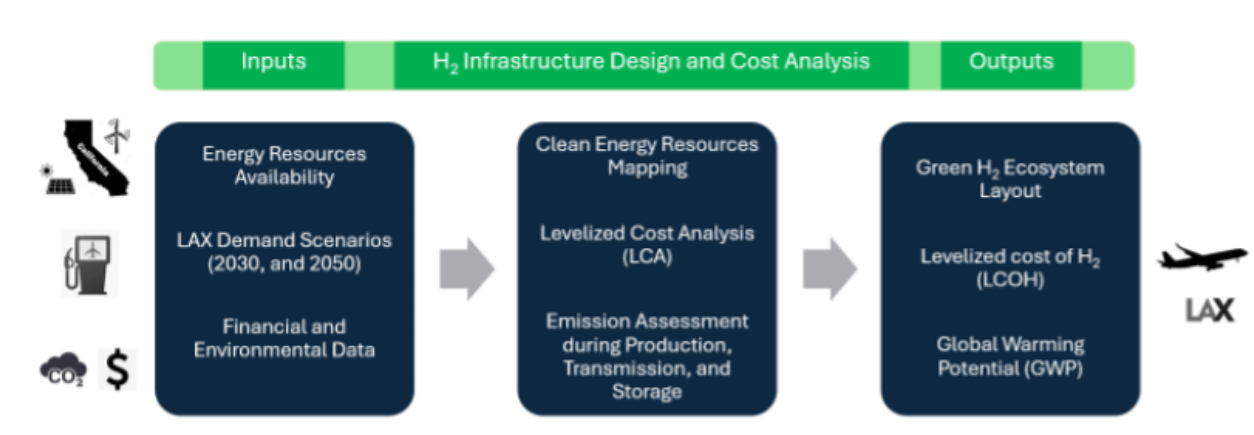
Fig. 7.1   Methodology framework proposed for the provision of green hydrogen at LAX

7.1.2. Economy and Environmental Analyses

Levelized cost analysis can be employed to assess and compare the economic feasibility of hydrogen technologies. LCOH is the levelized cost of producing a unit of hydrogen ($/kg). Thus, the purpose of this study is to calculate LCOH based on various supply chain pathways, which are developed and described in section 2.8. LCOH can be determined by taking into account the plant's lifespan (N) and using the following equations[171, 172]:

$$\text{LCOH} = \frac{\text{Total Annual Cost}}{\text{Annual Hydrogen Production}} = \frac{\left(\sum_i \left(\text{CAPEX}_i \times \text{CRF}_i + \text{OPEX}_i\right)\right)}{m_{H_2}} \quad (7.1)$$

$$\text{CRF} = \frac{d \cdot (1+d)^N}{(1+d)^N - 1} \tag{7.2}$$

Where:

Table 7.1   Definitions of Terms

Term	Definition
i	Index of the section (production, transmission, liquefaction, storage, etc.) involved in the HSC.
CAPEX_i	Capital cost of technology (balance of plant, electrical infrastructure and interconnection, installation and indirect costs, owner's costs, and site and land costs, etc.).
OPEX_i	Operation and maintenance cost of a particular technology (fixed costs including administrative fees, administrative labor, insurance, operating labor, taxes, etc.; project management; maintenance costs; variable cost components; maintenance components; and replacement costs).
m_{H_2}	Annual hydrogen mass produced (kg).
CRF_i	Capital recovery factor of component i, which transforms the investment cost into an annual payment.
d	Discount rate.
N	Number of periods (years) over which the project will operate.

By combining the annuity technique with operating and maintenance costs, a hydrogen project's capital costs are effectively transformed into yearly payments. This annuity technique is intended to facilitate cost comparisons between technologies with varying lifespans [173]. The discount rate significantly affects the LCOH [174], and can be obtained from the Weighted Average Cost of Capital (WACC) reflecting the required return on the invested capital [173]. Discount rates can vary based on the type of investment, location, and technologies involved in the renewable energy sector [175]. The average discount rate applied to renewable energy projects ranges from 3% to 10% [176–180]. For this work, a discount rate of 8% is assumed, considering the technological risks associated with green hydrogen production projects for the aviation industry. Table 7.2 provides a summary of all cost items considered in the LCOH calculations.

In this study, hydrogen is assumed to be produced solely using renewable electricity from solar and/or wind primary energy. Therefore, hydrogen is the only gas whose leakage from the supply chain sections can have global warming implications. H_2 is considered an indirect climate forcer, contributing to global warming by reacting with OH radicals (leading to an increased methane lifetime in the troposphere), producing more ozone (in the troposphere), and generating stratospheric water vapor [181]. To quantify emitted hydrogen radiative forcing implications, GWP, a metric used to compare the radiative forcing effects of various trace gases to those of CO_2 with the units of $\frac{kg_{CO_2}}{kg_{H_2,emitted}}$, is commonly employed. The GWP of a gas is estimated by comparing its total absorbed energy over a range of time horizons, such as 20, 50, 100, or 500 years, to the total energy that can be absorbed by an equivalent mass of CO_2 as the index gas [182]. In this work, the most typically applied 100-year time horizon is selected for converting hydrogen emissions to a common scale of CO_2 equivalent. This approach provides a perspective on the long-term (100-year) global warming impact of the hydrogen lifecycle for meeting LAX's demand. To estimate the CO_2 equivalent forcing caused by hydrogen leakage across the hydrogen supply chain, a GWP_{100} of 11 as reported by Warwick et al. [181] is adopted. This GWP_{100} value is reasonable within the literature-reported range of 8 to 12.8 [183, 184]. Thus, by multiplying the hydrogen emissions from each component (ranging from electrolysis to transport and end-use at LAX) by the GWP_{100} of 11 $\frac{kg_{CO_2}}{kg_{H_2,emitted}}$, the CO_2 equivalent for every stage in the hydrogen supply chain and the total CO_2 equivalent radiative forcing for each of the proposed supply scenarios is determined.

7.1.3. Renewable Energy Resources Availability

Providing renewable electricity for hydrogen production to meet LAX's fleet consumption requires a vast amount of solar and wind energy resources on a scale of 600-2500 MW. Due to area constraints and airport policies, on-site solar and wind fields at LAX are not feasible. Therefore, capacity maps can be used to identify regions with high renewable energy potential around LAX. California ranks among the top states in the nation regarding solar resources, with the average year-round solar energy incident on the surface estimated to be between 5 and 6.15 kWh/m²/day, equivalent to 208 to 256 W/m² [185]. The significant solar energy capacity is approximately situated in San Bernardino, Riverside, San Diego, and Imperial counties, all within a roughly 500 km radius of LAX.

In terms of wind energy capacity, there is the possibility of having both onshore and offshore facilities in the LAX vicinity. Considerable wind resources are available off the coast of California, showing some significant "outstanding" and "excellent" wind resources (wind speed at 50 m between 7.5 and 8.8 m/s) near LAX, as well as onshore wind potential in regions northeast of the airport, between Bakersfield and Barstow (Tehachapi Mountains), stretching to the Nevada border. These areas are considered to have good-to-outstanding wind potential, capable of generating wind power in the range of 400 to 800 W/m² for electrolysis to produce hydrogen for LAX.

7.1.4. Hydrogen Production

Hydrogen can be produced from a variety of pathways, involving fossil fuels (for instance, steam methane reforming (SMR) of natural gas), biomass, and water electrolysis. The environmental consequences and efficiency of hydrogen generation are contingent upon the production method. This work aims to study hydrogen production through electrolysis, specifically using renewable electricity derived from solar and wind power sources (i.e., clean zero-emissions production, often dubbed green hydrogen). Currently, alkaline electrolyzers (AEL) and proton exchange membrane (PEM) electrolysis technologies are most commonly used for water electrolysis. These contribute

176

only around 4% of worldwide hydrogen demand, while the vast majority of hydrogen production is from SMR of natural gas [186]. Hydrogen production through AEL technology is becoming the most economically attractive solution due to its technological maturity, sustainability, and low cost for industrial applications compared to PEM electrolysis systems [187]. Both electrolysis technologies rely on direct current (DC) to split water [188]. To transmit utility-scale electricity over longer distances, either high voltage alternating current (HVAC) cables or high voltage direct current (HVDC) cables can be employed, depending upon the distance. For shorter distribution lengths (below 200 km for onshore and over 60 km for the subsea case), HVAC is preferred due to ease of integration with the electric grid, although HVAC has higher electrical transmission losses compared to HVDC [189]. In this work, the average costs of electricity transmission via HVDC and HVAC are normalized per kilometer, as shown in Table 7.2.

After electrolysis, hydrogen must be compressed before pipeline injection, with reciprocating piston compressors recommended for handling high hydrogen flow rates [190]. The techno-economic parameters for electrolysis and compression stages are detailed in Table 7.2. The costs for electrolysis systems include stacks, cooling, drying, control, and replacement (20% of CAPEX) but exclude compression [53, 178]. Electrolysis stacks typically produce hydrogen at 30 bar, requiring 13 liters of fresh water per kilogram of H_2 generated [53]. The water must meet high purity standards (resistivity > 1 MΩ·cm) as per ASTM guidelines [191]. Although AELs are less sensitive to water quality than PEMs, both technologies require purified water for long-term stability [192]. Given LAX's proximity to the Pacific Ocean, reverse osmosis (RO) is considered a feasible approach for desalinating seawater for electrolysis.

The electric consumption for AEL and PEM electrolysis systems is projected to be 50 kWh/kgH_2 (66% efficiency) and 45 kWh/kgH_2 (78% efficiency) for 2030 and 2050, respectively (comprising the stack degradation that reduces performance by 3-5% over the course of the lifespan) [53, 177, 193]. As shown in Table 7.2, the techno-economic parameters for both technologies are similar for 2030 and converge by 2050. Both systems face H_2 loss due to crossover through the membrane, leakage,

venting, and purging [194, 195]. With no specific data to differentiate leakage rates, a 3% loss for 2030 and 1.5% for 2050 will be assumed for both technologies.

As mentioned above, the electric power required for the green hydrogen supply to LAX comes from solar and wind farms located around the airport. A microgrid infrastructure (Figure 7.2) is proposed, independent of grid electricity, to produce green hydrogen via electrolysis. The intermittent nature of solar and wind power necessitates the deployment of short- and long-term storage systems to maintain stable electricity. Batteries can serve as a viable short-term storage system, while storing hydrogen is an economic strategy for handling surplus power for long-term periods (seasonal storage). As depicted in Figure 7.2, in the case of a mismatch between the total generated power from renewable resources and the load demand, the battery will charge or discharge first. If the imbalance remains, the hydrogen storage system will come into play. Hydrogen generated from surplus power is stored in above-ground storage tanks. Currently, storing hydrogen in above-ground tanks is costly; however, cost reductions are predicted for this technology, reaching $350/kg H2 by 2050 as shown in Table 7.2.
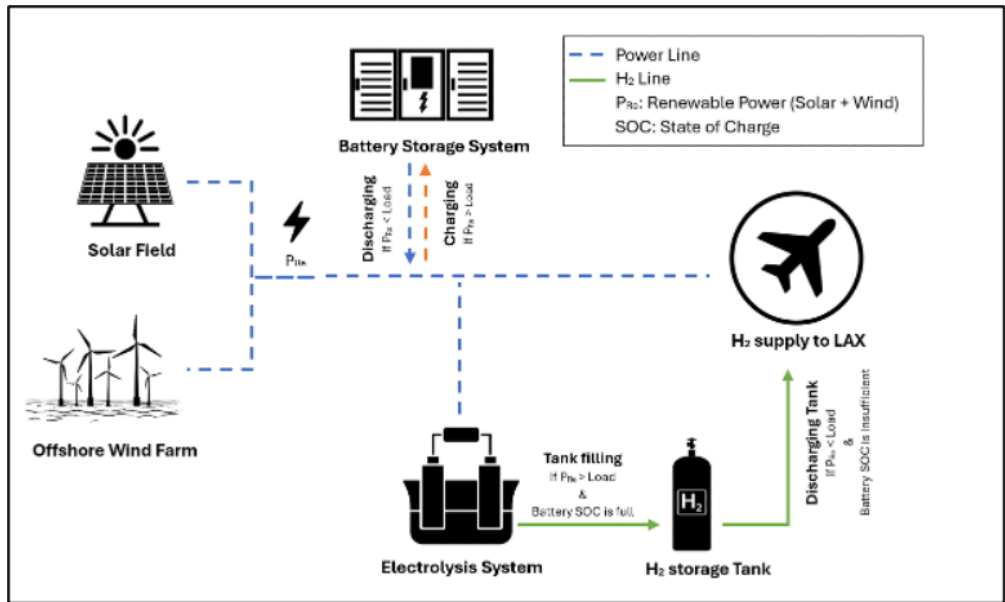

Fig. 7.2   Schematic of the proposed stand-alone microgrid structure based on short-term storage (battery) and long-term storage (hydrogen tank) capabilities

7.1.5. Liquefaction and Storage

The energy density of LH_2 is almost three times larger than that of compressed hydrogen at 350 bar. Although compressed hydrogen has been used in small aircraft, for larger aircraft utilizing LH_2 is more likely due to its higher energy density, particularly for travel over long distances or with heavy payload [196]. Hydrogen is liquefied by cooling it down to below its critical temperature of -240 °C, requiring storage in vacuum-insulated containers that can keep the hydrogen below its boiling point of -253 °C at 1 atm. This cryogenic cooling process results in a significant reduction in the volume of hydrogen, contributing to highly efficient hydrogen storage. Although hydrogen liquefaction is acknowledged as a well-established technology, the high energy consumption and operational costs remain obstacles for widespread adoption in hydrogen liquefaction plants [197]. Many aviation applications certainly merit liquefaction investments and operating costs.

There are two conventional large-scale liquefaction processes: the Hampson–Linde (or Joule–Thomson expansion) and Claude cycles [3]. The Hampson–Linde cycle involves cooling compressed hydrogen gas via heat exchange. After cooling below its inversion temperature, isenthalpic Joule–Thomson expansion through a throttling valve partially liquefies the hydrogen. The remaining gas is re-circulated and mixed with new feed. Liquid nitrogen can be used for precooling, but adjusting pressure is crucial for adequate pre-cooling. The Claude cycle involves isentropic expansion of compressed hydrogen between heat exchangers, reducing temperature before isenthalpic expansion [198]. This process does not require liquid nitrogen and has higher efficiency compared to the Hampson-Linde process. The Claude cycle is preferred for larger LH_2 plants with capacities above 3 tons per day (tpd), due to its higher efficiency and lower operating costs, despite potentially higher investment costs [199]. The electric energy consumption for liquefaction plants is currently around 11 kWh/kgH_2 [200], with a projected reduction to 6 kWh/kgH_2 for large-scale plants in the future [190, 199, 201]. For this work, 11 kWh/kgH_2 is considered for the 2030 case, and 6 kWh/kgH_2 for the 2050 case. The cost parameters for the liquefaction plant are listed in Table 7.2.

This study considers spherical LH_2 storage tanks, similar to those reported by NASA [202]. Located

at launch pad 39B at NASA Kennedy Space Center, Florida, this tank is the largest LH_2 storage facility globally. The evacuated glass bubbles insulation system significantly reduces boil-off to a maximum of 0.048% per day compared to former perlite-based insulation technologies. For future larger LH_2 storage facilities, boil-off gas can be stored in pressurized vessels for further utilization, improving infrastructure efficiency and reducing environmental impact [203].
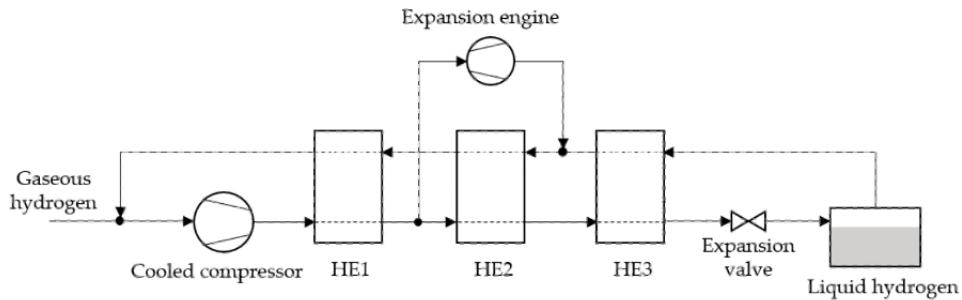

Fig. 7.3   Schematic diagram of the Claude process for liquefying hydrogen [3].

Filling the LH_2 storage tank requires a cryogenic pump. Techno-economic data is limited as most cryopumps are not yet economically mature for large-scale use. For the LCOH calculations, cryopump parameters from Hoelzen et al. [53] are used, as shown in Table 7.2. An electricity consumption of 0.1 kWh per kg of LH_2 flow rate was assumed by Hoelzen et al. [201].

7.1.6. LH_2 Transmission

A gallon of hydrogen has an incredibly small mass of 0.00075 kg (at 1 atm pressure and 0°C), compared to around 2.75 kg for gasoline. Hence, transportation of substantial amounts of H_2 requires either liquefaction or pressurizing it as a compressed gas. Determining the total cost and the most effective distribution option depends heavily on the production location. A large centrally located hydrogen production facility produces more hydrogen for a smaller per-unit cost, but because it is farther away from the point of consumption, transportation costs rise. On the other hand, distribution costs are lower for decentralized production facilities that produce hydrogen locally, but production costs could be greater because of smaller production and liquefaction facilities. Currently, hydrogen can be delivered to the specified application point by cryogenic liquid tanker trucks or

tube trailers, or by pipelines (in particular, for regions with substantial demand) [204]. Gaseous hydrogen transportation might not be necessary if hydrogen is produced on-site or near the airport. In such cases, hydrogen gas is liquefied at or adjacent to the airport. Because of the large hydrogen volume involved, underground pipelines are the preferred form of delivery if gaseous hydrogen supply to an airport is required. With minor modifications to the present infrastructure, it is possible to utilize the natural gas pipelines that are currently in operation [205]. However, in this paper, only new hydrogen pipelines will be considered, and Table 7.2 presents the associated economic data.

7.1.7. LH_2 Distribution at the Airport

LH_2 can be stored in tanks at or close to the airport after H_2 has been liquefied or if H_2 has already been supplied in its liquid state. The main purpose of LH_2 storage is to reduce daily and seasonal fluctuations in fuel use [201]. There are two means to transport LH_2 from the storage facility to the aircraft tank: either using a pipeline dispenser system or refueling trucks [206]. The infrastructure and daily fuel consumption at the airport will determine which distribution system would be preferred. The tanker fleet size might be easily adjusted to meet LH_2 demand. The fuel tanker option entails lower capital costs but comes at the expense of higher operating costs and increased ground traffic congestion near the gate [207]. However, finding sufficient spaces at airports for a larger fleet is a concern due to the limited loading capacity of a single LH_2 refueling vehicle [201]. On the other hand, pipelines and hydrant systems for LH_2 refueling offer better safety and the possibility of faster aircraft refueling, which might result in lower turnaround times. The current pipeline system for Jet A-1 cannot be used because insulation is required to minimize heat input to LH_2 [208]. Installing a pipeline and hydrant refueling system would have higher initial expenditures than employing refueling trucks, but it has an extended operating lifespan of several decades. Thus, the size of the pipeline system, plus its associated costs, is more fixed than it would be for refilling trucks [209]. To connect the pipeline or the LH_2 tank on the refueling truck to the LH_2 storage onboard the aircraft, a dispensing device is required for both refueling modes. The

refueling truck can have this dispensing device placed on it, while for LH_2 pipes, a dispensing truck that runs between aircraft stands is used [208]. Publications on LH_2 pipelines are scarce and this technology has not yet been widely commercialized. In Table 7.2, the 2030 cost parameters for LH_2 pipeline and hydrant systems are based on the work by Hoelzen et al. [201]. For the 2050 values, a 20% cost reduction is assumed in this work. A vacuum-jacketed pipeline was proposed by NASA as an option to transport LH_2 for shorter distances [210]. For the LH_2 pipeline, a minimum diameter of 254 mm is assumed to minimize the friction inside the pipe [201, 211]. According to the literature, the reported LH_2 refueling flow rate ranges between 13 and 20 kg LH_2/s [208, 210, 212], and in this work, a LH_2 flow rate of 20 kg LH_2/s will be used. Hydrant pipelines are widely used at large airports to refuel aircraft. At this rate one of the BWB-365 tanks with 2916 kg LH_2 capacity will refuel in 2 minutes 30 seconds. In contrast, deploying cryogenic hydrant refueling pipelines for LH_2 injection to aircraft tanks does not appear feasible by 2040 due to their nearly five times higher cost compared to conventional Jet-A fueling hydrant infrastructure [213]. Consequently, the near-term viability of refueling aircraft via LH_2 trucks is much higher. However, in this work, the economic differences between these two distribution methods will be assessed. Figure 7.4 summarizes the advantages and disadvantages of using trucks and pipelines for delivering LH_2 to the aircraft refueling sites at the airport.

For both LH_2 distribution cases at the airport, cryogenic pumps are needed to increase the pressure of LH_2. A cryogenic pump could be installed at the storage tank to fill the LH_2 truck and, in the case of LH_2 pipeline, to increase LH_2 flow for aircraft refueling. For the aircraft refueling site, Hoelzen et al. [201] suggested employing trucks that can be equipped with an extra cryopump, and the LH_2 pipeline and hydrant system featuring a mobile dispenser unit comprising a truck and cryopump system. Table 7.2 provides the economic factors related to the distribution of LH_2 at the airport, including the cryogenic pump, dispenser truck, pipeline and hydrant system, and refilling truck.

Brewer suggested a loop design that circulates around the airport to and from the storage tanks to maintain a constant supply rate of LH_2 via underground vacuum-jacketed pipes, covering all the

gates used for refueling hydrogen-powered aircraft [210]. This circulation strategy helps minimize heat leakage into the distribution lines regardless of the LH_2 flow rate, and enables cooling with the liquefaction plant near the storage, thereby lowering the venting of boil-off gas. Previous work has recommended the use of a separate line for recovering boil-off gas that occurs during the refueling of airplanes [201, 210], which is included in our analyses.

Challenges

Ramp traffic and vehicle congestion	Infrastructure Costs
Truck emissions (GHG, AQ)	Maintenance Costs
Potential losses during transfer[4]	Leak detection
Heat source if truck has IC engine (ignition source)	Development timelines & permitting

Advantages

Less infrastructure	Boil-off recovery (up to 96%)
Lower capital cost	Lower operating cost
Commercially available	Potentially safer
Minimal permitting	Faster delivery

Fig. 7.4   Benefits and drawbacks of delivering LH2 hydrogen inside an airport via trucks and pipelines [4]

7.1.8. LAX LH_2 Demand and HSC Scenarios

The magnitude of the potential LH_2 demand that must be provided to LAX must be estimated to design the hydrogen supply network. Amy and Kunycky [54] converted the 2012 yearly demand of 1,500 M gal of jet fuel at LAX (which was reported in [214]) to liquid hydrogen demand, estimating 55 M lit in a 100% hydrogen-based scenario at LAX for the year 2019. In the current work, conservative scenarios with a 5% hydrogen-based fleet for 2030 and a 20% hydrogen-based fleet for 2050 were assumed. These percentages consider all types of commercially operated airplanes at LAX, including regional, single-aisle, medium, and wide-body aircraft and the range of possible alternative fuels available for flight (e.g., batteries, sustainable aviation fuel). Considering the growth in both efficiency and passenger volume projected by the U.S. Energy Information Administration (EIA) [215], these values correspond to a daily demand of 3.3 M lit in 2030 and 16.78 M lit in 2050 at LAX. It should also be noted that, to ensure stability in LH_2 pricing and supply to meet demand,

two days of demand for LH_2 storage is proposed at LAX.

The hydrogen supply chain includes multiple stages, from production, transmission, distribution, and end-use. Factors such as the airport's size, geographical location, and scale of demand will influence the design of the supply pathways [216]. Therefore, creating an efficient and dependable supply network requires a thorough understanding of the system network, the trade-offs between different technologies, and the availability of local resources [217]. Figure 7.5 illustrates various options for supplying LH_2 to LAX. For scenarios A-D, hydrogen is produced from renewable electricity outside of LAX airport, while in scenarios E and F, on-site production is considered. Due to the large estimated LH_2 demand at LAX (3.3 and 16.5 million liters scenarios), transporting compressed gaseous H_2 (GH_2) via road tankers does not seem logical and may result in severe traffic congestion near LAX. Therefore, pipelines and LH_2 trucks are preferably proposed to supply green hydrogen to LAX. The LH_2 supply scenarios are summarized as follows:

- **Supply chain A:**
  - Hydrogen production off-site → off-site liquefaction → transmission via trucks to LAX → LH_2 storage → distribution via LH_2 pipelines for fueling aircraft
- **Supply chain B:**
  - Hydrogen production off-site → off-site liquefaction → transmission via trucks to LAX → distribution via trucks for fueling aircraft
- **Supply chain C:**
  - Hydrogen production off-site → transmission via pipelines to LAX → liquefaction at LAX → distribution via LH_2 pipelines for fueling aircraft
- **Supply chain D:**
  - Hydrogen production off-site → transmission via pipelines to LAX → liquefaction at LAX → distribution via trucks for fueling aircraft
- **Supply chain E:**
  - Hydrogen production on-site → liquefaction at LAX → LH_2 storage → distribution via LH_2

184

trucks for fueling aircraft

- **Supply chain F:**

  – Hydrogen production on-site → liquefaction at LAX → LH$_2$ storage → distribution via LH$_2$ pipelines for fueling aircraft
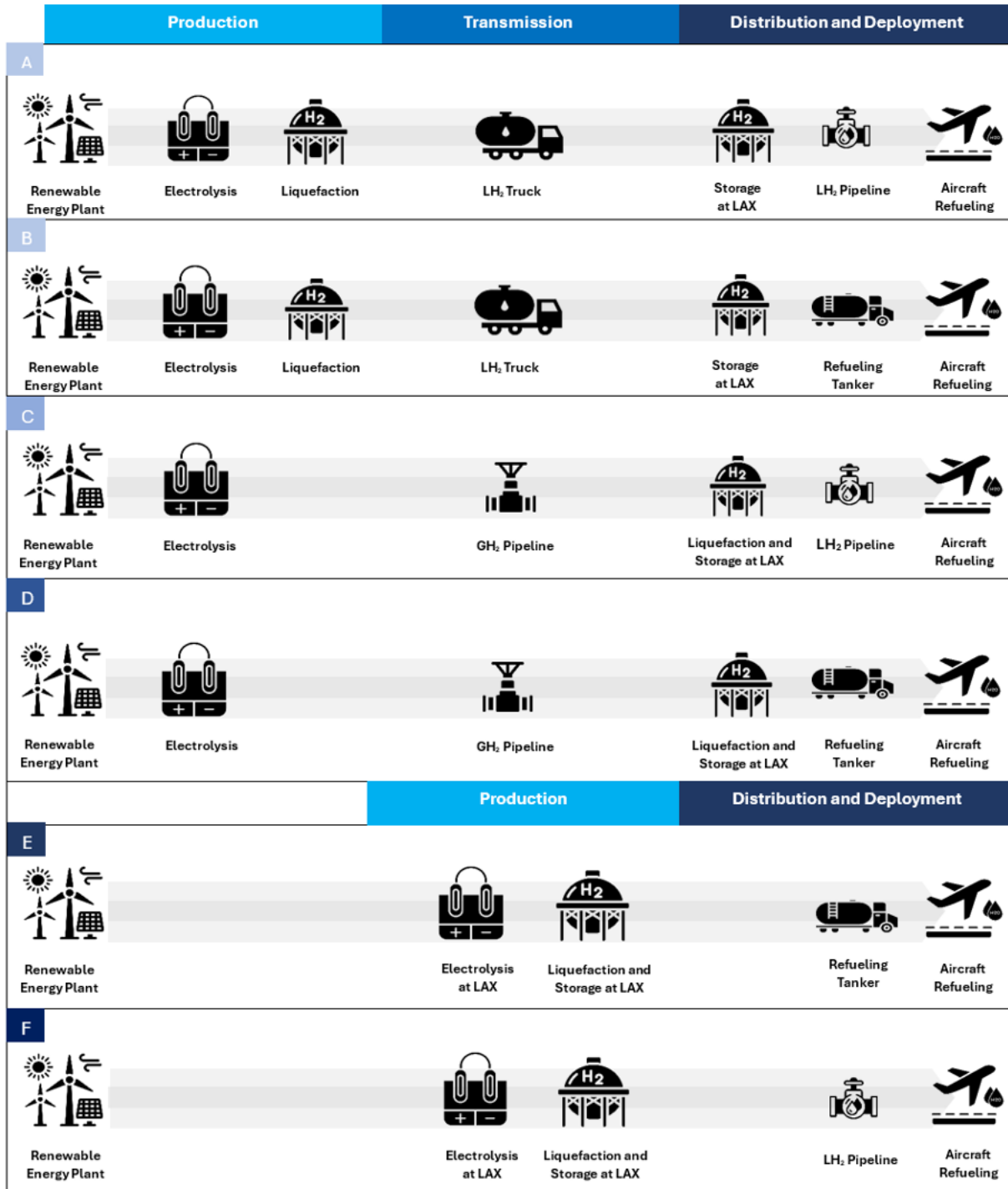
Fig. 7.5 Various renewable H2 supply chain pathways proposed for LAX's transition towards a hydrogen-powered fleet, including A-D) off-site, and E & F) on-site production

Table 7.2 Cost and Performance Parameters for Different Energy Components

Stage	Component	Parameter	Unit	2030	2050	Supply Pathways	Ref.
Production	Utility-scale PV	CAPEX	$/kW	760	632	A-F	[218]
		OPEX	$/kW	16	13		
		Lifetime	Yr	20	30		
	Wind Onshore	CAPEX	$/kW	1150	923	A-F	[218]
		OPEX	$/kW	27	23		
		Lifetime	Yr	20	30		
	Wind Offshore	CAPEX	$/kW	2650	2250	A-F	[218]
		OPEX	$/kW	87	72		
		Lifetime	Yr	20	30		
	Li-ion Battery System	CAPEX	$/kWh	200	100	A-F	[[219], [220]]
		OPEX	$/kWh	5	2		
		Lifetime	Yr	15	15		
		CRF	-	0.12	0.12		
	DC or AC Lines & Substations	CAPEX	Mn $/km	3	4	A-F	[[189], [221], [222]]
		OPEX	$/km	30,000	40,000		
		Lifetime	Yr	50	50		
		CRF	-	0.082	0.082		
	Seawater Desalination	CAPEX	$/m3/day	2500	900	A-F	[[223],[224],[225]]
		OPEX	$/m3/day	25	9		
		Lifetime	Yr	25	30		
		CRF	-	0.094	0.088		
	PEM Electrolysis System	CAPEX	$/kW	780	240	A-F	[53], [177], [178], [194], [195], [226]
		OPEX	$/kW	20	6		
		Lifetime	Yr	10	15		
		CRF	-	0.15	0.12		
		Losses	% of H2 throughput	3	1.5		
	Alkaline Electrolysis System	CAPEX	$/kW	480	240	A-F	[53], [177], [178], [194], [195], [226]
		OPEX	$/kW	12	6		
		Lifetime	Yr	10	15		
		CRF	-	0.15	0.12		
		Losses	% of H2 throughput	3	1.5		
	Gas Compressor	CAPEX	$/kW	1489	1243	A-F	[[53], [190]]
		OPEX	$/kW	30	25		
		Lifetime	Yr	15	15		
		Losses	% of kgH2 feed	0.5	0.4		
	Liquefaction Plant	CAPEX	Mn $/tpd	1.3	0.5	A-F	[[53]]
		OPEX	$/tpd	52000	20000		
		Lifetime	Yr	20	25		
		CRF	-	0.1	0.094		
		Losses	% of kg H2 feed	1	0.5		
Transmission	LH2 Truck	CAPEX	$/unit	700000	640000	A-F	[[53], [227], [228]]
		OPEX	$/unit	84000	77000		
		Lifetime	Yr	20	20		
		CRF	-	0.1	0.1		
	GH2 Pipeline	CAPEX	Mn $/km	3	2.2	C and D	[[53], [190], [229], [230]]
		OPEX	$/km	30000	22000		
		Lifetime	Yr	40	50		
		Losses	% of H2 throughput	0.5	0.4		
Storage	LH2 Storage Tank	CAPEX	$/kgH2	35	26	A-F	[53], [202], [231]
		OPEX	$/kgH2	0.7	0.52		
		Lifetime	Yr	20	30		
		Losses	% of H2 stored/day	0.048	0.03		
Distribution	LH2 Dispenser Truck	CAPEX	$/unit	90000	90000	B, D, and E	[[201]]
		OPEX	$/unit	2700	2700		
		Lifetime	Yr	20	20		
		CRF	-	0.1	0.1		
	LH2 Pipeline and Hydrant System	CAPEX	Mn $/km	10	8	A, C, and F	[[201]]
		OPEX	$/km	300000	240000		
		Lifetime	Yr	40	50		
		Losses	% kgH2 feed and km length	0.175	0.175		
	LH2 Cryogenic Pump	CAPEX	$/kgH2/h	354	264	A, C, and F	[[53], [232]]
		OPEX	$/kW	11	8		
		Lifetime	Yr	10	10		
		Losses	% of H2 throughput	0	0		

a) Assuming a 380 kV double circuit line for 2030 and a 500 kV double circuit line for 2050 (both overhead lines), Right of Way (ROW) cost is not included in the calculations.

b) Assuming reverse osmosis (RO) technology for seawater desalination (electrical energy consumption ≈ 3 kWh/m^3).

c) The estimated amount of electricity used for compression is between 0.7 and 1.0 kWh/kg [200].

d) The truck capacity is 4,300 kg of LH$_2$, OPEX includes the driver's salary, and the trucks are assumed to be fuel-cell powered with a fuel economy of 10 miles per kg of H$_2$ [233].

e) Assuming diameters of 250 mm (10 in) for 2030 and 500 mm (20 in) for 2050, with pressures typically between 30 and 120 bar, and a H$_2$ velocity of 10 m/s to 20 m/s.

f) Spherical tank with an external diameter of 24 m and a storage volume of 4,700 m^3 as reported by NASA.
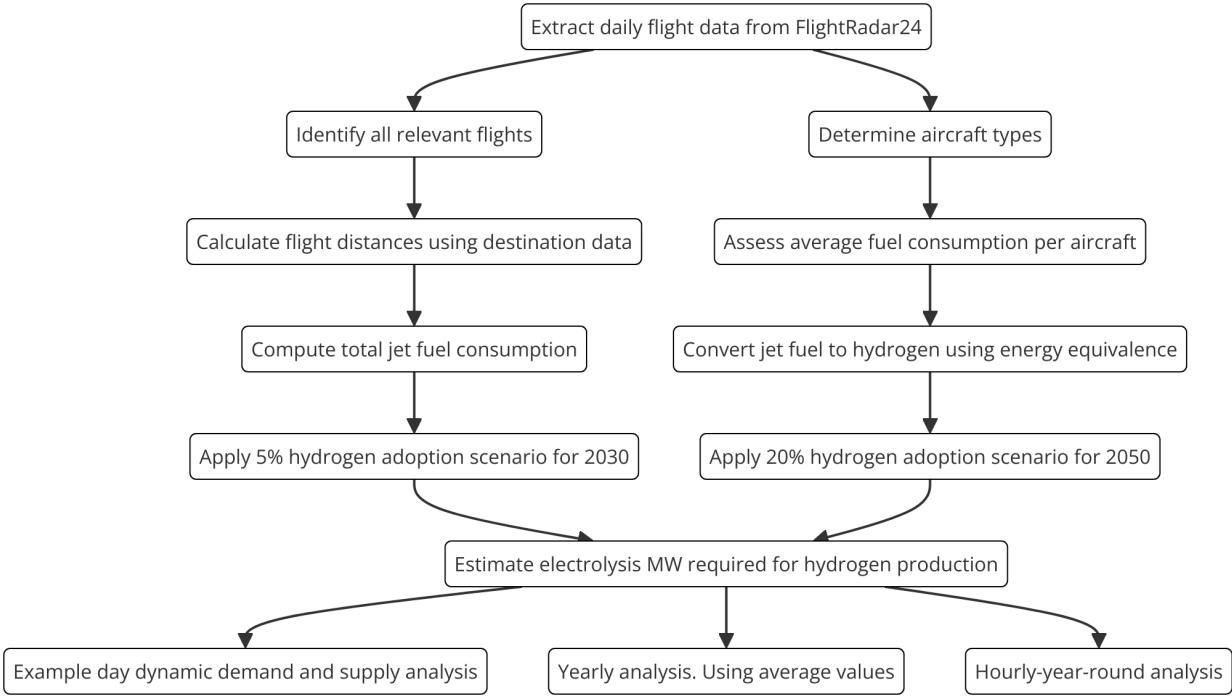
7.2. Results and Discussion

Fig. 7.6   Technical Workflow for Estimating Hydrogen Usage at LAX in 2023 and 2050: This diagram outlines the process of analyzing flight data, calculating fuel consumption, and converting jet fuel to hydrogen for different adoption scenarios, using an example day as source of data [5]

188

Figure 7.6 illustrates the methodology used to estimate hydrogen usage at LAX for the years 2023 and 2050. The workflow begins by analyzing flight data from a representative day to calculate fuel consumption based on aircraft type, thrust-specific fuel consumption (TSFC), and distance flown. This is followed by converting the corresponding jet fuel requirements into hydrogen for various adoption scenarios, assuming equal efficiency and consumption rates. Although hydrogen fuel cells offer higher efficiencies, a fleet using only hydrogen combustion is assumed for simplicity and conservatism. Additionally, it is assumed that 5% of total airport fuel consumption will be hydrogen in 2030, increasing to 20% by 2050, in alignment with predictions such as those by [234], which project hydrogen contributing 15-20% to zero-emissions aviation by 2050. While the final LCOH values found in Section 7.3 and 7.5 assume constant hydrogen production year-round, understanding the hourly demand behavior and modeling around it in a separate analysis, found in 7.2.2, provides a crucial foundation for projecting future fuel needs and assessing potential hydrogen integration at the airport.

Energy Mix Scenario Analysis

The energy mix analysis incorporates both solar and wind power generation to meet the daily power demands. Solar power generation is modeled based on solar radiation, adjusted by the area of solar panels and the efficiency of the solar cells, as shown in the equation:

$$\text{SolarPower}_{GW}(i) = \frac{\text{SolarRadiation}_{W/m^2}(i) \times \text{SolarArea} \times \text{SolarEfficiency}}{10^9} \quad (7.3)$$

Wind power generation depends on the wind speed, air density, and the sweep area of the turbines, with efficiency losses accounted for, as represented by:

$$\text{WindPower}_{GW}(i) = \frac{0.5 \times \text{AirDensity} \times \text{SweepArea} \times \text{WindSpeed}_{m/s}(i)^3 \times \text{RotorEfficiency} \times \text{NumberOfTurbines}}{10^9}$$

$$(7.4)$$

7.2.1. Airport Dynamics

These equations allow for the precise calculation of hourly power generation from renewable sources, which is critical for balancing supply with the adjusted power needs. In this scenario, which differs from the main analysis by focusing on an almost instantaneous response to airport energy demand, the setup—whether utilizing a battery system or hydrogen storage—effectively manages short-term fluctuations in power generation and demand. The system stores excess energy during periods of low demand and quickly discharges it when generation falls short, ensuring that the airport's energy needs are met in real-time without the need for excessive buffer storage. This approach provides a reliable and consistent power supply throughout the day, tailored to the airport's immediate operational requirements.
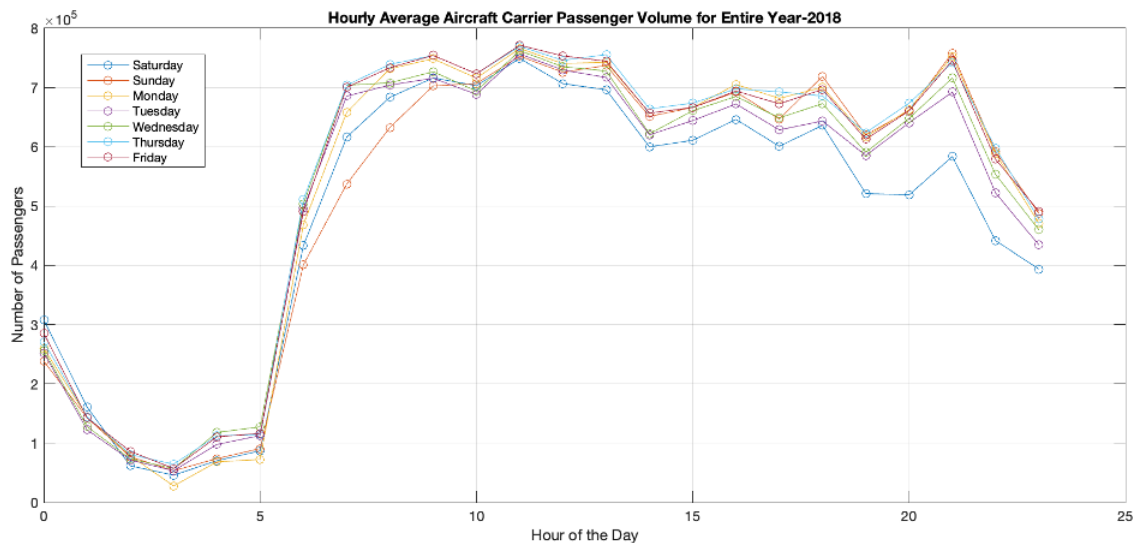

Fig. 7.7   Hourly distribution of aircraft carrier passengers over a year, scaled to 87.5 million total passengers, showing variation by day of the week.

Figure 7.7 illustrates the hourly average passenger volume at an aircraft carrier for the entire year of

2018, broken down by day of the week. The plot shows a distinct peak in passenger numbers during the morning hours, followed by a gradual decrease throughout the day, with slight variations across different days of the week. This data represents the average across the entire year, with July 21, 2024 being used as an example for further analysis in subsequent discussions. This data was extrapolated by combining daily aircraft class-specific flight volumes from OPSNET (Operational Network) [235] with hourly flight volume data from LAWA (Los Angeles World Airports) [236] to create detailed hourly aircraft class-specific time profiles. The original data used for this analysis was obtained from Gurney et al. [237], and while the specific datasets are not fully available anymore, the extrapolation was based on their work.
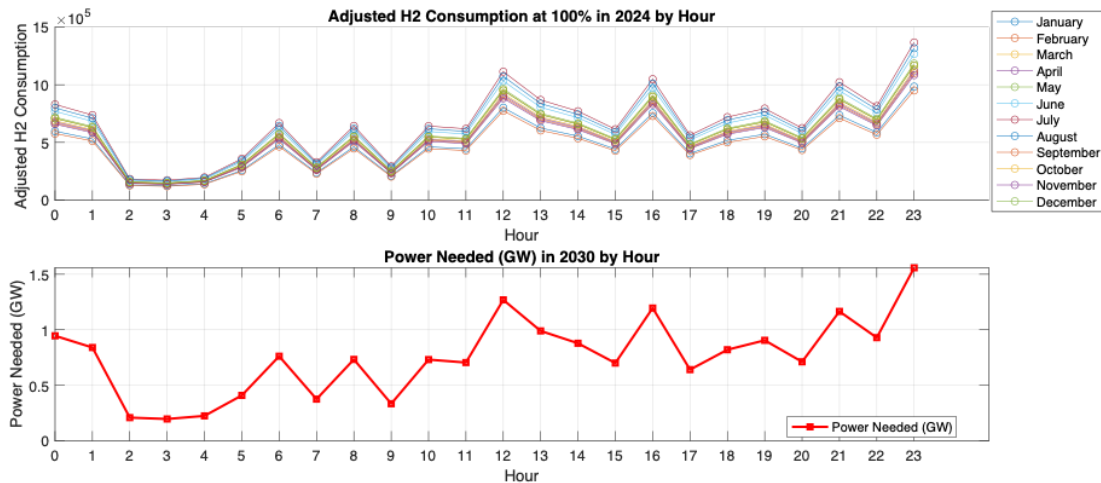

Fig. 7.8   Hourly adjusted H$_2$ consumption by month (top) and corresponding power needed in GW (bottom), with peak power demand occurring in the late evening.

Figure 7.8 illustrates the hourly variation in hydrogen consumption and corresponding power demand throughout the day. The top graph shows that hydrogen consumption varies by month [236], with higher consumption during months with increased passenger traffic, such as July and August. Conversely, the lowest hydrogen consumption occurs in February, a month with lower passenger activity. The bottom graph indicates that power demand increases throughout the day, peaking in the late evening around 23:00. This peak in power demand coincides with the highest levels of hydrogen consumption, emphasizing the critical role of hydrogen storage and supply systems in

meeting energy requirements during times when renewable energy sources, such as solar power, are less available. The alignment of hydrogen consumption and power demand underscores the necessity for efficient energy management to ensure a stable and continuous energy supply.
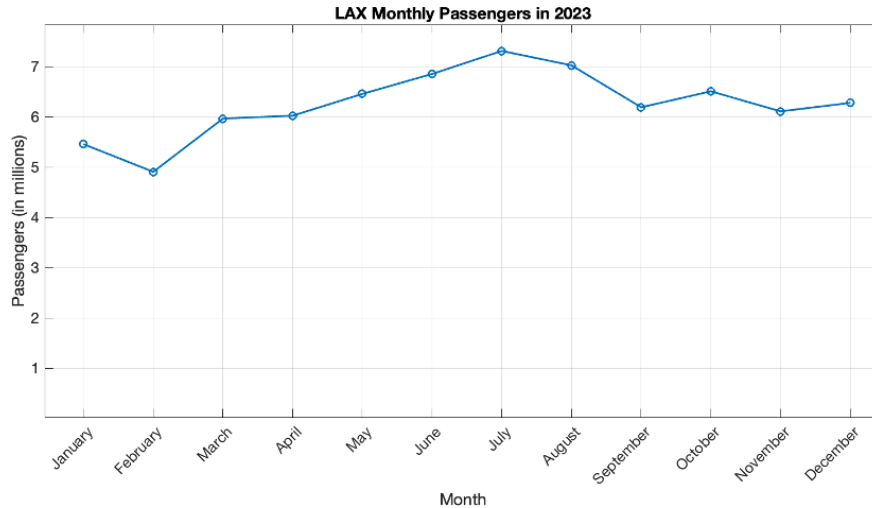

Fig. 7.9 **LAX Monthly Passengers in 2023, showing a peak in July with 7.5 million passengers, followed by a decline in the later months of the year.**

Figure 7.9 depicts monthly passenger traffic at LAX in 2023 [236]. A clear seasonal pattern is evident, with peak travel occurring during the summer months (June-August), likely due to school holidays and vacations. The total number of passengers served by LAX in 2023 was a remarkable 75 million. Interestingly, these summer peaks coincide with periods of higher solar radiation, offering potential opportunities for increased solar energy generation to support the airport's energy needs.

Figure 7.10 presents average hourly solar radiation (GHI) and wind speed data for two locations. Location 1 (34.487882°, -117.91008°), which is located offshore the coast of Los Angeles, California, exhibits a pronounced diurnal and seasonal solar radiation pattern, with peak GHI values reaching approximately 1000 W/m² during summer months and minimal radiation in December. Wind speed, measured at 100 m, at (34.487882°, -117.91008°) in Pearblossom, California, displays a less pronounced seasonal variation compared to solar radiation. However, there is a noticeable diurnal pattern with generally higher wind speeds during nighttime hours and lower speeds during daylight. Pearblossom is chosen for its good radiation values, cheap land, and proximity to LAX
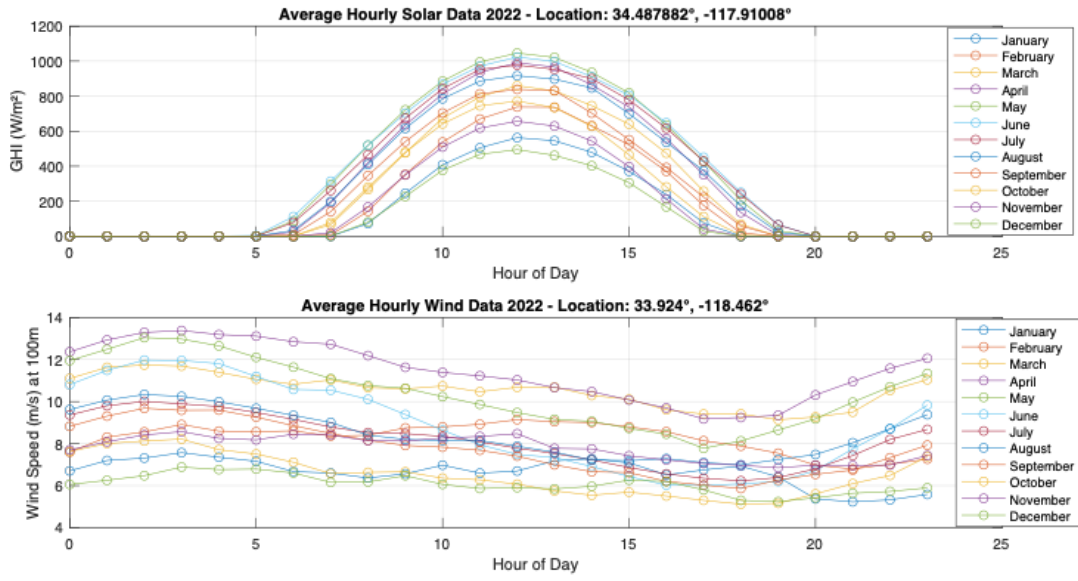
Fig. 7.10 **(Top) Global Horizontal Irradiance (GHI) throughout the day for each month, peaking around midday. (Bottom) Wind speed at 100 meters height, with variations throughout the day across different months, generally higher.**

(approximately 50-60 miles). Offshore wind across from LAX is a good choice due to its consistent wind patterns and potential for wind energy generation, which complements the solar radiation profile. Additionally, the proximity to major aviation hubs like LAX can help reduce transmission costs and leverage existing infrastructure. The higher capital and maintenance costs associated with offshore wind farms are offset by their higher energy yield and the strategic location close to the airport but still far enough from land to not cause major environmental concerns.

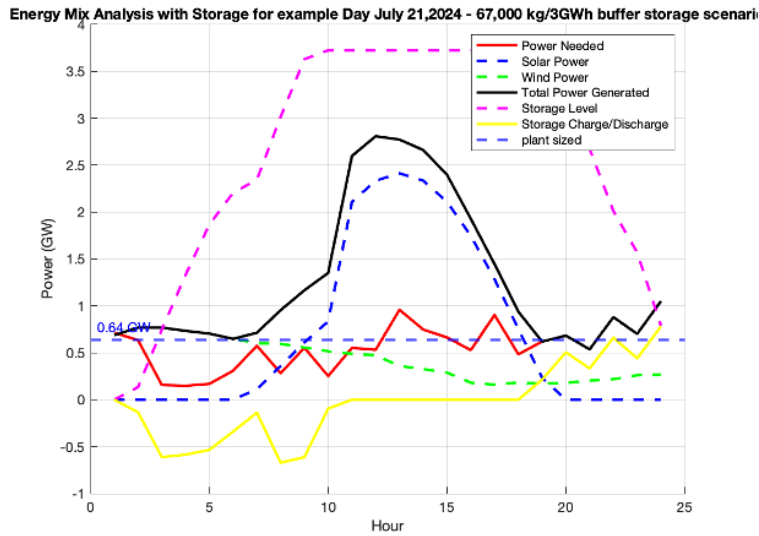### 7.2.2. Dynamic Energy Demand Limited to Single Example Day

Fig. 7.11 Energy mix and storage analysis for July 21, 2024, with power generation, storage dynamics, and a 67,000 kg or 3 GWh buffer scenario for no buffer storage scenario.

Figure 7.11 illustrates a fictional scenario where hourly power demand at the airport must be supplied continuously, demonstrating how solar (2.4 GW) and wind (0.77 GW) generation trends align with the example day's energy demand pattern. With a storage capacity of 3.7 GW, the system balances fluctuations between supply and demand. Solar and wind require 0.65 km² and 1.35 km² of land, respectively. To meet the daily hydrogen demand of 305,796.98 kg, 640 MW of electrolysis power is needed, along with a 67,000 kg/3 GWh buffer to ensure stable supply during peak periods.

7.3. Actual Scenario Cost Analysis Using Averaged hourly values

Actual Scenario Cost Analysis 2030

In the 2030 scenario, the power mix consists of a maximum solar power generation of 0.6914 GW and a maximum wind power generation of 0.7546 GW, with a battery capacity of 1.9 GWh, as shown in Figure 7.12. This combination is designed to meet LAX's projected energy needs while supporting hydrogen production via electrolysis. The power mix leans slightly more toward wind

energy due to its relatively higher capacity and consistent generation profile, which is essential for a stable supply of renewable electricity, but mainly due to the close proximity of the wind farm to the electrolysis site. Additionally, this analysis aids in understanding hourly demand patterns, even though the actual LCOH analysis in following sections assumes a constant hydrogen production rate throughout the year.
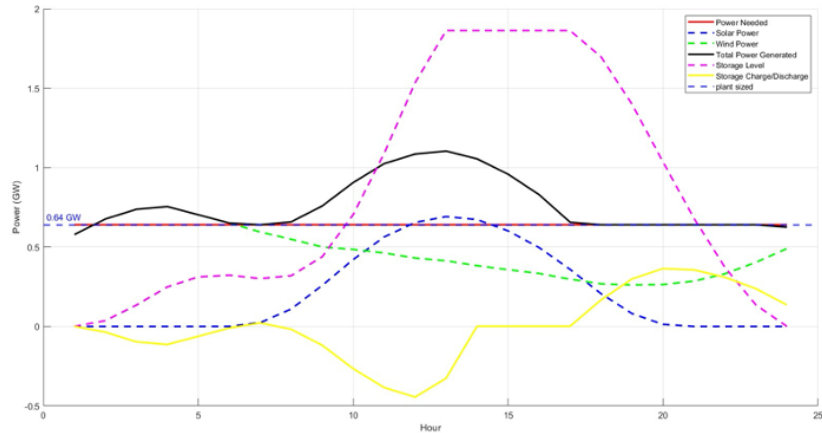

Fig. 7.12   Power Mix for 2030 - Maximum Solar and Wind Power Generation, and Battery Capacity.

Figure 7.12 presents the Levelized Cost of Hydrogen (LCOH) for LAX across four scenarios (A, B, C, and D), using both Proton Exchange Membrane (PEM) and Alkaline Electrolysis (AEL) technologies. The LCOH values range from approximately $5.56/kg to $5.9/kg for the different scenarios. Notably, Scenario A (AEL) has the lowest LCOH at $5.56/kg, while Scenario C (PEM) has the highest at $5.9/kg. This difference arises due to the lower CAPEX and OPEX associated with AEL compared to PEM, despite PEM's higher efficiency. The variation in LCOH between the scenarios is also influenced by the delivery pathways: Scenario A involves off-site liquefaction and truck transport, which are less costly than pipeline-based pathways depicted in Figure 7.13.
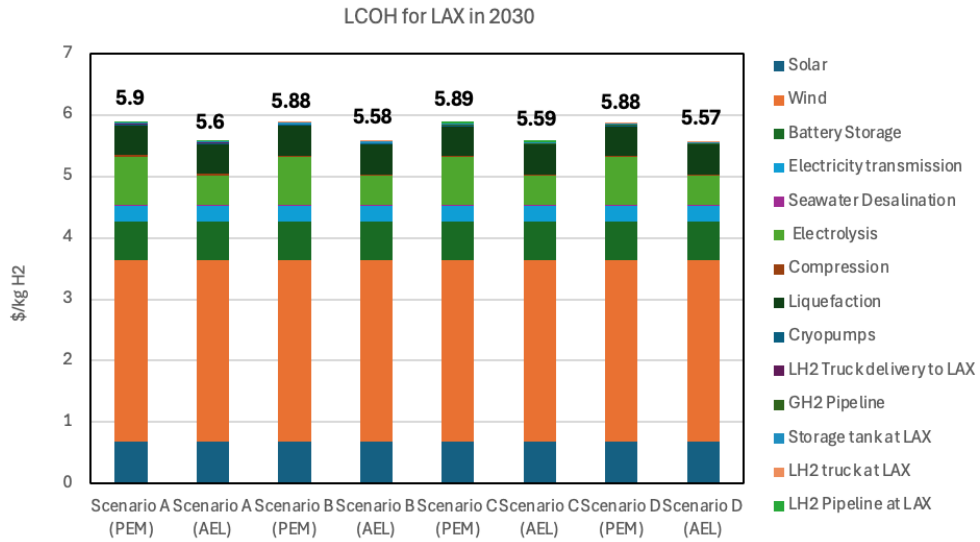
Fig. 7.13   Levelized Cost of Hydrogen (LCOH) for LAX across four scenarios (A, B, C, and D), using both PEM and AEL technologies.
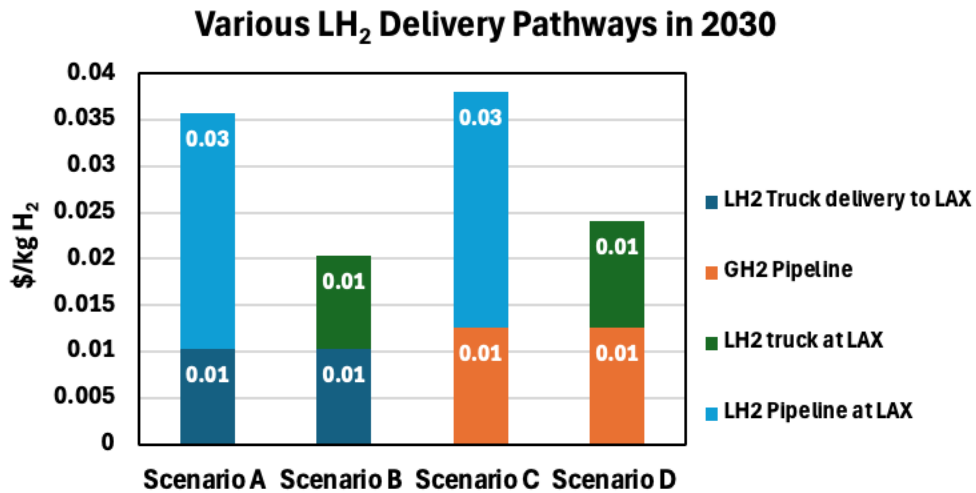

Fig. 7.14   Various LH2 Delivery Pathways to LAX in 2030 for Scenarios A, B, C, and D
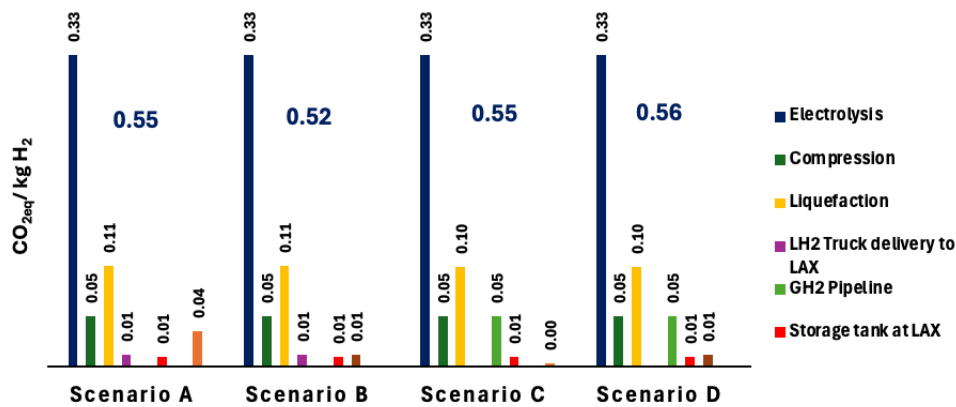
Fig. 7.15   Carbon Intensity of LH2 Supply to LAX in 2030 for Scenarios A, B, C, and D.

Figure 7.13 shows that the costs of LH_2 delivery pathways in 2030 with truck-based scenarios are lower. This is mostly due to close proximity and is expected to be contrary for longer distances. Although it is referred to as green hydrogen when produced from all renewable primary energy, it is important to mention that hydrogen production can result in hydrogen emissions or leakage. While hydrogen is not a greenhouse gas, its emission into the atmosphere can indirectly contribute to global warming potential through reactions with hydroxyl radicals in the troposphere. Figure 7.14 indicates that the carbon intensity for LH_2 supply to LAX in 2030 ranges from 0.52 to 0.56 kg CO_2-eq/kg H_2. Scenario B shows the lowest carbon intensities, whilst scenario D has the highest, mainly due to pipeline leakage.

Actual Cost Analysis 2050

By 2050, the power mix expands significantly, with a maximum solar power generation of 2.6999 GW and maximum wind power generation of 3.0185 GW, supported by an increased storage capacity of 7.25 GWh, as seen in Figure 7.16. The increase in renewable energy capacity is necessary to meet LAX's higher energy demands due to increased hydrogen adoption. This larger capacity also reflects anticipated technological advancements and cost reductions in renewable energy deployment.

197
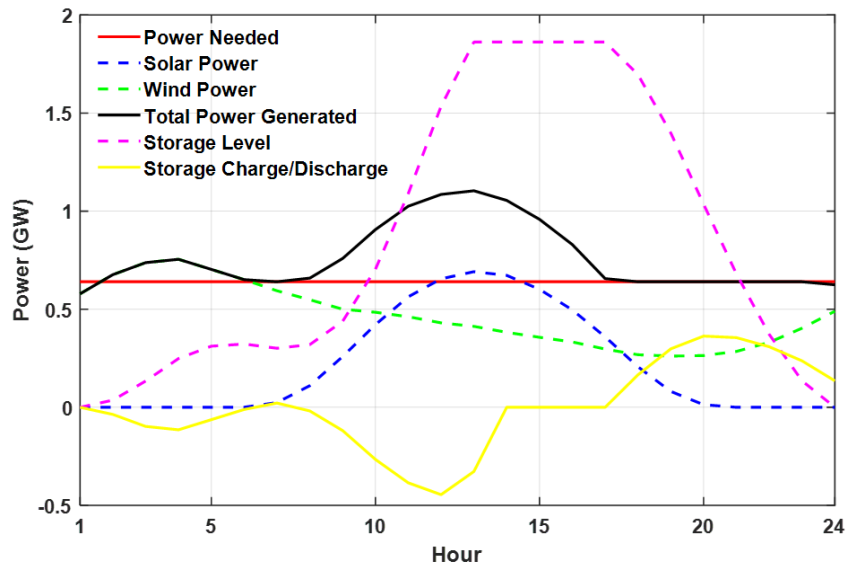
Fig. 7.16 Power Mix for 2050 - Maximum Solar and Wind Power Generation, and Storage Capacity.

The cost breakdown in Figure 7.17 reveals a marked decrease in LCOH for 2050, with values ranging from \$2.96/kg to \$2.98/kg across all scenarios. This reduction is primarily driven by improved efficiencies in electrolysis (with AEL and PEM achieving greater operational efficiencies and lower CAPEX) and reduced costs for hydrogen liquefaction and distribution. The differences in costs between the scenarios are marginal by 2050, suggesting that technological improvements have narrowed the cost gap between different delivery methods.

Fig. 7.17 Cost Breakdown of Electrolysis, Compression, Liquefaction, and Distribution of LH2 to LAX in 2050.

Fig. 7.18 Various LH2 Delivery Pathways to LAX in 2050 for Scenarios A, B, C, and D.

Fig. 7.19 Carbon Intensity of LH2 Supply to LAX in 2050 for Scenarios A, B, C, and D.

Figure 7.18 shows that hydrogen delivery via trucks remains more viable due to the short distance.

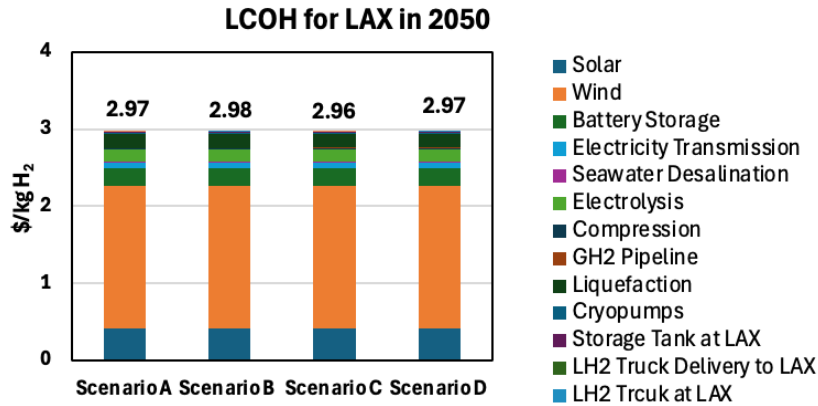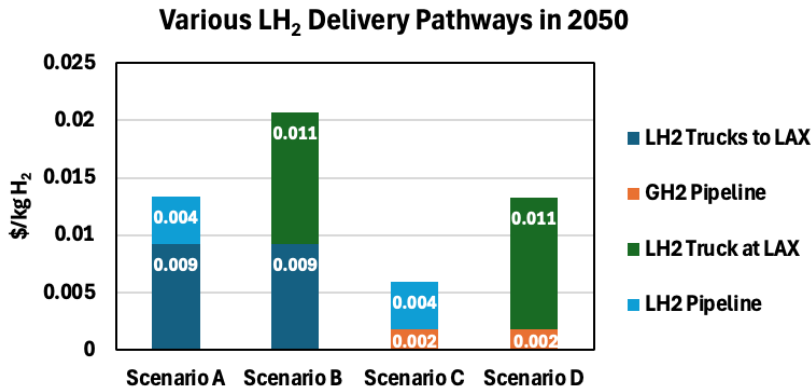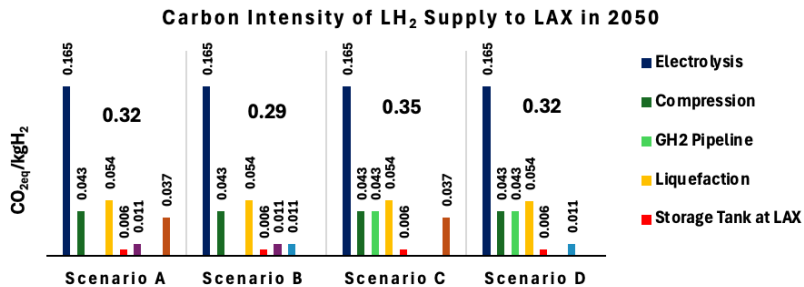Moreover, due to lower CAPEX, we see a substantial reduction in delivery costs by 2050. Finally, Figure 7.19 demonstrates that the carbon intensity of LH2 supply to LAX decreases in 2050, with values ranging from 0.29 to 0.35 kg CO2-eq/kg H2. The reduction in carbon emissions results from increased renewable energy use and improved efficiency in hydrogen production and distribution processes. Scenarios involving pipeline use (Scenarios C and D) exhibit slightly higher carbon intensities due to the energy required for compression and transport, whereas truck-based delivery (Scenarios A and B) maintains lower carbon emissions.

7.4. Mapping Power Systems and Infrastructure

Table 7.3   Projected Solar and Offshore Wind Power Capacities, Required Areas, and Area Efficiency for 2030 and 2050.

Year	Solar Power (GW)	Solar Power Area (km²)	Offshore Wind Power (GW)	Offshore Wind Power Area (km²)
2030	0.70	4.0	0.76	110
2050	2.69	12.0	3.02	300
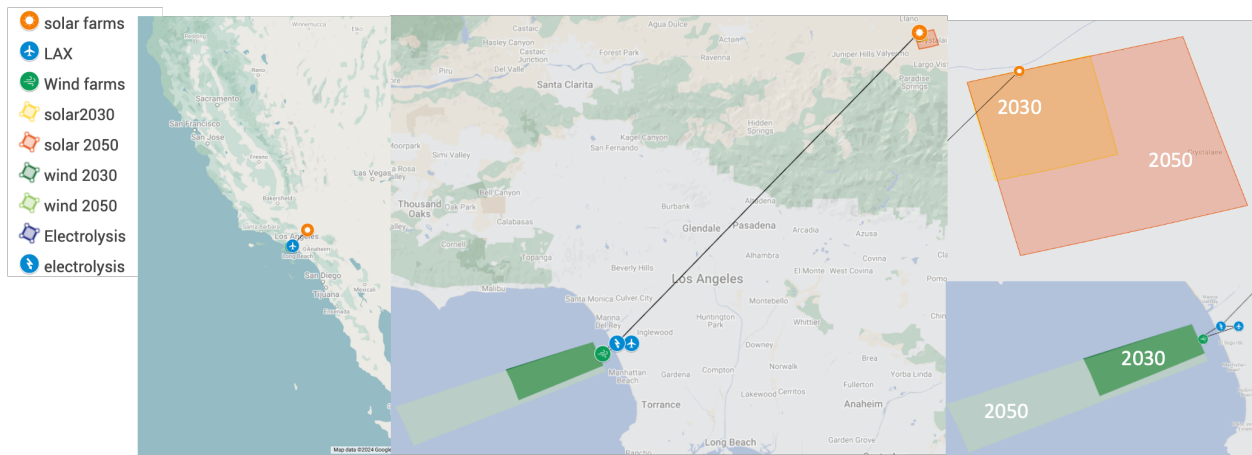
Fig. 7.20   Projected Locations of Solar and Offshore Wind Farms Near Los Angeles International Airport (LAX) for 2030 and 2050.

The analysis in Table 7.3 and Figure 7.20 illustrates the projected reductions in area requirements for solar and offshore wind power generation near LAX by 2030 and 2050. Solar power areas increases from 4.0 km² to 12.0 km², while offshore wind areas increase from 110 km² to 300 km², driven by larger turbines and floating platforms. Figure 7.20 shows these planned locations, indicating

200

strategic siting to optimize transmission and support energy demands near LAX while minimizing land use conflicts.

7.5. Hourly Year-Round Analysis of Energy Mix

A detailed year-round hourly analysis shows that maintaining continuous hydrogen production requires strategies beyond annual averages. While many studies rely on annual averages [238, 239], similar to our simplified analysis showcased in Section 7.2, do not account for the variability in renewable energy supply, making uninterrupted production challenging without seasonal storage solutions. Two scenarios are analyzed in this case with an increase in solar power capacity as well as the addition of seasonal storage that deemed necessary in the more fluctuated year-hourly analysis.

In Southern California, depleted oil and gas fields in the Los Angeles and Ventura Basins could provide geological storage at a lower cost, estimated between $1 to $10 per kg of hydrogen, leveraging existing infrastructure and favorable geological conditions. Gaseous tank storage is approximately $300-500, with Department of Energy goal for 2020 as $333 [240, 241]. The levelized storage cost range for various storage technologies according to [240] is: Line packing: $0.05 or less per kg H2; Salt cavern: $0.6-1.2 per kg H2; Above ground pressurized tank (GH2): $0.3-0.5 per kg H2. In case where above ground storage is used assumption is $450 per kg including compression.

The use of above-ground storage results in an LCOH for 2030 ranging from $6.73 to $7.06 and for 2050 ranging from $3.65 to $3.67 leading to approximately a 17-19% increase in LCOH. These values are based on the increase in capacity and seasonal storage, with details of the analysis provided in Section 7.5. An alternative analysis based on geological storage with optimistic assumptions can be found in Section C.2 in the Appendix which leads to only a 4-10% in LCOH. Nevertheless, this increase in values is expected, where the addition of yearly storage and operation in an independent grid—where there is only a single constant source of consumption—results in a significant increase in LCOH.

Table 7.4   Energy Storage and Generation Capacities for 2030

Parameters	Values
Maximum Solar Power Generated	1.2771 GW
Maximum Wind Power Generated	0.7546 GW (capped at 0.75 GW)
Battery Storage Capacity	1.9 GWh
Seasonal Storage Capacity	32.0 GWh
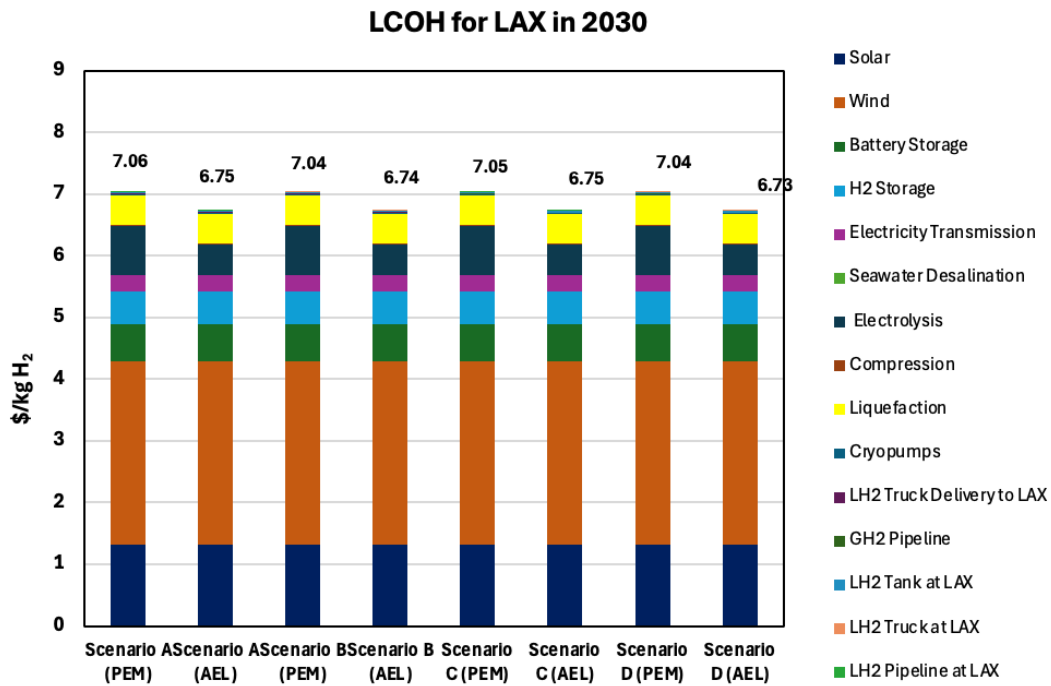
Fig. 7.21   Levelized Cost of Hydrogen (LCOH) for LAX in 2030 across different scenarios, considering hourly-year-round operation with above-ground hydrogen seasonal storage.

As shown in Figure 7.21, the Levelized Cost of Hydrogen (LCOH) for LAX in 2030 ranges from $6.73 to $7.06 per kg of H_2, depending on the scenario considered. These values reflect the costs associated with hourly-year-round operation and above-ground hydrogen seasonal storage.

The storage capacities, as outlined in Table 7.4, show a maximum solar power generation of 1.2771 GW (an increase from previous analysis) and a capped wind power generation at 0.75 GW. The battery storage capacity is 1.9 GWh, complemented by a seasonal storage capacity of 32.0 GWh (960,096 kg hydrogen) or 4 days storage. These capacities highlight the need for robust storage solutions to handle the hourly variability in renewable energy generation and weather patterns and maintain a stable supply of hydrogen throughout the year given.
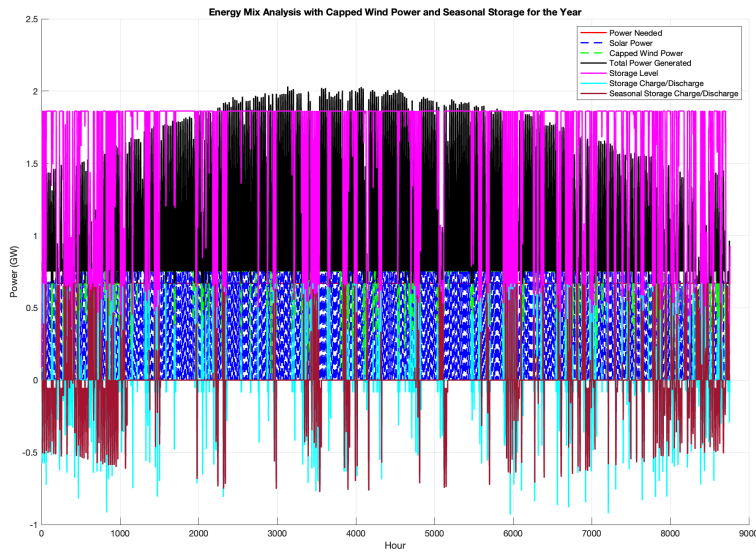
Fig. 7.22   Power needed, generated, and storage dynamics over one year (2030), showing solar power, capped wind power, total power generated, storage levels, and storage charge/discharge cycles. This is based on hourly-year-round operation with above-ground hydrogen seasonal storage.
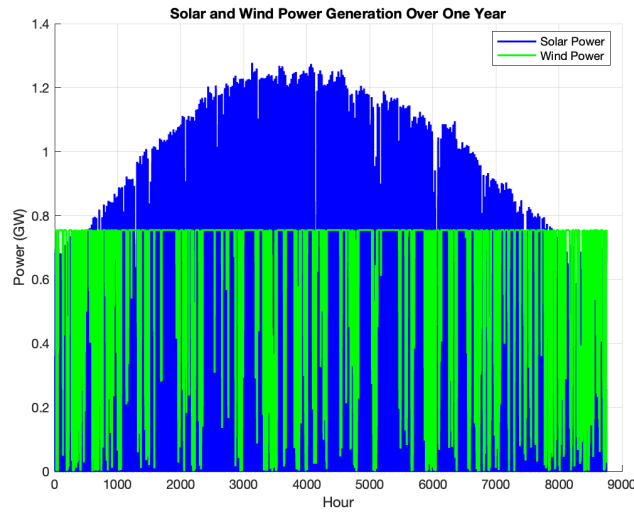
Fig. 7.23 **Solar and wind power generation over one year (2030), illustrating the variability and total power contribution from each source. This analysis is for hourly-year-round operation with above-ground hydrogen seasonal storage.**

Fig. 7.24 **Seasonal storage dynamics over one year (2030), displaying the seasonal storage level and charge/discharge activities. The costs are considered for hourly-year-round operation with above-ground hydrogen seasonal storage.**

Figure 7.22 demonstrates the multiple factors needed to balance an independent grid, including battery storage and seasonal hydrogen storage that is dispatched throughout the year. Seasonal storage is primarily dispatched during winter and the last two months of the year, with some minor variations due to unpredictable weather patterns. Figures 7.23 and 7.24 further illustrate the variability in solar and wind generation and the corresponding seasonal storage dynamics, showing

204

how these elements work together to maintain a stable energy supply for hourly-year-round operation at LAX in 2030.

2050 Hourly Year-Round Analysis

Table 7.5   Energy Storage and Generation Capacities for 2050

Parameters	Values
Maximum Solar Power Generated	5.12 GW
Maximum Wind Power Generated	3.0185 GW
Battery Storage Capacity	7.6 GWh
Seasonal Storage Capacity	128 GWh
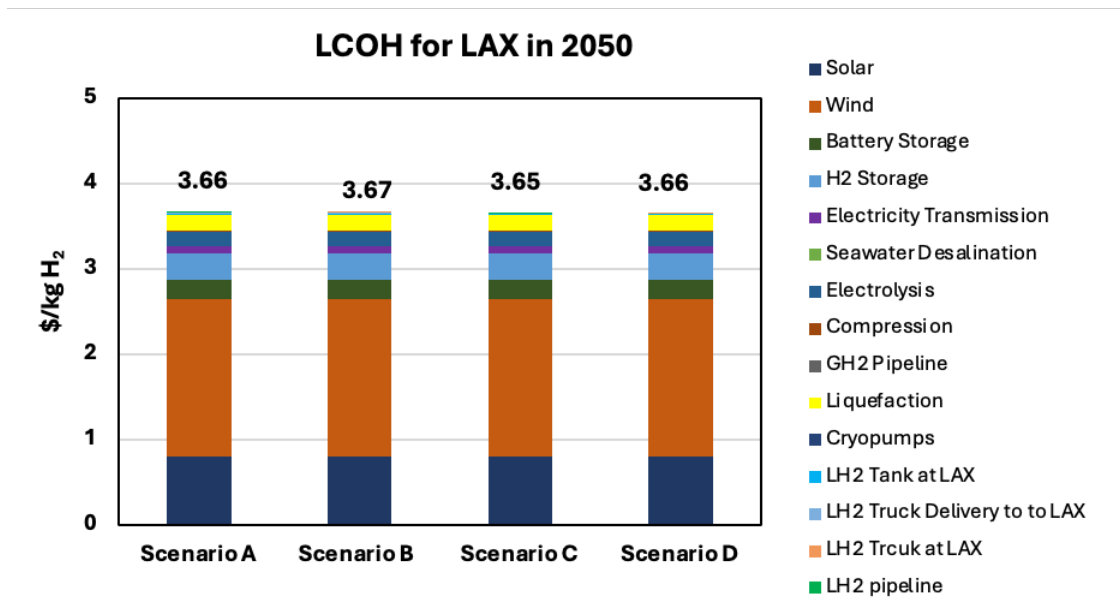
Fig. 7.25   Levelized Cost of Hydrogen (LCOH) for LAX in 2050 across different scenarios, considering hourly-year-round operation with above-ground hydrogen seasonal storage.

Figure 7.25 provide insights into the energy storage and generation dynamics for 2050, based on hourly-year-round operation with above-ground hydrogen seasonal storage. Levelized Cost of

Hydrogen (LCOH) for LAX in 2050 ranges from \$3.65 to \$3.67 per kg, reflecting the impact of increased capacity and storage solutions. The expanded storage capacities, including 7.6 GWh of battery storage and 128 GWh of seasonal storage (as shown in Table 7.5), help balance the grid and mitigate fluctuations, particularly during periods of low renewable generation, ensuring a stable energy supply throughout the year.
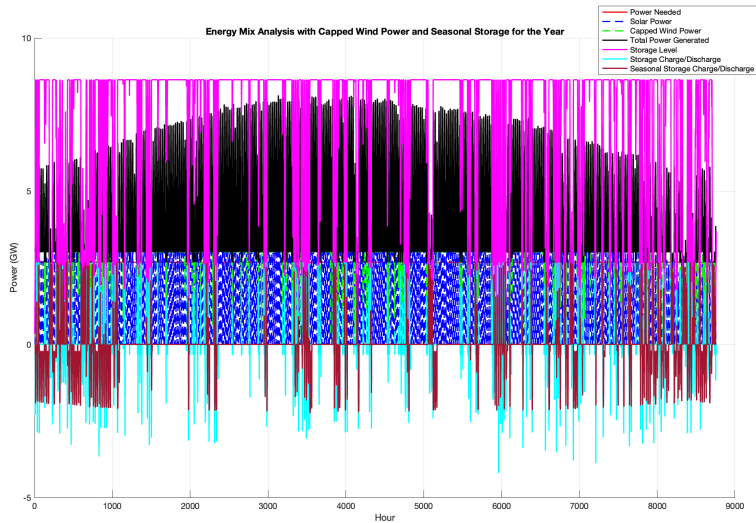
Fig. 7.26   Power needed, generated, and storage dynamics over one year (2050), showing solar power, wind power, total power generated, storage levels, and storage charge/discharge cycles. Costs are based on hourly-year-round operation with above-ground hydrogen seasonal storage.
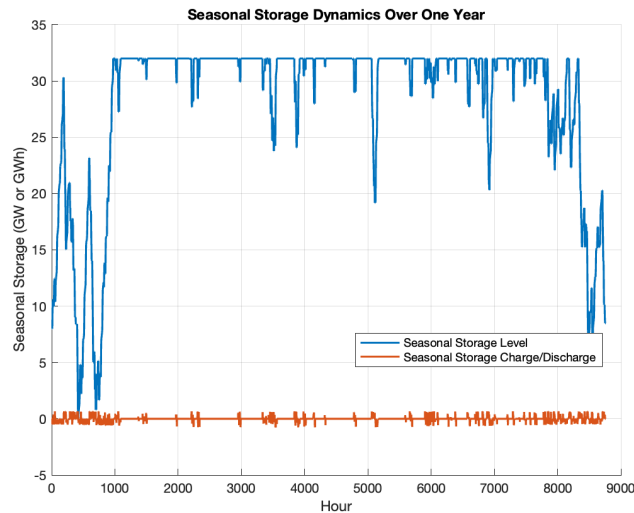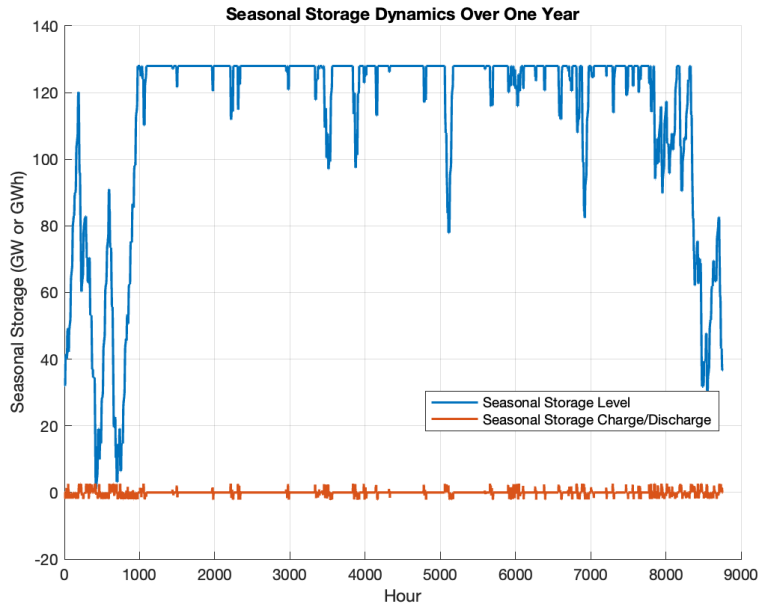
Fig. 7.27   Seasonal storage dynamics over one year (2050), displaying the seasonal storage level and charge/discharge activities. Costs are calculated for hourly-year-round operation with above-ground hydrogen seasonal storage.
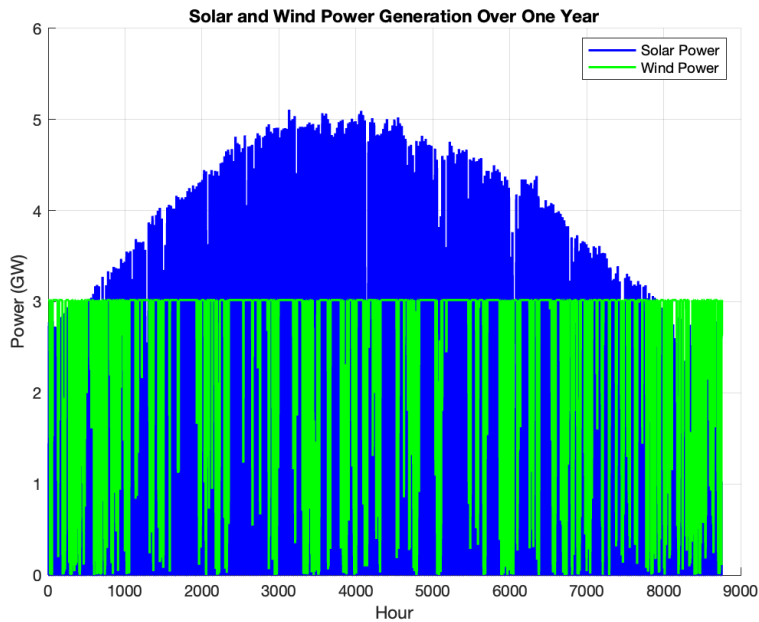
Fig. 7.28   Solar and wind power generation over one year (2050), illustrating the variability and total power contribution from each source. Costs are considered for hourly-year-round operation with above-ground hydrogen seasonal storage.

Figure 7.26 illustrates the power balance for 2050, integrating solar, wind, battery, and seasonal

hydrogen storage to stabilize the grid. Seasonal storage is primarily dispatched during winter and year-end, with adjustments for weather variability. Figure 7.27 shows the charge and discharge cycles that maintain supply stability, while Figure 7.28 highlights the variability in renewable generation, underscoring the need for flexible storage to ensure reliable, year-round operation at LAX.

7.6. Conclusion

This analysis demonstrates the viability and cost-effectiveness of different hydrogen supply strategies for Los Angeles International Airport (LAX) in 2030 and 2050, focusing on both economic and environmental impacts. By 2030, the lowest Levelized Cost of Hydrogen (LCOH) is achieved in Scenario A (AEL) at $5.56/kg, while Scenario C (PEM) reaches the highest at $5.9/kg. Truck-based delivery is more economical due to the short distances involved, with carbon intensities ranging from 0.52 to 0.56 kg CO2-eq/kg H2, where Scenario B shows the lowest emissions. By 2050, renewable energy capacity increases substantially, with solar generation reaching 2.6999 GW and wind generation 3.0185 GW, supported by a storage capacity of 7.25 GWh. This leads to a reduced LCOH between $2.96/kg and $2.98/kg across all scenarios due to enhanced efficiency and technological advancements. The carbon intensity also drops to 0.29 to 0.35 kg CO2-eq/kg H2, with truck-based delivery scenarios (A and B) maintaining lower emissions compared to pipeline-based scenarios (C and D). Overall, the results highlight the importance of optimizing renewable energy use and delivery methods to achieve cost-effective and environmentally sustainable hydrogen supply for aviation.

A more detailed, though not entirely identical for every year due to different weather patterns, hourly year-round analysis showcased in section 7.5 provides greater consistency across years compared to using average solar and wind patterns throughout the entire year. The results, are based on 2022 solar and wind data as shown in Figures 7.23 and 7.28.

The use of above-ground hydrogen storage results in LCOH costs for 2030 ranging from $6.73

to $7.06 and for 2050 between $3.65 and $3.67, reflecting the impacts of increased capacity and seasonal storage. These costs are in line with expectations whenever hourly year-round variability is included in the equation showcasing a 17-19% increase LCOH for 2030 and 2050.

Under more optimistic geological assumptions, LCOH costs are expected to increase conservatively by 4-10%, depending on the seasonal hydrogen storage capacity available in Southern California in addition to battery storage. A significantly higher increase in LCOH, ranging from $0.5 to $1, is anticipated if above-ground gaseous storage is utilized. Additional details on these findings can be found in Section C.1.

This study can be considered preliminary research on LAX's capability to incorporate green LH2 into its fuel portfolio for modified aircraft engines expected in the coming decades. The LCOH in reality would naturally differ from the estimates provided here due to simplified assumptions and the complexity of LH2 supply chain scenarios to LAX and surrounding regions, particularly the construction of solar and wind sites, pipelines and electricity transmission lines. Despite this, the long-term LCOH and carbon intensity results from this study indicate a promising future for implementing LH2 fuel for carbon-free flights at LAX. Further rigorous life-cycle analysis and the adoption of optimization techniques (such as linear programming approaches) are recommended to expand the understanding of environmental repercussions and reduce the final LCOH, respectively. Additionally, assessing the costs associated with modifying aircraft design for hydrogen-powered propulsion is another essential area for future research. While green hydrogen is currently an expensive commodity, in the long run, it has the potential to be a powerful decarbonization tool for the aviation sector. This scenario becomes even more plausible with substantial government funding supporting the transition towards sustainability.

This study can be considered preliminary research on LAX's capability to incorporate green LH2 into its fuel portfolio for modified aircraft engines expected in the coming decades. The LCOH in reality would naturally differ from the estimates provided here due to simplified assumptions and the complexity of LH2 supply chain scenarios to LAX and surrounding regions, particularly

the construction of solar and wind sites, pipelines, and electricity transmission lines. Despite this, the long-term LCOH and carbon intensity results from this study indicate a promising future for implementing LH2 fuel for carbon-free flights at LAX. Further rigorous life-cycle analysis and the adoption of optimization techniques (such as linear programming approaches) are recommended to expand the understanding of environmental repercussions and reduce the final LCOH. Assessing the costs associated with modifying aircraft designs for hydrogen-powered propulsion is also an essential area for future research. While green hydrogen is currently expensive, in the long run, it has the potential to become a powerful decarbonization tool for aviation, especially with substantial government funding supporting the transition to sustainability.

In this context, it's important to consider the varying impact of hydrogen adoption across airports of different sizes, based on local renewable energy resources and fuel demand. Smaller airports may lean towards decentralized refueling stations, catering to regional flights and general aviation, with simpler logistics and lower volumes. Larger airports, however, will require more robust infrastructure, such as centralized production facilities and extensive storage systems, to support high-capacity hydrogen supply chains for major commercial airlines. Establishing hydrogen hubs across the United States could facilitate a nationwide delivery network, improving the distribution and reliability of hydrogen as an aviation fuel. Nonetheless, challenges remain, including the high costs of hydrogen production and storage, limited infrastructure, regulatory barriers, and the need for standardized fueling protocols.

8. Summary and Conclusions

The story of this dissertation unfolds by developing a comprehensive methodology for retrofitting aircraft with hydrogen power systems, analyzing their economic and environmental viability. It begins with the Cessna Citation XLS+, where initial retrofitting concepts are tested to understand the feasibility and impacts of hydrogen combustion and fuel cell technologies. The focus then shifts to the Cessna S550, where dynamic modeling is employed to assess how these systems handle real flight dynamics. The study also explores low altitude turbo-prop aircraft and new configurations of PEMFC and battery-electric. Furthermore, more advanced concepts are analyzed by sizing and analyzing Blended Wing Body (BWB) designs with hydrogen power, comparing their performance and benefits against conventional aircraft retrofits. The story culminates in an exploration of the costs and infrastructure required to supply green hydrogen to airports, from production to fueling aircraft, offering insights into the transition toward a sustainable aviation future.

The dissertation lays ground to a hydrogen retrofit methodology and starts by retrofitting a Cessna Citation XLS+ with hybrid power systems combining hydrogen combustion and Solid Oxide Fuel Cell/Gas Turbine (SOFC/GT) technologies, focusing on performance, emissions, lifecycle, and cost. Modifications include designing liquid hydrogen tanks to meet insulation, sizing, center of gravity, and power constraints, resulting in a 5% takeoff weight reduction for hydrogen combustion and 0.4% for the SOFC hybrid, while necessitating a reduction in passenger capacity to accommodate cryogenic tanks.

Building on this analysis, the dissertation transitions to dynamic modeling of the Cessna S550 Citation S/II equipped with an SOFC/GT system. This phase examines whether hydrogen-powered engines can effectively respond to flight dynamics, revealing that while the hybrid configuration demonstrates high efficiency (up to 71.4%) and responsiveness, battery storage integration is crucial

211

to handle rapid power demands during critical flight phases such as takeoff, descent, and landing.

The narrative then shifts to more futuristic designs, focusing on the hydrogen-powered Blended Wing Body (BWB) models—BWB-365 and BWB-162. These designs are analyzed to compare their performance against conventional aircraft retrofits, demonstrating significant improvements in fuel efficiency (22.7% and 28.7%, respectively) over traditional Tube and Wing designs. The BWB-365 achieves a 61% reduction in fuel consumption per passenger-kilometer and a 22% reduction in takeoff weight compared to the Boeing 777-300ER, while the BWB-162 shows a 52% reduction in fuel consumption, albeit with an 11% increase in takeoff weight relative to the Boeing 737-800. However, integrating the SOFC/GT powertrain into these designs presents space challenges for hydrogen storage, potentially necessitating fuselage extensions to maintain payload capacity. Despite these obstacles, hydrogen-powered aircraft offer considerable environmental benefits, particularly in reducing NOx emissions, though further research is needed to address system integration and the slower startup times of SOFC/GT systems.

Finally, the study also examines the retrofitting of the ATR42-600 with hydrogen power systems, highlighting the trade-offs in adapting current aircraft designs. The PEMFC-powered variant, despite advancing hydrogen integration, results in a 46% reduction in seating capacity (from 48 to 26 passengers) due to lower efficiency and increased hydrogen volume requirements. The SOFC-powered variant shows a smaller impact, with a 29% reduction in seating capacity (from 48 to 34 passengers), while the hydrogen combustion option requires a 38% decrease in seats (from 48 to 30 passengers) to accommodate storage needs. The ATR42-600 was the only aircraft analyzed with both PEMFC and battery-electric configurations for direct comparison, as these setups were not feasible for other aircraft and mission profiles while maintaining a constant range approach and assuming no electric compression for PEMFC. The battery-electric variant achieved a limited range of approximately 150 nmi (278 km), compared to the conventional 702 nmi (1,302 km), underscoring the challenges of current battery technology in aviation.

The dissertation concludes by exploring the costs and logistics of delivering green hydrogen to

airports, with a case study focused on Los Angeles International Airport. It assesses future hydrogen supply strategies for 2030 and 2050, factoring in production, delivery, and infrastructure needs. By 2030, the Levelized Cost of Hydrogen (LCOH) is estimated between \$5.56/kg and \$5.9/kg, with truck-based delivery being more economical. By 2050, the expansion of renewable energy capacity could lower LCOH to \$2.96–\$2.98/kg, with reduced carbon intensities.

However, when accounting for hourly year-round operation, the LCOH increases by 17–19% with above-ground storage, reaching a minimum of \$6.73 by 2030 and \$3.65 by 2050. In contrast, if below-ground geological storage is utilized, the increase is more modest, ranging from 4–10%, with LCOH reaching \$5.75 in 2030 and \$3.29 in 2050.

These insights emphasize the importance of optimizing both renewable energy use and hydrogen delivery methods to ensure a sustainable and cost-effective transition to hydrogen-powered aviation.

Future work could focus on several key areas to advance hydrogen-powered aviation technologies. A primary area of research would be the lifecycle analysis (LCA) of hydrogen-powered blended wing body (BWB) aircraft, assessing both the environmental and economic sustainability of these systems throughout their operational lifespan and comparing them to conventional aircraft technologies. Additionally, research into airport infrastructure changes required for BWB aircraft, such as passenger loading mechanisms and landing strip width, would be valuable. Furthermore, the integration of high-temperature proton exchange membrane fuel cells (HT-PEMFCs) could be explored, taking advantage of their reduced cooling requirements and enhanced overall system efficiency. Laboratory experiments could also be conducted to investigate the effects of altitude on the performance of low-temperature and high-temperature PEMFCs, as well as solid oxide fuel cell (SOFC) hybrid systems, ensuring these technologies are robust and effective under varying flight conditions. Additionally, research into the fueling and defueling dynamics of liquid and cryo-compressed hydrogen tanks could address key operational challenges, including the complexities of managing these systems during ground operations and boarding procedures for BWB aircraft.

Bibliography

[1] ATR Aircraft, "ATR 42-600 Fact Sheet," , 2020. URL `https://www.atr-aircraft.com/wp-content/uploads/2020/07/Factsheets_-_ATR_42-600.pdf`, accessed: 2024-09-09.

[2] Norebbo, "ATR 42 Blank Illustration Templates," , 2024. URL `https://www.norebbo.com/atr-42-blank-illustration-templates/`, accessed: 2024-09-09.

[3] Aziz, M., "Liquid Hydrogen: A Review on Liquefaction, Storage, Transportation, and Safety," *Energies*, Vol. 14, No. 18, 2021, p. 5917.

[4] "Integration of Hydrogen Aircraft into the Air Transport System: An Airports Operations and Infrastructure Review," , 2021.

[5] "Flight Radar 24," , ???? URL `https://www.flightradar24.com/data/aircraft/n550we#32fc8cee`, retrieved 28 November 2023.

[6] Overton, J., "Fact Sheet: The Growth in Greenhouse Gas Emissions from Commercial Aviation," , 2019. Retrieved December 15, 2021, from https://www.eesi.org/papers/view/fact-sheet-the-growth-in-greenhouse-gas-emissions-from-commercial-aviation.

[7] Yılmaz, , İlbaş, M., Taştan, M., and Tarhan, C., "Investigation of Hydrogen Usage in Aviation Industry," *Energy Conversion and Management*, Vol. 63, 2012, pp. 63–69. https://doi.org/10.1016/j.enconman.2011.12.032.

[8] Owen, B., Lee, D. S., and Lim, L., "Flying into the Future: Aviation Emissions Scenarios to 2050," *Environmental Science & Technology*, Vol. 44, No. 7, 2010, pp. 2255–2260. https://doi.org/10.1021/es902530z.

[9] Hoelzen, J., Silberhorn, D., Zill, T., Bensmann, B., and Hanke-Rauschenbach, R., "Hydrogen-Powered Aviation and Its Reliance on Green Hydrogen Infrastructure – Review and Research

Gaps," *International Journal of Hydrogen Energy*, Vol. 47, No. 5, 2022, pp. 3108–3130. https://doi.org/10.1016/j.ijhydene.2021.10.239.

[10] Airbus, "Airbus Reveals New Zero-Emission Concept Aircraft," , 2020. Retrieved December 15, 2021, from https://www.airbus.com/en/newsroom/press-releases/2020-09-airbus-reveals-new-zero-emission-concept-aircraft.

[11] Seeckt, K., and Scholz, D., "Jet versus Prop, Hydrogen versus Kerosene for a Regional Freighter Aircraft," *Deutscher Luft- und Raumfahrtkongress*, 2009.

[12] Collins, J. M., and McLarty, D., "All-Electric Commercial Aviation with Solid Oxide Fuel Cell-Gas Turbine-Battery Hybrids," *Applied Energy*, Vol. 265, 2020, p. 114787. https://doi.org/10.1016/j.apenergy.2020.114787.

[13] Owen, B., Lee, D. S., and Lim, L., "Flying into the Future: Aviation Emissions Scenarios to 2050," *Environmental Science & Technology*, Vol. 44, No. 7, 2010, pp. 2255–2260. https://doi.org/10.1021/es902530z.

[14] Bergero, C., Gosnell, G., Gielen, D., Kang, S., Bazilian, M., and Davis, S. J., "Pathways to Net-Zero Emissions from Aviation," *Nature Sustainability*, Vol. 6, No. 4, 2023, pp. 404–414. https://doi.org/10.1038/s41893-022-01046-9.

[15] Daggett, D., Hendricks, R., and Walther, R., "Alternative Fuels and Their Potential Impact on Aviation," Tech. rep., 2006.

[16] Corchero, G., and Montañés, J. L., "An Approach to the Use of Hydrogen for Commercial Aircraft Engines," *Proceedings of the Institution of Mechanical Engineers, Part G: Journal of Aerospace Engineering*, Vol. 219, No. 1, 2005, pp. 35–44. https://doi.org/10.1243/095441005x9139.

[17] ICAO, "Sustainable Aviation Fuels Guide," , 2017. Montreal.

[18] Warr, R. L., and Greenwell, B. M., "A Hierarchical Nonparametric Bayesian Model That Integrates Multiple Sources of Lifetime Information to Model Large-Scale System Reliability," , 2014. ArXiv preprint arXiv:1412.4260.

[19] Hoelzen, J., Silberhorn, D., Zill, T., Bensmann, B., and Hanke-Rauschenbach, R., "Hydrogen-Powered Aviation and Its Reliance on Green Hydrogen Infrastructure Review and Research Gaps," *International Journal of Hydrogen Energy*, Vol. 47, No. 5, 2022, pp. 3108–3130. https://doi.org/10.1016/j.ijhydene.2021.10.239.

[20] Scheelhaase, J., Maertens, S., and Grimme, W., "Synthetic Fuels in Aviation – Current Barriers and Potential Political Measures," *Transportation Research Procedia*, Vol. 43, 2019, pp. 21–30. https://doi.org/10.1016/j.trpro.2019.12.015.

[21] Salam, M. A., Habib, M. S., Arefin, P., Ahmed, K., Uddin, M. S., Hossain, T., and Papri, N., "Effect of Temperature on the Performance Factors and Durability of Proton Exchange Membrane of Hydrogen Fuel Cell: A Narrative Review," *Material Science Research India*, Vol. 17, No. 2, 2020, pp. 179–191. https://doi.org/10.13005/msri/170210.

[22] Pratt, J., Brouwer, J., and Samuelsen, G., "Experimental Performance of an Air-Breathing PEM Fuel Cell at High Altitude Conditions," 2005. https://doi.org/10.2514/6.2005-953.

[23] Zhang, J., Tang, Y., Song, C., Xia, Z., Li, H., Wang, H., and Zhang, J., "PEM Fuel Cell Relative Humidity (RH) and Its Effect on Performance at High Temperatures," *Electrochimica Acta*, Vol. 53, No. 16, 2008, pp. 5315–5321. https://doi.org/10.1016/j.electacta.2008.02.074.

[24] Beney, A., "Investigation into the Heat Up Time for Solid Oxide Fuel Cells in Automotive Applications," Ph.D. thesis, University of Guelph, 2018.

[25] McLarty, D., Brouwer, J., and Samuelsen, S., "Fuel Cellgas Turbine Hybrid System Design Part I: Steady State Performance," *Journal of Power Sources*, Vol. 257, 2014, pp. 412–420. https://doi.org/10.1016/j.jpowsour.2013.11.122.

[26] Freeh, J. E., Pratt, J. W., and Brouwer, J., "Development of a Solid-Oxide Fuel Cell/Gas Turbine Hybrid System Model for Aerospace Applications," 2004. https://doi.org/10.1115/gt2004-53616.

[27] Hovakimyan, G., Brouwer, J., and Samuelsen, S., "Quasidynamic Modeling & Analysis of Fuel Cell Performance on Aircraft," , 2014.

[28] Wikipedia, "Solid Oxide Fuel Cell," , 2020. In Wikipedia. Retrieved December 2020, from https://en.wikipedia.org/wiki/Solid$_o$xide$_f$uel$_c$ell.

[29] Epstein, A. H., and O'Flarity, S. M., "Considerations for Reducing Aviation's CO2 with Aircraft Electric Propulsion," *Journal of Propulsion and Power*, Vol. 35, No. 3, 2019, pp. 572–582. https://doi.org/10.2514/1.b37015.

[30] Sziroczak, D., Jankovics, I., Gal, I., and Rohacs, D., "Conceptual Design of Small Aircraft with Hybrid-Electric Propulsion Systems," *Energy*, Vol. 204, 2020, p. 117937. https://doi.org/10.1016/j.energy.2020.117937.

[31] Winnefeld, C., Kadyk, T., Bensmann, B., Krewer, U., and Hanke-Rauschenbach, R., "Modelling and Designing Cryogenic Hydrogen Tanks for Future Aircraft Applications," *Energies*, Vol. 11, No. 1, 2018, p. 105. https://doi.org/10.3390/en11010105.

[32] Baroutaji, A., Wilberforce, T., Ramadan, M., and Olabi, A. G., "Comprehensive Investigation on Hydrogen and Fuel Cell Technology in the Aviation and Aerospace Sectors," *Renewable and Sustainable Energy Reviews*, Vol. 106, May 2019, pp. 31–40. https://doi.org/10.1016/j.rser.2019.02.022.

[33] Kadyk, T., Winnefeld, C., Hanke-Rauschenbach, R., and Krewer, U., "Analysis and Design of Fuel Cell Systems for Aviation," *Energies*, Vol. 11, No. 2, 2018, p. 375. https://doi.org/10.3390/en11020375.

[34] Abu Kasim, A., Chan, M., and Marek, E., "Performance and Failure Analysis of a Retrofitted Cessna Aircraft with a Fuel Cell Power System Fuelled with Liquid Hydrogen," *Journal of Power Sources*, Vol. 521, 2022, p. 230987. https://doi.org/10.1016/j.jpowsour.2022.230987.

[35] Massaro, M. C., Biga, R., Kolisnichenko, A., Marocco, P., Monteverde, A. H. A., and Santarelli, M., "Potential and Technical Challenges of On-board Hydrogen Storage Technologies Coupled with Fuel Cell Systems for Aircraft Electrification," *Journal of Power Sources*, Vol. 555, January, 2023, p. 232397. https://doi.org/10.1016/j.jpowsour.2022.232397.

[36] Rupiper, L. N., Skabelund, B. B., Ghotkar, R., and Milcarek, R. J., "Impact of Fuel Type on the Performance of a Solid Oxide Fuel Cell Integrated with a Gas Turbine," *Sustainable Energy Technologies and Assessments*, Vol. 51, 2022, p. 101959. https://doi.org/https://doi.org/10.1016/j.seta.2022.101959.

[37] Seitz, A., Nickl, M., Troeltsch, F., and Ebner, K., "Initial Assessment of a Fuel Cell—Gas Turbine Hybrid Propulsion Concept," *Aerospace*, Vol. 9, No. 2, 2022. https://doi.org/10.3390/aerospace9020068.

[38] Adler, E. J., and Martins, J. R. R. A., "Blended Wing Body Configuration for Hydrogen-Powered Aviation," *Journal of Aircraft*, Vol. 61, No. 3, 2024, pp. 887–901. https://doi.org/10.2514/1.C037582.

[39] Karpuk, S., Ma, Y., and Elham, A., "Design Investigation of Potential Long-Range Hydrogen Combustion Blended Wing Body Aircraft with Future Technologies," *Aerospace*, Vol. 10, No. 6, 2023, p. 566. https://doi.org/10.3390/aerospace10060566.

[40] Valencia, E. A., Hidalgo, V., Laskaridis, P., Nalianda, D., Singh, R., and Liu, C., "Design Point Analysis of a Hybrid Fuel Cell Gas Turbine Cycle for Advanced Distributed Propulsion Systems," *51st AIAA/SAE/ASEE Joint Propulsion Conference*, Orlando, Florida, 2015, p. 3802. https://doi.org/10.2514/6.2015-3802.

[41] Felder, J., Kim, H., and Brown, G., "Turboelectric Distributed Propulsion Engine Cycle Analysis for Hybrid-Wing-Body Aircraft," *47th AIAA Aerospace Sciences Meeting including the New Horizons Forum and Aerospace Exposition*, American Institute of Aeronautics and Astronautics, Orlando, Florida, 2009, p. 1132. https://doi.org/10.2514/6.2009-1132.

[42] Rossi, I., Traverso, A., and Tucker, D., "SOFC/Gas Turbine Hybrid System: A Simplified Framework for Dynamic Simulation," *Applied Energy*, Vol. 238, 2019, pp. 1543–1550. https://doi.org/10.1016/j.apenergy.2019.01.092.

[43] Roberts, R. A., and Brouwer, J., "Dynamic Simulation of a Pressurized 220kW Solid Oxide Fuel-Cell–Gas-Turbine Hybrid System: Modeled Performance Compared to Measured Results," *Journal of Fuel Cell Science and Technology*, Vol. 3, No. 1, 2006, pp. 18–25. https://doi.org/10.1115/1.2133802.

[44] Mueller, F., Jabbari, F., Brouwer, J., Roberts, R., Junker, T., and Ghezel-Ayagh, H., "Control Design for a Bottoming Solid Oxide Fuel Cell Gas Turbine Hybrid System," *Journal of Fuel Cell Science and Technology*, Vol. 4, No. 3, 2007, pp. 221–230. https://doi.org/10.1115/1.2713785.

[45] Pourabedin, G., "Dynamic Modeling of Planar Solid Oxide Fuel Cell System for Regional Jet Aircraft Application (Simple System)," *International Journal of Modern Studies in Mechanical Engineering*, Vol. 4, No. 2, 2018. https://doi.org/10.20431/2454-9711.0402003.

[46] Chakravarthula, V. A., "Transient Analysis of a Solid Oxide Fuel Cell/ Gas Turbine Hybrid System for Distributed Electric Propulsion," , 2016.

[47] Zhang, B., Maloney, D., Farida Harun, N., Zhou, N., Pezzini, P., Medam, A., Hovsapian, R., Bayham, S., and Tucker, D., "Rapid Load Transition for Integrated Solid Oxide Fuel Cell – Gas Turbine (SOFC-GT) Energy Systems: A Demonstration of the Potential for Grid Response," *Energy Conversion and Management*, Vol. 258, 2022, p. 115544. https://doi.org/10.1016/j.enconman.2022.115544.

[48] Ahrend, P. N., "Solid Oxide Fuel Cell Hybrid Systems for Dynamic Rail Applications," Ph.D. thesis, University of California, Irvine, 2020.

[49] Ferrari, M. L., Rossi, I., Sorce, A., and Massardo, A. F., "Advanced Control System for Grid-Connected SOFC Hybrid Plants: Experimental Verification in Cyber-Physical Mode," *Journal of Engineering for Gas Turbines and Power*, Vol. 141, No. 9, 2019, p. 091019. https://doi.org/10.1115/1.4044196.

[50] McLarty, D. F., "Fuel Cell Gas Turbine Hybrid Design, Control, and Performance," , 2010.

[51] Uppink, L., Ganguli, M., and Riedel, R., "Making Net-Zero Aviation Possible: An Industry-Backed, 1.5°C-Aligned Transition Strategy," , 2022.

[52] Carter, S., Li, J., Mitchell, A., Saposnik, M., Riedel, R., and Hyde, D., "Target True Zero: Infrastructure for Alternative Propulsion Flight," , 2023.

[53] Hoelzen, J., Koenemann, L., Kistner, L., Schenke, F., Bensmann, A., and Hanke-Rauschenbach, R., "H2-Powered Aviation–Design and Economics of Green LH2 Supply for Airports," *Energy Conversion and Management: X*, Vol. 20, 2023, p. 100442.

[54] Amy, C., and Kunycky, A., "Hydrogen as a Renewable Energy Carrier for Commercial Aircraft," , 2019.

[55] Gössling, S., and Dolnicar, S., "Review of Air Travel Behavior and Climate Change," *Wiley Interdisciplinary Reviews: Climate Change*, Vol. 14, No. 1, 2023, p. e802. https://doi.org/10.1002/wcc.802.

[56] Nojoumi, H., Dincer, I., and Naterer, G., "Greenhouse Gas Emissions Assessment of Hydrogen and Kerosene-Fueled Aircraft Propulsion," *International Journal of Hydrogen Energy*, Vol. 34, No. 3, 2009, pp. 1363–1369. https://doi.org/10.1016/j.ijhydene.2008.11.017.

[57] Barton, D. I., Hall, C. A., and Oldfield, M. K., "Design of a Hydrogen Aircraft for Zero Persistent Contrails," *Aerospace*, Vol. 10, No. 8, 2023. https://doi.org/10.3390/aerospace10080688.

[58] Liu, Y., Sun, X., Sethi, V., Nalianda, D., Li, Y.-G., and Wang, L., "Review of Modern Low Emissions Combustion Technologies for Aero Gas Turbine Engines," *Progress in Aerospace Sciences*, Vol. 94, October 2017, pp. 12–45. https://doi.org/10.1016/j.paerosci.2017.08.001.

[59] Stefan, E., Talic, B., Larring, Y., Gruber, A., and Peters, T. A., "Materials Challenges in Hydrogen-Fuelled Gas Turbines," *International Materials Reviews*, Vol. 67, No. 5, 2022, pp. 461–486. https://doi.org/10.1080/09506608.2021.1981706.

[60] Ahluwalia, R., Hua, T., Peng, J.-K., Lasher, S., McKenney, K., Sinha, J., and Gardiner, M., "Technical Assessment of Cryo-Compressed Hydrogen Storage Tank Systems for Automotive Applications," *International Journal of Hydrogen Energy*, Vol. 35, No. 9, 2011, pp. 4171–4184. https://doi.org/10.1016/j.ijhydene.2010.02.074.

[61] Wilson, J. A., Wang, Y., Carroll, J., Raush, J., Arkenberg, G., Dogdibegovic, E., Swartz, S., Daggett, D., Singhal, S., and Zhou, X.-D., "Hybrid Solid Oxide Fuel Cell/Gas Turbine Model Development for Electric Aviation," *Energies*, Vol. 15, No. 8, 2022. https://doi.org/10.3390/en15082885.

[62] Scholz, A. E., Michelmann, J., and Hornung, M., "Fuel Cell Hybrid-Electric Aircraft: Design, Operational, and Environmental Impact," *Journal of Aircraft*, Vol. 60, No. 1, 2022, pp. 606–622. https://doi.org/10.2514/1.C036952.

[63] Collins, J. M., and McLarty, D., "All-Electric Commercial Aviation with Solid Oxide Fuel Cell-Gas Turbine-Battery Hybrids," *Applied Energy*, Vol. 265, 2020, p. 114787. https://doi.org/10.1016/j.apenergy.2020.114787.

[64] Tornabene, R., Wang, X., Steffen, J., C.J., and Freeh, J., "Development of Parametric Mass and Volume Models for an Aerospace SOFC/Gas Turbine Hybrid System," *Proceedings of the ASME Turbo Expo 2005: Power for Land, Sea, and Air*, Turbo Expo 2005, Vol. 5, ASME, Reno, Nevada, USA, 2005, pp. 135–144. https://doi.org/10.1115/GT2005-68334.

[65] Haran, K. S., Kalsi, S., Arndt, T., Karmaker, H., Badcock, R., Buckley, B., Haugan, T., Izumi, M., Loder, D., Bray, J. W., Masson, P., and Stautner, E. W., "High Power Density Superconducting Rotating

Machines—Development Status and Technology Roadmap," *Superconductor Science and Technology*, Vol. 30, No. 12, 2017, p. 123002. https://doi.org/10.1088/1361-6668/aa833e.

[66] Winnefeld, C., Kadyk, T., Bensmann, B., Krewer, U., and Hanke-Rauschenbach, R., "Modelling and Designing Cryogenic Hydrogen Tanks for Future Aircraft Applications," *Energies*, Vol. 11, No. 1, 2018, p. 105. https://doi.org/10.3390/en11010105.

[67] Rivard, E., Trudeau, M., and Zaghib, K., "Hydrogen Storage for Mobility: A Review," *Materials*, Vol. 12, No. 12, 2019. https://doi.org/10.3390/ma12121973.

[68] Colozza, A. J., and Kohout, L., "Hydrogen Storage for Aircraft Applications Overview," Tech. Rep. NASA/CR-2002-211867, NASA, September 2002.

[69] Hamel, C., Sassi, A., Botez, R., and Dartigues, C., "Cessna Citation X Aircraft Global Model Identification from Flight Tests," *SAE International Journal of Aerospace*, Vol. 6, No. 1, 2013, pp. 106–114. https://doi.org/10.4271/2013-01-2094.

[70] Takahashi, T., *Aircraft Performance and Sizing, Volume I: Fundamentals of Aircraft Performance*, Aerospace Engineering Collection, Momentum Press, New York, New York, 2017.

[71] Shevell, R. S., *Fundamental Principles of Flight*, 2nd ed., Prentice Hall, Hoboken, New Jersey, 1989.

[72] Palies, P. P., "Hydrogen Thermal-Powered Aircraft Combustion and Propulsion System," *Journal of Engineering for Gas Turbines and Power*, Vol. 144, No. 10, 2022, p. 101007. https://doi.org/10.1115/1.4055270.

[73] Ocko, I. B., and Hamburg, S. P., "Climate Consequences of Hydrogen Emissions," *Atmospheric Chemistry and Physics*, Vol. 22, No. 14, 2022, pp. 9349–9368. https://doi.org/10.5194/acp-22-9349-2022.

[74] Wayson, R. L., Fleming, G. G., and Iovinelli, R., "Methodology to Estimate Particulate Matter Emissions from Certified Commercial Aircraft Engines," *Journal of the Air & Waste Management Association*, Vol. 59, No. 1, 2009, pp. 91–100. https://doi.org/10.3155/1047-3289.59.1.91.

[75] Therkelsen, P., Werts, T., McDonell, V., and Samuelsen, S., "Analysis of NOx Formation in a Hydrogen-Fueled Gas Turbine Engine," *Journal of Engineering for Gas Turbines and Power*, Vol. 131, No. 3, 2009, p. 031507. https://doi.org/10.1115/1.3028232.

[76] Khan, M. A. H., Brierley, J., Tait, K. N., Bullock, S., Shallcross, D. E., and Lowenberg, M. H., "The Emissions of Water Vapour and NOx from Modelled Hydrogen-Fuelled Aircraft and the Impact of NOx Reduction on Climate Compared with Kerosene-Fuelled Aircraft," *Atmosphere*, Vol. 13, No. 10, 2022. https://doi.org/10.3390/atmos13101660.

[77] Prewitz, M., Bardenhagen, A., and Beck, R., "Hydrogen as the Fuel of the Future in Aircrafts – Challenges and Opportunities," *International Journal of Hydrogen Energy*, Vol. 45, No. 46, 2020, pp. 25378–25385. https://doi.org/10.1016/j.ijhydene.2020.06.238.

[78] Ingenito, A., Agresta, A., Andriani, R., and Gamma, F., "NOx Reduction Strategies for High Speed Hydrogen Fuelled Vehicles," *International Journal of Hydrogen Energy*, Vol. 40, No. 15, 2015, pp. 5186–5196. https://doi.org/10.1016/j.ijhydene.2015.02.100.

[79] Stettler, M. E. J., Koudis, G. S., Hu, S. J., Majumdar, A., and Ochieng, W. Y., "The Impact of Single Engine Taxiing on Aircraft Fuel Consumption and Pollutant Emissions," *The Aeronautical Journal*, Vol. 122, No. 1258, 2018, p. 1967–1984. https://doi.org/10.1017/aer.2018.117.

[80] Di Mascio, P., Corazza, M. V., Rosa, N. R., and Moretti, L., "Optimization of Aircraft Taxiing Strategies to Reduce the Impacts of Landing and Take-Off Cycle at Airports," *Sustainability*, Vol. 14, No. 15, 2022. https://doi.org/10.3390/su14159692.

[81] Khardi, S., "Optimization of Aircraft Fuel Consumption and Reduction of Pollutant Emissions: Environmental Impact Assessment," *Advances in aircraft and spacecraft science*, Vol. 1, No. 3, 2014, pp. 311–330. https://doi.org/10.12989/aas.2014.1.3.311.

[82] Gierens, K., "Theory of Contrail Formation for Fuel Cells," *Aerospace*, Vol. 8, No. 6, 2021. https://doi.org/10.3390/aerospace8060164.

[83] Spangenberg, D., Minnis, P., Bedka, S., Palikonda, R., Duda, D., and Rose, F., "Contrail Radiative Forcing

over the Northern Hemisphere from 2006 Aqua MODIS Data," *Geophysical Research Letters*, Vol. 40, No. 3, 2013, pp. 595–600. https://doi.org/10.1002/grl.50168.

[84] Koroneos, C., Dompros, A., Roumbas, G., and Moussiopoulos, N., "Advantages of the Use of Hydrogen Fuel as Compared to Kerosene," *Resources, Conservation and Recycling*, Vol. 44, No. 2, 2005, pp. 99–113. https://doi.org/10.1016/j.resconrec.2004.09.004.

[85] Detsios, N., Theodoraki, S., Maragoudaki, L., Atsonios, K., Grammelis, P., and Orfanoudakis, N. G., "Recent Advances on Alternative Aviation Fuels/Pathways: A Critical Review," *Energies*, Vol. 16, No. 4, 2023. https://doi.org/10.3390/en16041904.

[86] Kakoulaki, G., Kougias, I., Taylor, N., Dolci, F., Moya, J., and Jäger-Waldau, A., "Green Hydrogen in Europe – A Regional Assessment: Substituting Existing Production with Electrolysis Powered by Renewables," *Energy Conversion and Management*, Vol. 228, January 2021, p. 113649. https://doi.org/10.1016/j.enconman.2020.113649.

[87] Al-Breiki, M., and Bicer, Y., "Comparative Life Cycle Assessment of Sustainable Energy Carriers Including Production, Storage, Overseas Transport, and Utilization," *Journal of Cleaner Production*, Vol. 279, January, 2021, p. 123481. https://doi.org/10.1016/j.jclepro.2020.123481.

[88] Howarth, R. W., and Jacobson, M. Z., "How Green is Blue Hydrogen?" *Energy Science & Engineering*, Vol. 9, No. 10, 2021, pp. 1676–1687. https://doi.org/10.1002/ese3.956.

[89] Ajanovic, A., Sayer, M., and Haas, R., "The Economics and the Environmental Benignity of Different Colors of Hydrogen," *International Journal of Hydrogen Energy*, Vol. 47, No. 57, 2022, pp. 24136–24154. https://doi.org/10.1016/j.ijhydene.2022.02.094.

[90] Ghorbani, B., Zendehboudi, S., Saady, N. M. C., Duan, X., and Albayati, T. M., "Strategies To Improve the Performance of Hydrogen Storage Systems by Liquefaction Methods: A Comprehensive Review," *American Chemical Society Omega*, Vol. 8, No. 21, 2023, pp. 18358–18399. https://doi.org/10.1021/acsomega.3c01072.

[91] Hoelzen, J., Silberhorn, D., Zill, T., Bensmann, B., and Hanke-Rauschenbach, R., "Hydrogen-Powered Aviation and Its Reliance on Green Hydrogen Infrastructure – Review and Research Gaps," *International Journal of Hydrogen Energy*, Vol. 47, No. 5, 2022, pp. 3108–3130. https://doi.org/10.1016/j.ijhydene.2021.10.239.

[92] Yang, B., Mane, M., and Crossley, W. A., "An Approach to Evaluate Fleet Level CO2 Impact of Introducing Liquid-Hydrogen Aircraft to a World-Wide Network," *AIAA Aviation and Aeronautics Forum and Exposition*, AIAA paper 2022-3313, Chicago, Illinois, 2022. https://doi.org/10.2514/6.2022-3313.

[93] Xing, H., Stuart, C., Spence, S., and Chen, H., "Fuel Cell Power Systems for Maritime Applications: Progress and Perspectives," *Sustainability*, Vol. 13, No. 3, 2021, p. 1213. https://doi.org/10.3390/su13031213.

[94] Chua, K., Yang, W., Er, S., and Ho, C., "Sustainable Energy Systems for a Remote Island Community," *Applied Energy*, Vol. 113, January 2014, pp. 1752–1763. https://doi.org/10.1016/j.apenergy.2013.09.030.

[95] Varbanov, P. S., Wang, B., Klemeš, J. J., Kabli, M. R., Shahzad, K., and Ocłoń, P., "Municipal Power Plan Optimisation Accounting for Environmental Footprints," *Energy Conversion and Management*, Vol. 254, February, 2022, p. 115296. https://doi.org/10.1016/j.enconman.2022.115296.

[96] Sobieralski, J. B., and Mumbower, S., "Jet-Setting During COVID-19: Environmental Implications of the Pandemic-Induced Private Aviation Boom," *Transportation Research Interdisciplinary Perspectives*, Vol. 13, March 2022, p. 100575. https://doi.org/10.1016/j.trip.2022.100575.

[97] Khan, M. A. H., Brierley, J., Tait, K. N., Bullock, S., Shallcross, D. E., and Lowenberg, M. H., "The Emissions of Water Vapour and NOx from Modelled Hydrogen-Fuelled Aircraft and the Impact of NOx Reduction on Climate Compared with Kerosene-Fuelled Aircraft," *Atmosphere*, Vol. 13, No. 10, 2022, p. 1660. https://doi.org/10.3390/atmos13101660.

[98] Fuglestvedt, J., Shine, K., Berntsen, T., Cook, J., Lee, D., Stenke, A., Skeie, R., Velders, G., and Waitz, I., "Transport Impacts on Atmosphere and Climate: Metrics," *Atmospheric Environment*, Vol. 44, No. 37, 2010, pp. 4648–4677. https://doi.org/10.1016/j.atmosenv.2009.04.044.

[99] Skowron, A., Lee, D. S., and De León, R. R., "Variation of Radiative Forcings and Global Warming Potentials from Regional Aviation NOx Emissions," *Atmospheric Environment*, Vol. 104, 2015, pp. 69–78. https://doi.org/10.1016/j.atmosenv.2014.12.043.

[100] Jungbluth, N., and Meili, C., "Recommendations for Calculation of the Global Warming Potential of Aviation Including the Radiative Forcing Index," *The International Journal of Life Cycle Assessment*, Vol. 24, 2019, pp. 404–411. https://doi.org/10.1007/s11367-018-1556-3.

[101] Königshofer, B., Boškoski, P., Nusev, G., Koroschetz, M., Hochfellner, M., Schwaiger, M., Đani Juričić, Hochenauer, C., and Subotić, V., "Performance Assessment and Evaluation of SOC Stacks Designed for Application in a Reversible Operated 150 kW rSOC Power Plant," *Applied Energy*, Vol. 283, 2021, p. 116372. https://doi.org/10.1016/j.apenergy.2020.116372.

[102] Eichhorn Colombo, K. W., Schütz, P., and Kharton, V. V., "Reliability Analysis for a Multi-Stack Solid Oxide Fuel Cell System Subject to Operation Condition-Dependent Degradation," *Journal of Quality in Maintenance Engineering*, Vol. 28, No. 1, 2022, pp. 102–130. https://doi.org/10.1108/JQME-04-2020-0021.

[103] Nakajo, A., Mueller, F., McLarty, D., Brouwer, J., herle, J. V., and Favrat, D., "The Effects of Dynamic Dispatch on the Degradation and Lifetime of Solid Oxide Fuel Cell Systems," *Journal of The Electrochemical Society*, Vol. 158, No. 11, 2011, p. B1329. https://doi.org/10.1149/2.032111jes.

[104] Ido, A., Asano, K., Morita, H., Yamamoto, T., and Mugikura, Y., "Degradation Analysis of SOFC Performance (1) — Severe Operation with High Fuel Utilization," *ECS Transactions*, Vol. 91, No. 1, 2019, p. 801. https://doi.org/10.1149/09101.0801ecst.

[105] Tucker, D., Abreu-Sepulveda, M., and Harun, N. F., "SOFC Lifetime Assessment in Gas Turbine Hybrid Power Systems," *Journal of Fuel Cell Science and Technology*, Vol. 11, No. 5, 2014, p. 051008. https://doi.org/10.1115/1.4028158.

[106] Staffell, I., Ingram, A., and Kendall, K., "Energy and Carbon Payback Times for Solid Oxide Fuel Cell Based Domestic CHP," *International Journal of Hydrogen Energy*, Vol. 37, 2012, pp. 2509–2523. https://doi.org/10.1016/j.ijhydene.2011.10.060.

[107] Lanzini, A., Madi, H., Chiodo, V., Papurello, D., Maisano, S., Santarelli, M., and Herle, J. V., "Dealing with Fuel Contaminants in Biogas-Fed Solid Oxide Fuel Cell (SOFC) and Molten Carbonate Fuel Cell (MCFC) Plants: Degradation of Catalytic and Electro-Catalytic Active Surfaces and Related Gas Purification Methods," *Progress in Energy and Combustion Science*, Vol. 61, No. 7, 2017, pp. 150–188. https://doi.org/10.1016/j.pecs.2017.04.002.

[108] Mougin, J., Ravel, S., de Vito, E., and Petijean, M., "Influence of Fuel Contaminants on SOFC Operation:

Effect on Performance and Degradation Mechanisms," *The Electrochemical Society Transactions*, Vol. 7, No. 1, 2007, p. 459. https://doi.org/10.1149/1.2729124.

[109] Fragiacomo, P., Piraino, F., Genovese, M., Corigliano, O., and De Lorenzo, G., "Experimental Activities on a Hydrogen-Powered Solid Oxide Fuel Cell System and Guidelines for Its Implementation in Aviation and Maritime Sectors," *Energies*, Vol. 16, No. 15, 2023. https://doi.org/10.3390/en16155671.

[110] Mendonça, C., Ferreira, A., and Santos, D. M. F., "Towards the Commercialization of Solid Oxide Fuel Cells: Recent Advances in Materials and Integration Strategies," *Fuels*, Vol. 2, No. 4, 2021, pp. 393–419. https://doi.org/10.3390/fuels2040023.

[111] Zeng, Z., Qian, Y., Zhang, Y., Hao, C., Dan, D., and Zhuge, W., "A Review of Heat Transfer and Thermal Management Methods for Temperature Gradient Reduction in Solid Oxide Fuel Cell (SOFC) Stacks," *Applied Energy*, Vol. 280, No. 12, 2020, p. 115899. https://doi.org/10.1016/j.apenergy.2020.115899.

[112] Sanz-Morère, I., Eastham, S. D., Speth, R. L., and Barrett, S. R. H., "Reducing Uncertainty in Contrail Radiative Forcing Resulting from Uncertainty in Ice Crystal Properties," *Environmental Science & Technology Letters*, Vol. 7, No. 6, 2020, pp. 371–375. https://doi.org/10.1021/acs.estlett.0c00150.

[113] McLarty, D., Jones, N., Mikeska, H., Mills, A., and Panossian, N., "The Efficient Allocation of Grid Energy Resources Including Storage (EAGERS)," , 2018. Retrieved 8 September 2023 from https://github.com/CESI-Lab/EAGERS.

[114] Ormerod, R. M., "Solid Oxide Fuel Cells," *Chemical Society Reviews*, Vol. 32, No. 1, 2003, pp. 17–28. https://doi.org/10.1039/b105764m.

[115] Dicks, A. L., and Rand, D. A. J., *Fuel Cell Systems Explained*, John Wiley Sons, 2018.

[116] McLarty, D., Brouwer, J., and Samuelsen, S., "A Spatially Resolved Physical Model for Transient System Analysis of High Temperature Fuel Cells," *International Journal of Hydrogen Energy*, Vol. 38, No. 19, 2013, pp. 7935–7946. https://doi.org/10.1016/j.ijhydene.2013.03.070.

[117] Wilson, J. A., Wang, Y., Carroll, J., Raush, J., Arkenberg, G., Dogdibegovic, E., Swartz, S., Daggett, D., Singhal, S., and Zhou, X.-D., "Hybrid Solid Oxide Fuel Cell/Gas Turbine Model Development for Electric Aviation," *Energies*, Vol. 15, No. 8, 2022, p. 2885. https://doi.org/10.3390/en15082885.

[118] Lee, G. J., "More Efficient Dynamic Operation of Fueled Dispatchable Power Generation in a High Renewable Penetration Grid," Ph.D. thesis, University of California, Irvine, 2022.

[119] McLarty, D., Brouwer, J., and Samuelsen, S., "Hybrid Fuel Cell Gas Turbine System Design and Optimization," *Journal of Fuel Cell Science and Technology*, Vol. 10, No. 4, 2013, p. 041005.

[120] Alsamri, K., De la Cruz, J., Emmanouilidi, M., Huynh, J., and Brouwer, J., "Methodology for Assessing Retrofitted Hydrogen Combustion and Fuel Cell Aircraft Environmental Impacts," *Journal of Propulsion and Power*, Vol. 40, No. 1, 2024, pp. 1–16. https://doi.org/10.2514/1.B39405.

[121] Jane, F. T., *Jane's All the World's Aircraft*, Jane's all the world's aircraft, 1909. [26].

[122] Radebaugh, R., *Cryocoolers for Aircraft Superconducting Generators and Motors*, Vol. 1434, 2012. [28].

[123] "FAA, 2022-03967," , ???? URL https://www.federalregister.gov/d/2022-03967, retrieved 12 November 2023.

[124] Kammermann, J., Bolvashenkov, I., Tran, K., Herzog, H.-G., and Frenkel, I., "Feasibility Study for a Full-Electric Aircraft Considering Weight, Volume, and Reliability Requirements," *2020 IEEE Conference on Electrical and Computer Engineering*, 2020. https://doi.org/10.1109/ICOECS50468.2020.9278461, [31].

[125] Saeedmanesh, A., Colombo, P., McLarty, D., and Brouwer, J., "Dynamic Behavior of a Solid Oxide Steam Electrolyzer System Using Transient Photovoltaic Generated Power for Renewable Hydrogen Production," *Journal of Electrochemical Energy Conversion and Storage*, Vol. 16, No. 4, 2019. https://doi.org/10.1115/1.4043340, [32].

[126] Kandepu, R., Imsland, L., Foss, B. A., Stiller, C., Thorud, B., and Bolland, O., "Modeling and Control of a SOFC-GT-Based Autonomous Power System," *Energy*, Vol. 32, No. 4, 2007, pp. 406–417. https://doi.org/10.1016/j.energy.2006.07.034, [33].

[127] Brouwer, J., "Hybrid Gas Turbine Fuel Cell Systems," , 2003. [34].

[128] Kroeze, R. C., and Krein, P. T., "Electrical Battery Model for Use in Dynamic Electric Vehicle Simulations," *Proceedings of the IEEE Vehicle Power and Propulsion Conference*, 2008. [35].

[129] Ding, Y., Cano, Z. P., Yu, A., Lu, J., and Chen, Z., "Automotive Li-Ion Batteries: Current Status and Future Perspectives," *Electrochemical Energy Reviews*, Vol. 2, 2019, pp. 1–28. [36].

[130] Clarke, M., and Alonso, J. J., "Lithium–Ion Battery Modeling for Aerospace Applications," *Journal of Aircraft*, Vol. 58, No. 6, 2021, pp. 1323–1335. [37].

[131] Sabatier, J., Francisco, J. M., Guillemard, F., Lavigne, L., Moze, M., and Merveillaut, M., "Lithium-Ion Batteries Modeling: A Simple Fractional Differentiation Based Model and Its Associated Parameters Estimation Method," *Signal Processing*, Vol. 107, 2015, pp. 290–301. [38].

[132] Yao, L. W., Aziz, J. A., Kong, P. Y., and Idris, N. R. N., "Modeling of Lithium-Ion Battery Using MATLAB/Simulink," *Proceedings of the IEEE International Conference on Electric and Hybrid Vehicles*, 2013. [39].

[133] Wang, Z., Feng, G., Liu, X., Gu, F., and Ball, A., "A Novel Method of Parameter Identification and State of Charge Estimation for Lithium-Ion Battery Energy Storage System," *Journal of Energy Storage*, Vol. 49, 2022, p. 104124. [40].

[134] Lin, C., Yu, Q., and Xiong, R., "A Study on the Impact of Open Circuit Voltage Tests on State of Charge Estimation for Lithium-Ion Batteries," *Applied Energy*, Vol. 205, 2017, pp. 892–902. [41].

[135] Schmalstieg, J., Käbitz, S., Ecker, M., and Sauer, D. U., "A Holistic Aging Model for Li (NiMnCo) O2 Based 18650 Lithium-Ion Batteries," *Journal of Power Sources*, Vol. 248, 2014, pp. 507–521. [42].

[136] Karpuk, S., Ma, Y., and Elham, A., "Design Investigation of Potential Long-Range Hydrogen Combustion Blended Wing Body Aircraft with Future Technologies," *Aerospace*, Vol. 10, No. 6, 2023, p. 566. https://doi.org/10.3390/aerospace10060566.

[137] Wells, D. P., Horvath, B. L., and Mccullers, L. A., "The Flight Optimization System Weights Estimation Method," Tech. rep., 2017. URL http://www.sti.nasa.gov.

[138] McDonald, R. A., and Gloudemans, J. R., "Open Vehicle Sketch Pad: An Open Source Parametric Geometry and Analysis Tool for Conceptual Aircraft Design," *AIAA Science and Technology Forum and Exposition, AIAA SciTech Forum 2022*, American Institute of Aeronautics and Astronautics Inc, AIAA, 2022. https://doi.org/10.2514/6.2022-0004.

[139] Kimmel, W. M., and Bradley, K. R., "A Sizing Methodology for the Conceptual Design of Blended-Wing-Body Transports," Tech. Rep. NASA/CR-2004-213016, 2004.

[140] Liebeck, R. H., "Design of the Blended Wing Body Subsonic Transport," *Journal of Aircraft*, Vol. 41, No. 1, 2004, pp. 10–25. https://doi.org/10.2514/1.9084.

[141] Marchman, J. F., Walz, A., Grey, K., and Virginia Polytechnic Institute and State University. University Libraries, *Aerodynamics and Aircraft Performance*, Virginia Tech Publishing, Blacksburg, VA, ISBN: 9781949373622, 2018.

[142] Alsamri, K., Rezaei, S., Chung, V., Huynh, J., and Brouwer, J., "Dynamic modeling of Hydrogen SOFC/GT powered Aircraft with integration analysis," *AIAA SCITECH 2024 Forum*, 2024, p. 1532. https://doi.org/10.2514/6.2024-1532.

[143] Zhang, B., Maloney, D., Farida Harun, N., Zhou, N., Pezzini, P., Medam, A., Hovsapian, R., Bayham, S., and Tucker, D., "Rapid Load Transition for Integrated Solid Oxide Fuel Cell – Gas Turbine (SOFC-GT) Energy Systems: A Demonstration of the Potential for Grid Response," *Energy Conversion and Management*, Vol. 258, 2022, p. 115544. https://doi.org/10.1016/j.enconman.2022.115544, URL https://doi.org/10.1016/j.enconman.2022.115544.

[144] McLarty, D. F., "Fuel Cell Gas Turbine Hybrid Design, Control, and Performance," Ph.D. thesis, University of California, Irvine, 2010. URL https://www.proquest.com/dissertations-theses/fuel-cell-gas-turbine-hybrid-design-control/docview/758398393/se-2?accountid=14509.

[145] NASA Glenn Research Center, "High power density SOFC: Technology solution power generation and storage," Tech. Rep. NP-2017-07-2426-HQ, NASA Glenn Research Center, 2017.

[146] NASA Technology Transfer Program, "High Power Density Solid Oxide Fuel Cell," NASA Tech Briefs, n.d. URL https://www.techbriefs.com/component/content/article/tb/pub/briefs/energy/33394.

[147] Felder, J. L., Brown, G. V., DaeKim, H., and Chu, J., "Turboelectric Distributed Propulsion in a Hybrid Wing Body Aircraft," Technical Report ISABE-2011-1340, NASA Glenn Research Center, Cleveland, Ohio, July 2011.

[148] Asghari, M., "Integration of Solid Oxide Fuel Cell with Liquid Desiccant Cooling for Generation of Combined Cooling and Power for Data Center Application," , 2022.

[149] McFarland, C., and Agarwal, R. K., "A Simple Model of Thermal Insulation Design for Cryogenic Liquid Hydrogen Tank," Technical report, McKelvey School of Engineering, Washington University in St. Louis, April 2022. https://doi.org/10.7936/3ens-v661.

[150] Choi, D., Lee, S., and Kim, S., "A Thermodynamic Model for Cryogenic Liquid Hydrogen Fuel Tanks," *Applied Sciences*, Vol. 14, No. 9, 2024, p. 3786. https://doi.org/10.3390/app14093786.

[151] Andersson, G. Z., "Mathematical Modeling and Simulation of Cryogenic Liquid Hydrogen Storage," Master's thesis, Lund University, 2023. URL: http://lup.lub.lu.se/student-papers/record/9116856.

[152] International Civil Aviation Organization, "ICAO Aircraft Engine Emissions Databank," , 2023. URL https://www.easa.europa.eu/en/domains/environment/icao-aircraft-engine-emissions-databank, accessed: 2024-06-04.

[153] Hasanzadeh, A., Chitsaz, A., Mojaver, P., and Ghasemi, A., "Stand-Alone Gas Turbine and Hybrid MCFC and SOFC-Gas Turbine Systems: Comparative Life Cycle Cost, Environmental, and Energy Assessments," *Energy Reports*, Vol. 7, 2021, pp. 4659–4680. https://doi.org/https://doi.org/10.1016/j.egyr.2021.07.050, URL https://www.sciencedirect.com/science/article/pii/S2352484721005151.

[154] Lundberg, W. L., Israelson, G. A., Moeckel, M. D., Veyo, S. E., Holmes, R. A., Zafred, P. R., King, J. E., and Kothmann, R. E., "A High Efficiency PSOFC/ATS-Gas Turbine Power System," 2001. https://doi.org/10.2172/859228, URL https://www.osti.gov/biblio/859228.

[155] Sinha, A. A., Srivastava, K., Rajpoot, A. S., Choudhary, T., Pandey, S., and Sanjay, "A Thermodynamic Approach to Analyze Energy, Exergy, Emission, and Sustainability (3E-S) Performance by Utilizing Low Temperature Waste Heat in SOFC–CHP-TEG System," *International Journal of Hydrogen Energy*, Vol. 63, 2024, pp. 1088–1104. https://doi.org/https://doi.org/10.1016/j.ijhydene.2024.03.194, URL https://www.sciencedirect.com/science/article/pii/S0360319924010322.

[156] He, Z. J., Chang, C., and Follen, C., "NOx Emissions Performance and Correlation Equations for a Multipoint LDI Injector," *53rd AIAA Aerospace Sciences Meeting*, 2015, p. 0098. https://doi.org/10.2514/6.2015-0098.

[157] FuelCell Energy, "Solid Oxide Fuel Cell Spec Sheet," , 2022. URL https://go.fuelcellenergy.com/hubfs/ Solid%20Oxide%20Fuel%20Cell%20Spec%20Sheet.pdf.

[158] Murphy, D. M., and Koop, T., "Review of the Vapour Pressures of Ice and Supercooled Water for Atmospheric Applications," *Quarterly Journal of the Royal Meteorological Society: A Journal of the Atmospheric Sciences, Applied Meteorology and Physical Oceanography*, Vol. 131, No. 608, 2005, pp. 1539–1565. https://doi.org/10.1256/qj.04.94.

[159] FlightAware, "FlightAware: CPA881 Flight History from KLAX to VHHH," , December 2023. URL https://www.flightaware.com/live/flight/CPA881/history/20231210/0730Z/KLAX/VHHH, accessed: 2023-06-22.

[160] Jane, F. T. F. T., "Jane's all the world's aircraft." *Jane's all the world's aircraft.*, 1909.

[161] Page, M., and Vassberg, J., "BWB Enabling Technologis," *33th ICAS Congress 2022*, Stockholm, Sweden, 2022. URL https://www.icas.org/ICAS_ARCHIVE/ICAS2022/data/papers/ICAS2022_0392_paper.pdf.

[162] De Miguel, N., Acosta, B., Moretto, P., and Ortiz Cebolla, R., "The Effect of Defueling Rate on the Temperature Evolution of On-Board Hydrogen Tanks," *International Journal of Hydrogen Energy*, Vol. 40, No. 42, 2015, pp. 14768–14774. https://doi.org/10.1016/j.ijhydene.2015.06.038.

[163] Sgueglia, A., Schmollgruber, P., Benard, E., Bartoli, N., and Morlier, J., "Preliminary Sizing of a Medium Range Blended Wing-Body Using a Multidisciplinary Design Analysis Approach," *MATEC Web of Conferences*, Vol. 233, EDP Sciences, 2018, p. 00014. https://doi.org/10.1051/matecconf/201823300014.

[164] Reist, T. A., and Zingg, D. W., "Aerodynamic Design of Blended Wing-Body and Lifting-Fuselage Aircraft," *34th AIAA Applied Aerodynamics Conference*, American Institute of Aeronautics and Astronautics, Washington, DC, 2016. https://doi.org/10.2514/6.2016-3874.

[165] Malik, V., Srivastava, S., Bhatnagar, M. K., and Vishnoi, M., "Comparative study and analysis between Solid Oxide Fuel Cells (SOFC) and Proton Exchange Membrane (PEM) fuel cell–A review," *Materials Today: Proceedings*, Vol. 47, 2021, pp. 2270–2275.

[166] Cappuzzo, F., "Application of Model Based Systems Engineering for the Conceptual Design of a Hybrid-Electric ATR 42-500: From System Architecting to System Simulation," *Proceedings of the ASME Turbo Expo 2020: Turbomachinery Technical Conference and Exposition*, 2021. https://doi.org/10.1115/GT2020-15329.

[167] Gunnam, R. S., "Design of a Regional Hybrid Transport Aircraft," Master's thesis, San Jose State University, San Jose, CA, May 2024. A Project Presented to The Faculty of the Department of Aerospace Engineering, In Partial Fulfillment of the Requirements for the Degree of Master of Science in Aerospace Engineering.

[168] The Airline Pilots Forum, "ATR Aircraft Limitations," , 2024. URL https://www.theairlinepilots.com/forumarchive/atr/atr-limitations.pdf, accessed: 2024-09-14.

[169] "International Travel Returns: Top 10 Busiest Airports in the World Revealed," , 2023.

[170] Shirmohammadi, F., Sowlat, M. H., Hasheminassab, S., Saffari, A., Ban-Weiss, G., and Sioutas, C., "Emission Rates of Particle Number, Mass and Black Carbon by the Los Angeles International Airport (LAX) and Its Impact on Air Quality in Los Angeles," *Atmospheric Environment*, Vol. 151, 2017, pp. 82–93.

[171] Short, W., Packey, D. J., and Holt, T., "A Manual for the Economic Evaluation of Energy Efficiency and Renewable Energy Technologies," , 1995.

[172] Zheng, Y., You, S., Huang, C., and Jin, X., "Model-Based Economic Analysis of off-Grid Wind/Hydrogen Systems," *Renewable and Sustainable Energy Reviews*, Vol. 187, 2023, p. 113763.

[173] Morgenthaler, S., Ball, C., Koj, J. C., Kuckshinrichs, W., and Witthaut, D., "Site-Dependent Levelized Cost Assessment for Fully Renewable Power-to-Methane Systems," *Energy Conversion and Management*, Vol. 223, 2020, p. 113150.

[174] Coppitters, D., De Paepe, W., and Contino, F., "Surrogate-Assisted Robust Design Optimization and Global Sensitivity Analysis of a Directly Coupled Photovoltaic-Electrolyzer System under Techno-Economic Uncertainty," *Applied Energy*, Vol. 248, 2019, pp. 310–320.

[175] Steffen, B., "Estimating the Cost of Capital for Renewable Energy Projects," *Energy Economics*, Vol. 88, 2020, p. 104783.

[176] "Projected Costs of Generating Electricity 2020 Edition," , 2020.

[177] (IRENA), I. R. E. A., "Making the Breakthrough: Green Hydrogen Policies and Technology Costs," , 2021.

[178] Khan, M. H. A., Daiyan, R., Han, Z., Hablutzel, M., Haque, N., Amal, R., and MacGill, I., "Designing Optimal Integrated Electricity Supply Configurations for Renewable Hydrogen Generation in Australia," *iScience*, Vol. 24, No. 6, 2021.

[179] Liu, B., Liu, S., Guo, S., and Zhang, S., "Economic Study of a Large-Scale Renewable Hydrogen Application Utilizing Surplus Renewable Energy and Natural Gas Pipeline Transportation in China," *International Journal of Hydrogen Energy*, Vol. 45, No. 3, 2020, pp. 1385–1398.

[180] Povacz, L., and Bhandari, R., "Analysis of the Levelized Cost of Renewable Hydrogen in Austria," *Sustainability*, Vol. 15, No. 5, 2023, p. 4575.

[181] Warwick, N., Griffiths, P., Keeble, J., Archibald, A., Pyle, J., and Shine, K., "Atmospheric Implications of Increased Hydrogen Use," , 2022.

[182] on Climate Change (IPCC), I. P., "The IPCC Scientific Assessment," , 1990.

[183] Hauglustaine, D., Paulot, F., Collins, W., Derwent, R., Sand, M., and Boucher, O., "Climate Benefit of a Future Hydrogen Economy," *Communications Earth Environment*, Vol. 3, No. 1, 2022, p. 295.

[184] Derwent, R. G., "Global Warming Potential (GWP) for Hydrogen: Sensitivities, Uncertainties and Meta-Analysis," *International Journal of Hydrogen Energy*, Vol. 48, No. 22, 2023, pp. 8328–8341.

[185] Jacobson, M. Z., Delucchi, M. A., Ingraffea, A. R., Howarth, R. W., Bazouin, G., Bridgeland, B., Burkart, K., Chang, M., Chowdhury, N., and Cook, R., "A Roadmap for Repowering California for All Purposes with Wind, Water, and Sunlight," *Energy*, Vol. 73, 2014, pp. 875–889.

[186] Ji, M., and Wang, J., "Review and Comparison of Various Hydrogen Production Methods Based on Costs and Life Cycle Impact Assessment Indicators," *International Journal of Hydrogen Energy*, Vol. 46, No. 78, 2021, pp. 38612–38635.

[187] Haoran, C., Xia, Y., Wei, W., Yongzhi, Z., Bo, Z., and Leiqi, Z., "Safety and Efficiency Problems of Hydrogen Production from Alkaline Water Electrolyzers Driven by Renewable Energy Sources," *International Journal of Hydrogen Energy*, 2023.

[188] Yodwong, B., Guilbert, D., Phattanasak, M., Kaewmanee, W., Hinaje, M., and Vitale, G., "AC-DC Converters for Electrolyzer Applications: State of the Art and Future Challenges," *Electronics*, Vol. 9, No. 6, 2020, p. 912.

[189] Miao, B., Giordano, L., and Chan, S. H., "Long-Distance Renewable Hydrogen Transmission via Cables and Pipelines," *International Journal of Hydrogen Energy*, Vol. 46, No. 36, 2021, pp. 18699–18718.

[190] Hydrogen, and Office, F. C. T., "3.2 Hydrogen Delivery," , 2015.

[191] Becker, H., Murawski, J., Shinde, D. V., Stephens, I. E. L., Hinds, G., and Smith, G., "Impact of Impurities on Water Electrolysis: A Review," *Sustainable Energy Fuels*, Vol. 7, No. 7, 2023, pp. 1565–1603.

[192] Khan, M. A., Al-Attas, T., Roy, S., Rahman, M. M., Ghaffour, N., Thangadurai, V., Larter, S., Hu, J., Ajayan, P. M., and Kibria, M. G., "Seawater Electrolysis for Hydrogen Production: A Solution Looking for a Problem?" *Energy Environmental Science*, Vol. 14, No. 9, 2021, pp. 4831–4839.

[193] Buttler, A., and Spliethoff, H., "Current Status of Water Electrolysis for Energy Storage, Grid Balancing and Sector Coupling via Power-to-Gas and Power-to-Liquids: A Review," *Renewable and Sustainable Energy Reviews*, Vol. 82, 2018, pp. 2440–2454.

[194] Economics, F., "Fugitive Hydrogen Emissions in a Future Hydrogen Economy," , 2022.

[195] Esquivel-Elizondo, S., Hormaza Mejia, A., Sun, T., Shrestha, E., Hamburg, S. P., and Ocko, I. B., "Wide Range in Estimates of Hydrogen Emissions from Infrastructure," *Frontiers in Energy Research*, Vol. 11, 2023, p. 1207208.

[196] Penke, C., Falter, C., and Batteiger, V., "Pathways and Environmental Assessment for the Introduction of Renewable Hydrogen into the Aviation Sector," *Progress in Life Cycle Assessment 2019*, 2021, pp. 41–52.

[197] Degirmenci, H., Uludag, A., Ekici, S., and Karakoc, T. H., "Analyzing the Hydrogen Supply Chain for Airports: Evaluating Environmental Impact, Cost, Sustainability, Viability, and Safety in Various Scenarios for Implementation," *Energy Conversion and Management*, Vol. 293, 2023, p. 117537.

[198] Nandi, T. K., and Sarangi, S., "Performance and Optimization of Hydrogen Liquefaction Cycles," *International Journal of Hydrogen Energy*, Vol. 18, No. 2, 1993, pp. 131–139.

[199] Ohlig, K., and Decker, L., "The Latest Developments and Outlook for Hydrogen Liquefaction Technology,"
2014, pp. 1311–1317.

[200] Yang, C., and Ogden, J., "Determining the Lowest-Cost Hydrogen Delivery Mode," *International Journal of
Hydrogen Energy*, Vol. 32, No. 2, 2007, pp. 268–286.

[201] Hoelzen, J., Flohr, M., Silberhorn, D., Mangold, J., Bensmann, A., and Hanke-Rauschenbach, R., "H2-
Powered Aviation at Airports–Design and Economics of LH2 Refueling Systems," *Energy Conversion and
Management: X*, Vol. 14, 2022, p. 100206.

[202] Fesmire, J. E., and Swanger, A., "DOE/NASA Advances in Liquid Hydrogen Storage Workshop," , 2021.

[203] Burke, A., Ogden, J., Fulton, L., and Cerniauskas, S., "Hydrogen Storage and Transport: Technologies and
Costs," , 2024.

[204] of Energy Efficiency, D.-T. O., and (EERE), R. E., "Hydrogen Delivery," , ???? URL https://www.energy.
gov/eere/fuelcells/hydrogen-delivery.

[205] Sherif, S. A., Barbir, F., and Veziroglu, T. N., *Principles of Hydrogen Energy Production, Storage and
Utilization*, 2003.

[206] Hanks, G. W., Andrews, D. G., Brende, B., Eckert, E. E., Hamamoto, M., Kimble, R. H., Kreitinger,
R. L., Miyatake, H. J., Momenthy, A. M., and Taylor, R. A., "An Exploratory Study to Determine the
Integrated Technological Air Transportation System Ground Requirements of Liquid-Hydrogen-Fueled
Subsonic, Long-Haul Civil Air Transports," , 1976.

[207] Sefain, M. J., "Hydrogen Aircraft Concepts and Ground Support," , 2005.

[208] Mangold, J., Silberhorn, D., Moebs, N., Dzikus, N., Hoelzen, J., Zill, T., and Strohmayer, A., "Refueling of
LH2 Aircraft—Assessment of Turnaround Procedures and Aircraft Design Implication," *Energies*, Vol. 15,
No. 7, 2022, p. 2475.

[209] Hromadka, M., and Cíger, A., "Hydrant Refueling System as an Optimisation of Aircraft Refuelling,"
Transport Problems, Vol. 10, 2015.

[210] Brewer, G. D., "LH2 Airport Requirements Study," , 1976.

[211] Jones, L., Wuschke, C., and Fahidy, T. Z., "Model of a Cryogenic Liquid-Hydrogen Pipeline for an Airport Ground Distribution System," *International Journal of Hydrogen Energy*, Vol. 8, No. 8, 1983, pp. 623–630.

[212] Brewer, G. D., *Hydrogen Aircraft Technology*, Routledge, 2017.

[213] Undertaking, H. J., "Hydrogen Powered Aviation: A Fact-Based Study of Hydrogen Technology, Economics, and Climate Impact by 2050," , 2020.

[214] Davidson, C., Newes, E., Schwab, A., and Vimmerstedt, L., "Overview of Aviation Fuel Markets for Biofuels Stakeholders," , 2014.

[215] "Annual Energy Outlook 2021: With Projections to 2050," , 2021.

[216] "FlyZero | Hydrogen Infrastructure and Operations," , 2022.

[217] Riera, J. A., Lima, R. M., and Knio, O. M., "A Review of Hydrogen Production and Supply Chain Modeling and Optimization," *International Journal of Hydrogen Energy*, Vol. 48, No. 37, 2023, pp. 13731–13755.

[218] Vimmerstedt, L., Akar, S., Mirletz, B., Sekar, A., Stright, D., Augustine, C., Beiter, P., Bhaskar, P., Blair, N., and Cohen, S., "Annual Technology Baseline: The 2022 Electricity Update," , 2022.

[219] Vartiainen, E., Masson, G., Breyer, C., Moser, D., and Román Medina, E., "Impact of Weighted Average Cost of Capital, Capital Expenditure, and Other Parameters on Future Utility-scale PV Levelised Cost of Electricity," *Progress in Photovoltaics: Research and Applications*, Vol. 28, No. 6, 2020, pp. 439–453.

[220] Sens, L., Piguel, Y., Neuling, U., Timmerberg, S., Wilbrand, K., and Kaltschmitt, M., "Cost Minimized Hydrogen from Solar and Wind–Production and Supply in the European Catchment Area," *Energy Conversion and Management*, Vol. 265, 2022, p. 115742.

[221] Fasihi, M., and Breyer, C., "Baseload Electricity and Hydrogen Supply Based on Hybrid PV-Wind Power Plants," *Journal of Cleaner Production*, Vol. 243, 2020, p. 118466.

[222] Lauf, J., and Zimmermann, R., "Costs of Building New Energy Infrastructure and Transporting," , 2023.

[223] Ghaffour, N., Missimer, T. M., and Amy, G. L., "Technical Review and Evaluation of the Economics of Water Desalination: Current and Future Challenges for Better Water Supply Sustainability," *Desalination*, Vol. 309, 2013, pp. 197–207.

[224] Shokri, A., and Fard, M. S., "Techno-Economic Assessment of Water Desalination: Future Outlooks and Challenges," *Process Safety and Environmental Protection*, Vol. 169, 2023, pp. 564–578.

[225] Im, S. J., Jeong, S., Jeong, S., and Jang, A., "Techno-Economic Evaluation of an Element-Scale Forward Osmosis-Reverse Osmosis Hybrid Process for Seawater Desalination," *Desalination*, Vol. 476, 2020, p. 114240.

[226] "The Future of Hydrogen Seizing Today's Opportunities," , 2019.

[227] Petitpas, G., Simon, A. J., Moreno-Blanco, J., and Aceves, S. M., "Liquid Hydrogen Infrastructure Analysis," , 2017.

[228] Yang, C., and Ogden, J., "Determining the Lowest-Cost Hydrogen Delivery Mode," *International Journal of Hydrogen Energy*, Vol. 32, No. 2, 2007, pp. 268–286.

[229] Insights, H., "A Perspective on Hydrogen Investment, Market Development and Cost Competitiveness," , 2021.

[230] Sens, L., Piguel, Y., Neuling, U., Timmerberg, S., Wilbrand, K., and Kaltschmitt, M., "Cost Minimized Hydrogen from Solar and Wind–Production and Supply in the European Catchment Area," *Energy Conversion and Management*, Vol. 265, 2022, p. 115742.

[231] Swanger, A., "World's Largest Liquid Hydrogen Tank Nearing Completion," , 2022.

[232] Reuß, M., Grube, T., Robinius, M., Preuster, P., Wasserscheid, P., and Stolten, D., "Seasonal Storage and Alternative Carriers: A Flexible Hydrogen Supply Chain Model," *Applied Energy*, Vol. 200, 2017, pp. 290–302.

[233] Marcinkoski, J., Vijayagopal, R., Adams, J., James, B., Kopasz, J., and Ahluwalia, R., "DOE Advanced Truck Technologies–Subsection of the Electrified Powertrain Roadmap," , 2019.

[234] Davis, J., "Aviation Sustainability: Our Future," In partnership with ALI and University of Limerick, 2024.

[235] Administration, F. A., "The Operations Network (OPSNET): Official Source of FAA," , ????

[236] Airports, L. A. W., "Official Source of Los Angeles World Airports (LAWA)," , ????

[237] Gurney, K., Patarasuk, R., Liang, J., Song, Y., O'Keeffe, D., Rao, P., Whetstone, J., Duren, R., Eldering, A., and Miller, C., "The Hestia Fossil Fuel CO2 Emissions Data Product for the Los Angeles Megacity (Hestia-LA)," *Earth System Science Data*, Vol. 11, 2019, pp. 1309–1335. https://doi.org/https://doi.org/10.5194/essd-11-1309-2019.

[238] Amy, C., and Kunycky, A., "Hydrogen as a renewable energy carrier for commercial aircraft," *arXiv preprint arXiv:1910.05632*, 2019.

[239] Hoelzen, J., Koenemann, L., Kistner, L., Schenke, F., Bensmann, A., and Hanke-Rauschenbach, R., "H2-powered aviation–Design and economics of green LH2 supply for airports," *Energy Conversion and Management: X*, Vol. 20, 2023, p. 100442.

[240] Burke, A., Ogden, J., Fulton, L., and Cerniauskas, S., "Hydrogen Storage and Transport: Technologies and Costs," 2024.

[241] U.S. Department of Energy, "Hydrogen Storage," , n.d. URL https://www.energy.gov/eere/fuelcells/hydrogen-storage, accessed: 2024-09-16.

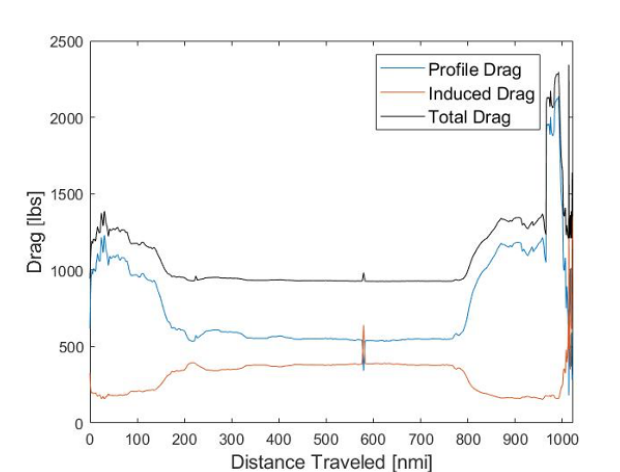# A. Dynamic modeling of SOFC/GT

Fig. A.1   Drag profile of the example Cessna S550 Citation S/II flight trajectory from East Hampton Airport (HTO) to Palm Beach International Airport (PBI)
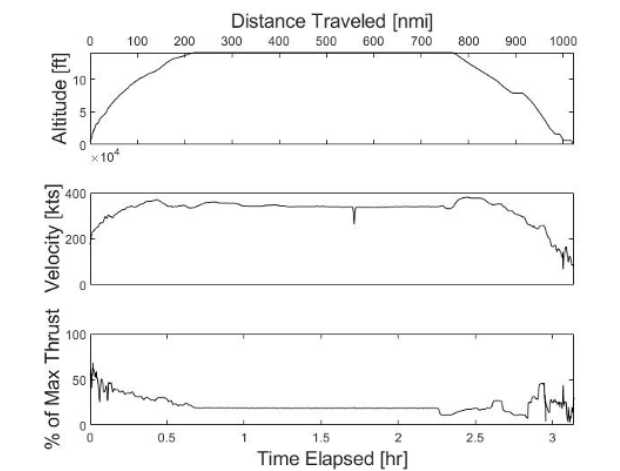

Fig. A.2   Aircraft altitude, velocity, and modeled percentage of maximum thrust versus distance traveled and time of the example Cessna S550 Citation S/II flight trajectory from East Hampton Airport (HTO) to Palm Beach International Airport (PBI)
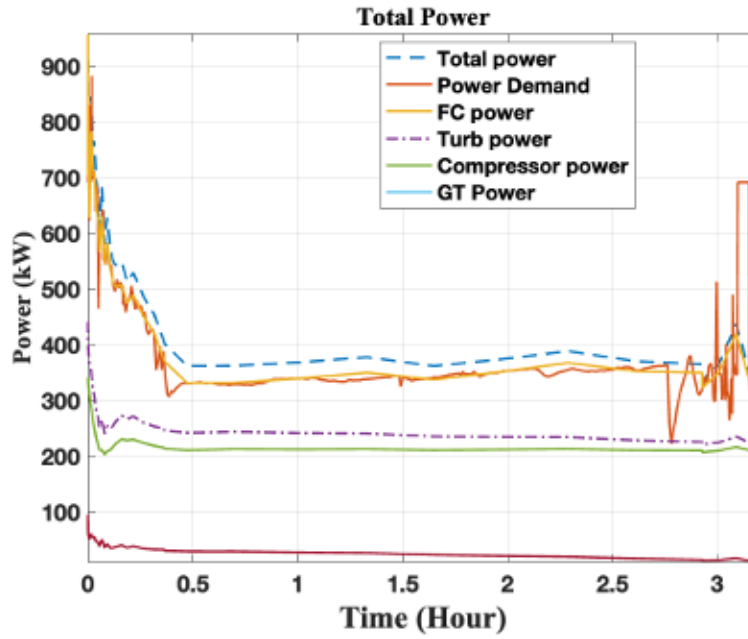
Fig. A.3 Power profile for the second mission profile analyzed.

Table A.1 Proportional and integral gains for SOFC/GT controls

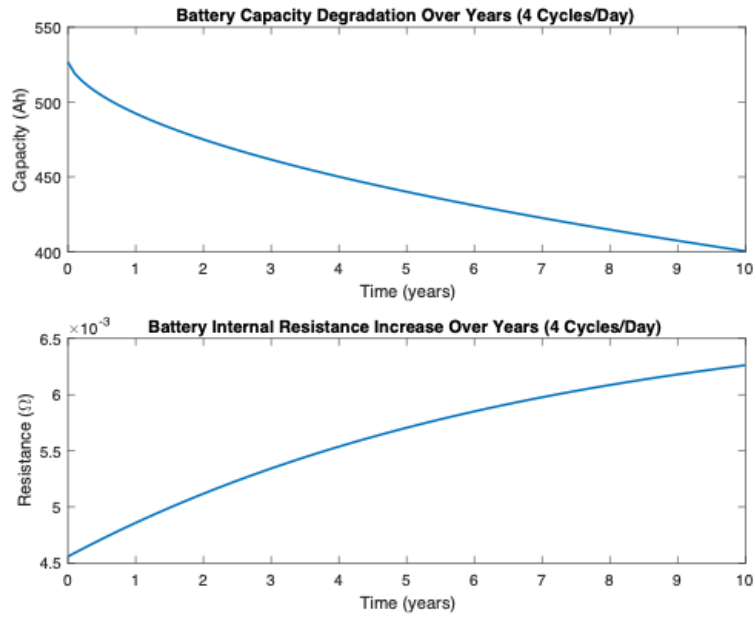| Manipulated Variable	Controlled Variable	Gain	Proportional Gain
Tcathout	RPM	1e-3	1e-2
RPM	GenPower	1	1e2
Current Density	Fuel Cell Power (FCPower)	2	0
Fuel flow	Turbine Inlet Temperature (TIT)	0	0
Cold Bypass	Cathode Inlet Temperature (Tin)	1e-1	2
Recycle	Oxidant Bypass (OXBypass)	0	1
Blower	Blower Outlet Temperature (BlowerT)	1e-3	1e-2

Fig. A.4 Battery degradation and internal resistance after 10 years

B. Design Methodology of BWB

B.1. Emission tables

Table B1   Fuel Burnt and Emissions by Flight Segment for Example Flight Trajectory from SFO to HKG Aboard a B777-300ER

Segment	Fuel Burnt (kg)	CO_2 (kg)	H_2O (kg)	NOx (kg)	CO (kg)	HC (kg)
Taxi	91.316	282.06	112.91	0.50324	3.1575	0.33202
Takeoff	33.966	106.91	42.719	1.7346	0.0042458	0.0010869
Climb	3124.4	9834	3929.8	113.85	0.42804	0.074985
Cruise	1.3158e+05	4.1416e+05	1.655e+05	5263.2	9.2106	1.579
Descent	2397	7543.2	3013	47.94	1.1985	0.043146
Approach	270.89	851.75	340.67	4.3791	0.58511	0.013003
Total		4.3278e+05	1.7294e+05	5431.6	14.584	2.0432

Table B2   Fuel Burn and Emissions by Flight Segment for Example Flight Trajectory from SFO to HKG Aboard a Hydrogen BWB-365

Segment	Fuel Burn (kg)	H_2O Emissions (kg)	NOx Emissions (kg)
Taxi	11.92	107.25	0.01
Takeoff	4.43	39.89	0.00
Climb	407.71	3669.43	0.39
Cruise	17170.54	154534.90	16.35
Descent	312.80	2815.17	0.30
Approach	35.35	318.14	0.03
Total		161484.78	17.08

Table B3   Emissions and Fuel Burnt for Different Flight Segments for Example Flight Trajectory from SFO to BOS Aboard a B737-800

Segment	Fuel Burnt (kg)	CO_2 (kg)	H_2O (kg)	NO_x (kg)	CO (kg)	HC (kg)
Taxi	15.779	48.964	19.559	0.067848	0.40867	0.048914
Takeoff	6.1638	19.396	7.7498	0.12636	0.0036983	0.00061638
Climb	731.4	2301.6	919.59	12.726	0.3657	0.07314
Cruise	10453	32898	13146	156.8	3.1359	0.52265
Descent	607.28	1909.9	763.17	4.2509	0.91092	0.12146
Approach	43.754	137.5	55.012	0.41566	0.14001	0.0043754
Total		37315	14911	174.38	4.9649	0.77115

Table B4   Fuel Burn and Emissions by Flight Segment for Example Flight Trajectory from SFO to BOS Aboard a Hydrogen BWB-162

Segment	Fuel Burn (kg)	H_2O Emissions (kg)	NOx Emissions (kg)
Taxi	2.71	24.38	0.00
Takeoff	1.06	9.52	0.00
Climb	125.56	1130.06	0.12
Cruise	1794.50	16150.50	1.71
Descent	104.25	938.28	0.10
Approach	7.51	67.60	0.01
Total		18320.34	1.94

Table B5   Emission factors for different aircraft models.

kg/px-km	CO_2	H_2O	NOx	CO	HC
Kerosene B777-300ER	0.1121	0.044794	0.0014069	3.7774×10^{-6}	5.2922×10^{-7}
H_2 BWB-365	0	0.041827	4.4239×10^{-6}	0	0
Kerosene 737-800	0.059283	0.023689	0.00027704	7.8878×10^{-6}	1.2251×10^{-6}
H_2 BWB-162	0	0.029106	3.0821×10^{-6}	0	0
H_2 T&W-365	0	0.05414	5.7268×10^{-6}	0	0
H_2 T&W-162	0	0.040571	4.2895×10^{-6}	0	0

Table B6   Total CO$_2$ equivalent emissions for different aircraft models.

Aircraft	Total CO$_2$eq (kg/passenger-km)
Kerosene B777-300ER	0.17103
H$_2$ BWB-365	0.0026447
Kerosene 737-800	0.071802
H$_2$ BWB-162	0.0018405
H$_2$ T&W-365	0.0034233
H$_2$ T&W-162	0.0025653
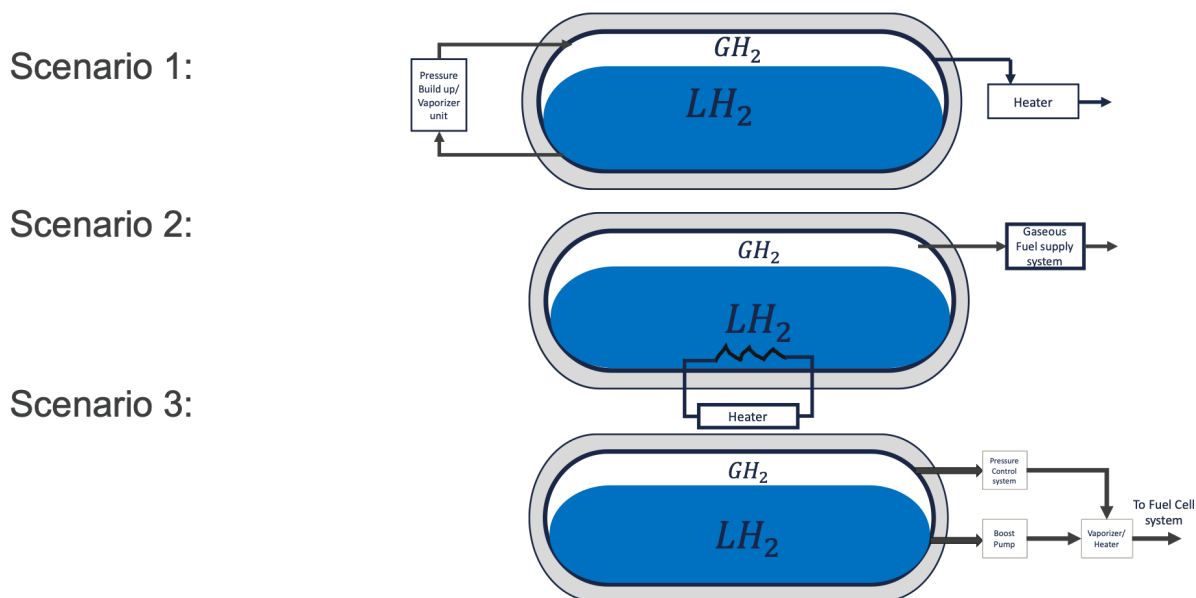
*Pressure values excluded

Fig. B.1   Three different hydrogen defueling scenarios for a liquid hydrogen (LH$_2$) tank. Scenario 1 depicts pressure build-up using a vaporizer unit and a heater. Scenario 2 adds direct heating within the tank. Scenario 3 incorporates a boost pump, pressure control system, and vaporizer/heater for liquid hydrogen extraction.

C. Hydrogen Airport Transformation

C.1. Hourly year-round analysis of energy mix

Our assessment demonstrates that to achieve stable production, a 20% increase in solar PV capacity is necessary. Additionally, multiple days of seasonal hydrogen storage are required to buffer against seasonal fluctuations in renewable power. To produce excess hydrogen, the electrolyzer current is dynamically adjusted, ramping up by increasing the current during surplus power periods to maximize hydrogen output. In Southern California, depleted oil and gas fields in the Los Angeles and Ventura Basins could provide geological storage at a lower cost, estimated between $0.35 to $1.00 per kg of hydrogen, leveraging existing infrastructure and favorable geological conditions. A $1.00 per kg assumption is made in this section. The following section presents the results of this analysis, with the LCOH for 2030 being $5.75 to $6.08 (appx. 3% increase), and $3.29 to $3.30 for 2050 (appx. 10% increase) when geological storage of $1 per kg.

C.2. Hourly Year-Round Analysis with geological seasonal storage

2030 Hourly Year-Round Analysis

Table C1 Power Generation and Storage Capacity for 2030

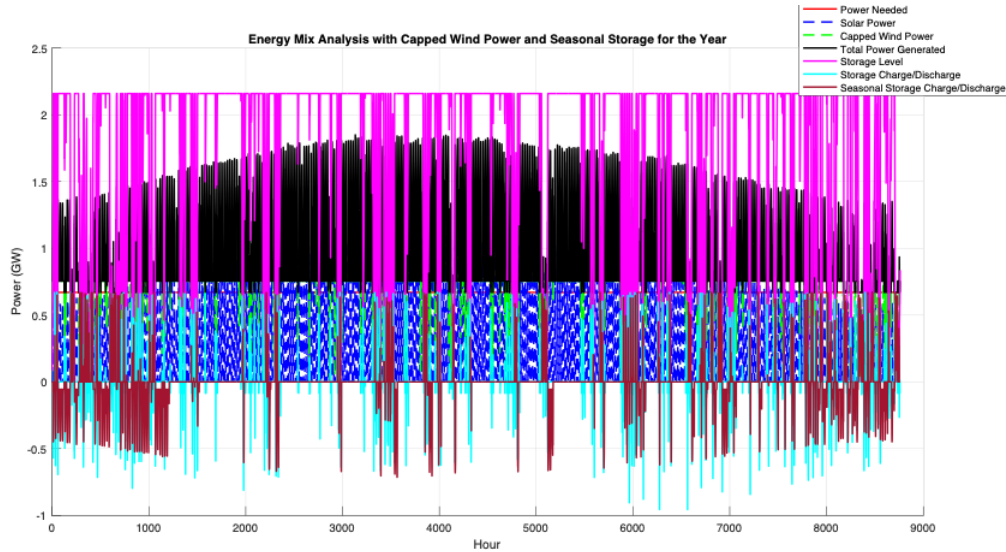| Parameter	Value
Maximum Solar Power Generated	1.0947 GW =
Maximum Wind Power Generated	0.7546 GW (capped at 0.75 GW)
Storage Capacity	2.203 GW
Seasonal Storage Capacity	50.0000 GW · hours (6 days hydrogen storage)

Fig. C.1 Power needed, generated, and storage dynamics over one year (2030), showing solar power, capped wind power, total power generated, storage levels, and storage charge/discharge cycles.
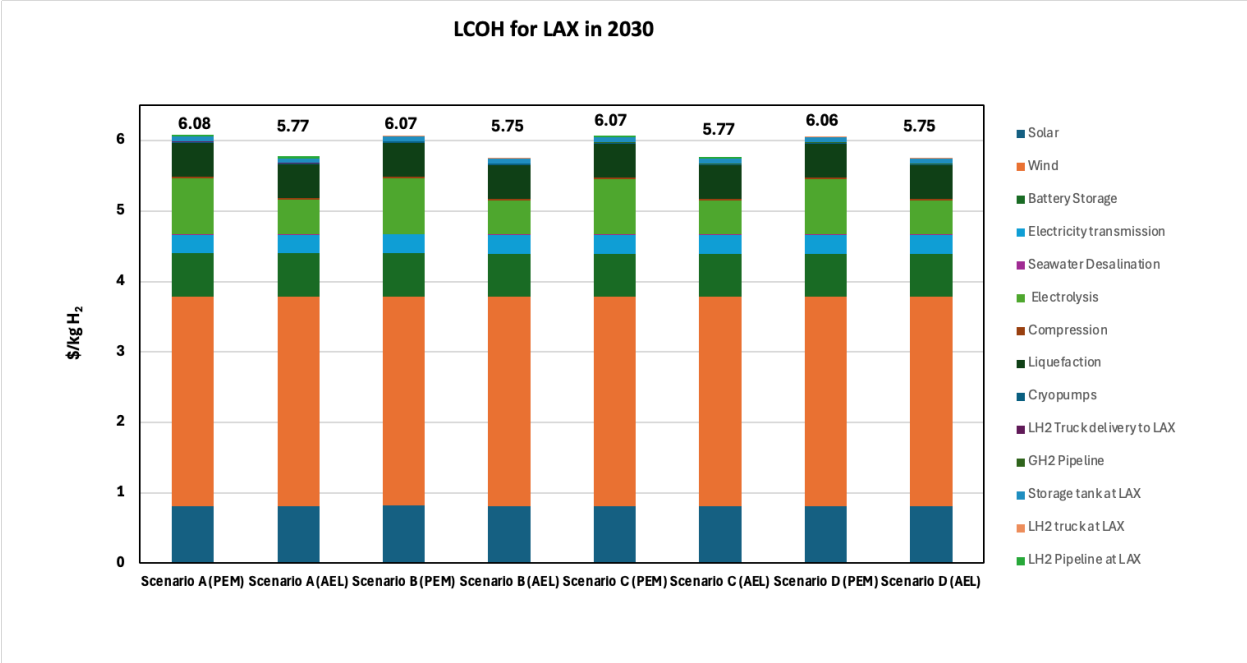
Fig. C.2   Levelized Cost of Hydrogen (LCOH) for LAX in 2030 under different scenarios using PEM and AEL technologies. Each bar represents the cost breakdown in \$/kg H$_2$ for various components such as solar, wind, battery storage, electrolysis, and transport.

2030 Hourly Year-Round Analysis

Table C2   Power Generation and Storage Capacity for 2050

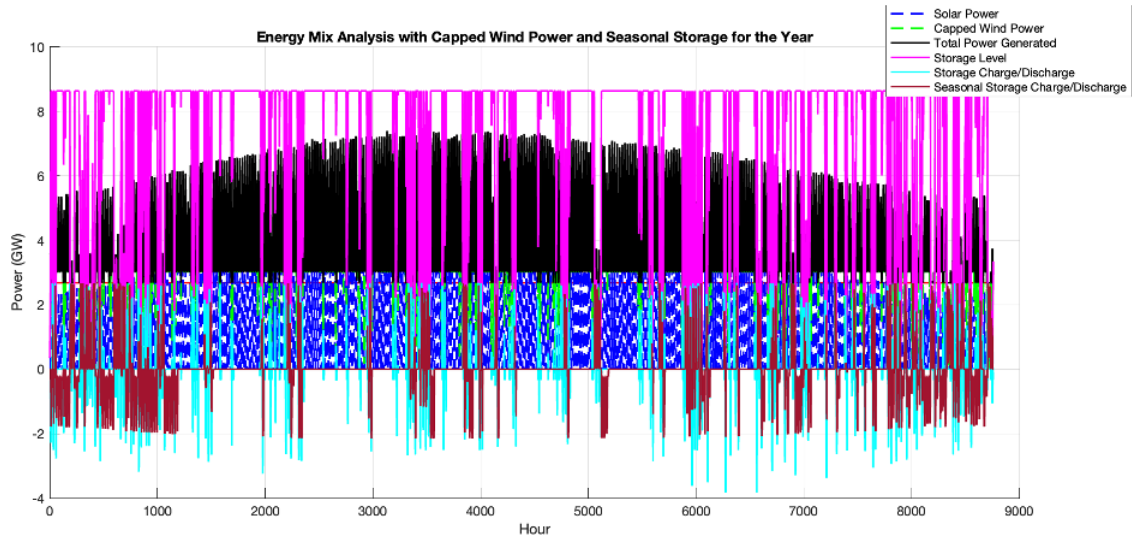| Parameter	Value
Maximum Solar Power Generated	4.3788 GW
Maximum Wind Power Generated	3.0184 GW (capped at 3.02 GW)
Storage Capacity	8.812 GW
Seasonal Storage Capacity	180.0000 GW · hours (5 days hydrogen storage)

Fig. C.3 **Power needed, generated, and storage dynamics over one year (2050), showing solar power, capped wind power, total power generated, storage levels, and storage charge/discharge cycles.**
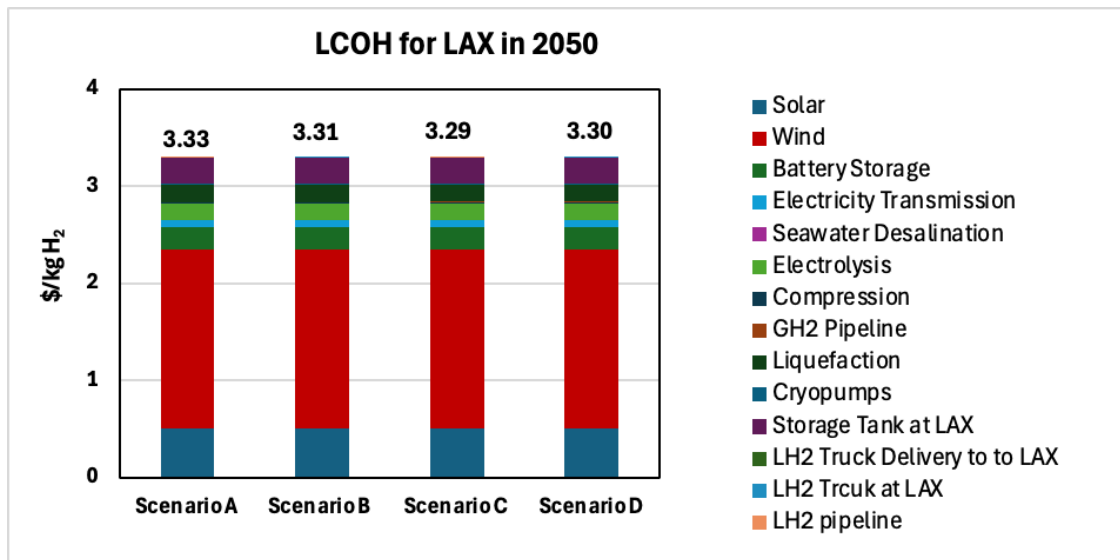

Fig. C.4 **Levelized Cost of Hydrogen (LCOH) for LAX in 2050 under different scenarios. The figure shows the cost breakdown in $/kg H_2 for various components such as solar, wind, battery storage, electrolysis, and different methods of hydrogen transport and storage. The total cost for each scenario is indicated above each bar.**